Departamento de Física Teórica
Facultad de Ciencias
Universidad Autónoma de Madrid
Abril 2009

Emission-line Star-Forming Dwarf Galaxies: Self-Consistent Evolutionary Models

Memoria que presenta para optar al grado de
Doctor en Ciencias Físicas

Mariluz Martín Manjón

Dirigida por

Dra. Ángeles Isabel Díaz Beltrán
Profesora Titular del Dpto. Física Teórica de la Universidad Autónoma de Madrid.

Dra. Mercedes Mollá Lorente
Investigadora del Dpto. Inv. Básica del CIEMAT.

Agradecimientos

Quien me conozca sabe que no suelo dejar las cosas para el final ni para el último momento, de hecho suelo ser bastante impaciente para todo. Sin embargo, parece que funciono mejor bajo presión y es cuando obtengo los mejores resultados de lo que en ese momento esté ocupando mi tiempo, ya sea un modelo o una gráfica a última hora de la tarde, un teclado para una canción poco antes de tener que grabarlo, bajar de 30 minutos el 6K el mismo día de la carrera, o los agradecimientos de esta Tesis a dos días de entregarla. Sabía lo que me iba a hacer sentir y eso precisamente quería evitar, pero llegados a este punto ... ahora o nunca!

Para Ángeles Díaz y Mercedes Mollá no tengo palabras para agradecerles su apoyo en todo momento, tanto en lo personal como en lo profesional. Les doy las gracias por lo que me han enseñado, por enriquecerme y motivarme, siendo ejemplo de esfuerzo y dedicación y por las fuerzas en los momentos de inseguridad. Gracias a Roberto Terlevich, inspiración para este trabajo, por su ayuda y atención. Aunque nos hayamos visto en contadas ocasiones, siempre me ha hecho llegar su apoyo y sentir su complicidad (gracias también por los trucos para no pasar frio en invierno con la bici!). A Marisa García-Vargas también quiero agradecerle su confianza para compartir proyectos e ideas, sus ánimos y buenos consejos. Elena Terlevich, Polis Papaderos, Janice Lee y un largo etcétera se suman a mis agradecimientos, así como el grupo *Estallidos-AYA-2007-67965-C03-03*, por hacerme sentir una más aunque estuviera empezando y darme la oportunidad de conocer cómo funciona un gran proyecto con grandes personas, y la Universidad Autónoma de Madrid por acogerme y hacer posible el desarrollo de este trabajo.

Marta Gavilán, ha sido como mi hermana mayor (y no mi madre como ella siempre dice que podría ser!), mi compañera de tesis y todo un ejemplo de fortaleza y valentía. Gracias por estar ahí, por compartir y ayudarme con las dudas, tanto de evolución química como de evolución de la vida. Me alegro de que lleguemos al final de este camino juntas. Gracias a Guille, Moni (y a la pequeña Vale!), Rubén, Raúl, Jesús, Manuel, Yago, Alcione, Carlos Hoyos, Marcelo, Enrique Pérez-Montero, Latifa, Héctor, Mike, y todos los compañeros que han pasado por el Observatorio y el 301, siempre dispuestos a echar una mano en todo lo que he necesitado en estos años. Gracias sobre todo por vuestra compañía...bueno, y por cerrar la ventana cuando tengo frío!. A Tomás, Javi, Jose, Sergio, Ernesto, Jose Oñorbe, María, Willy, a las recién llegadas Nuria y Paola, a Nico, con quien, desde el colegio, he compartido vocación e ilusión... son tantos! gracias por los almuerzos, las sobremesas con café, judías y palmeras blancas, por los momentos musicales con los Poves, por dar ánimos y hacer estos años tan amenos y divertidos,

Y cómo he echado de menos a Afri estos últimos años!! con ella si que he compartido inquietudes, sueños, aspiraciones y ganas de enfrentarnos a esto le pese a quien le pese. Gracias por esas tardes de estudio y nervios, y también de risas, de academia, de playa, de pavo y de charlas hasta las mil. Ay amiga! que ya está! Gracias a Ana, a Lourdes, a Carmen (y al pequeño Aníbal!) y a Elena, las mejores amigas que se pueden tener, las que sabes que van a estar ahí aunque no silbes, porque te quieren simplemente por ser tú. Gracias por ciudarme y estar conmigo. Gracias a Asiatics (a Joana y Sergio), y a Grupo Sub 1 (Marta y David), por darme momentos tan buenos y divertidos con la música, que me hacían desconectar y sobre todo disfrutar! Un esfuerzo y una dedicación, recompensados también con cuatro discos, que junto con esta Tesis, formarán la parte material de mi paso por aquí. Gracias a Suso con su divertida reaparición en escena, por sus peliculitas de después de comer. Gracias a Sus por las escapadas con nestea y chucherías, a Iván por convencerme de que es necesario ocuparse de uno mismo y ponerse manos a la obra cuando las cosas te superan, y por extensión a Olga Teresa por encenderme las luces para ver mejor. A los del cole por darme ánimos casi a diario, a mi profesora de física Mercedes y a toda la gente que ha estado ahí, de una manera u otra, todo este tiempo.

Gracias a mis zapatillas de correr, a mi bici, a la Dehesa de la Villa, a Guadarrama, a Cádiz y a Huelva por darme vida y descanso, físico y mental, aunque no siempre lo consiguieran.

Y ahora les toca a los que realmente han aguantado y soportado los nervios, la mala leche y borderías, las migrañas, los parches, han compartido las alegrías y han estado ahí siempre, pasara lo que pasara, para hacerme darme cuenta de lo realmente importante de la vida: Mi familia, todos, los que están y ya no están. Sin ellos nada de esto hubiera sido posible. Su apoyo, desde el momento en el que dije en casa que quería ser astrofísica con 13 años, ha sido el motor que ha me ha dado fuerzas para llegar hasta aquí y hasta mucho más lejos. A Dani, con su paciencia infinita y su amor incondicional, me ha dado todo lo que he necesitado en todo momento. Ha sabido sacar de mí lo mejor que tenía y hacerme ver que era capaz de muchas cosas que jamás hubiera imaginado. Por sacarme la sonrisa siempre con su ingenio y su dulzura. Gracias por estar aquí y compartir tus planes conmigo, y es que nos queda tanto por hacer juntos...

Y si, es largo, pero me queda alguien, la persona más especial y a la que sin duda va la dedicación de esta tesis. A ese "enanus" que bailaba al ritmo de la impresora destartalada que sacaba la tesis de mi hermano y que, unos 10 años después, va a poner el termómetro debajo del flexo de su habitación para ir a la lectura de la mía. A quien con 2 añitos se sabía los planetas y reconocía la Galaxia del Sombrero, la Nebulosa de la Cabeza de Caballo, y

recitaba que "la Luna es un satélite que da vueltas alrededor de la Tierra". A él, que con solo 7 se enfrentó a lo más difícil que te puede traer la vida, con una fuerza y valentía por la que le admiraré siempre.

A mi sobrino Javi.

Madrid, Abril 2009

Contents

ABSTRACT

We have computed a series of realistic and self-consistent models able to reproduce the observable characterstics of HII galaxies in a star bursting scenario. Our models combine different codes of chemical evolution, evolutionary population synthesis and photoionization. The emitted spectrum of HII galaxies is calculated by means of the photoionization code CLOUDY, using as ionizing spectrum the spectral energy distribution (SED) of the modelled HII galaxy. These SED have been computed using new and updated stellar population models, obtained according to the star formation and the metal enrichment histories given by a chemical evolution model. Each model is characterized by three parameters which determine the evolution of a given galaxy: the initial efficiency of star formation, the attenuation or streght of these bursts, and the elapsed time between them. Our model technique gives results that reproduces the observed abundances, diagnostic diagrams and equivalent width vs colour relations for local HII galaxies in every evolutionary stage, and can be extrapolated to other objects under different suumed star formation scenarios.

RESUMEN

Hemos realizado una serie de modelos teóricos auto-consistentes capaces de reproducir las características observables de galaxias HII bajo un escenario de formación estelar de brotes instantáneos. Nuestros modelos combinan diferentes códigos de evolución química, de síntesis evolutiva de poblaciones y de fotoionización. El espectro emitido es reproducido mediante el códgo de fotoionización CLOUDY, el cual es producido por una población ionizante cuya distribución espectral de energía ha sido determinada a partir de un código de síntesis evolutiva, el cual ha sido aplicado según una historia de formación estelar y enriquecimiento químico dado por un código de evolución química. Cada modelo se caracteriza por tres parámetros de entrada que determinan la evolución de la galaxia: la eficiencia inicial de formación estelar, la fuerza o atenuación de los brotes de formación estelar y el tiempo transcurrido entre ellos. Nuestra técnica de modelización da resultados que reproducen tanto las abundancias químicas observadas, como los colores, diagramas de diagnóstico de líneas de emisión y relaciones de la anchura equivalente con colores para cada fase evolutiva de las galaxias HII, pudiendo ser extrapolada a otros objetos bajo diferentes escearios de formación estelar.

Chapter 1

Introduction.

The knowledge about how the star formation takes place in galaxies results extremely important in order to understand the process of galaxy formation in the Universe. If this star formation has been either a continuous process and therefore we could find real young galaxies in our Local Universe, or has reached a maximum in a previous epoch, have been considered for decades without reaching a consensus.

In a hierarchical scenario of galaxy formation, Dwarf Galaxies are the building blocks of the more massive systems as elliptical or spiral galaxies. Local Group dwarf galaxies offer a unique window to their detailed properties, being a unique well-studied most useful sample of low-luminosity galaxies close enough to be resolved into individual stars, that will allow a better understanding of star formation processes, their conditions, metallicity, masses and environmental influences.

On the other hand, dwarf irregulars in the Local Universe constitute a sample of objects that appear chemically unevolved even allowing the determination of primordial abundances. They represent the dominant population, by number, of the present-day Universe (Marzke & daCosta, 1997), and they were almost certainly much more numerous at past epochs (Ellis, 1997). Therefore, dwarf galaxies are very interesting objects to focus on: knowing how the star formation takes places in these systems, we will be able to understand how it proceeds in more distant objects in the Universe.

The types of local Dwarf Galaxies.

Dwarf Irregular galaxies, **dIrr**, are the most common type of dwarfs in the Local Universe. They contain a great amount of neutral and molecular gas and they show evidences for star formation at low-moderate rates. Their star formation histories are not homogeneous: some of them show an almost constant star formation along Hubble time, while others show an episodic star formation with different intensities. The star formation in these galaxies is not mainly produced by density waves due to their small sizes, it is mostly triggered by some different mechanisms as interactions with other objects, ram pressure or tidal stripping, which are responsible of the possible morphological evolution between the different types of dwarf galaxies.

Dwarf Ellipticals, **dE**, are galaxies with low luminosity and a smooth surface brightness distribution. They are typically dominated by an old population, however, it has been demonstrated that some of them have had several star formation episodes, even quite recently (Grebel, 1998). They are gas poor, and sometimes showing less gas than expected for their stellar populations, which make us think that there must be a gas loss process or that this gas is in an unobservable phase.

Dwarf Spheroidals, **dSph**, are the smallest galaxies and they show the lowest surface brightnesses. They are satellites of the large galaxies as MWG. Their star formation histories are diverse but in general they show old populations. Some of them show early episodes of star formation, more than 10-12 Gyr old, others show intermediate populations of 8-6 Gyr, and other ones relatively recent star formation, in the last 1-2 Gyr, which makes the distinction from dIrr more difficult. They are usually identified as dE, but authors refers to dSph to describe galaxies around the MWG, and dE to the galaxies around M31.

Low surface brightness galaxies, **LSBGs** have surface brightnesses fainter than 23 mag/arcsec^2 and low integrated luminosities. Many dE could be classified as LSBGs, even some dIrr. These type of galaxies are very difficult to detect and the knowledge of their stellar population is very poor and incomplete. Column density of HI is very low, lower than the empirical threshold for star formation found for normal galaxies (Kennicutt, 1989), and because of that, the star formation rates (SFRs) are low. However, gas mass fractions of these galaxies are higher than in other types. LSBG looks like gas rich and still unevolved galaxies, both chemically and photometrically, which may be related to their low stellar mass densities

And finally, Blue Compact Dwarf galaxies, **BCDs**, the smallest galaxies with high central surface brightness. BCDs have in general a central region which contains one or more star forming knots, identified as the

starburst region, and an underlying more extended host galaxy. Their central morphology is irregular due to the active star formation, and contains poor information about the extended light distribution which traces the dominant stellar mass. Noeske et al. (2001) found low surface brightness galaxies as companions of BCDs, which could be determinant of their evolution and star formation. Blue compact dwarfs show a low mass to light ratio in the starburst region indicating that most of the stellar mass in the host galaxy. These host galaxies have similar properties to LSBGs (Cairós et al., 2001a, 2002; Telles & Terlevich, 1997), and their gas content may serve as important fuel for star formation in these galaxies.

Cairós et al. (2001b) have grouped the BCDs in four categories according to the position and morphology of the star formation (SF) knots: nuclear starburst, which are galaxies with a prominent central starburst; extended starburst, galaxies with star formation spread over the entire galaxy, chain starburst, objects in which the SF knots are aligned to form a chain and finally, cometary starburst, galaxies with a *cometary* appearance, that is the star formation concentrated in one side of the galaxy. This finding introduces additional complications, because it opens the possibility that different mechanisms may operate in BCDs and that galaxies classified as BCD may actually have different star formation histories and evolutionary paths.

In the present work we will concentrate on **HII galaxies**, a subset of Blue Compact Dwarf Galaxies. They are gas rich and nearly dust free star-forming dwarfs galaxies, whose optical spectra are dominated by strong and narrow emission lines, which means that they are currently experiencing intense star formation in small volumes (Sargent & Searle, 1970).

The star formation episodes are called **star bursts** (Searle & Sargent, 1973). This term have dual notions of intensity and duration. The relevant quantities which define a starburst must be averaged over a finite cell and time and scaled according to the type of object that we are studying. The star formation episode must produce enough massive stars to ionize the surrounding gas, as well as winds and SNe, but there is not a common definition.

Observations indicate that HII galaxies are in general metal poor systems, showing oxygen abundance values between 0.02 and $0.4Z_{\odot}$ (Kunth & Sargent, 1986). Their spectral energy distributions are characterized by intense emission lines produced by the gas ionized by massive stars. However, these very young stellar populations and low metallicities do not necessary mean that these galaxies are really young systems experiencing their first burst of star formation as said by Sargent & Searle (1970). It seems clear that they are currently experiencing a star formation episode but it could be not the

first one.

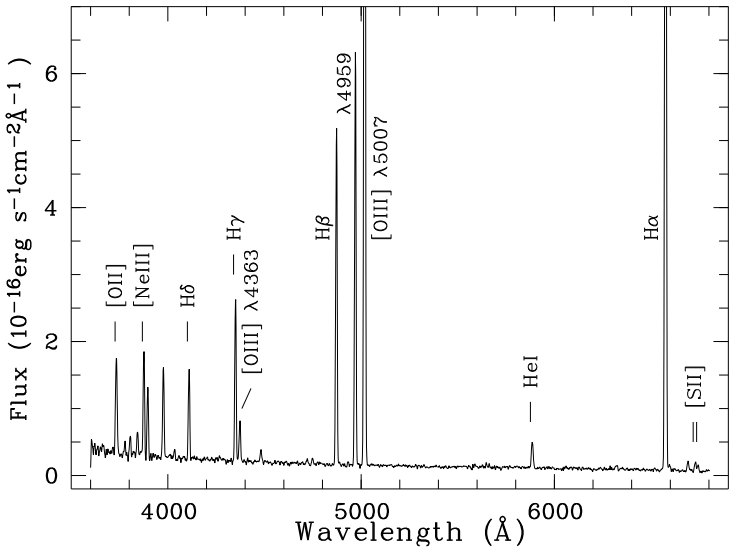

Figure 1.1: Spectrum of the nearby extreme metal-poor dwarf galaxy HS 0822+3542 taken with the Nordic Optical Telescope (NOT) on La Palma. The spectrum is dominated by strong emission lines of hydrogen, oxygen, helium, neon and sulphur (Kniazev et al. 2000).

Recent photometric observations indicate that most of these objects host stellar populations which are at least $10^7 - 10^8$ yr old, reaching in some cases a few Gyr (Telles et al., 1997; Legrand, 2000; Tolstoy, 2003; Cairós et al., 2003; van Zee et al., 2004; Thuan & Izotov, 2005). Even in the most metal-poor galaxy known, Izw18, the best candidate to *primordial galaxy*, there is an underlying population of some 10^8–10^9 yr (Izotov & Thuan, 2004; Aloisi et al., 2005).

Surface brightness and colour profiles indicate that these objects show colours redder than corresponding to the burst population and the analysis of their colour-magnitude diagram shows the presence of old stellar populations. In Figure 1.2 the colour maps for Mrk 35 (Cairós et al., 2007) are shown. In this figure different stellar populations can be detected: the active star formation region, blue and centered, and the extended old component, redder and surrounding the active region.

There are some other indications that seem to confirm that there are older stars than the ones that ionize the gas. Surveys of strong emission line HII galaxies find only a few of them with equivalent widths of H_β, which can be taken as an age indicator for the ionizing population, larger than 200 Å , as can be seen in Figure 1.3, pointing to the existence of underlying populations

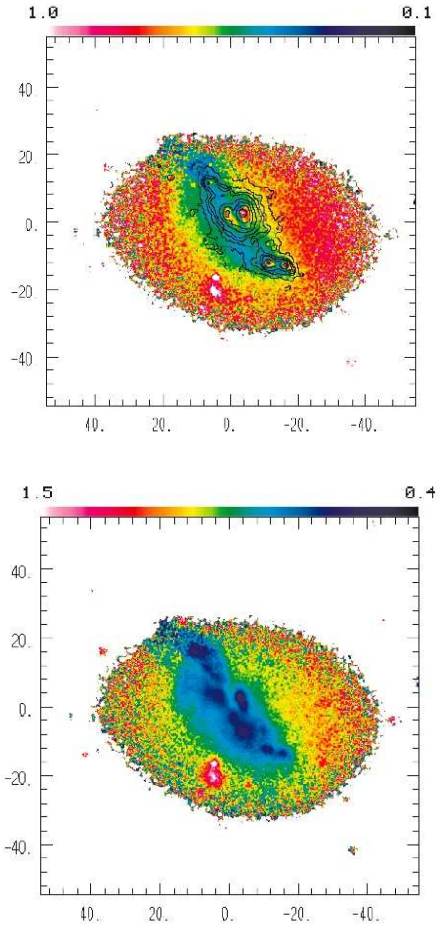

Figure 1.2: Colour maps for Mrk 35 from Cairós et al. (2007). Upper panel shows (B-V) colour and lower panel (B-R)

with ages of several Myr, even Gyr, in BCDs and/or HII galaxies. .

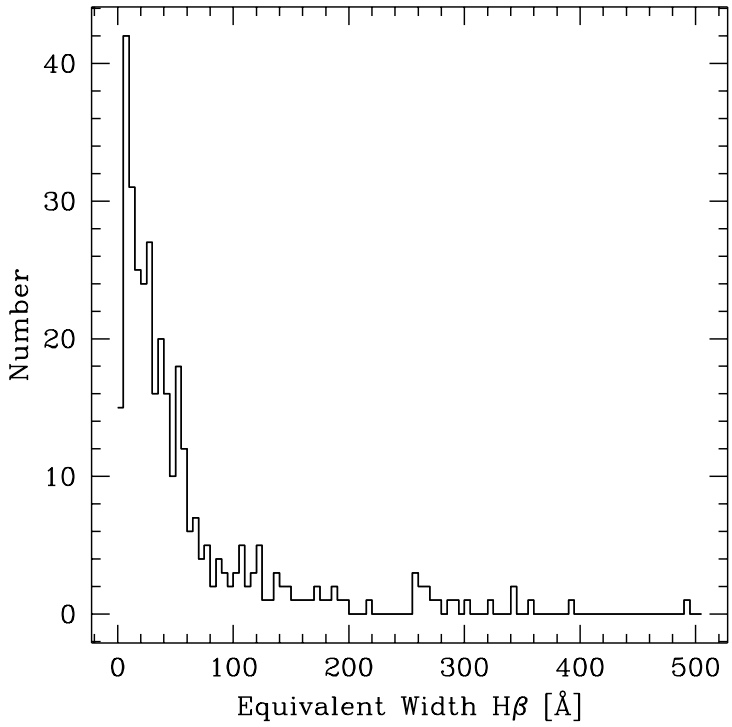

Figure 1.3: Distribution of equivalent width of H_β for HII galaxies from Terlevich et al. (2004)

Terlevich et al. (2004) have shown that the equivalent width of the H_β line, EW(H_β), and the (U-V) colour in HII galaxies show an anti-correlation which cannot be interpreted in terms of a single stellar population (SSP). It can be seen in Figure 1.4, were the EW(H_β) is plotted against a continum ratio pseudo-colour smilar to (U-V): at a given EW(H_β) the data are displaced to colours redder than those predicted by the models.

The most likely explanation is that the ionizing population, that is, the most recent episode of star formation, is overimposed on an older stellar population evolved enough as to produce a redder (U-V) colour (Stasińska et al., 2001).

There is also an inverse correlation between EW(H_β) and the gas oxygen abundance, $12 + log(O/H)$ (Figure 1.5) which could be interpreted in terms of galactic chemical evolution: as the average age and the total mass of the stellar population increases, the EW(H_β) decreases and the mean metallicity of the interstellar medium increases. High metallicity HII galaxies show lower EW(H_β) and low metallicity HII galaxies have high EW(H_β). As we

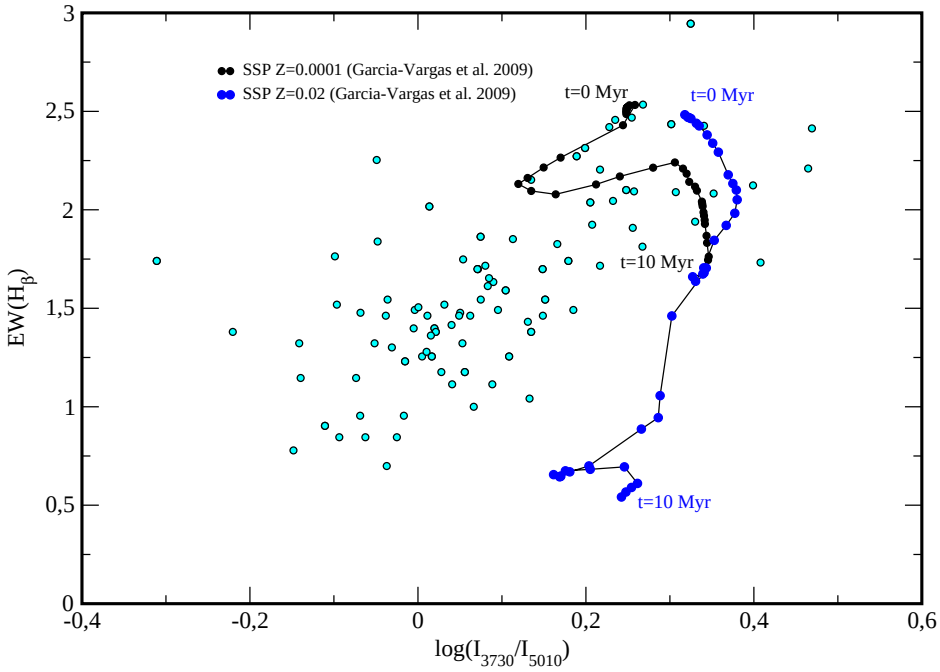

Figure 1.4: EW(H_β) versus a continuum pseudo-colour similar to (U-V) for HII galaxies from Terlevich et al. (1991). Blue and black lines correspond to single stellar population sequences from t=0 to t=10 Myr for two metallicities, Z=0.0001 and Z=0.02 respectively.

see in Figure 1.5 there are two time-scales involved in the evolution of the metallicity-EW(H_β) plane: one about 10^7 years after the starburst, where EW(H_β) decreases rapidly at almost constant oxygen abundance, showing that there is no change in the metal content of the ionized gas during the evolution of the burst, and other longer time-scale: 10^9 yr, where there is a cosmological evolution of the metal content of the inter stellar medium, ISM, which can be seen in the accumulated stellar population contriution. Then, more than one generation of stars is needed in order to cover the values of the oxygen abundance shown by HII galaxies. The dispersion in this EW-metallicity plot could be explained by the combination of these two evolutionary time-scales.

1.1 Star formation scenarios.

A still unresolved question is how the star formation history proceeds in HII galaxies. **Are they dominated by several star formation bursts or by modes that are more quiescent and continuous?** Studies

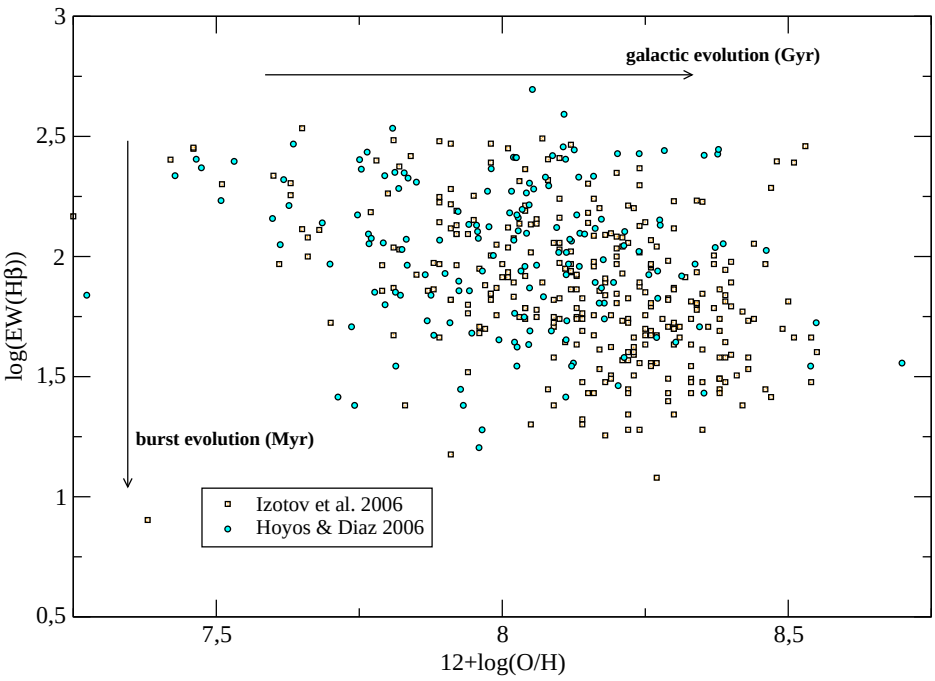

Figure 1.5: EW(H_β) versus oxygen abundance for galaxies taken from Hoyos & Díaz (2006) and Izotov et al. (2006). The two time-scales are shown (see the text)

using present-day integrated properties of galaxies as UBV colours and H_α-based SFR (Tinsley, 1968; Gallagher et al., 1984; Kennicutt, 1998; van Zee, 2001; Bruzual & Charlot, 2003) and complemented with CMD studies have been made for a long time to stablish their evolution. Optical colours and current SFR can be explained in the majority of dIrrs by a star formation history with a constant and a relatively low SFR, contrary to the starburst-phase argument (Legrand & Kunth, 1998; van Zee, 2001), however low-luminosity galaxies selected by emission lines or blue colours show star bursting evidences (Haro, Zwicky, Markarian, KISS or SDSS samples) at least for the current generation of stars which dominates the spectra. Both samples are not statistically complete at all and selection effects can bias the results.

The high surface brightness of the central region of a few parsec of diameter seen in most compact star-forming galaxies is caused by thousands of new stars formed in a violent star formation process, supposed to be brief because the central region can not have enough gas to feed these episodes for more than 10^9 yr. Kunth & Sargent (1986) studied IZw 18 and showed that a starburst comparable to the present one could be sufficient to account

for the observed oxygen abundance of this galaxy, but such SFR can not be maintained for a long time without producing an excessive chemical enrichment and consuming all the available gas.

In spite of the common agreement that the current population of massive stars in these galaxies have been formed in a starburst and the existence of an older underlying stellar population, a consensus about their complete history of star formation has not been reached. Three scenarios have been postulated:

a) A **bursting** star formation: the star formation takes place in short but intense episodes separated by long quiescent periods of very low or null activity (Bradamante et al., 1998).

b) A **gasping** star formation: The star formation takes places as long episodes of SF of moderate intensity separated by short quiescent periods (Tosi et al., 1991; Aparicio & Gallart, 1995; Recchi & Hensler, 2004).

c) A **continuous** star formation: The star formation is continuous and of low intensity during the galaxy life, with superimposed sporadic bursts (Legrand, 2000).

It is not easy to discriminate between scenarios. The very low metallicities, the lack of dust, and the optical colours argue in favour of a bursting star formation with long quiescent periods (e.g. Marconi et al., 1994).

Lee et al. (2004) used the Hα component of the 11HUGS, sample of star forming galaxies, to quantify the prevalence of starbursts in dwarf galaxies in the present day universe. To identify dwarf galaxies undergoing a starburst they use as threshold a value of EW(Hα) of 100Å , and systems with EW(H_β) values smaller than this are considered post-starburst galaxies. The number fraction of dwarf galaxies suffering a starburst is around 6%, and the fraction of stars formed in such systems is 23%. Therefore a continuous, steady state of star formation dominates the present epoch, and it is the mode that operates during the vast majority of the time and in which most of stars are being created. Inactive star forming periods rarely occur and inter-burst states must be characterized by low-levels of star formation rather than its complete cessation, the SFR in the burst mode being 4 times greater than in the quiescent mode. Recent IR observations of BCDs show an excess in the K-band (Figure 1.6) suggesting the presence of a diffuse evolved intermediate mass star population in addition to the old red giant population (Doublier, 1999). The red excess seen in BCDs can not be due only to the young red

giant population, there must be some other older red giant population and intermediate AGB stars (Schulte-Ladbeck & Hopp, 1998), This intermediate mass stellar population of AGBs shows ages between 100 Myr and 5 Gyr, resulting from a mixed underlying population of these stars and red giant stars with ages greater than 10 Gyr .

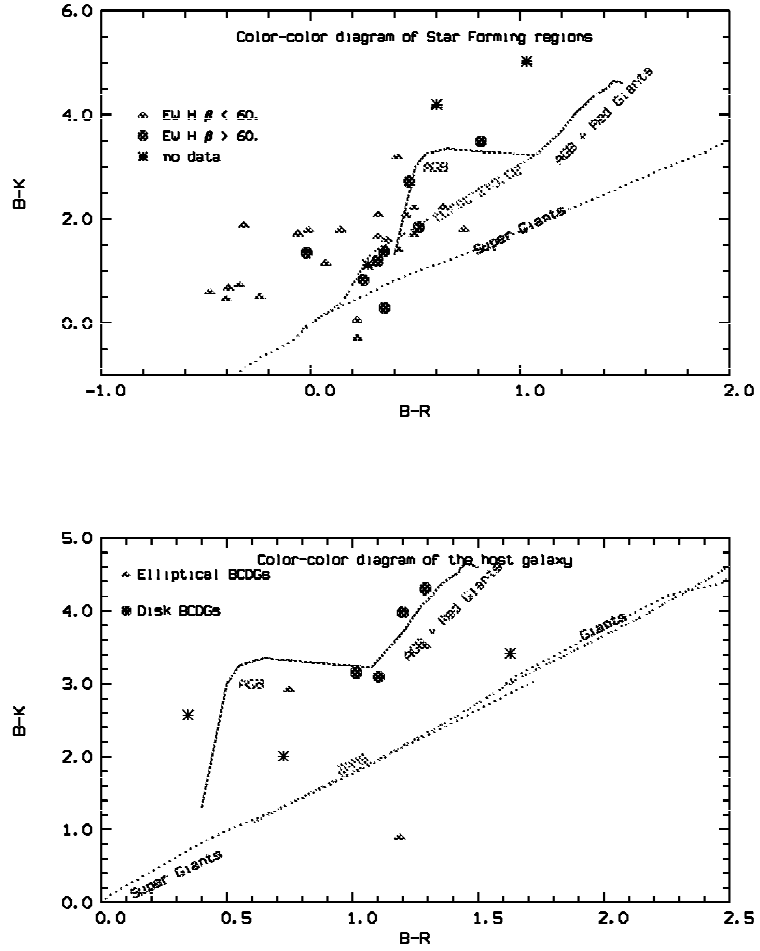

Figure 1.6: Colour-colour diagrams for a sample of BCDs (upper pannel) and their host galaxies (lower panel) from Doublier (1999).

Chemical evolution models with a gasping star formation seem to be good describing some local dIrr as I Zw18 (Recchi & Hensler, 2004), NGC6822 (Marconi et al., 1995), Sextans B (Tosi et al., 1991) and LMC (Gallagher et al., 1996), but it is not easy to differentiate from a bursting process (a). The most remarkable differences in this framework is that short episodes of

star formation enrich the ISM in a time scale of few tens of Myr while long-lasting episodes enrich gradually the ISM in a longer time scale, and any further episode of SF does not leave an appreciable imprint on the chemical evolution. The abundance values, which increase too rapidly in bursting models, maintain the observed values for longer in gasping models, and more adequate ages for the star population observed, are obtained (Recchi et al., 2001, 2002). This picture, however, does not entirely exclude the possibility that their star formation histories be composed by burst cycles when examined with an accurate time resolution, that appear constant when averaged over a Hubble time. It does not exclude neither that the star formation propagates through the galaxy, taking place in individual luminous short lived HII regions. Studying the most luminous HII regions one might get the illusion to witness a sudden starburst event although the average SFR might have been continuous.

Legrand (2000) suggests that the star formation occurs continuously at a very low rate, and the metallicity slowly but continuously increases. Legrand (2001) and Tajiri & Kamaya (2002) claim that since the blue compact dwarfs have plenty of HI, the galactic winds are not strong enough to blow away all of the ISM; that is why BCD keep the HI envelope by themselves, with a continuous not bursting SF. However, Kamaya (2005) shows that a weak galactic wind or mass loss is compatible with episodic star formation histories in BCD, and we can go back to a soft bursting scenario (b) or even to scenario (a).

If the starbursts episodes in BCDs are intermitent, this could mean that these galaxies could be just a phase in the life of a dwarf galaxy, and other galaxies without the conspicuous starburst should also be found, showing similar properties to galaxies without such intense star formation events, as quiescent blue low surface brightness dwarfs (see section 1.3). Sánchez Almeida et al. (2008) obtain a relationship between the duration time of the starburst phase and the quiescent periods, based on the number of objects of each type of their sample, finding that if the time of the burst phase is 10 Myr, the time in quiescence is at least 0.27 Gyr, which means that there will be several starburst episodes along the life of a dwarf galaxy. Then, the ranges in properties exhibited by dwarfs would be a consequence of observing them at different times in their star formation "cycles", and the frequency distributions of galaxies in the various phases could correspond to the time spent in each of those phases.

The chemical evolution point of view.

The star formation history determines the chemical enrichment of the galaxy. Bursts models produce a high amount of massive stars, which, through SNe explosions and winds produced by Wolf Rayet stars, are responsible for the metal enrichmen in relatively short time-scales. A continuous star formation has a lesser impact on the ISM. A discrete star-bursting scenario strongly affects the abundance ratios, such as N/O, Fe/O and C/O. The yields are somewhat metallicity dependent (Maeder, 1992), and the element production by subsequent generations of stars will depend on how fast the ISM is enriched.

The main problem that arises from the chemical evolution of dwarf galaxies is that the oxygen abundances measured in dIrr and BCDs are lower than predicted by the Closed Box Model (without outflows or inflows) with for their observed gas franction, as shown in Figure 1.7. Chemical evolution models for dwarf galaxies try to answer the question of if it is neccesarry a gas loss process to explain the observed abundances or if they can be interpreted in terms of any other mechanism as gas infall, metallicity dependent yields, insufficient sensitivity in molecular hydrogen measurements, etc. The mass loss would also explain the different active and quiescent phases of a dwarf galaxy.

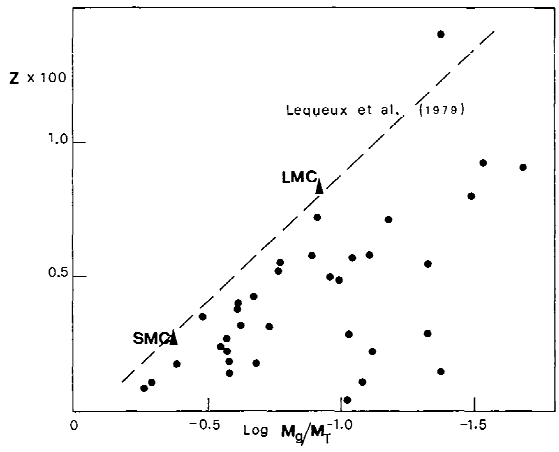

Figure 1.7: Dwarf galaxies lie below the limit of the simple Closed Box Model relation (dashed line) between metallicity and gas mass fraction.

Early chemical evolution models were based on the Closed Box Model (CBM) and addressed the oxygen abundances of HII galaxies (Lequeux,

1979) concluding that Wolf Rayet winds were needed in order to produce less oxygen from SNe.

The first models assuming a bursting star formation were those from Matteucci & Chiosi (1983). They tryied to justify the dispersion in the gas-metallicity diagrams: the data show a range of metallicity values for a given M_{gas}/M_{tot} ratio, all of them below the theoretical line given by the Closed Box Model, and moreover, different for different galaxies. Three possible explanations were suggested:

(A) the Initial Mass Function, IMF, is not universal and it changes from galaxy to galaxy,

(B) different gas outflows are present,

(C) different amounts of gas infall occurs.

In order to cover the region below the CBM limit, several models have been done obtaining different results and withmore or less success suceed in reproducing the abundance ratios and their dispersions. A continuous wind proportional to the star formation rate has been consedered. .

Later models of Matteucci & Tosi (1985) included galactic winds (from 0 to 20 times the SFR), obtaining that, in order to reproduce the N/O dispersion, up to 15 successive bursts of star formation are necessary. If this scenario is correct, the galaxy looses a great amount of metals, showing blue colours during several Gyr; after that, galaxies would show red colours due to the old stellar populations, which is not observed in dwarf galaxies.

This oscillating behaviour reproduce the dispersion observed at low metallicities. Massive stars eject oxygen after 4 Myr of the star formation burst in explosion of SN. The N/O ratioremains low until the ejection of N by intermediate mass stars rises this ratio. When the next burst takes place, before the oxygen ejection by massive stars, galaxies show a high N/O ratio, maintaining the value reached in the previous inter-burst period. 4 Myr after the burst takes place, oxygen is ejected againand the N/O ratio decreases, indicating that the object is in a more evolved stage of the burst. Thus, the inter-burst time also determines the dispersion in N/O. If these periods are long, intermediate stars have had enough time to evolve and eject nitrogen, and the N/O ratio increases. The dispersion in the N/O vs O/H plot could also be due to self enrichment of HII regions according to Pilyugin (1993), who assumes that the elements ejected by massive stars are only mixed within its own HII region, and not with the surrounding medium.

Bradamante et al. (1998) and Marconi et al. (1994) use selective winds (not all the elements are ejected to the ISM) and a bursting scenario, changing the lower mass cutt-off of the IMF in order to produce less intermediate mass stars, and hence less nitrogen abundance. However, they fail to reproduce some abundance ratios. Similar results are obtained by Larsen et al. (2001)

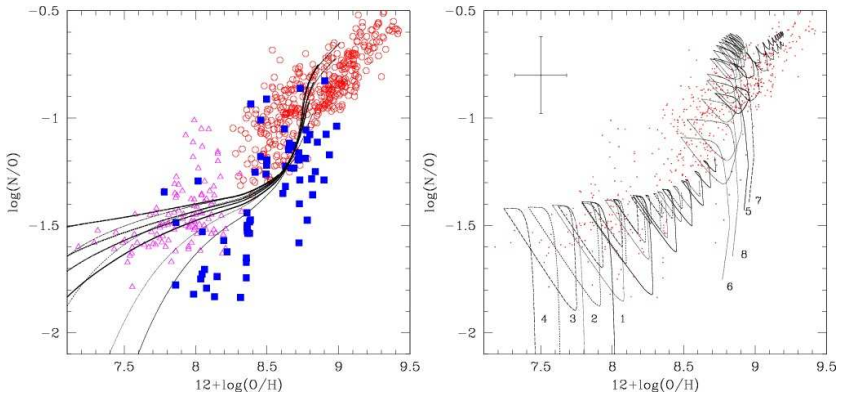

Figure 1.8: N/O vs O/H for a sample of galaxies from Mouhcine & Contini (2002). The left panel shows model predictions assuming a continuous star formation scenario with different star formation timescales. The right panel shows model predictions assuming a bursting star formation scenario.This figure shows clearly the dichotomy between the models which reproduce the scatter in the metal-poor region (12+log(O/H) $\leq$ 8), and those which reproduce the scatter in the metal-rich region (12+log(O/H) $>$ 8)

using selective galactic winds and hidrodynamical simulations. Mouhcine & Contini (2002) compute models with continuous and bursting star formation (Figures 1.8). They find that the variation of the star formation efficiency in continuous models reproduce the scatter in N/O for low mass HII galaxies, while bursting star formation models explain the scatter for both, low mass and more massive galaxies, which is explained in terms of the time delay between the ejection of oxygen and nitrogen into the ISM.

Gasping models made by Recchi et al. (2001, 2002) obtain good results for one burst and two-burst models. However, the single burst model is not consistent with the observed underlying population. The two-burst model made for I Zw 18 takes into account a quiescent period of 300 Myr and a burst duration of 4-15 Myr. The galactic winds only occurs during the second, more intense burst, ejecting most of the metals produced and reproducing this way the low abundances shown in this galaxy.

Continuous star formation models also seems to reproduce the N/O dispersion shown by low metallicity galaxies, assuming low star formation rates. However, for higher values of O/H, these models do not work.

Using a set of generalized models for different types of galaxies, Mollá et al. (2006) obtain N/O abundance ratios in good agreement with most observational trends for both low and high O/H abundances. Their models assume, for different galaxy masses, different collapse time-scales and different star formation effciencies. The combination of these two parameters

produce different star formation histories, having an important impact on the resulting N/O ratio. However, they do not discard the existence of gas outflows in some galaxies.

1.2 Evolutionary connections among dwarf galaxies.

Are we really talking about different star formation scenarios or mechanisms for different kind of objects or about the same object in different evolutionary stages? What are the connections among the different dwarf galaxies which can really justify each of these assumptions?.

Same object at different evolutionary stages.

There are evidences pointing towards the existence of an evolutionary link between dIrr, BCDs and dE (e.g. Evans et al., 1990). The gas poor galaxies (dE) must have contained gas sometime in order to form the observed old stellar population, and BCD may have different periods of intense star formation and quiescence, presenting different stages on their evolution. Their structural parameters are quite similar forming continuous sequences in different parameter spaces. The strong correlation between mass and metallicity found for both dE and dIrr seem to indicate that the less massive galaxies are unable to retain the heavy elements produced by each stellar generation. Regarding the luminosity-surface brightness relation, dE and dIrr follow identical trends in velocity dispersions, core radius, central surface brightness and absolute magnitudes. Thus evolutionary connections are likely to exist.

There are two possible connections or evolution/change mechanisms between dwarfs:

-external or passive : due to interactions or any other external effects with the environment, which means that a field galaxy will not evolve in the same way as a galaxy in a cluster or dense environment.

-internal or active : the evolution of the galaxy is due to internal physical processes, like gas expulsion or gas consumption, both produced by the star formation.

DSph could have been dIrr in the past and have lost their gas due to ram pressure stripping from the MWG of which they are satellites. The dIrr to dSph transformation could be possible on a time scale of about 4 Gyr thanks to the interaction with the MWG according to the models of Pasetto et al. (2003).

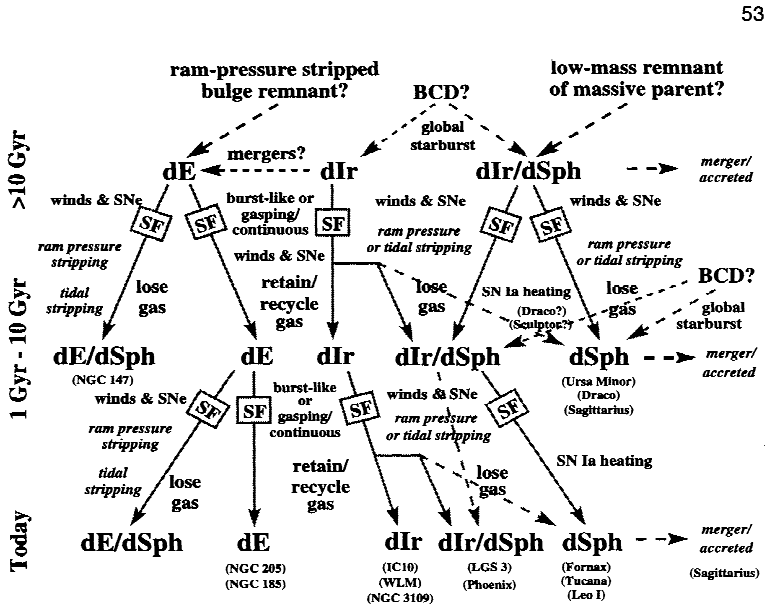

Figure 1.9: Evolutionary scheme between dwarf galaxies of the Local Group and the possible mechanisms which make the evolution to proceed (Grebel 1997)

Thuan (1985) suggested that gas rich dwarfs could evolve into dEs after the HI envelope is stripped for both external and internal reasons. Some dE seem to have an important population of young or intermediate stars, so in active star formation stages they must have been similar to dIrr or even BCDs, depending on the duration or extension of their star formation episode. A dIrr converts more than 90% of its initial gas in stars during a long period of low star formation rate. A modest number of SNe can be enough to remove the gas in small galaxies and changing into a dE in 1-2 Gyr after star formation. On the other hand, Legrand (2000) conclude that stellar winds are not strong enough to blow out the material to the ISM, and that dIrr seems to be able to maintain a constant low star formation over a Hubble time, so there is no need of an evolutionary connection with another type of dwarf galaxy and the only possible change to a dE must be for a external reason like mergers or tidal stripping MacLow & Ferrara (1998) and Brighenti & D'Ercole (1999) argue that only extremely low mass galaxies remove their gas due to a starburst: hot gas (including most of metals ejected by massive stars) will scape, but the colder gas will stay. If this scenario is "cyclic" it would be possible to form additional generations of stars, as observed in BCDs, where more than one star formation episode takes place. Then, the question is: can a BCD be considered a dIrr in a very

active phase?. Papaderos et al. (1996a,b) find that the link between dIrr or dE and BCDs is not realistic unless their structure change during the bursting phase. Hosts of BCD galaxies have significantly different characteristics from other normal dwarf galaxies. They have, on average, higher central surface brightness than dIrrs and are a factor of 2 smaller in their exponential scale length.These results could be interpreted by a new evolutionary picture: if dIrrs end as dE after several BCD phases, the underlying host must undergo changes in its structural properties. The evolutionary link would then be possible only if the underlying component can adjust its structural properties to change the global gravitational potential due to the mass loss caused by the starburst processes. Therefore, according to Papaderos et al. (1996a) (see also **?**)apa96b, sal99, tell97, BCDs cannot be hosted by just any dwarf galaxy.

However, due to their extreme nature, it has been difficult to determine what kind of galaxy hosts BCDs. Telles & Terlevich (1997) found the colours of the underlying component of BCD to be consistent with those of LSBGs. Salzer & Norton (1999) showed that BCD hosts have a factor of 2 higher content of HI gas at a given absolute B magnitude than the more quiescent dIrr, and low luminosities. This low surface brightness component should exist before the starburst, and should survive the BCD phase. Then, during the non bursting phase, it can be considered a quiescent low surface brightness galaxy. es BCDs and their host galaxy tend to show similar luminosities, the brighter the BCD the brighter the host. Sánchez Almeida et al. (2008) study a sample of BCDs to find quiescent blue compact candidates (QBCDs), trying to set the characteristics of these galaxies during the non-bursting period. If there are galaxies like the BCD hosts without the starburst, it could mean that they are the same objects in different evolutionary stages. If there are not galaxies without that bursting component, we could say that the BCD phase ends with the host. These authors find that there are around 30 QBCDS candidates per BCD. The lifetime of the galaxies in the BCD phase should be thirty times shorter than the lifetime of QBCDs, so there should be several BCD episodes during the lifetime of the galaxy without exhausting the gas reservoir of their LSBG host, which has enough fuel to power the star formation during a Hubble time. According to the luminosity functions and HI structures of both BCDs and QBCDs, they also find that the two samples overlap, which means that the two sets form a single continuous sequence. Simpson & Gottesman (2000) find the same evolutionary scheme according to the HI kinematics and structures of BCDs and LSBG. An inverse evolutionary scenario from dE to gas-rich dwarfs has been suggested by Silk et al. (1987).

Another important piece of the evolutionary scene are the Luminous

Compact Blue Galaxies (Jangren et al., 2000). LCBGs at intermediate redshifts have colours, sizes, surface brightnesses, luminosities, velocity widths, excitation, SFR and mass-to-light ratios similar to the most luminous low-mass starbursts in the Local Universe (Guzmán, 1999; Koo et al., 1995; Hoyos et al., 2005; Hoyos & Díaz, 2006) . They appear to represent a link in redshift, size, and luminosity between Lyman-break galaxies and HII galaxies today. LCBGs play a key role over the cosmological time scale. They are the major contributors to the observed SFR density enhancement in the Universe at z< 1 (at least 40%) and have been suggested to be the progenitors of present day dE (Koo et al., 1995) and dSph (Hoyos et al., 2007). These galaxies were 10 times more numerous in the past 5-8 Gyr than they are today, what means that they have evolved more than any other galaxy. They show evidences for an older underlying population which makes the colour of the extended low surface brightness region redder than the starburst regions. But, after the current star burst, what kind of object will they become? There are not evidence against the idea that LCBGs are related with dSph (Guzmán, 1997; Koo et al., 1995; Hoyos et al., 2007) and dIrr (Noeske et al., 2006; Guzmán, 1997), and will depend on the ability of the galaxy to retain their ISM. The kinetic energy of the burst seems to be strong enough to blow out the gas, thus halting the star formation process. Depending on the age and strength of the current starburst and the extent of the underlying population, they will fade from their past time until the present to have the characteristics of today's dSph. If this connection is confirmed, it would be the first time that a high redshift object is identified as a progenitor of today's object.

Same initial conditions and different environments: different final object.

There is not an unified scenario to explain all the characteristics of dwarf galaxies. Skillman & Bender (1995) try to clarify the arguments given to unify the evolutionary scenarios. The two ways that have been usually proposed for the dIrr to loose the gas and become a dE are revised finding some problems and inconsistencies. Binggeli (1994) give some arguments for the idea that dE and dIrr have the same origin and they evolve in a parallel way, because the evolutionary conclusions are based on studies of present day dwarfs. dE have a dominant early burst of SF, while dIrr do not show any evidence of such an event. What makes to a low mass galaxy to evolve in some of these two ways? this is called the dwarf galaxy SF crisis (Skillman & Bender, 1995). The evolution of dE/dSph galaxies is probably related to their

environment, and they could have the same origin than dI, but with the gas stripped, because dIrr are not likely to passively evolve into dEs. The true distinction between dIrr and dE can be traced to an event very early in their history. The initial conditions determine how a dwarf galaxy resolves its star formation crisis, but not present environment, the very early environment . Dekel & Silk (1986) suggested that both dE and dIrr lose their mas in winds after an early burst of star formation, but dIrr are able to retain a small fraction while dE loss the entire gas content due to the tidal interactions of the cluster environment. Wyse & Silk (1985) argued that if dIrrs blow out the gas, there will not be successive generations of stars to built up the metallicity. If the early star formation history is the distinguishing factor between dE and dIrr, there is a lot of observational work to do.

1.3 Aims and methodology.

In order to study how the star formation takes place in galaxies, a number of works (Shi et al., 2006, and references therein) have computed purely chemical evolution models (hereinafter CEM) for the study of BCD and dwarf irregular galaxies (Chiosi & Matteucci, 1982; Marconi et al., 1994; Recchi et al., 2002, 2003; Recchi & Hensler, 2007, and others). Most of them assume that the star formation occurs in bursts (in any of the three possible scenarios, (a), (b) or (c) explained in the previous section) and include the effects of galactic winds and/or gas infall. However, most of them limit the study to the evolution of nitrogen and oxygen abundances (Henry et al., 2000; Larsen et al., 2001) and/or the luminosity-metallicity relation (Mouhcine & Contini, 2002). Vázquez et al. (2003) used the information coming from the chemical evolution models from Carigi et al. (2002) to perform the next step and combine chemical and spectral evolution for irregular galaxies. Their models exclude however the early stages of evolution, i.e. during the nebular stage when the most massive stars dominate the energy output. Krüger et al. (1991) compute chemical and photometric evolution models for star burst galaxies. Fritze-v. Alvensleben (1999) made Chemically Consistent Evolutionary Synthesis Models and present results for the photometric, spectral, and chemical evolution of galaxies of various types in the Local Universe and at high redshift. Other authors include chemical evolution in their evolutionary synthesis models and applied them to other type of galaxies, as early type galaxies (Vazdekis et al., 1997), or low surface brightness spirals (van den Hoek et al., 2000). Other works are focused on the ionized gas properties, and make models using SSPs of a given metallicity and applying a photoionization code to obtain the emission lines

and studying diagnostic diagrams and/or abundances obtained by empirical calibrations (Stasińska & Izotov, 2003; Stasińska et al., 2001; Stasińska & Leitherer, 1996; Dopita et al., 2006; Moy et al., 2001, and Martín-Manjón et al. 2009 in preparation). Some of them ignore the star formation history of the galaxy or do not take into account any underlying population, these studies being valid only for the study of the current stellar generation of the galaxy.

A code combining chemical evolution, evolutionary synthesis and photo-ionization models has not been applied yet for the spectral analysis of BCD and HII galaxies, but to elliptical and massive galaxies by Bressan et al. (1994). In this work, we include the chemical evolution model results in the computation of the spectral energy distributions which are used as ionizing source for a photo-ionization code. We want to study the viability of a theoretical model which combines these three well calibrated tools in order to understand the hypotheses of star formation and reproduce the properties of these galaxies.

Our method allows the simultaneous use of the whole available information for the galaxy sample concerning, on the one hand, the ionized gas – emission lines intensities and equivalent widths, elemental abundances, gas densities – which defines the present time state of the galaxy, and ,on the other hand, spectro-photometric parameters – colours, absorption spectral indices, SEDs — defined by the stellar populations and their evolution with time and thus related to the galaxy star formation history. This is done in a self-consistent way, that is using the same assumptions regarding stellar evolution, model stellar atmospheres and nucleosynthesis, and using a realistic age-metallicity relation.

This work includes some steps to follow in order to achieve our purposes:

1. Study of the viability of a self-consistent theoretical model to reproduce the observable characteristics of HII galaxies. The emitted spectrum of HII galaxies is reproduced by means of the photoionization code, using as ionizing spectrum the spectral energy distribution of the modelled HII galaxy, calculated using a stellar population synthesis model, which is, in turn, calculated according to a star formation history and a metallicity evolution given by a chemical evolution code. These three tools, combined will give us a unique model that we use to reproduce the observations.

2. Realization and application of a new population synthesis code to improve the spectral energy distributions and extend the metallicity ranges covered in the model (see Appendix). This new grid will allow us to fit the models for low metallicity galaxies, as the HII galaxies are.

3. The computation of a grid of theoretical models, varying the initial conditions of the gas, and also the different parameters which determine the

results of the models to reproduce the widest range of observed objects in all their evolutionary stages under every possible star formation scenarios.

4. Comparison of our results with a sample of HII galaxies observations to differenciate the characteristics that can be reproduced modifying an specific parameter of the model.

In the next chapter we are going to describe the theoretical tools used and combined in a self-consistent way. The codes are going to be explained: the chemical evolution code, the evolutionary synthesis code and the photoionization code. All of them have some general characteristics, common in every code of this kind, as initial conditions, ingredients and output results. However the application to our models is quite particular and some changes have been done to the original codes. A model of successive bursts requires an special treatment in order to take into account not only the current burst of star formation, with the characteristics of the ionized gas or the ionizing population, but also the characteristics of the underlying populations in the continuum, chemical abundances and colours.

In Chapter 3 a detailed explanation of the star-bursting models is made. The first model was computed as a viability proof for this kind of procedure. It has been called *first set of models*. The results obtained did work to reproduce the observable features of HII galaxies, and, according to this first set of results and conclusions, the *second set of models* was made. For this pupose some changes and new treatments of the parameters were performed. The *third set of models* constitute a fine tuning of the second to reproduce some characteristics not totally well reproduced before. Finally we obtain a grid of models that use three free input parameters that can be changed in order to obtain specific results able to reproduce the observable characteristics of the studied galaxies.

Chapter 4 presents the discussion of the results, the meaning of each input parameter and the implication on their variation over the results of the models. We eill discuss the influence of these parameters in the reproduction of the observable characteristics of HII galaxies, their possible star-formation scenarios and the connection among different type of dwarf galaxies.

The summary, final conclusions and future work is shown in Chapter 5. An appendix has been included to present synthetic emission line spectra of the HII regions photoionized by young star clusters using the new evolutionary synthesis code Popstar (Mollá, García-Vargas & Bressan, 2009, hereinafter MGVB09). Tables of one of the models have been included at the end of this work as an example. The tables of every model will be available on electronic format soon.

Chapter 2

Theoretical models used.

We want to study the viability of a model which combines the next three theoretical tools in a self-consistent way.

First of all, a chemical evolution code: we obtain the star formation history and the evolution of the state of the gas and chemical abundances that it contains. Secondly, an evolutionary population synthesis code, to obtain the spectra energy distributions corresponding to each evolutionary stage of the ionizing continuum of the system, and finally, a photoionization code to obtain the properties of the gas ionized by the massive stars of the current burst.

2.1 The chemical evolution code.

Chemical evolution models were developed to study the origin and the distribution of the different elements in stars and the gas of the ISM, and then understand the radial gradients of abundances observed in our Galaxy. Later, the codes were generalized to be applied to any region or galaxy. Every chemical model consist in the calculation of four variables: total mass of the system, M, the mass of gas, M_g, mass of stars, M_s, and the abundances of each chemical element, Z_i. To resolve the equations which includes this variables, we need some laws and initial conditions or hypotheses on the basic ingredients of the model.

2.1.1 Characteristics and basic ingredients.

The basic equations of a chemical evolution model are the ones which describe how the gas in converted into stars, whatever the process. The ingredients of every chemical evolution code are:

- Initial conditions: total mass, mass of gas, whether the stars form in a primordial moment or the gas is accreted later, the chemical composition of the initial gas (primordial or already enriched...)

- Initial Mass Function, $\phi(m)$: Which describes the distribution of stars as a function of mass.

- Star Formation Rate $\Psi(m)$: the amount of total mass transformed into stars for unit of time.

- Stellar evolution and nucleosynthesis, p_i(m,z): the stellar yields and yields per stellar generation.

- Other parameters: some possible infalls, outflows, or radial flows in the region we are going to study. f, E

- Formation and evolution scenario.

The code used for this work has been particularly developed from the code used for the Solar Neighbourhood by Ferrini et al. (1992) and applied to the whole Galaxy disc in Ferrini et al. (1994). That model described the galaxy as a two-zone system (halo and disc) in which the disc is a secondary structure formed by the gravitational accumulation of gas from the halo.

The IMF adopted for this work is the one developed by Ferrini et al. (1990):

$$\phi(m) = 2.01 \cdot m^{-0.52} \cdot 10^{[2.07 \cdot (logm)^2 + 1.92 \cdot logm + 0.73]^{1/2}}$$

The IMF is assumed to be universal in space and constant in time (Wyse, 1997; Scalo, 1998; Meyer et al., 2000). This IMF is very similar to Scalo's law (Scalo, 1986) and in good agreement with the expressions from Kroupa (2001) and Chabrier (2003).

The equations of the model are:

$$\frac{dM}{dt} = f$$

$$\frac{dM_s}{dt} = \Psi - E$$

$$\frac{dM_g}{dt} = -\Psi + E + f_H$$

$$M = M_s + M_g$$

where M_s is the mass of stars, M_g the mass of gas from the halo to the disk, f is the total gas flux, f_H is the flux coming from the halo, M is the total mass of the system, Ψ the star formation rate, and E the ejection of gas by the stars. Following the stellar evolution, the stars loose a certain amount of gas after some time τ, which leaves a remmant ω(m). This ejection is defined as:

$$E(t) = \int_{m_t}^{\infty} (m - \omega_m)\Psi(t - \tau_m)\phi(m)dm$$

where (m-ω_m) is the ejected mass by each star, $\Psi(t - \tau_m)$ is the number of stars formed in this time (t-τ_m), which ejects mass of gas after τ_m, and $\phi(m)$ is the initial mass function.

The ejected mass as an element i is calculated with the stellar yields, which are defined for every star with a mass m. The total yield per stellar generation is:

$$y_i = \frac{1}{1 - R}\int_{m_\tau}^{m_{up}} mp_i(m)\phi(m)dm$$

where R is the "return fraction"

$$R = \int_{m\tau}^{m_{up}} (m - \omega_m)\phi(m)dm$$

The standard multi-phase model of Ferrini et al. (1992, 1994) works with ejected masses by stars and it obtains the new ejected elements from the Q matrix, which are defined as the fraction of original mass of an element i from each star that is transformed and ejected as an element j

$$Q_{i,j}(m) = \frac{m_{exp,i,j}}{m_j} = \frac{m_{exp,i,j}}{mX_j}$$

Where $m_{exp,i,j}$ is the mass of the element i ejected as element j by each star per unit of time (t-$\tau(m)$), and X_j is the abundance of each element j in the gas.

Multiplying by the IMF and adding all the elements j which are transformed into i, we obtain the ejected mass fraction of element i per star of mass m

$$\frac{m_{exp,i}(m)}{m}\phi(m) = \sum_j \frac{m_{exp,i,j}}{m}\phi(m) = \sum_j Q_{i,j}(m)X_j$$

The quid of a numerical chemical evolution model is that it takes into account the gas ejected by massive stars when they die, and this gasis then added to the amount of available gas to form successive generations of stars.

2.1.2 Application to our models.

Observations and theoretical models suggest that the matter in the galactic system has different aggregation and interaction phases. The principal phases considered in the Ferrini code are:

- A stellar population, where we distinguish the stars able to create and eject heavy elements to the interstellar medium ($M > 4M_{\odot}$), and the stars which only eject hydrogen and He ($M < 4M_{\odot}$), that is, which do not produce an enrichment in the interstellar medium.

- Stellar remnants, as the endpoint of star evolution, that act as a matter sink, removing mass from the chemical evolution point of view.

- Interstellar material, where it can be distinguished two components in the disk, diffuse gas and clouds, and only one in the halo.

Following the previous description, the temporal dependence of the total gas mass fraction in each phase and the chemical abundances in the ISM are determinated by interactions between each phase and from which is obtained the star formation rate. The physical processes considered for the stellar evolution are:

-Formation of stars from the spontaneous fragmentation of the gas in the halo.

-Formation of stars from the gas in the halo and the clouds

-Cloud formation from the diffuse gas in the disk

-Gas accumulation from the halo to the disk

-Restriction of processed matter from the stars.

In the present work, all the gas is assumed to be within an only region from $t = 0$, that is, the infall of gas has been eliminated as an input parameter of the code. The matter is assumed to be in different phases:

- A stellar population as described before

- Stellar remnants

- Interstellar diffuse gas out of which stars are forming following a simple Schmidt law. No molecular component is explicitly considered in the present work.

A bursting star formation has been assumed taking place in successive bursts along the time evolution. At any time, the available gas for each burst

is the sum of the gas left after the previous burst of star formation and the gas ejected by massive stars during the inter-burst periods.

The basic equations to study the behaviour of the mass of stars and gas are, therefore, simplified:

$$\frac{dM}{dt} = 0 \tag{2.1}$$
$$\frac{dM_s}{dt} = \Psi - E \tag{2.2}$$
$$\frac{dM_g}{dt} = -\Psi + E \tag{2.3}$$
$$M = M_s + M_g \tag{2.4}$$

where $M_s(t)$ is the mass in stars, $M_g(t)$ is the mass of gas, M is the total mass of the system, $\Psi(t)$ the star formation rate and E(t) the ejection rate of mass from the stars to the ISM. A part of the restituted gas consists of enriched material, $E_Z(t)$, which is created in the interior of the stars and is ejected when they die. To compute both quantities, ejected gas and element production, we use the Q_{ij} *matrix* formalism introduced by Talbot & Arnett (1973) and described before. This forlmalism is very useful to treat elemental abundances which increase at different rate in the interstellar medium, that is, the non-solar ratios (Portinari et al., 1998). In the present work we adopt the same matrix prescription as in Gavilán et al. (2006), which is an updated version from the one given in Ferrini et al. (1992) and Galli et al. (1995) calculated following the method described by Portinari et al. (1998).

Nucleosynthesis yields for massive stars have been taken from Woosley & Weaver (1995). For low and intermediate mass stars, we have used the yields from Gavilán et al. (2005). The combination of these sets of stellar yields, with our assumed IMF producing the required yields per stellar generation, has been completely revised and calibrated with the Milky Way Galaxy (MWG) in Gavilán et al. (2005, 2006), where other stellar yields sets have been used and analysed too. It also reproduces observations of spiral and irregular galaxies (Mollá & Díaz, 2005), obtaining reasonable results even for nitrogen abundances in low-metallicity objects (Mollá et al., 2006). For type I supernova explosion releases, model W7 from Nomoto et al. (1984), as revised by Iwamoto et al. (1999), has been taken, while the rate of this type of SNIa explosions are included through a table given by Ruiz-Lapuente (private communication), following works of Ruiz-Lapuente et al. (2000).

We have assumed that the gas is used to form stars with a given efficiency called H:

$\Psi = H \cdot M_g$

If there would not be gas ejection from massive stars, as it would be the case for instance in the firsts moments of the evolution, ($E = 0$), then:

$$\frac{dM_s}{dt} = HM_g \tag{2.5}$$

$$\frac{dM_g}{dt} = -HM_g \tag{2.6}$$

That is, the consumed gas rate would be a function that depends on the available gas at a given time, being a decreasing function of time through the parameter H, which defines the star formation efficiency. Then:

$$\frac{dM_g}{M_g} = -Hdt \Rightarrow M_g(t) = M_{g0}e^{-Ht} \tag{2.7}$$

A change in the star formation rate implies a change in the value of the parameter H or efficiency:

$$H = \frac{ln\frac{M_{g,0}}{M_g}}{\Delta t} \tag{2.8}$$

We have run models considering the star formation as a set of successive bursts in a region with a total mass of gas of 100×10^6 $M_\odot$. In each burst a certain amount of gas is consumed to form stars. The code solves the chemical evolution equations to obtain, in each time step, the abundances of 15 elements: H, D, ^{3}He, ^{4}He, C, ^{13}C, O, N, Ne, Mg, Si, S, Ca, Fe, and nr where *nr* are the isotopes of the neutron rich elements, synthesized from ^{12}C, ^{13}C, ^{14}N and ^{16}O inside the CO core. We have taken time steps of Δt= 0.5-0.7 Myr [1], from the initial time, $t = 0$, up to the final one, $t = 13.2$ Gyr. Also, at each time step, the star formation rate and the mass in each phase – low mass, massive stars and remnants, total mass in stars created, and mass of gas– are computed.

2.2 Evolutionary synthesis code.

The study of the stellar content in integrated populations like galaxies or stellar clusters has used evolutionary synthesis models as the principal tool. The spectral energy distribution is computed for an age and an IMF, supposing that all the stars have been formed in an instantaneous burst. The direct comparison of observations against models (spectral energy distributions, colours,...) give to us the main properties of the stellar populations involved.

[1]This small time step allows to take into account the fast evolutionary phases of the most massive stars considered.

2.2.1 Characteristics and basic ingredients.

The ingredients of any evolutionary synthesis model are:

- IMF
- Isochrones (or stellar tracks)
- Atmosphere models or empirical stellar libraries
- Synthesis code

The inputs for the model are the stellar tracks and the stellar spectra of individual stars. Evolutionary synthesis models try to obtain the age and metallicity of the populations, assuming that the proportion of stars at different evolutionary phases is obtained by the isochrones, the equivalent to the colour-magnitude diagram for a population of a given age and metallicity. After that, an spectral energy distribution is assigned to each star of an isochrone, and it is multiplied by the number of stars in this phase, given by the IMF. The sum of all contributions gives as result the complete SED of the system for each age and metallicity, that is, a Single Stellar Population model.

In this work we have used two SSPs model results:

The first one are the resulting SEDs from García-Vargas,Bressan, & Díaz (1995); García-Vargas et al. (1998, hereinafter GV95) as updated in Mollá & García-Vargas (2000), and it has been used for the first set of models. The second ones correspond to the results from MGVB09 (Mollá , García-Vargas & Bressan 2009, submitted), used for the second and third set of models.

GV95 Single Stellar Populations

The required inputs are the stellar isochrones and the stellar atmosphere models for the individual stars. Those works used the set of 50 isochrones from the Padova group from Bertelli et al. (1994) for ages between 4 Myr and 20 Gyr, for 5 metallicities between 1/50 and 2.5 $Z_{\odot}$ (Z=0.0004, 0.004, 0.008, 0.02 and 0.05). To this set of isochrones they have added other 18 isochrones from Bressan et al. (1993) and Fagotto et al. (1994a) with ages from 0.5 to 4 Myr, used in García-Vargas,Bressan, & Díaz (1995) and García-Vargas et al. (1998) for the youngest stellar populations of 4 metallicities Z=0.004, 0.008, 0.02 and 0.05. That means that for the lowest metallicity, $Z = 0.0004$, only isochrones older than 4 Myr are available.

In both cases, isochrones give the number of stars in each phase assuming that stellar clusters were formed with a standard Salpeter IMF with $m_{low} =$

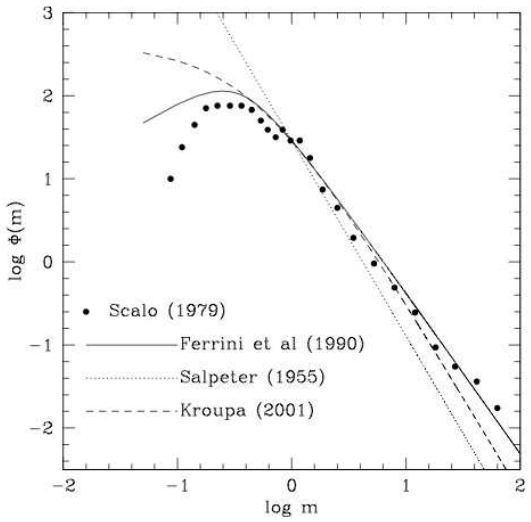

Figure 2.1: Comparison between different IMFs taken from Mollá & Díaz (2005). Differences for low masses are more noticeable than for high masses.

0.6 $M_\odot$ and m_{up} = 100 $M_\odot$. This IMF, although using the same lower and upper limits, is not exactly the one used in the multiphase chemical evolution code, what implies some differences in the resulting spectra, mainly for the oldest and the youngest stellar populations. It could be though that we are violating the self-consistency of the models. Nevertheless, the next figure shows the differences between the IMFs of Scalo, Kroupa, Salpeter and Ferrini. They are very similar during almost the whole mass spectrum, with only some differences for very high and very low masses. They are, however, smaller than 10% (Mollá & Díaz, 2005) and therefore we assume that this inconsistency will not produce very important differences in the final results (see Figure 2.1)

The emergent spectral energy distribution (SED) was synthesized by calculating the number of stars in each point of the H-R diagram and assigning to it the most adequate stellar atmosphere model. The models of Clegg & Middlemass (1987) and Lejeune et al. (1997) have been used for stars with $T_{eff} \geq 50000$ K (last evolutionary stages of massive stars) and $2500 \leq T_{eff} < 50000$ K, respectively.

To each SED computed for a stellar cluster, it was added a continuum nebular emission contribution as explained in García-Vargas et al. (1998). The gas is assumed to have an electron temperature, T_e which depends on Z. The assumed values are T_e =18000, 11000, 9000, 6500 and 4000 K for

Z=0.0004, 0.004, 0.008, 0.02 and 0.05, respectively, selected according to the average value obtained by García-Vargas,Bressan, & Díaz (1995). The free-free, free-bound emission by hydrogen and neutral helium, and the two photon hydrogen-continuum have been calculated by means of the atomic data from Aller (1984) and Ferland (1980).

The SEDs for the complete sets of 68 (50 for Z=0.0004) isochrones were calculated with the same code as in Mollá & García-Vargas (2000) [2] for the cited metallicities. Therefore they finally have a set of 68 SEDs for SSP of different ages for 4 metallicities each, and 50 for ages older than 4 Myr for Z=0.0004, which we use as a spectral library.

MGVB09 Single Stellar Populations.

This grid is composed by Single Stellar Populations (SSP) for six different IMF's. Three of them are Salpeter (1955) power laws $\propto m^{-(\alpha+1)}$ with α =1.35 and different masses limits: a) between 0.85 and 120 $M_\odot$, and b) between 1.00 and 100 $M_\odot$. The others IMFs are Salpeter (1955), Ferrini et al. (1990), Kroupa (2002) and Chabrier (2003) functions, all with masses between 0.15 and 100 $M_\odot$, expressed, respectively, as:

$$\phi(m)_{SAL} = m^{-2.35} \tag{2.9}$$

$$\phi(m)_{FER} = 10^{-\sqrt{0.73+logm\times(1.92+logm2.07)}}/m^{-1.52} \tag{2.10}$$

$$\phi(m)_{KRO} = \begin{cases} m^{-0.35}\ 0.15 \leq m/M_\odot < 0.08 \\ 0.08 * m^{-1.3} 0.08 \leq m/M_\odot < 0.50 \\ 0.04 * m^{-2.3} 0.50 \leq m/M_\odot < 100 \end{cases} \tag{2.11}$$

$$\phi(m)_{CHA} = \begin{cases} \frac{0.086}{mln10} e^{-(logm-log0.22)^2}/(2.0.57^2) 0.15 \leq m/M_\odot < 1 \\ \\ \frac{0.0443}{ln10} m^{-2.3} 1 \leq m/M_\odot \leq 100 \end{cases} \tag{2.12}$$

$$\tag{2.13}$$

For this work we have used the Ferrini IMF results in order to avoid any inconsistency with the chemical evolution code. Now both codes use the same IMF, and the complete self-consistency of the model is saved.

The basic isochrones used are those from Bressan,Granato, & Silva (1998) for six different metallicities: Z = 0.0001, 0.0004, 0.004, 0.008, 0.02 and 0.05. The age coverage is from $logt$ = 5.00 to 10.30 with a variable time resolution which is $\Delta(logt) = 0.01$ in the youngest stellar ages. The WC and WN stars are identified in the isochrones according to their surface abundances.

[2] Although in that work, applied to old elliptical galaxies, the SEDs corresponding to ages younger than 4 Myr and those for Z=0.0004, were not used

The atmosphere models are from Lejeune et al. (1997) with an excellent coverage in effective temperature, gravity and metallicities, for stars with Teff$\leq$ 25000 K. For O, B and WR they have taken the NLTE blanketed models by Smith, Norris, & Crowther (2002) at Z=0.001, 0.004, 0.008, 0.02 and 0.04. There are 110 for O-B stars, with 25000 K Teff $\leq$ 51500 K and 2.95 $\leq \log g \leq$ 4.00, calculated with the code by Pauldrachet al. (2001), and 120 for WR stars (60 WN + 60 WC), calculated with the code CMFGEN by Hillier, & Miller (1998), with 30000 K $\leq T^* \leq$ 120000 K and $1.3R_\odot \leq R^* \leq 20.3R_\odot$ for WN, and with $40000K \leq T^* \leq$ 140000 K and $0.8R_\odot \leq R^* \leq 9.3R_\odot$ for WC. T* and R* are the temperature and the radius at a Roseland optical depth of 10.

To assign a model in the H-R diagram they use the more appropriate model in Teff and $\log g$ except for the WR cases, in which we do not use the effective temperature (since isochrones give the hydrodynamic one while atmospheres use the effective temperature at a Rosseland optical depth of 10). They use the relationships among opacity, mass loss and velocity wind. For post-AGB and PN with Teff from 50000 to 220000 K they take the NLTE models by Rauch (2003). These models include all elements from H to Ni. Teff ranges between 50000 K and 190000 K and $\log g$ between 5.00 and 8.00. For higher temperatures they use black bodies. For the emission of the nebular continuum, they have included the hydrogen and helium (both He and He^+) free-free and free-bound emission as well as the 2-photon continuum.

The use of NLTE blanketed models produce less hard ionizing photons than old models (e.g. García-Vargas,Bressan, & Díaz, 1995) as we will see in next sections. It explains in a natural way the emission line ratios in low excitation high metallicity HII regions. Previous work needed a steeper IMF or mass segregation in small cluster, in disagreement with evidences from HST of the existence of very massive stars even in small clusters.

2.2.2 Application to our models.

Once the SEDs for every the stellar generations are computed, they must be convolved with the star formation history (SFH) in order to calculate the corresponding SED for a region where more than a burst take place:

$$L_\lambda(t) = \int_0^t S_\lambda(\tau, Z(t'))\Psi(t')dt' \tag{2.14}$$

where $\tau = t - t'$ is the age of the stellar population created in a time t' and S_λ being the SED for each SSP of age τ and metallicity Z reached in that time t'. A SED from the SSP library, S_λ, must be assigned to each time step according

to its corresponding age and metallicity taking into account the SFH, $\Psi(t)$, and the AMR, $Z(t)$, obtained from the chemical evolution model, to finally calculate $L_\lambda(t)$ by the above integration. However the metallicity changes continuously while the available SEDs have only 4 or 5 possible values. We have, therefore, interpolated logarithmically between the two SSP of the same age τ closest in metallicities to Z(t') to obtain the corresponding $S_\lambda(\tau, Z(t'))$. The final result is the total luminosity at each wavelength λ.

When this process is applied to the stellar population created by the first burst two problem arise. On the one hand the initial metallicity is Z= 0 and, although during the first Myr after the creation of the first stars the metallicity increases, it does not reach the minimum Z=0.0004 for García-Vargas,Bressan, & Díaz (1995) or Z=0.0001 for MGVB09 , and therefore we must extrapolate with the available SEDs of the youngest SSPs. Due to the uncertainties in the evolution of the *quasi*-zero-metallicity stars, we have preferred to assign to this first burst metallicity a minimum value of 0.0028 (smaller than the one reached at the end of the first burst but still valid for extrapolating without creating instability numerical problems) for the models made with GV95 and the lower Z=0.0001 to the models made with MGVB09 when is needed. On the other hand we must use two different pairs of metallicities to extrapolate with the SEDs of SSPs: Z=0.004 and 0.008 before 4 Myr and Z=0.0004 and 0.004 after 4 Myr, since SEDs for the most-metal-poor and youngest SSPs are not available in GV95. This problem does not arise for models made with MGVB09, which includes SSPs with very low metallicities .

In this way we obtain the SED corresponding to the whole stellar population, including the ionizing continuum proceeding from the last formed stellar population.

2.3 Photoionization code.

This code computes the spectrum emitted by a low density gas irradiated by an energetic continuum. The ionizing radiation's energy is converted into a photoelectrons kinetic energy, which is eventually degraded into the observed emission line or continuum spectrum. The ionization and level populations are given by the balance of microphysical processes, and the used temperature is the kinetic temperature of the electrons, which needs large scale numerical simulations to be understood.

The balance between processes of ionization and recombination determines the level of ionization of the gas, which depends on temperature of electrons, given by heating-cooling processes. The code solves the equations

of statistical and thermal equilibrium, equations that balance the ionization-neutralization processes, and heating-cooling processes, respectively. The physics of these processes can be found in several works like Osterbrock (1989) and Aller (1984), specially the case of a low density nebula ionization, which is the case that we are going to treat here.

2.3.1 Characteristics and basic ingredients.

The photo-ionization code CLOUDY (Ferland et al., 1998) is a large-scale spectral synthesis code designed to simulate fully physical conditions within an astronomical plasma and predict the emitted spectrum. Its 96.0 and 98 versions have been used in order to obtain the emission lines. CLOUDY works by dividing a spherical nebula into a set of thin concentric shells, whose thicknesses is small enough for the physical conditions to be nearly constant. The gas is assumed to be ionized by the massive stars belonging to the current burst of star formation whose SED has been previously calculated by the combination of the chemical and evolutionary synthesis models.

The goal of emission line analysis is to deduce the properties of the clouds that produce the observed spectrum. The basic parameters that describe the conditions in a cloud and the resulting spectrum are : the characteristics of the incident continuum, the gas density , its geometry and its chemical composition.

Incident continuum.

The incident continuum is the external continuum emitted by the central object, which strikes the illuminated face of the cloud

Continuum intensity or luminosity

The most important parameter in photoionization problems is the flux of ionizing photons striking the illuminated face of the cloud. This is given by:

$$\Phi(H) = \int_{\nu_1}^{\infty} \frac{4\pi J_\nu}{h\nu} d\nu$$

[photons cm$^{-2}s^{-1}$]

where J_ν is the intensity. In equilibrium, the ionization rate is equal to the recombination rate. The balance equation is:

$$n_{atom} < \sigma > \Phi(H) = n_e n_{ion} \alpha(T)$$

where $\alpha(T)$ is the recombination coefficient, and $< \sigma >$ is the cross section. Then the resulting level of ionization is:

$$\frac{n_{ion}}{n_{atom}} = \frac{\Phi(H)}{n_e}\frac{<\sigma>}{\alpha(T)} \approx U\frac{<\sigma>}{c\alpha(T)}$$

where c is the speed of light. In the last equation we can see the ionization parameter, U, defined as:

$$U = \frac{\Phi(H)}{n_H c}$$

being n_H=n_e the density of hydrogen atoms. Both terms are used to parametrize the radiation field, but the flux of ionizing photons has the benefit of directly exposing the dependence on the separation between the cloud and the central source.

Continuum shape

The shape of ionizing continuum must be specified. It is a fundamental parameter since it give us information about the source of ionization. The unities of the continuum must be Rydbergs, which is the natural unit of energy in photoionization problems. 1 Rydberg is nearly equal to the ionization potential of hydrogen, 13.6 eV.

Chemical composition.

The abundances must be specified to obtain the emission line intensities of these elements. Both the hydrogen recombination and forbidden collisional lines are optically thin and their intensity fluxes are proportional to the abundance of the ion which produce them. The program considers the lightest 30 elements in details and all stages of ionization are treated.

Density of the gas.

The emissivity of a line, that is, the energy released per unit volume and time, is a function of the gas density. Considering the nebula in equilibrium, the density corresponds to the total hydrogen density, as the sum given by:

$n(H) = N(H^0) + n(H^+) + n(H^-) + 2n(H_2) + 2n(H_2^+) + ..$

that is, the density of hydrogen atoms.

Geometry.

Cloudy always considers a spherical geometry, but if the inner radius is much more larger than the thickness of the cloud, it takes a plane-parallel approximation The gas density is assumed as constant and it fills its volume.

2.3.2 Application to our models.

We have specified for the models the number of ionizing photons striking the illuminated face of the cloud. This number is defined as:

$$Q(H) = \int_{\nu_0}^{\infty} \frac{L_\nu}{h\nu} d\nu$$

where $L\nu$ is the continuum luminosity, taken from ν= 1Ryd to infinity, obtained directly from the SED of the models.

Although the input parameter for the model is Q(H), a given model is characterized by its ionization parameter U defined in terms of Q(H) as:

$$U = Q(H)/4\pi c n_H R^2 \tag{2.15}$$

where n_e is the electron density, assumed constant for simplicity and equal to 100 cm^{-3}, and $Q(H)$ is the number of Lyman ionizing photons, which reach the gas at a velocity c.

Because of the use of the number instead of the flux of ionizing photons, a radius for the nebula must be specified, which has a special treatment depending on the model.

Geometry considerations: region size and shape.

The photoionized gas is assumed to be spherically symmetric around a point source of radiation and the run of pressure or density in the gas is imposed by external conditions. This allows for a treatment of plane-parallel geometry as special case in which the gas may be regarded as a thin shell. A closed geometry has been taken for the calculations. All the photons which scape from the illuminated face of the cloud towards the star, go on to strike the other side of the nebula. This geometry ensures the case B of recombination and the approximation on the spot.

We have chosen two different assumptions for the radius of the emitting gas from the ionizing source in the nebula for each set of models. First of all, a constant radius based on observational data has been applied for the first set of models. The other assumption for the radius of the shell is based on the expanding atmospheres of massive stars with strong winds, which have been applied to the second set of models.

For the first set of models, made with GV95 SSPs, we have assumed the emitting gas to be located at a distance R = 500 pc at the beginning of the evolution. This size is characteristic of HII galaxies (Telles et al., 1997). For the first burst we have obtained the stellar density using this radius as follows:

$$\rho_\star = \frac{M_\star}{4\pi R^2} \tag{2.16}$$

where $M_\star$ is the mass in stars formed in the current burst and R is the radius of the region. The radius is then subsequently adjusted in the successive burst to keep constant this stellar density configuration. The radii obtained are constant within each burst, but they change from burst to burst, decreasing along galaxy evolution. This results in all cases in a plane-parallel geometry.

The energy injection from massive stars, via the combined effects of supernovae and stellar winds can shape the interstellar medium and create expanding structures (Franco, 2003). We derive the radius of the modelled region from the mechanical energy from the expanding atmospheres of massive stars with strong winds for the second grid of models, made with MGVB09 SSPs. Castor et al. (1975) demonstrated that an early-type star with a strong stellar wind can blow out a large cavity or "bubble" in the surrounding gas, if it is assumed to be compressed into a thin spherical shell. The wind-driven shell begins to evolve with an initial phase of free expansion followed by an adiabatic expansion phase, and then the material collapses into a thin, cold shell as a result of radiative cooling. At this stage the gas traps the ionization front and the radiative phase begins. In this phase the ionizing photons are absorbed and the region cools via emission in the Balmer lines. In this process, the radius of the outer shok, R_s, evolves as:

$$R_s = 1.6(\epsilon/n)^{1/5} t^{3/5} pc \tag{2.17}$$

where ϵ is the total mechanical energy (SN + stellar winds) per unit time injected in units of 10^{36} ergs s^{-1}, n is the interstellar medium density in units of cm^{-3}, and t the age of the shell in units of 10^4. We have extrapolated this bubble geometry to a shell structure formed by the combined effects of the mechanical energy deposition from the winds coming from massive stars in the ionizing cluster and from SN explosions. Then, the ionized gas is assumed to be located in a thin spherical shell at that distance R_s from the ionizing source. This approach has been previously used by Dopita et al. (2006) and has the advantage of eliminating the ionization parameter as a free variable in the models since now it is computed from the physical parameters of the evolving young cluster.

The gas elemental abundances are those reached at the end of the starburst previous to the current one. Fifteen element abundances have been introduced in the code: He, C, N, O, Ne, Na, Mg, Al, Si, S, Ar, Ca, Fe and

Ni, all calculated from the chemical evolution model, except for Na, Ar and Ni which are not computed in the model and are scaled to the solar ratio (Asplund et al., 2005). Dust grains mixed with the ionized gas have been taken into account including the depletion in refractory elements (Si, Fe, CA, Si, Mg) taken from Garnett et al. (1995). It has to be taken into account since the grains can affect to the UV photons absortion and decrease the electronic temperature. The models assume that the nebula is ionization bounded and no dust has been included in the models The shape of the ionizing continuum is defined by the pair of values (ν(Ryd), logνL_ν) (Eq. 2.14) obtained from the ionizing spectrum given directly by the evolutionary synthesis code.

Chapter 3

The Star-Bursting Models.

3.1 First set of models: the test.

This first set of models were made in order to check the viability of this kind of models with te combination of the three theoretical codes.

3.1.1 Description of the model.

The first grid of models have been run considering the star formation as a set of successive burst in a region with a total mass of 100×10^6 $M_\odot$, and a radius of 500 pc. This radius have been obtained according to the constant density of stellar mass through the successive bursts method. Every galaxy experiences 11 star formation bursts along its evolution of 13.2 Gyr, that is one each 1.3 Gyr. In each bursts a certain amount of gas is consumed to form stars, determined by the efficiency of the burst. According to that, we have computed two types of models:

BURST MODELS*:* All bursts have the same efficiency of star formation. The same percentage of the available gas is taken to form stars in every burst.

ATTENUATED BURST MODELS: The initial efficiencies are reduced in the successive burst by a factor n, corresponding to the number of the burst:

$$\psi_n = \frac{\psi_0}{n} \tag{3.1}$$

For each type of model, we have taken two initial efficiencies, following Eq.2.8:

-H=20 (1/H = 0.5 Myr), the model uses $\sim$ 64% of the gas for star formation in each time step.

-H=8 (1/H = 1.25 Myr), that uses $\sim$ 33% of the gas to form stars in each time step

This set of models have been made in steps of time of =0.5 Myr, from initial time of t=0 to t=13.2 Gyr. With the chemical evolution code we obtain the abundances of 15 elements, the star formation rate and the mass in each phase - low mass, massive stars and remnants, total mass in stars created and mass of gas. This amounts to a total of 26348 stellar generations or SSPs each one with this corresponding age and metallicity. The evolutionary synthesis model used for this set are those from GV95. Once the spectra of the ionizing population is obtained, we use the photoionization code in order to get the emission lines produced by these stars.

3.1.2 Results.

Chemical evolution.

Star Formation Rates.

The star formation rate is one of the main results of the different models since it drives the behaviour of all the other quantities. In Fig. 3.1 the star formation history for each of the 4 computed models is shown. In all of them the first burst is strong, while the successive bursts are less intense since the amount of gas available has decreased in spite of the ejected gas produced by the massive stars. In Attenuated Models (right panels), the first burst has the same star formation rate as in Bursts Models (left panels), since the initial efficiency is the same for both. The successive star formation episodes have a smaller star formation rate in Attenuated Bursts Models than the corresponding ones in Bursts Models due to the attenuation factor included in the inputs.

Hoyos et al. (2004) have estimated the star formation rates for the sample of 39 local HII galaxies of different morphologies from Telles et al. (1997), which were selected from the most luminous of the Terlevich et al. (1991) catalogue and with H_β equivalent widths between 30 and 280 Å . These star formation rates were obtained from the Hα luminosity, by assuming $T_e = 10^4$ K and case B recombination. They are in the range from 0.5 to 7 $M_\odot yr^{-1}$, marked by dotted lines in Fig. 3.1, indicating that these HII galaxies have high star formation rates. These findings are in agreement with those from Taylor et al. (1994) who found star formation rates in the range of 10^{-4} to 10 $M_\odot yr^{-1}$. Our models produce SFR between the observed values after the sixth burst, which corresponds to 6.5 Gyr after the beginning of star formation, except Burst Model with the lower efficiency, where every burst

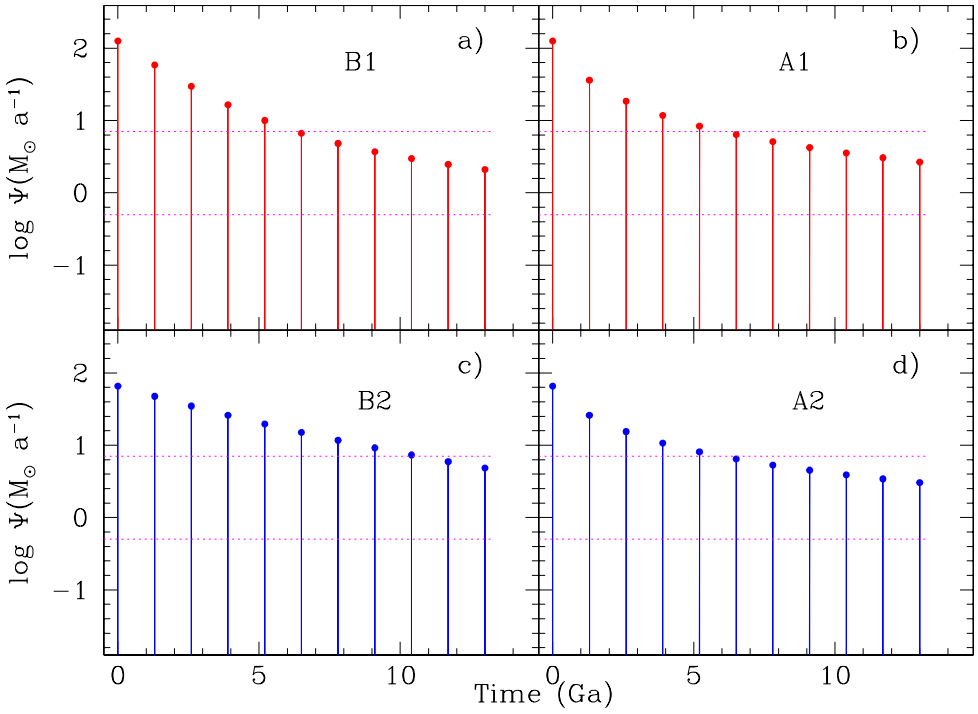

Figure 3.1: Star formation history for: a) burst model 1 (B1); b) attenuated burst model 1 (A1); c) burst model 2 (B2); and d) attenuated burst model 2 (A2). Dotted lines represent the upper and lower limits to the SFR estimated for BCD and/or HII galaxies by Hoyos et al. (2004).

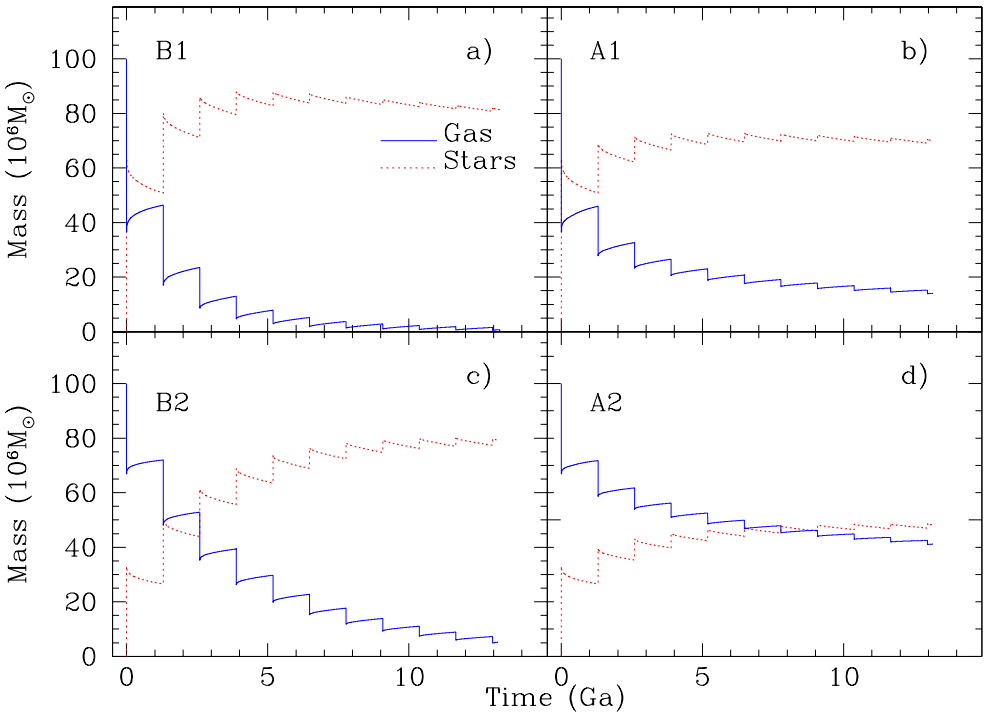

Figure 3.2: Time evolution of the gas and star mass for models: a) B1; b) A1; c) B2; and d) A2.

before the ninth-tenth show higher SFR than observed.

Since the star formation consumes gas, the averaged gas mass decreases with time following Eq.(6), as can be seen in Fig. 3.2. The chemical evolution code, however, takes into account the mass of gas ejected from massive stars during their evolution and, therefore, the gas mass increases during a given burst. On the other hand, the mass of stars which increases in each burst and globally due to the star formation, decreases during each burst as the most massive stars end their lives. It is interesting to note that models with smaller efficiencies, H, in the lower panels of Figs. 3.1 and 3.2, consume less gas in each burst and, as a consequence, the star formation rate remains higher, and declines more slowly, than in models with higher values of H shown in the upper panels.

Elemental abundances.

The element content of the gas is usually measured through the oxygen abundance, given as $12 + log(O/H)$. Oxygen contributes more than 40%

to the mass in metals and is mainly created within massive stars. Since these stars are very short lived, their products are ejected very rapidly to the interstellar medium (ISM) and hence the value of its oxygen abundance increases with time, as shown in Fig. 3.3. In that figure we see how O/H increases abruptly when a burst takes places remaining more or less constant between each two of them.

Observational data from Terlevich et al. (1991) and Hoyos & Díaz (2006) show that most of the HII galaxies have metallicity distributions between $7.5 < 12 + \log(\mathrm{O/H}) < 8.5$. These limits are shown as dashed lines in Fig. 3.3. The first limit is reached with the first burst in all cases. It can be seen that models of type 1 (dotted lines) show oxygen abundances higher than the observed upper limit. The efficiency of the first burst is so high that a large number of massive stars are formed, and hence the oxygen abundance reaches rather high values in a very short time. Also the oxygen abundance of Bursts Models with the lower efficiency reaches values higher than shown by data from the third burst onwards ($12 + log(O/H) > 8.5$). Only Attenuated Bursts models with 33% shows oxygen abundances within the range of HII galaxies during the whole evolution since the attenuation of the bursts keeps the star formation lower than in the other three cases. The star formation efficiency taken for Attenuated Bursts Model with 33% of initial efficiency results to be an upper limit for HII galaxies in oxygen abundances and it may reproduce the most metal rich systems.

Abundance ratios also give information about the star formation process, essentially the time scale or duration of the bursts, when the production of the elements involved takes place in stars in different mass ranges. This is the case for the N/O ratio. Oxygen is very quickly ejected by the most massive stars. Nitrogen, however, may be created in stars of all masses. Moreover, the production of nitrogen may take place in two ways: 1) the main process requires another element like carbon or oxygen, to synthesize N through the CNO cycle, thus N shows, at least in part, a secondary behaviour. In that case the N abundance has to be proportional to the initial abundance of heavy elements and hence the N/O ratio grows with metallicity. There is, however, a proportion of N which must have a primary origin, as suggested by the data in Fig. 3.4 (Izotov & Thuan, 1999; Izotov et al., 2005, 2006) shown by (green) dots which exhibit a constant N/O ratio. Nitrogen may be produced by low and intermediate mass stars (Gavilán et al., 2006) and therefore its contribution may appear in the ISM a certain time after the massive stars have died. In fact, N grows more slowly than the oxygen abundance in the range $7.6 < 12 + log(O/H) < 8.2$, which may be explained by this primary behaviour (see Mollá et al., 2006, for details). In Fig. 3.4 we can see the oscillating behaviour of the N/O ratio shown by our computed models due

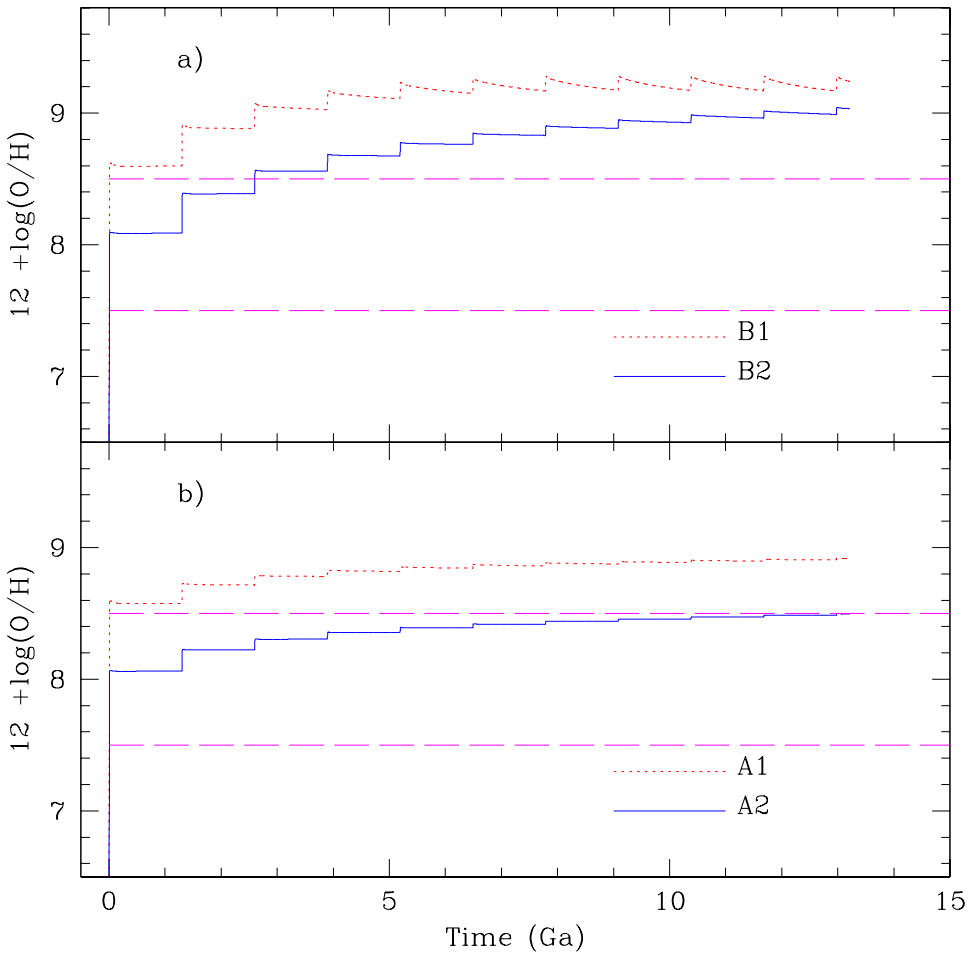

Figure 3.3: Time evolution of the oxygen abundance, given as $12 + log(O/H)$, for the 4 kinds of computed models: a) models of type B burst modes) and b) models of type A attenuated models) with dotted lines corresponding to models of type 1 and solid lines corresponding to models of type 2. The dashed lines limit the range of data taken from Terlevich et al. (1991) and Hoyos & Díaz (2006).

to the successive bursts of star formation followed by quiescent periods. At the beginning of a given burst, the N/O ratio decreases, as the O is created and ejected by the most massive stars in the burst; then it increases during the quiescent periods between bursts as the low and intermediate mass stars die and eject their synthesized nitrogen while the oxygen abundance remains constant.

According to the results of this section, Attenuated Bursts Model with 33% of initial efficiency is the one better reproducing the observations, since the total mass, the gas fraction, the star formation rate and the oxygen abundances are within the range shown by data.

Therefore, from now onwards, in what regards the ionizing continuum and emission line properties **only the Attenuated Bursts Model (A2) will be analysed by the moment.**

Evolutionary stellar population synthesis.

The number of ionizing photons.

The convolution of the results of the chemical evolutionary code with the single stellar populations of the synthesis evolutionary code gives us directly the SED, L_λ, in time steps of logt= 0.05.

From this SED the number of hydrogen ionizing photons, coming from hot and young stars of the first spectral types (O-B), can be calculated as:

$$Q(H) = \int_{\nu_0}^{\infty} \frac{L_\nu}{h\nu} d\nu \tag{3.2}$$

where L_ν is the continuum luminosity at frequency ν.

Fig. 3.5 shows the number of hydrogen ionizing photons as a function of time for Attenuated Bursts Model with lower efficiency. In the first burst, with a total mass of $\sim 30 \cdot 10^6$ $M_\odot$ forming stars, the number of massive ionizing stars is high and so it is the number of ionizing photons. The number of ionizing photons per unit stellar mass in our models is $\log(Q(H)/M_\odot) \sim 46.8$ at the starting of the first burst, corresponding to a Zero Age Stellar Population (ZASP) of very low metallicity and then decreases as the cluster ages. This initial number of ionizing photons per unit stellar mass is almost the same for the successive bursts although, decreasing slightly as the abundance increases.

Within each burst the number of ionizing photons decreases by almost two orders of magnitude from 0.5 to 10 Myr, as show in Fig. 3.6, and by almost 8 orders of magnitude by 100 Myr. Essentially no ionizing photons are available during the quiescent inter-burst periods. At the beginning of each successive

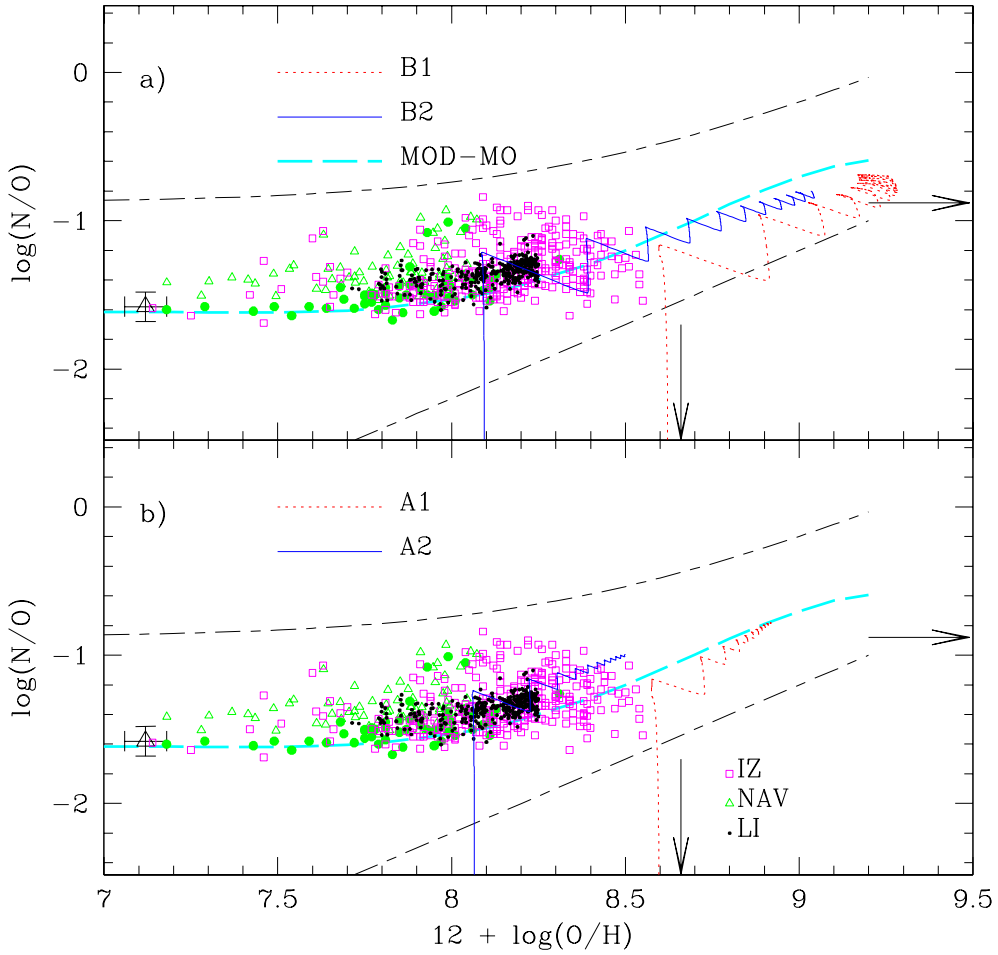

Figure 3.4: The logarithmic N/O ratio as a function of the oxygen abundance, given as $12+log(O/H)$, for our 4 kinds of computed models: a) type B models; b) type A models. The (black) dashed lines limit the range of data shown by extragalactic HII regions. The (green) dots and (magenta) squares correspond to the derived values for low metallicity galaxies from Izotov & Thuan (1999); Izotov et al. (2005, 2006); Hoyos & Díaz (2006); Liang et al. (2006); Nava et al. (2006), while the large triangle is the value for the lowest metallicity galaxy in the sample SBS 0335-052W. The long dashed (cyan) lines represents the averaged trend shown by chemical evolution models from Mollá et al. (2006) for spiral and irregular galaxies with continuous star formation. The arrows mark the solar values.

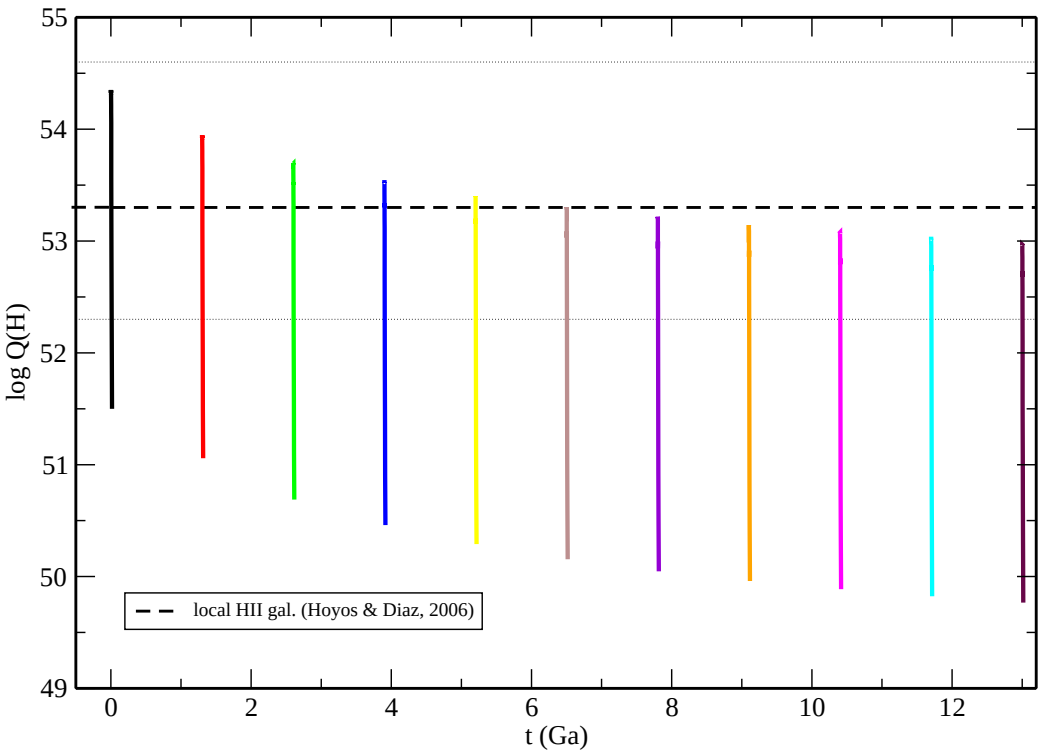

Figure 3.5: The time evolution of the hydrogen ionizing photons, Q(H), for model A2. The dotted line marks the mode of the distribution for local HII galaxies found by Hoyos & Díaz (2006). Each coloured line indicates the evolution within a burst. Different colour lines are used for different bursts.

burst, the number of ionizing photons raises abruptly but reaching a value progressively lower as less gas is available to form stars. Also, as the mean gas metallicity increases with time, the number of ionizing photons per unit stellar mass decreases (García-Vargas,Bressan, & Díaz, 1995). This effect increases with the age of the ionizing cluster reaching a factor of about 5 at 10 Myr.

The average number of ionizing photons observed for local HII galaxies is $\log(Q(H)) = 53.3$ (Hoyos & Díaz, 2006). This number of ionizing photons, marked as a dotted line in Fig. 3.5, is reached by model A2 at around the fifth or sixth burst of star formation, that is for the burst occurring 5.2-6.5 Gyr after the beginning of the formation of the galaxy, when the predicted star formation rate also fits the data (see Fig. 3.1). On the other hand, the average derived ionization parameter for the local HII galaxy sample is $logU = -2.5$ which in our models corresponds to an age of the ionizing population of about 6.5 Myr. It should be noted that during the first 7 Myr of a burst the number of ionizing photons remain essentially constant (see

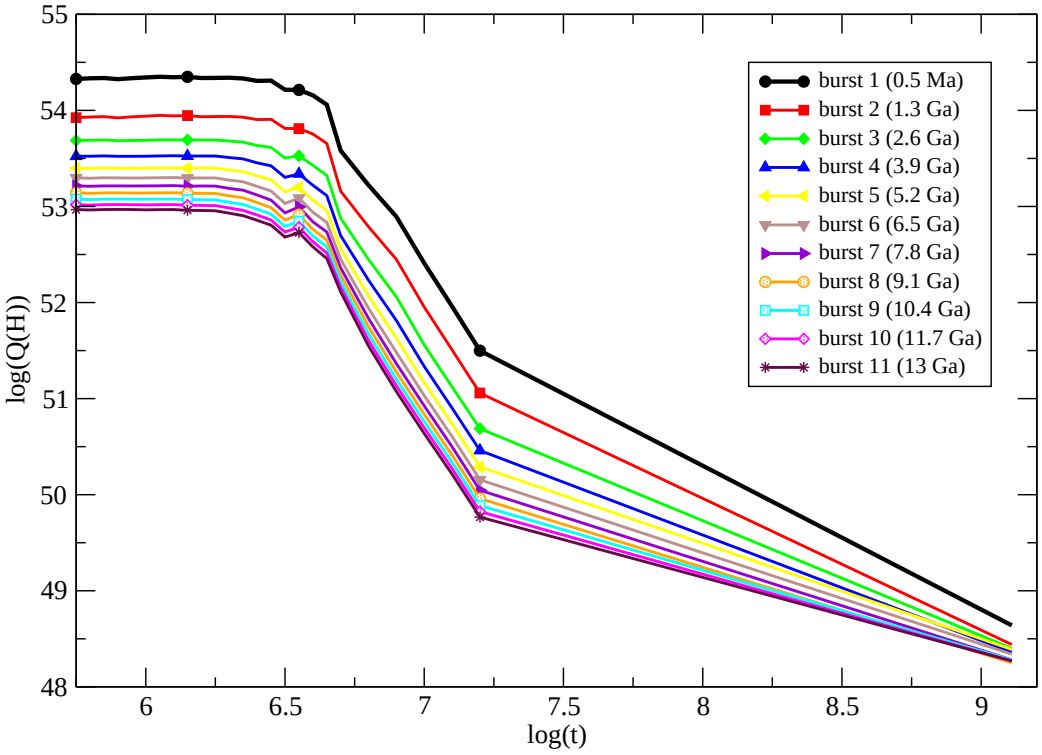

Figure 3.6: The time evolution of the number of ionizing photons for each of the successive bursts during the 1.3 Gyr inter-burst period. The burst number increases downwards. Different colour lines are used for the different bursts.

Fig. 3.6).

Therefore, if the current burst is identified with redshift $z = 0$, the formation of the galaxy would have taken place at a redshift $z \sim 0.7$ (using $H_0 = 74$ km.s^1.Mpc^{-1}, Macri et al., 2006). Since we have not included in the model any effect of the environment which can disrupt or strip the gas of the galaxy and change its morphology, or any gas loss mechanism, like outflows, at redshift $z \sim 1$ it is still a HII galaxy and its characteristics have to be compared with their counterparts at z>0. Thus, the first burst of star formation of the model can be compared with the LCBG-like HII galaxies (Hoyos & Díaz, 2006)

The observed number of ionizing photons for LCBGs at a redshift $0.46 < z < 0.7$, estimated as $\log(Q(H)) \sim 54.6$ (Hammer et al., 2001), would correspond to the value of the first burst of our models. According to these results, our model seems consistent with observations at these intermediate redshifts reproducing at the same time those corresponding to the more luminous local HII galaxies.

The colours of the stellar continuum.

The question of if these galaxies are young galaxies, experiencing their first burst of star formation or if, on the contrary, there exists an underlying population formed some Gyr ago, may be addressed by multi-colour photometry. Although a direct detection of the underlying population in LCBG or HII galaxies is complicated because the observed light is dominated by massive stars, the effect of an underlying stellar population should be easily seen in the observed colours of these galaxies, since any star forming burst previous to the currently observed one will contribute substantially to the total continuum luminosity at the different wavebands.

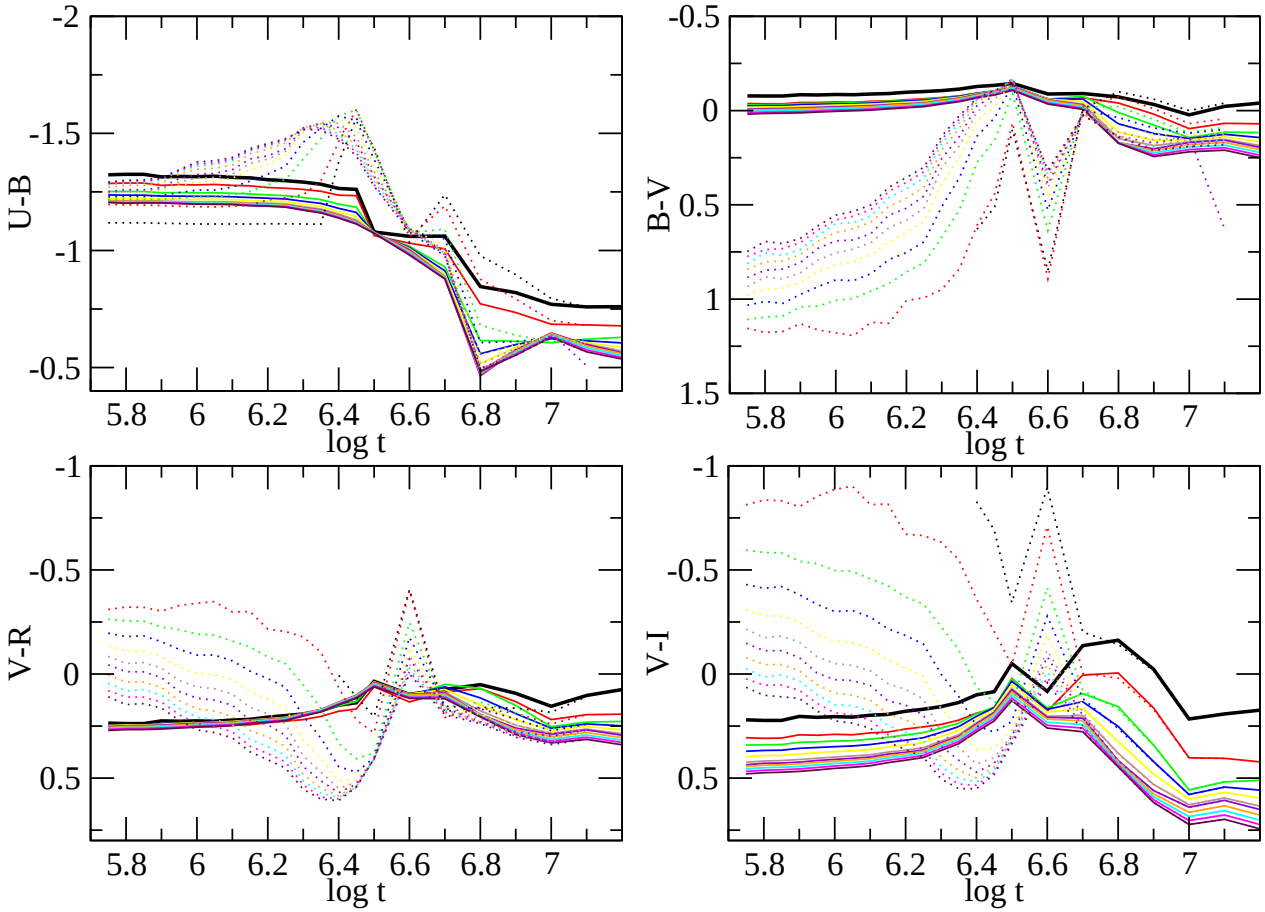

Figure 3.7: Time evolution of colours for model A2: a) U-B; b) B-V; c) V-R; d) V-I. The meaning of the (coloured) lines for different bursts is the same as in Fig. 3.5. Solid lines show the pure continuum colours while dotted lines also include the contribution by the strong emission lines.

In Fig. 3.7 we represent the time evolution of the continuum U-B, B-V, V-R and V-I colours for our model A2 along the first 10 Myr after each burst. The first burst –solid black thick line– follows the expected evolution of a single stellar population of very low metallicity, remaining bluer than during the subsequent bursts where the effect of the accumulated continua from the previous star formation episodes makes colours become redder than expected for a SSP. Even though they are also starbursts in themselves, their star formation efficiency is much lower than that of the first burst, and so is their contribution to the total continuum luminosity which results in redder colours. Furthermore, the metallicity, almost zero for the first burst, increases up to $Z = Z_{\odot}/5$ already during the second burst which also has an reddening effect over the colours.

Photoionization: the ionized gas.

The calculated SED in each time step can be used as input ionizing sources in the photo-ionization code to predict the emission lines intensities which provide information about the youngest stellar population which dominates the final spectra.

Emission line diagnostic diagrams.

Fig. 3.8 shows the relation between the [OIII]$\lambda\lambda$ 4959,5007/H_β and [OII]$\lambda\lambda$ 3727,3729/H_β ratios, which constitutes an excitation diagnostics for ionized nebulae. In this diagram, the most excited objects lie up and to the left while the objects with the lowest excitation are at the bottom right.

The data shown in the graph have been extracted mainly from two main sources. First, the compilation from Hoyos & Díaz (2006) which provides emission line measurements, corrected for extinction, published for local HII galaxies. The sample comprises 450 objects and constitutes a large sample of local HII galaxies with good-quality spectroscopic data. The sample is rather inhomogeneous in nature, since the data proceed from different instrumental setups, observing conditions and reduction procedures, but have been analysed in a uniform way. Data for these sample objects include the emission line intensities of: [OII]$\lambda\lambda$ 3727,29 Å , [OIII]$\lambda\lambda$ 4959,5007 Å , and [NII]$\lambda\lambda$ 6548,84 Å , all of them relative to H_β, and the equivalent widths of the [OII] and [OIII] emission lines – EW([OII]) EW([OIII]) –, and the H_β line, EW(H_β). As a second source, we have used the metal poor galaxy data from the Data Release 3 of Sloan Digital Sky Survey, taken from Izotov et al. (2006). The Sloan Digital Sky Survey (York et al., 2000) constitutes a large data base of galaxies with well defined selection criteria and observed in a

homogeneous way. The SDSS DR3 AbazaJian et al. (2005) provides spectra in the wavelength range from 3800 to 9300 Å for $\sim$ 530000 galaxies, quasars and stars. Izotov et al. (2006) extracted $\sim$ 2700 spectra of non-active galaxies with the [OIII]λ4363 Å emission detected above 1σ level. This initial sample was further restricted to the objects with an observed flux in the H_β emission line larger than $10^{-14} ergs^{-1} cm^{-2}$ and for which accurate abundances could be derived. They have also excluded all galaxies with both [OIII]λ4959/H_β < 0.7 and [OII]λ3727/$H_\beta > 1.0$. Applying all these selection criteria, they obtain a sample of $\sim$ 310 SDSS objects. Data for these sample objects include the emission line intensities of: [OIII]λ4959,5007 Å and [NII]λ6584 relative to H_β and the equivalent width of H_β. They also include the intensity of the [OII] $\lambda\lambda$ 3727,29 Å emission line for the lowest redshift objects.

The very young stellar population during the first Myr after each burst produces a high ionization, so the [OIII]/H_β ratio is high, then it decreases raising again at 4 Myr due to the presence of Wolf Rayet stars that produces a harder continuum (García-Vargas,Bressan, & Díaz, 1995; García-Vargas et al., 1998). After 5 Myr, the burst evolves to lower values of log[OIII]/H_β. Diagonal lines in this plot correspond to nearly constant ionization parameter and are swept along by the different successive bursts of a given age. High excitation objects, with high log[OIII]/H_β and low log[OII]/H_β ratios, have low metallicities and they are not reproduced by our model, which fits better the high metallicity sample, in the middle to right side of the panel.

It can be better seen in Fig. 3.9, which shows the relation between the excitation parameter, log([OIII]/H_β), and the metallicity indicator log([NII]/H_α) which gives information about the younger populations plus the star formation rate (Kennicutt et al., 1994). At the beginning of the evolution, as we saw in previous sections, the star formation rate is high, and the Hα emission of our model is strong. As the galaxy evolves, the Hα emission decreases while the [NII] emission increases due to the growth of metallicity.

Our models reproduce the general trend shown by data but cannot reproduce the lower metallicity (low [NII]/H_α ratio) objects to the left of the graph. This is due to the fact that the efficiency of the first burst, 33.1%, produces a metallicity which is already too high. A lower efficiency is therefore required to reproduce the observations of the less metallic objects.

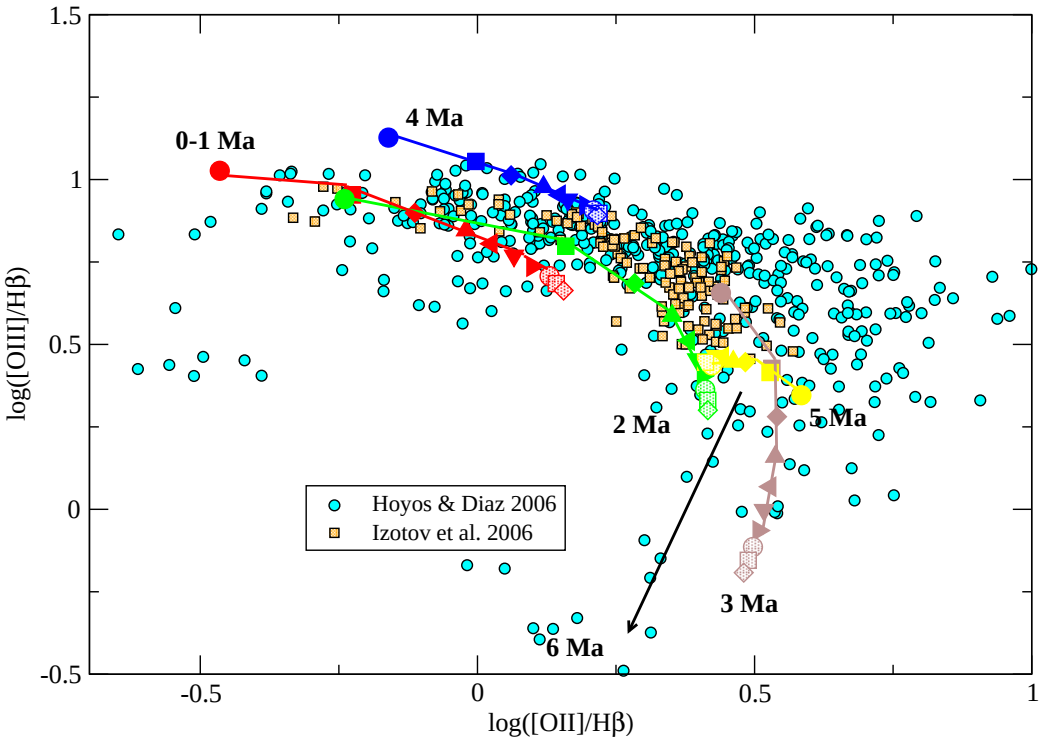

Figure 3.8: The relation between the oxygen line ratios for model A2. Solid coloured lines join the values reached at the same age by each different burst. Red, green, brown, blue and yellow colours correspond to ages 0-1, 2, 3, 4 and 5 Myr respectively. Different bursts, except the first one, are represented by different symbols: solid circles, squares, diamonds, triangles up, triangles left, triangles down and triangles right correspond to bursts at 1.3, 2.6, 3.9, 5.2, 6.5, 7.8 and 9.1 Gyr respectively. Open circles, squares and diamonds correspond to bursts at 10.4, 11.7 and 13.2 Gyr respectively. The data are from references cited in the text.

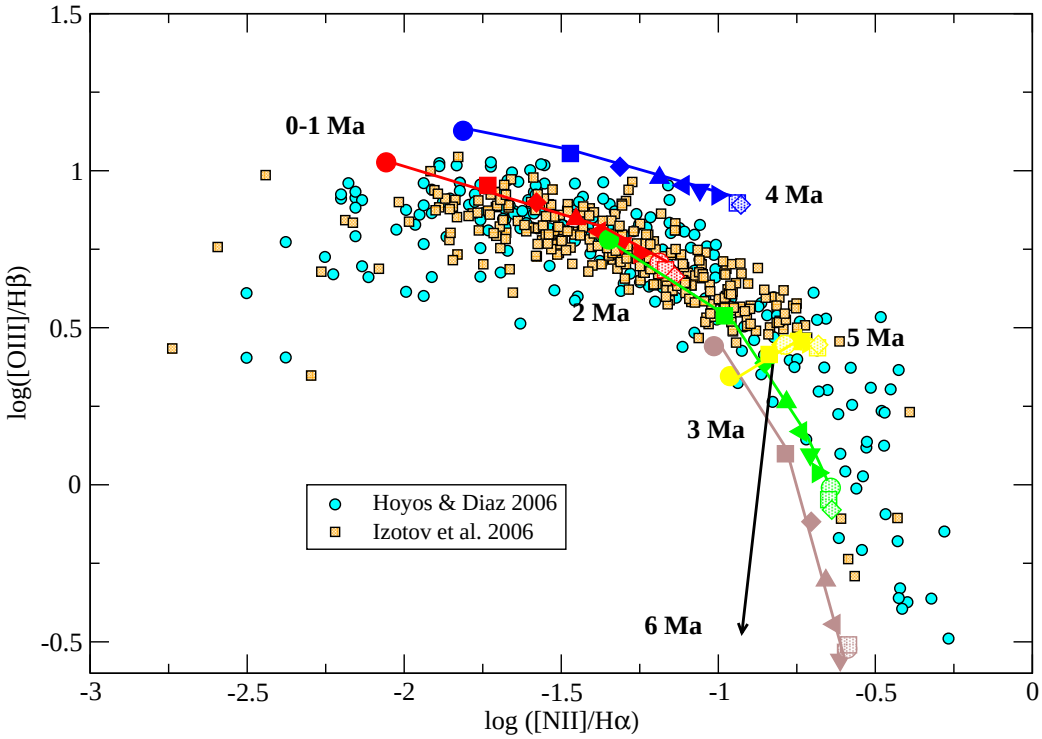

Figure 3.9: The relation between the excitation parameter, log([OIII]/H_β), and the metallicity indicator log([NII]/H_α) for model A2. The meaning of colours, symbols and lines is the same as in the previous figure.

Combined continuum and emission line diagnostics.

Continuum colours and the contribution of the emission lines.

Once the continuum spectral energy distributions and the different emission line fluxes are computed, we can calculate the contribution of these emission lines to the different broad band filters and then synthesize the colours of our model galaxies. These are the colours which are readily observable through integrated photometry.

We have done so taking into account only the strongest emission lines that contribute to the colour in each broad-band spectral interval at redshift zero. These are: [OII] $\lambda\lambda$ 3727, 3729 Å in U, H_β λ 4861 Å in B, [OIII]$\lambda\lambda$ 4959, 5007 Å in V, Hα λ 6563 Å in R and [SIII] $\lambda\lambda$ 9069, 9532 Å in I.

Figure 3.7 shows, with dotted lines, the new computed colours including the contribution by the different emission lines. As it can be seen the colours do not change by a large amount in the case of U-B or V-R. However the effect in the B-V and V-I colours is rather dramatic.

The equivalent width of H_β.

Dottori (1981) suggested the use of the equivalent width of H_β, EW(H_β), as an age estimator for HII regions, and applied this method to rank the ages of HII regions in the Magellanic Clouds. If a SSP is considered, the H_β emission is very high at the beginning of the burst, while the continuum at H_β, dominated by the most massive and luminous stars, is low hence producing a large value of EW(H_β). As the burst evolves, the H_β luminosity decreases as does the number of ionizing photons, and the contribution to the continuum increases thus lowering the value of EW(H_β). This case corresponds to the thick (black) line in Fig. 3.10.

The evolution of the equivalent width in our model is shown in Fig. 3.10. It is seen that the first burst, that corresponds to a SSP, has an initial equivalent width slightly greater than the successive bursts, which decreases with time reaching very low values ($<$ 40 Å) 6 Myr after the beginning. When a new burst takes place, new massive ionizing stars form and the EW(H_β) goes up again, although not as much as in the previous one due to the decreasing gas mass involved in the burst, increased metallicity and the accumulated contribution from the continua from the previous bursts. At any rate, even taking into account this contribution, the EW(H_β) remains a good age indicator for the age of the current burst, inside 10 Myr. On the other hand it is not possible to detect the presence of the underlying stellar populations for a given galaxy solely on the basis of this parameter.

The distribution of the EW(H_β) in HII galaxies shows that most of them

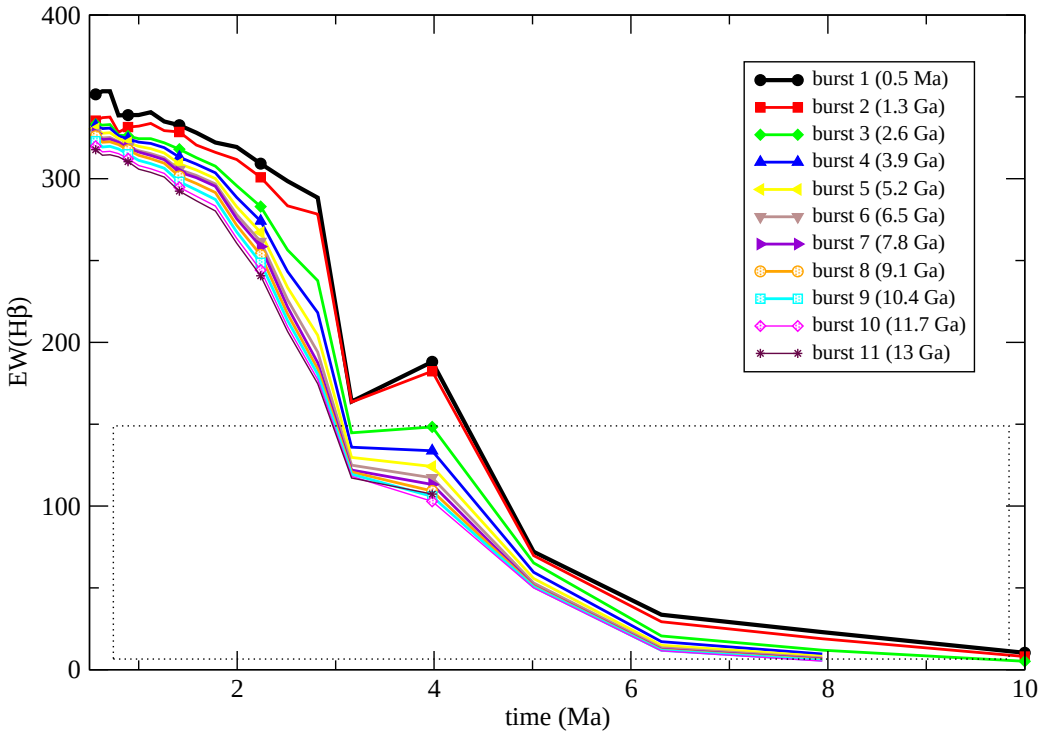

Figure 3.10: Time evolution of the H_β equivalent width of model A2. The black line corresponds to the first star burst of our model, a SSP with very low metallicity. The successive bursts are represented with the same colours as in Fig. 3.5.

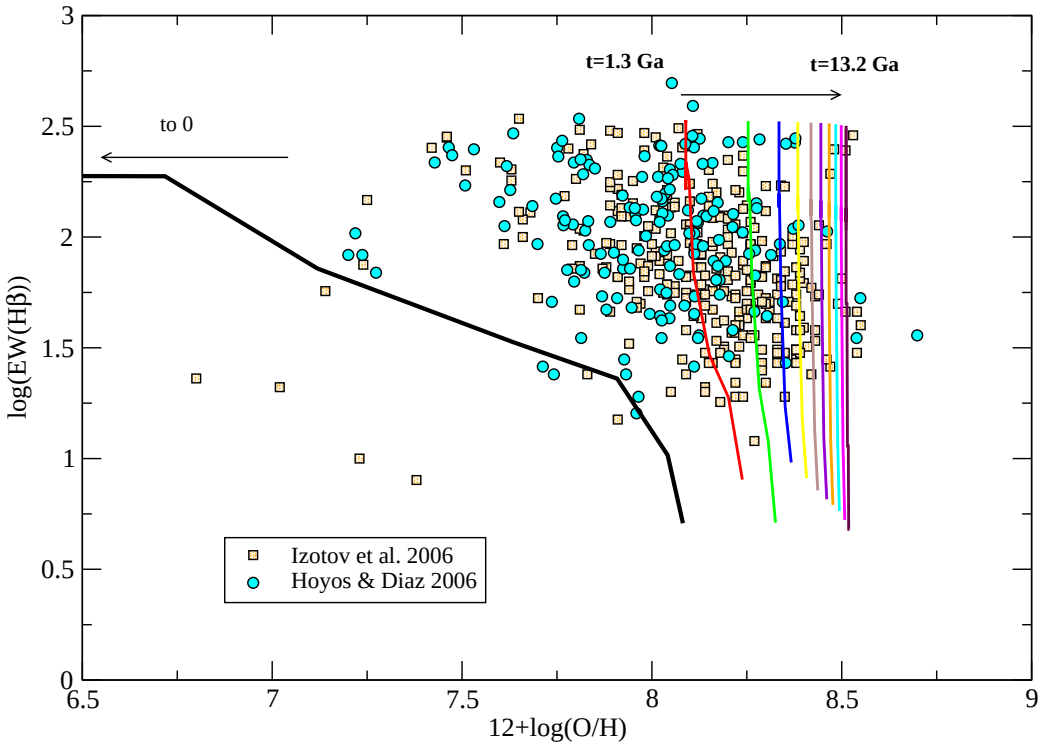

Figure 3.11: EW(H_β) as a function of the metallicity $12 + log(O/H)$ for the model A2. Colours have the same meaning than in Fig. 3.7. The first burst (solid black line) does not appear in the graph because its abundance is still the primordial one, $12+log(O/H) << 7$.

have values lower than 150 Å (Terlevich et al., 1991; Hoyos & Díaz, 2006) which, in our models, corresponds to ages greater than 3-4 Myr. Terlevich et al. (2004), from the application of inversion methods, have shown that, globally, this distribution is inconsistent with what is expected from a single burst scenario and resembles more the distribution obtained for a succession of short bursts separated by quiescent periods with little or no star formation.

These results are not that strong when samples showing a restricted metallicity range are analysed. However, as we have seen before, metallicity increases with time in a way which constrains the SFH which is best reproduced by our A2 model. Fig. 3.11 shows the evolution of the EW(H_β) with oxygen abundance. During the duration of the first burst the EW(H_β) decreases while the oxygen abundance increases from zero to $12+log(O/H) \sim 8$. The successive bursts start with this higher abundance and each of them evolves vertically in a 10 Myr time scale with the EW(H_β) decreasing rapidly at almost constant oxygen abundance. This occurs because the oxygen is

produced by the most massive stars in a very short time and therefore its abundance changes very little during the next 10 Myr after each burst (see Fig. 3.3). It is clear that our model is able to reproduce the most metallic galaxies in the samples taken from Hoyos & Díaz (2006) and Izotov et al. (2006) where this high abundance is explained as the consequence of the gas being processed by one or more previous generations of stars. An alternative scenario to produce such high oxygen abundances would be the occurrence of a very intense initial star formation burst, with a SFR of the order of 100 $M_{\odot}$ Myr^{-1}, out of the range observed in local HII galaxies (see Figures 3.3 and 3.1). On the other hand, galaxies $12 + log(O/H) \leq 8$ are not reproduced by our model. In order to fit these data, a model with a star formation efficiency lower than assumed, that is, < 33 %, should be used.

The most informative data to uncover the presence of underlying populations in HII galaxies consist of the combination of a line emission parameter, which characterizes the properties of the current burst of star formation, and a continuum colour which represents better the SFH in a longer time scale. Fig. 3.12, left panel, shows the equivalent width of H_{β} *vs* the U-V colour along the evolution of the galaxy for the successive stellar bursts. When a given burst occurs the EW(H_{β}) is high and decreases as the stellar population ages. We have over-plotted the results for the SSPs from the model Starburst99 (Leitherer et al., 1999, STB99) with two different metallicities as labelled. As expected, our results agree better with the higher metallicity STB99 model. The black line in the left panel, that represents a metal-poor SSP, is too blue compared with the data for a given EW(H_{β}). In order to decrease EW(H_{β}) and move the model colour to the red, a more metal-rich SSP was selected (dotted line at the left panel), but even such unrealistic high abundance does not reproduce the observations, as we have shown in Fig. 3.3. Therefore, the observed trend can not be explained as an age effect since EW(H_{β}) for low metallicity SSP does not reach values lower than 100Å and does not reproduces the colours, neither as a metallicity effect because such high abundances are not observed in HII galaxies. It is therefore necessary to include both effects simultaneously, as we have done, to see how the effect of an underlying older population contributing to the colour of the continuum makes it redder. From the observational point of view, U-V colours for HII galaxies are scarce, therefore we have compared our results with those from Hoyos & Díaz (2006) that include galaxies taken from Terlevich et al. (1991) and Salzer et al. (1995) providing the equivalent widths of both the [OII] and [OIII] lines. We have then computed pseudo-colours from the intensities of the adjacent continua of [OII]λ3727 and [OIII]λ5007 lines as:

$$EW_{[OII]\lambda3727}(\text{Å}) = \frac{[\text{OII}]\lambda3727(\text{ergs}^{-1})}{\text{I}_{\text{cont}}(3730)(\text{ergs}^{-1}\text{Å}^{-1})} \tag{3.3}$$

and

$$EW_{[OIII]\lambda5007}(\text{Å}) = \frac{[\text{OIII}]\lambda5007(\text{ergs}^{-1})}{\text{I}_{\text{cont}}(5010)(\text{ergs}^{-1}\text{Å}^{-1})} \tag{3.4}$$

$$log\left(\frac{I_{cont}(3730)}{I_{cont}(5010)}\right) = log\left(\frac{[OII]\lambda3727}{[OIII]\lambda5007}\frac{EW_{[OIII]\lambda5007}}{EW_{[OII]\lambda3727}}\right) \tag{3.5}$$

The right panel of Fig. 3.12 shows the equivalent width of H_β as a function of the pseudo-colour defined above for model A2 together with the observational data. It should be noted that no correction for extinction associated with the continuum light has been made. This correction amounts to about 0.15 dex for a standard reddening law and therefore a SSP would always be unable to reproduce the observed colours. Yet our Model A2 produce UV continuum colours which are too blue as compared with the bulk of the observations which indicates that our assumed degree of attenuation is too low.

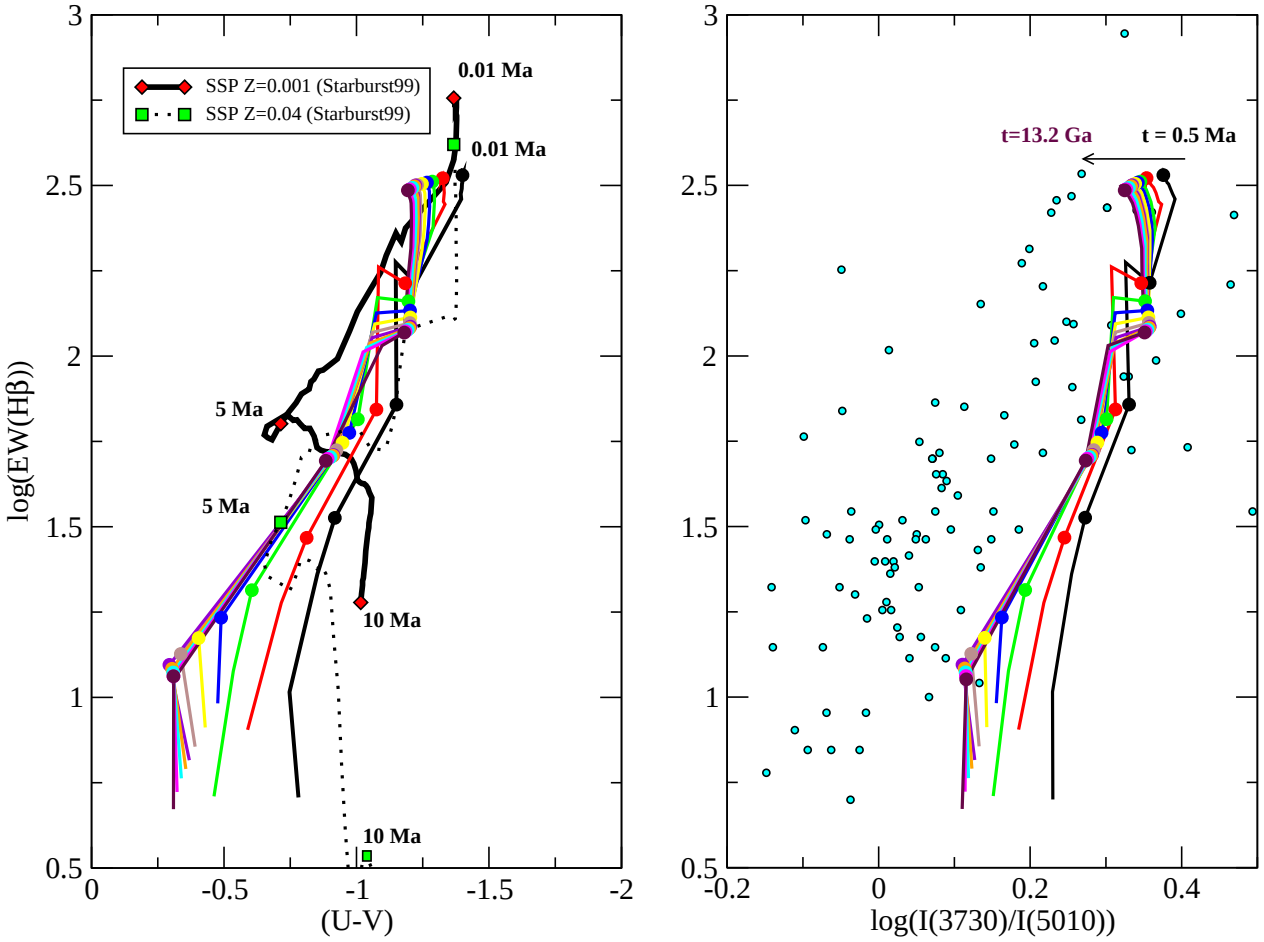

Figure 3.12: Left panel: The equivalent width of H_β as a function of the continuum colour for model A2. The results for the SSPs from the model Starburst99 Leitherer et al. (1999) with two different metallicities as labelled are overplotted. Colours have the same meaning as in Fig. 3.7. Right panel: The equivalent width of H_β as a function of the pseudo-colour defined by equations 3.3 to 3.5 for model A2. The data are from Terlevich et al. (1991) and Salzer et al. (1995). In both panels the large dots mark ages separated 2 Myr.

3.1.3 Conclusions.

For this part of the work each galaxy has been modelled assuming an initial amount of unprocessed gas of 10^8 $M_\odot$ in a region of 1 kpc of diameter. The evolution is computed along a total duration of 13.2 Gyr during which 11 successive starbursts, separated by 1.3 Gyr, take place. Four types of models have been computed with different properties: equal and attenuated bursts, and different values of the initial star formation efficiency. The only model which has proved to be able to fit the observational data is the Attenuated Bursts Model, A2, with 33% of initial efficiency. This type of model reproduces the star formation rate estimates of local HII galaxies and the oxygen abundances of the average metallicity objects although fails to account for the most metal deficient ones which would require models with lower star formation efficiencies than assumed.

We have computed the time evolution of the continuum colours with and without the inclusion of the emission lines. It is shown that both nebular continuum and line emission must be taken into account in the photometric studies of the underlying stellar populations of HII galaxies. The effect of the emission lines are more pronounced in the B-V and V-I colours.

The combination of parameters which characterize the current star formation on a time scale of Myr, such as the equivalent width of H_β, and the SFH over a time scale of Gyr, such as broad-band continuum colours, is found to provide an effective means to uncover the presence of underlying stellar populations. The comparison of models and observations show that in most HII galaxies SSP are unable to reproduce the relatively red colours shown by data with the observed H_β equivalent width values requiring the contribution of previous stellar generations. Our model, however, produces U-V colours that are too blue when compared with observations. A higher contribution of the previous bursts to the total continuum is needed, implying that the successive bursts that take place in HII galaxies should be even more attenuated than has been assumed in this first set of models.

3.2 Second set of models: fitting Attenuated Bursts Models.

Once tested the viability of this kind of models has been tested, we have been driven to two main conclusions :

-The Attenuated Bursts Model with the lower efficiency used (33%) provides an upper limit for the oxygen abundance of HII galaxie.

-The colours are still too blue as compared with observations, implying

that the successive bursts should be even more attenuated.

Following these conclusions, this second set of models considers more possibilities for Attenuated Models. First of all, we have to use a lower initial efficiency to explain low metallicity HII galaxies, and then obtain a lower limit in oxygen abundance, which can give us a complete range of efficiencies for this kind of galaxies. Once we have the whole efficiency range, we have to increase the attenuation to make the contribution of the underlying continuum to the colours higher than the contribution of the current burst of star formation.

3.2.1 Description of the model.

The second set of models is the continuation of the ***Attenuated Burst Models***, including low initial efficiencies and different attenuation modes for the successive bursts. The following models have been constructed:

Standard Attenuation Models (SAM): The attenuation is the same used for the first set of models of the previous section:

$$\psi_n = \frac{\psi_0}{n} \tag{3.6}$$

For this type of models we have assumed two initial efficiencies. The H values are:

-H =6 (1/H=1.25 Myr), which corresponds to an initial efficiency of 33%

-H =1.55 (1/H=0.5 Myr), which corresponds to an initial efficiency of 10%

High Attenuation Models, (HAM): The attenuation in the successive bursts is higher for this set of models, which makes the contribution of the underlying continuum to be higher than the current burst of star formation. This type of attenuation assumes a constant attenuation factor following the expression:

$$\psi_n = \psi_0 \cdot k^{(n-1)} \tag{3.7}$$

where n is the number of the current burst, and k is the attenuation factor. This factor can take values from 0 to 1 for attenuated models. [1]. For this set of models we have chosen k=0.65 and k=0.5 in order to compare with SAM and also between models with different attenuation factor. The lower the k values, the stronger the attenuation, the burst being less efficient each

[1] and higher than 1 if we want to build an increasing efficiency model; this kinds of models, however, are not included in this work

time. The higher the k value, the weaker the attenuation, then, the bursts are strong.

The star formation efficiencies taken for this models are:

-H =6 (1/H=1.25 Myr), corresponding to an efficiency of 33%

-H =1.55 (1/H=5 Myr), corresponding to an efficiency of 10%

With this values of H we computed models using the chemical evolution code [2], the evolutionary synthesis code and the photoionization code obtaining the results explained in the following sections.

3.2.2 Results.

Chemical evolution.

Star Formation Rates.

Now we have two different values for the initial efficiency for each model: **high efficiency** involving 33% of te initial mass of gas, and **low efficiency**, assuming only 10% of the gas. In Figure 3.2.2 the star formation rates of the six models are represented. For the Standard Attenuation Model, left panel, the SFR is high at the beginning of the evolution, but it decreases rapidly due to the progressive consumption of the available gas to form stars, as in the first set of models. In HAM (central and right panels) this decrease is, in addition, due to the attenuation factor, producing a lesser consumption of the gas. This means that there is more gas available for the next burst, baut the star formation rate is lower due to the strong attenuation. This effect is seen better in the model with k=0.5, where we obtain much lower SFR for the last bursts of star formation than in model with k=0.65, whose SFR is more similar to the SAM in the first bursts. The behaviour of the lower efficiency models is similar to the high efficiency ones, showing smaller star formation rates.

Elemental abundances.

The oxygen abundance delimits the range of possible efficiencies for the models of HII galaxies. In Figure 3.2.2 we can see that, with both efficiencies, 33% and 10% , we cover the whole range of oxygen abundances in HII galaxies, these efficiencies providing the upper and the lower limit respectively. Although they have different type of attenuation, SAM and

[2]The time step for this set of models is Δt=0.7 Myr instead of Δt=0.5 Myr. It does not have any important consequence because it is still small enough to take into account the fast evolutionary phases of the most massive stars considered.

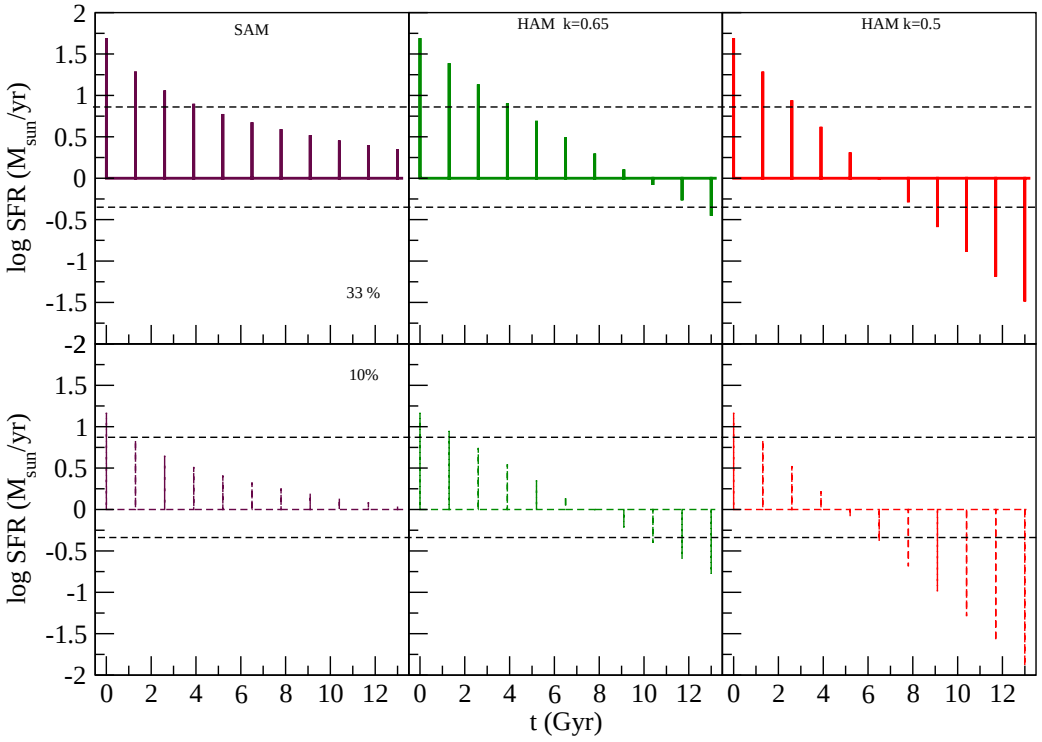

Figure 3.13: Star formation rates for SAM and HAM with both attenuation factors, k=0.5 and k=0.65. High efficiency models (33%) are represented in the upper panels, and low efficiency ones (10%) in the lower panels.

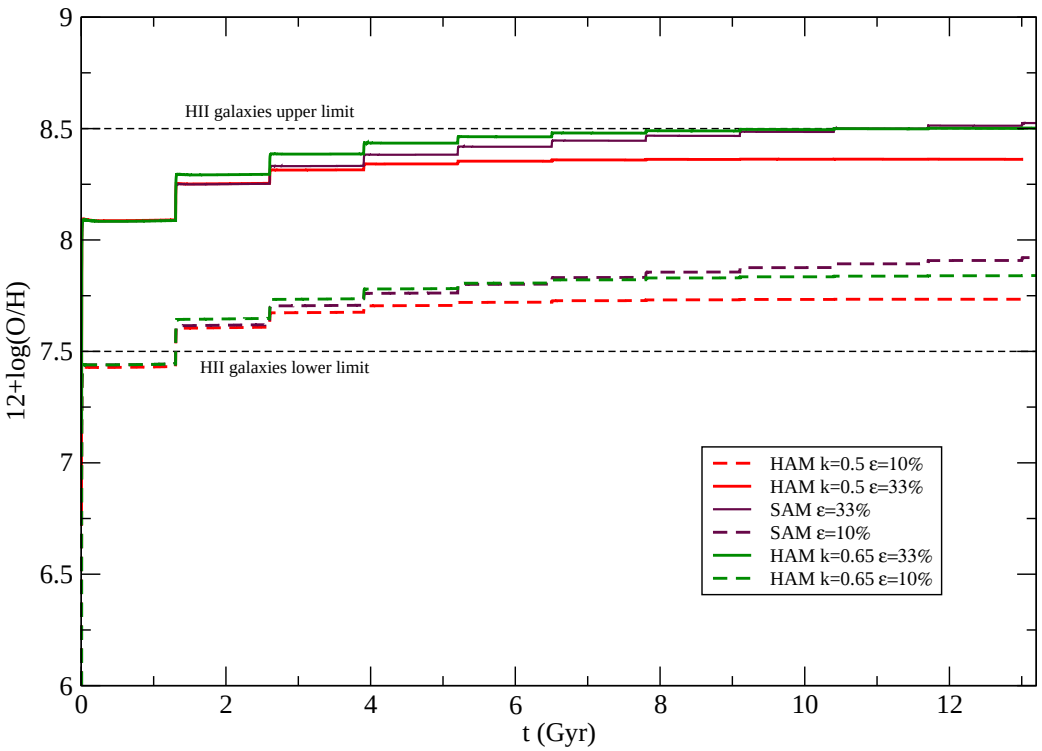

Figure 3.14: Evolution of the oxygen abundance for SAM and HAM with both attenuation factors, k=0.5 and k=0.65, and both efficiencies, high efficiency as thick lines and low efficiencies as dashed lines.

HAM with k=0.65 show a very similar behaviour in the oxygen abundance evolution. The last bursts are less efficient in HAM, however, they show a higher metallicity from the second to the eighth burst, being stronger than in SAM. For the k=0.5 model, the abundance does not grow as much as before and from the 5th-6th burst to the end, due to the high attenuation, the abundance is almost constant.

Models with both attenuation types, standard and high, with an efficiency of 33% reproduce the observational data which begin to show the secondary behaviour of the N/O ratio. Low efficiency models lie in the region where the nitrogen shows a constant value, indicating a primary trend (where green dots are located). The attenuation makes the model to cover a small range of oxygen abundance, but the nitrogen behaviour is similar for both SAM and HAM.

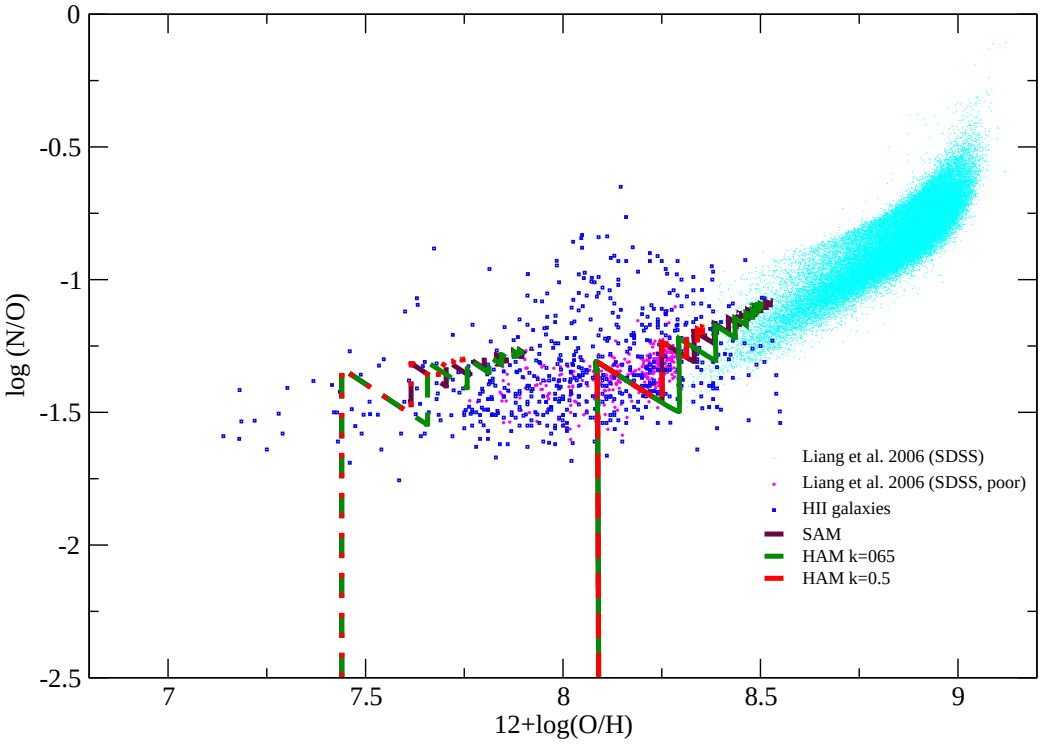

Figure 3.15: Evolution of the N/O ratio as a function of the oxygen abundance 12+log(O/H) for the second set of models. Thick solid lines represent high efficiency models and dashed lines low efficiency ones. As in Figure 3.4, data from Izotov et al. (2006); Hoyos & Díaz (2006); Izotov & Thuan (1999); Nava et al. (2006) correspond to low metallicity HII galaxies. Blue and magenta dots are high and low metallicity galaxies, respectively, of SDSS from Liang et al. (2006).

Evolutionary stellar population synthesis.

The use of a lower initial star formation efficiency implies a lower initial metallicity. For the previous models we had to assume a minimum initial metallicity to assign the correct single stellar population from GV95, but for low efficiency models this minimum value assigned to the first burst would not be correct. This method is valid only for metallicities $Z \geq 0.0028$, which prevents us from using small efficiencies for the star formation since, in that case, the abundances will be low during the the whole evolution. The use of PopStars from MGVB09 allow us to obtain the whole spectral range of the models for any initial efficiency, without a minimum initial metallicity assumption. Also, in this new set of models we have used Ferrini IMF for both the chemical evolution code and the evolutionary synthesis code in order to avoid any inconsistency.

The number of ionizing photons.

The evolution along every burst of the number of ionizing photons can be seen in fig 3.16

With the new libraries of SSPs from PopStars, the number of ionizing photons per stellar mass is lower than in models made with GV95, and we do not reach the values for the first bursts that we obtained with our previous models. Now, for the first burst of the models with an efficiency of 33% we obtain a value of logQ(H)=53.4, which is the value obtained for the 6th burst in the first set of models, identified with the z=0 value. This fact is due to two main reasons:

1. The use of Ferrini IMF in the chemical evolution code and for the SSPs. The differences are minimal, but it could affect the number of massive stars formed (Mollá & Díaz, 2005)

2. The use of NLTE model atmospheres for massive stars and WR from Smith, Norris, & Crowther (2002) which produce less ionizing photons and hence, a lower excitation in ionized regions, as we will see in the next section.

The colours of the stellar continuum.

In Figures 3.17 and 3.18 we represent the colour evolution of the models for each burst of star formation. Due to the very low metallicity of the first burst in every model, the colour has characteristics of a single stellar population with a very low metal content. In every model, a very pronounced reddening around log t=6.6 (4 Myr) in the first burst can be seen, produced by RGB stars. This did not happen in the first set of models because we could not use the lowest metallicity SSP to obtain the first burst spectrum, and this

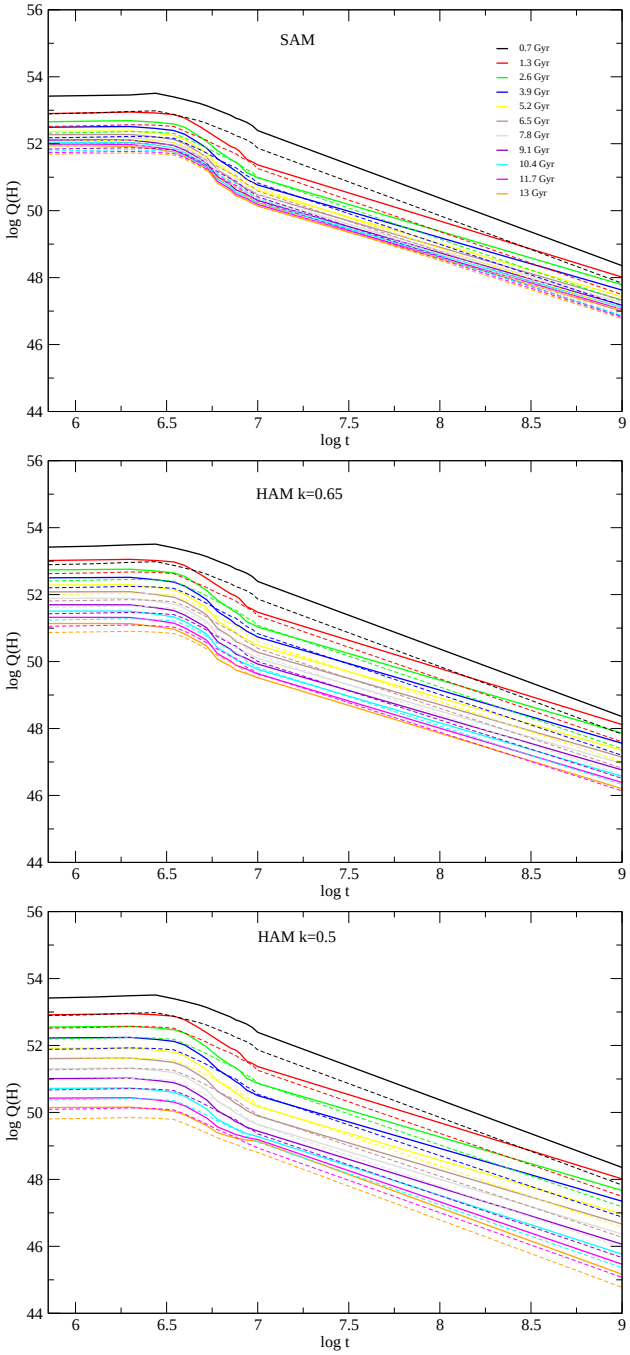

Figure 3.16: Evolution of the number of ionizing photons with time along 1 Gyr for every burst. Upper panel represents the SAM, center panel is the HAM with k=0.65 and lower panel is HAM with k=0.5. Each burst is represented by a different colour. Solid lines are high efficiency models and dashed lines low efficiency ones.

feature is not seen in metallicities higher than Z=0.0001. For the subsequent bursts the metallicity grows up quickly, leaving place to blue massive stars characteristics, as the blue bump produced by WR stars after $\backsim$ 4 Myr from the beginning of the star formation in every burst. There are some other differences between high and low efficiency models. The first bursts of every model are similar (SSP of low metallicity), but the subsequent bursts of low efficiency models do not show the reddening from burst to burst that the high efficiency model does because the metallicity does not grow as fast as it does in high efficiency models and the bursts maintain bluer colours.

HAM have a higher contribution from the non ionizing underlying continuum, which makes the colours to look redder for subsequent bursts and the young and blue population features dissapear. Meanwhile, SAM keep bluer colours, characteristic of the current burst of star formation. Even when the SFR of the models with k=0.65 is very similar to, or in some intermediate bursts even higher than, the SAM, the underlying population makes the colours redder each time with the last bursts even showing a very smooth, or null, evolution in colour. This effect is more pronounced in the k=0.5 models. From the first to the second burst there is not a very strong reddening due to the lower metallicity of the first burst. It is from the second to the third burst when the underlying population contributes more to the continuum and make the colours to become redder. The subsequent bursts suffer less reddening each time, with the model lines being closer to each other in the final bursts, because the SFR decreases with time too. This means that most of the underlying continuum which have a greater influence on the colour comes from the immediately previous burst, for models with 1.3 Gyr of inter-burst time.

Photoionization: the ionized gas.

In the previous set of models we used an initial radius of 500 pc at the beginning of the evolution, and then we adjusted this value in order to obtain a constant stellar mass density in every successive burst. For this new set of models we wanted to give a more physical meaning to the radius of the nebula and we have used the ionized region radius, obtained from the mechanical energy provided by the winds from massive stars and SNe, as explained in Chapter 2. This method has the advantage of constarining the ionization parameter. Now it is derived from physical parameters associated with the evolution of the ionizing cluster. The evolution of the radius with time, and with the number of ionizing photons can be seen in Figures 3.19.

The radius grows with time within each burst while the mechanical energy increases due to the strong winds of massive stars. From burst to burst the

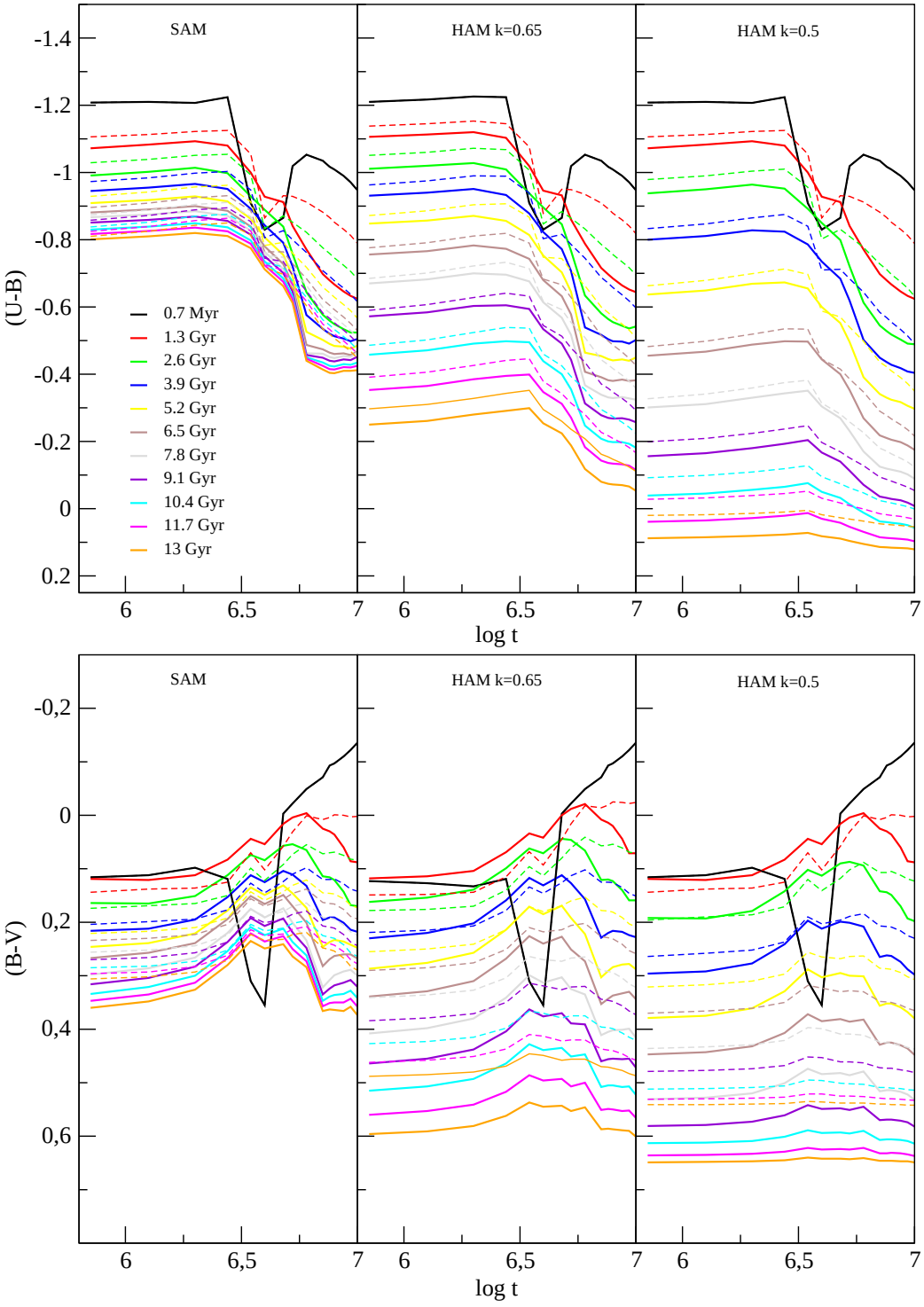

Figure 3.17: Evolution of the (U-B) and (B-V) continuum colours for the three models. The first burst of every models is shown by the black thick line. Solid lines correspond to high efficiency models and dashed lines to low efficiency ones. Each burst is represented with a different colour as labelled in the figure.

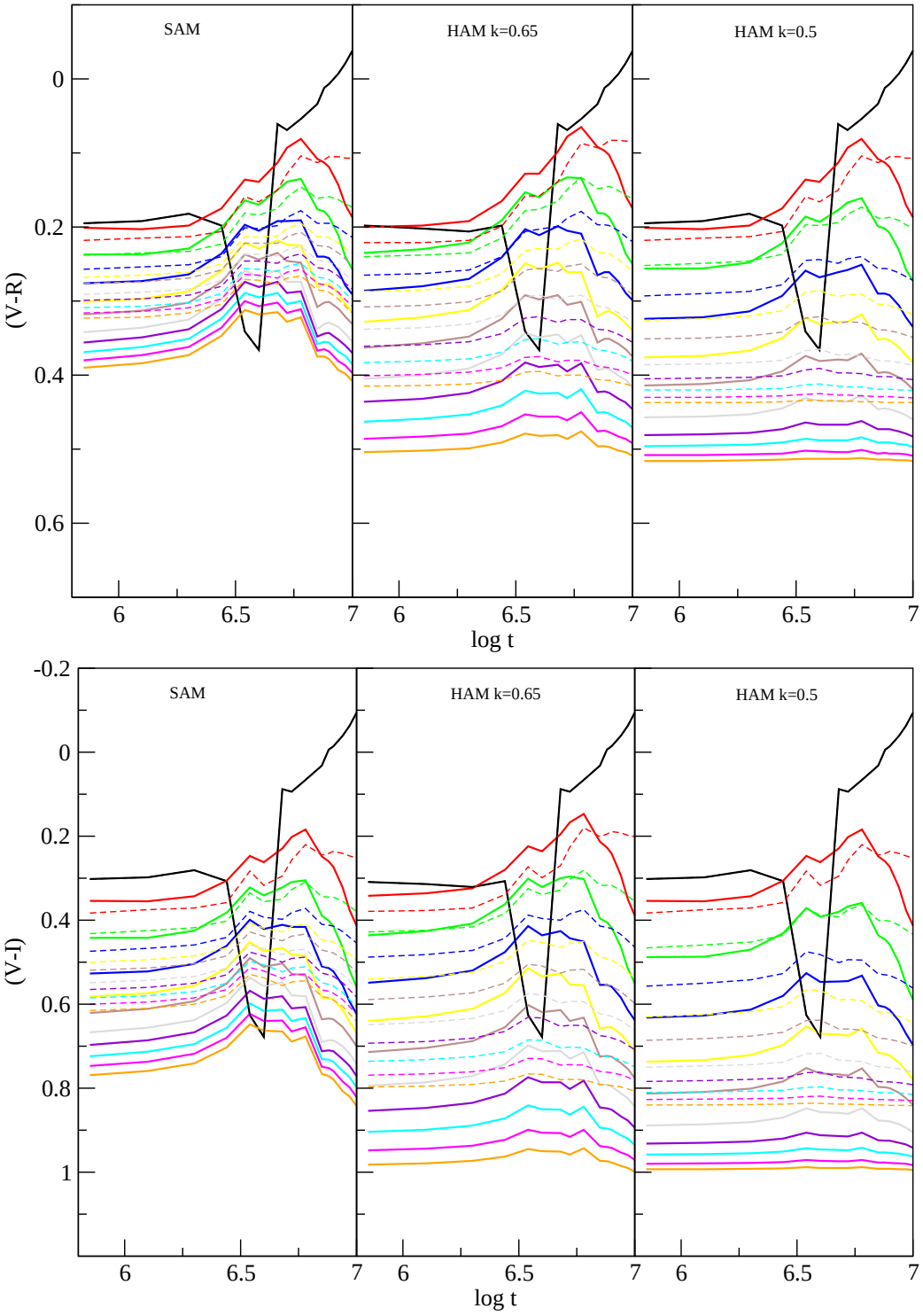

Figure 3.18: Evolution of the (V-R) and (V-I) continuum colours for the three models. The first burst of every models is represented by the black thick line. Solid lines correspond to high efficiency models and dashed lines to low efficiency ones. Each burst is represented with a different colour, similar to Figure 3.17 .

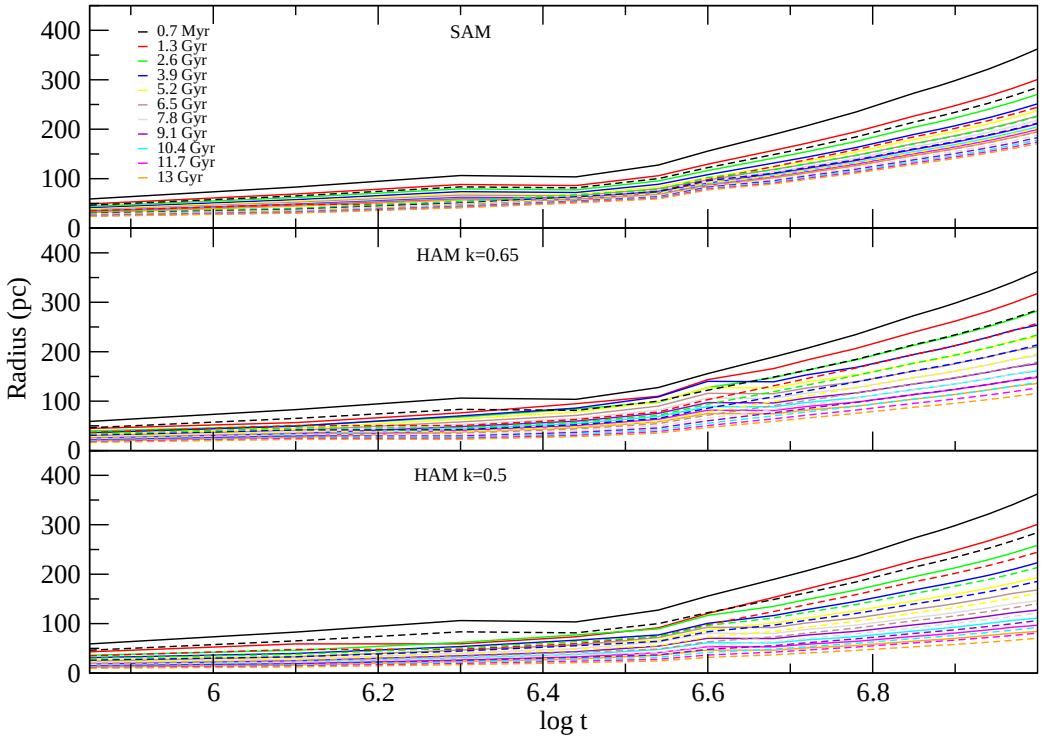

Figure 3.19: Evolution with time of the radius assumed for the nebula. Solid lines correspond to high efficiency models and dashed lines to low effciency ones. The colours of the bursts are similar to those shown in previous figures.

decreasing star formation rate makes the radius to decrease too; fewer massive stars are formed each time and we have less mechanical energy from their winds.

In SAM, this diminution is less conspicuous, the bursts are stronger and more similar to one another, specially the last ones. The evolution of the number of ionizing photons with the radius tells us how the ionization parameter changes with time:

$$U = \frac{Q(H)}{4\pi n_H c R^2} \tag{3.8}$$

The photoionization model is similar to the previous ones: case B of recombination and plane-parallel approximation.

Emission line diagnostic diagrams.

Once we have the radius of the different bursts, with the abundances of the elements, the density (assumed to be 100 cm^{-3}) and the ionizing continuum, we can apply the photoionization code to obtain the emission line intensities (Figures 3.20).

Standard Attenuation Models reproduce the trends shown by HII galaxies, with low efficiency models falling below the high efficiency ones in all panels, covering the region of the diagram occupied by the young and less metallic galaxies (high [OIII]/H_β and low [OII]/H_β), as expected. The initial efficiency of each model leads the star formation rate, that is, the number of massive stars which produce the ionizing photons. The higher the efficiency, the more ionizing photons we get, and also the higher the ionization parameter is obtained, producing a high excitation object. Models with different attenuation modes and the same initial efficiency do not show noteworthy differences, since it is the current burst of star formation which produces the emission lines that we observe, and the underlying population does not affect the ionization parameter. The ionization degree is driven by the efficiency of the bursts, not by the attenuation mode, or the attenuation factor.

The emission line intensities shown during the first burst is similar in all models with the same efficiency. Results from the HAM with k=0.65 are close to those from the SAM. In these models, the bursts are strong, although last bursts of HAM are not as strong as in SAM which makes the lines in the diagram corresponding to the successive bursts to be very close to each other. A great number of of massive stars are created, making the metallicity to grow very quickly. This rapid increase in metallicity makes the oxygen lines to become fainter even faster than in models with lower SFR. If the SFR is high, more massive stars are created and the interstellar medium is enriched faster.

In the k=0.5 model the lines in the diagrams are very close together, with little dispersion. As we said before, if the SFR is low, the metallicity does not grow so rapidly, and high values of [OIII]/H_β can be maintained for longer thus reproducing the upper region occupied by the observational data. However, none of these models with high efficiency is able to reach the highest part of the diagram where the galaxies with high excitation are. We obtain a lower number of ionizing photons with the use of MGVB09 for the same efficiency, and hence the excitation degree reached is lower.

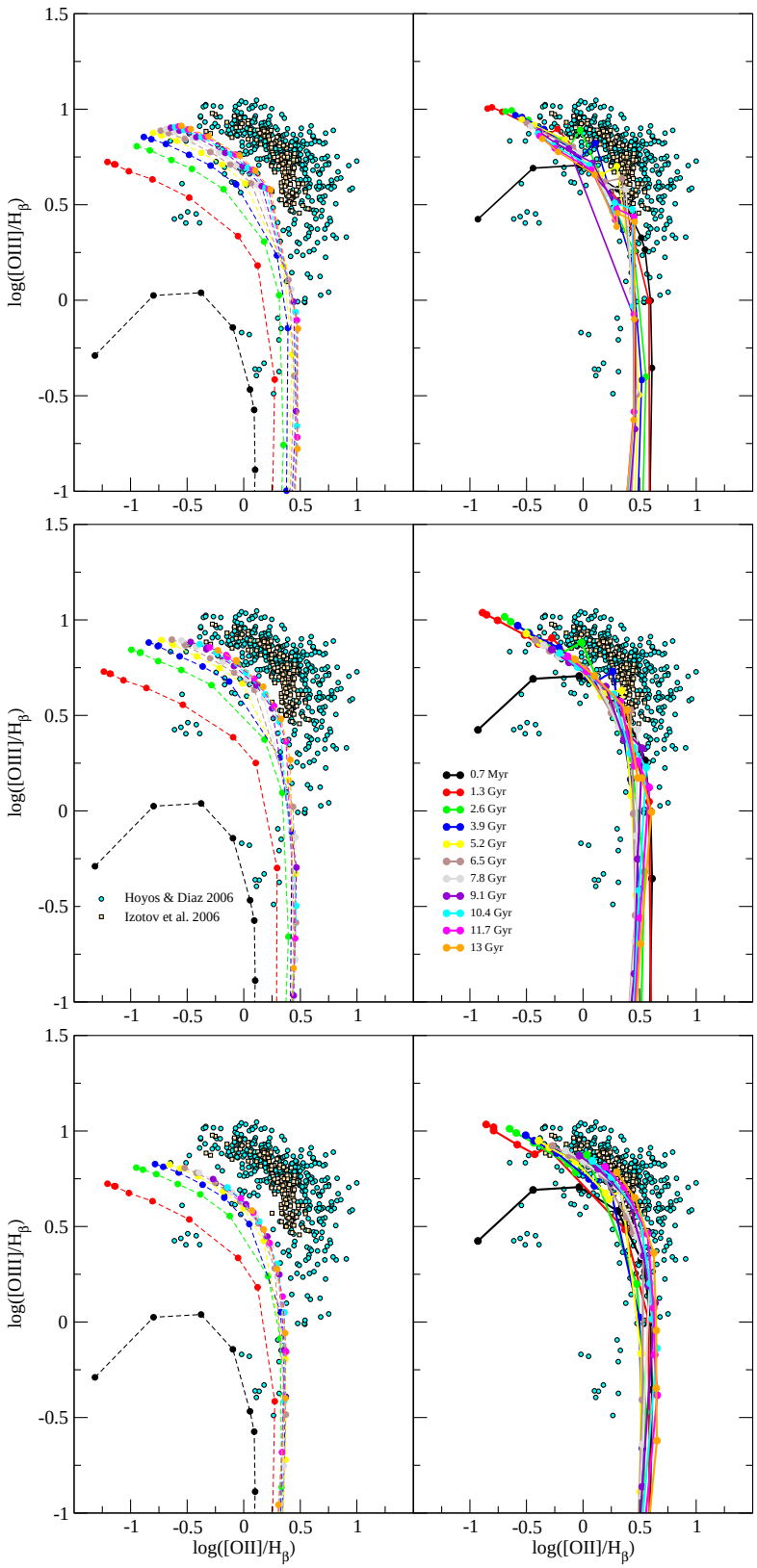

Figure 3.20: Excitation diagnostic diagrams for SAM (Upper panel) and HAM with both attenuation factors, k=0.65 (center panel) and k=0.5 (lower panel). Figures in the right are high efficiency models and the figures in the left correspond to models with low efficiency. Each colour define a different burst.

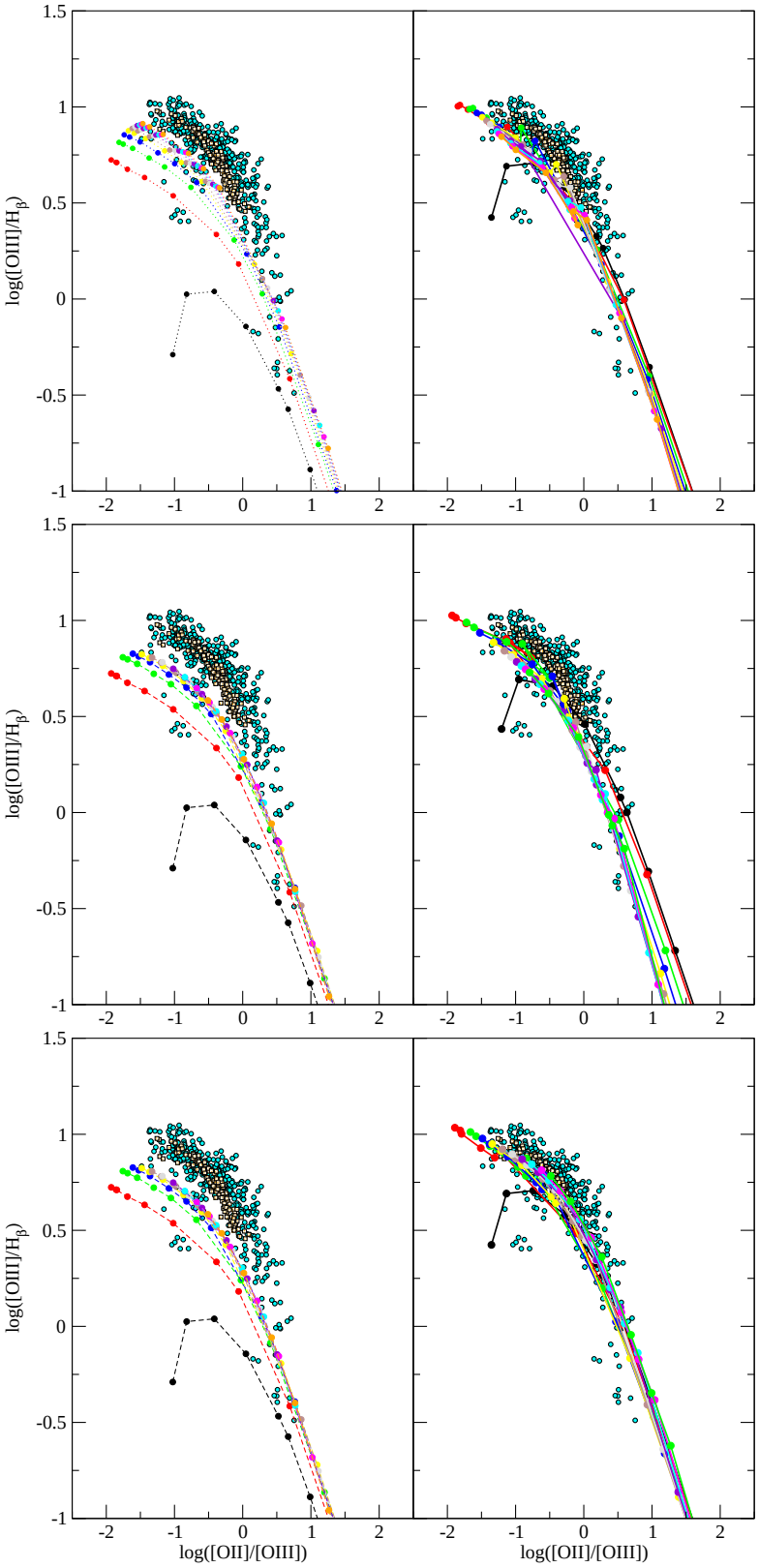

Figure 3.21: Diagnostic diagram involving oxygen line ratios for every model of the second set. Different colours correspond to different bursts, as labelled in Figure 3.20.

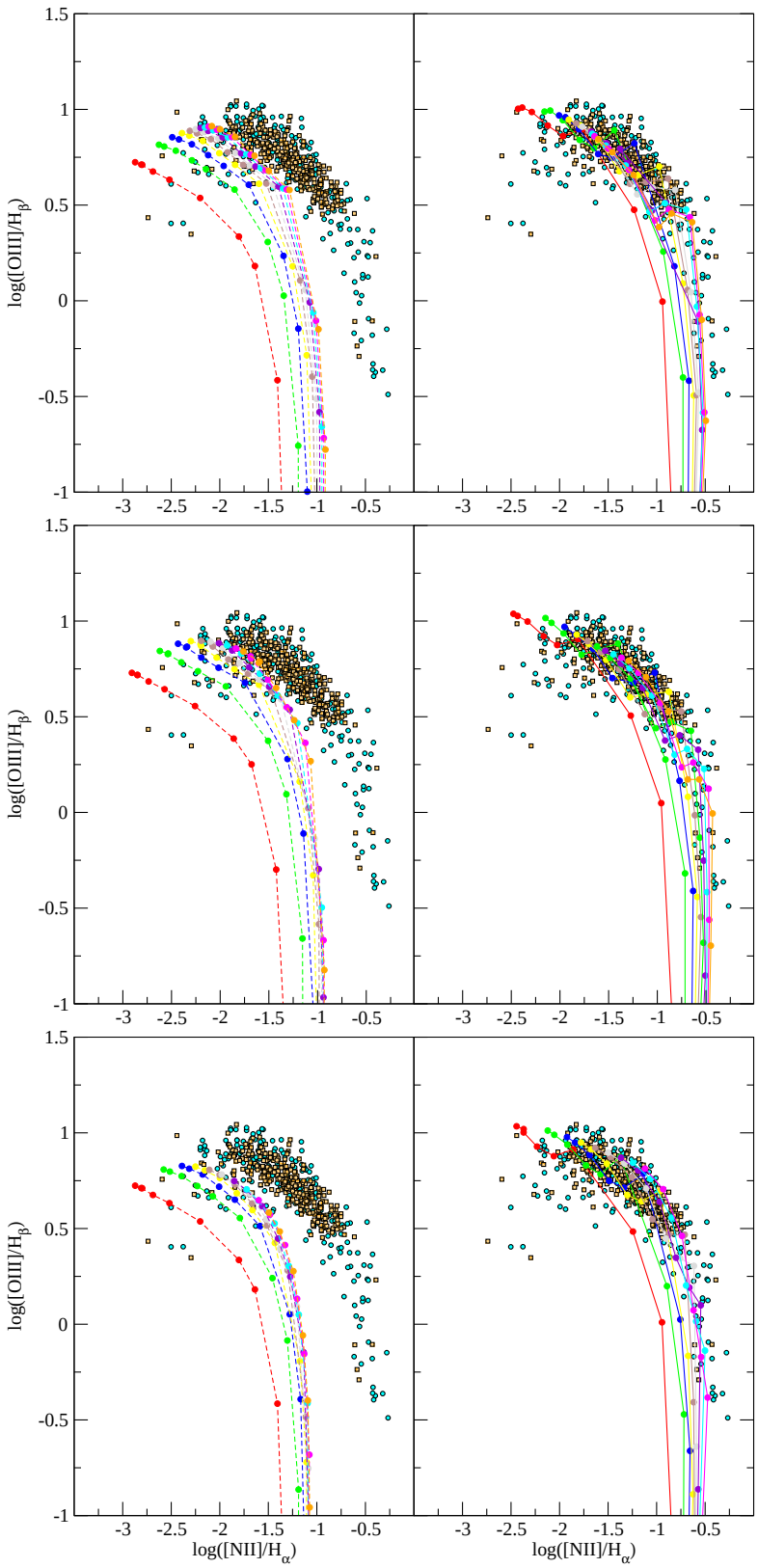

Figure 3.22: Metallicity indicator diagnostic diagram for SAM and HAM. The colours of the lines representing each burst are the same as in previous figures.

Combined continuum and emission line diagnostics.

Continuum colours and the contribution of the emission lines.

We have included the contribution of the emission lines to the U, B, V, R and I bands in order to obtain the colours readily observed, as we did for the first set of models. In Figures from 3.23 to 3.28 we have plotted the different colours computed for all the models. Solid lines correspond the continuum colours as calculated by the models, while dotted lines show the colours contaminated by the emission lines.

In SAM, the contribution of the emission lines is much more evident. The bursts are more similar to each other and the lines contribute with the same percentage to all the bursts. The (U-B) and (V-R) colours do not show a very intense contribution from the lines, which is relevant only during the first burst and at early ages due to the high intensity of the [OIII] and H_β emission lines. A major contribution from the emission lines is observed in the (B-V) vs (V-I) diagram. The [OIII] emission line is much more intense than H_β during the first 4 Myr of the burst, and [OIII] is also much more intense than the [SIII] lines, hence, the contribution to the V band by [OIII] is very important and makes these colours to be highly contaminated. In SAM with a low efficiency the same happens in every colour, but showing less dispersion since bursts are more similar to each other.

HAM show very important emission line contributions but it looks less evident due to the contribution from the underlying continuum that makes the colour to be redder than in SAM. The star formation is smoother in the subsequent bursts and the continuum from the previous ones makes the colours redder.

In B-V the continuum colours can be seen that, while the emission lines are intense in every burst, the continuum colours are much more redder in the subsequent burst. The combination of these two effects makes the total continuum colours of each burst to be bluer than the previous one, instead of redder, as we have seen in other colours. In k=0.5 models, this effect is seen too.

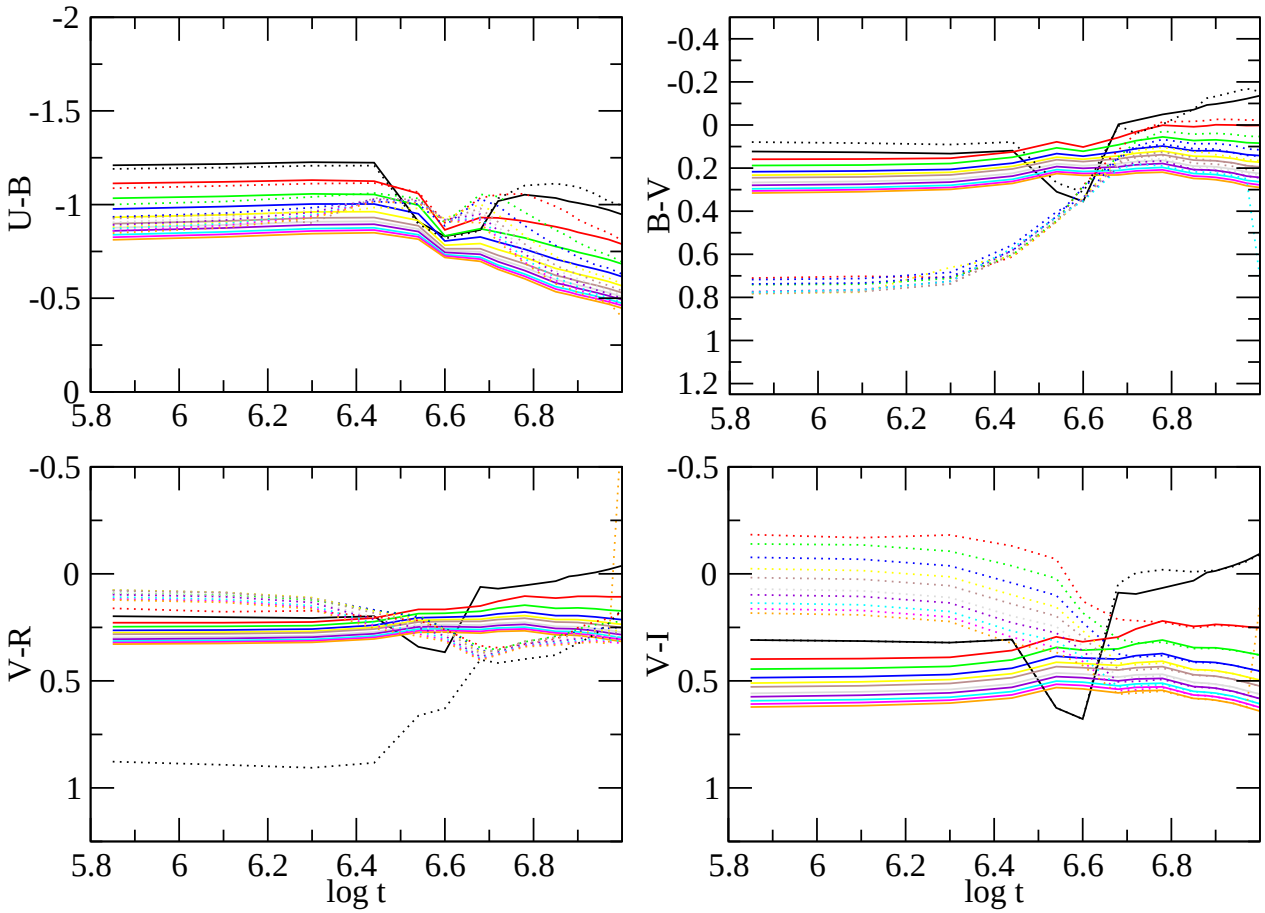

Figure 3.23: Stellar continuum colours (solid lines) and the contaminated colours with the emission lines (dotted lines) . SAM, 10%

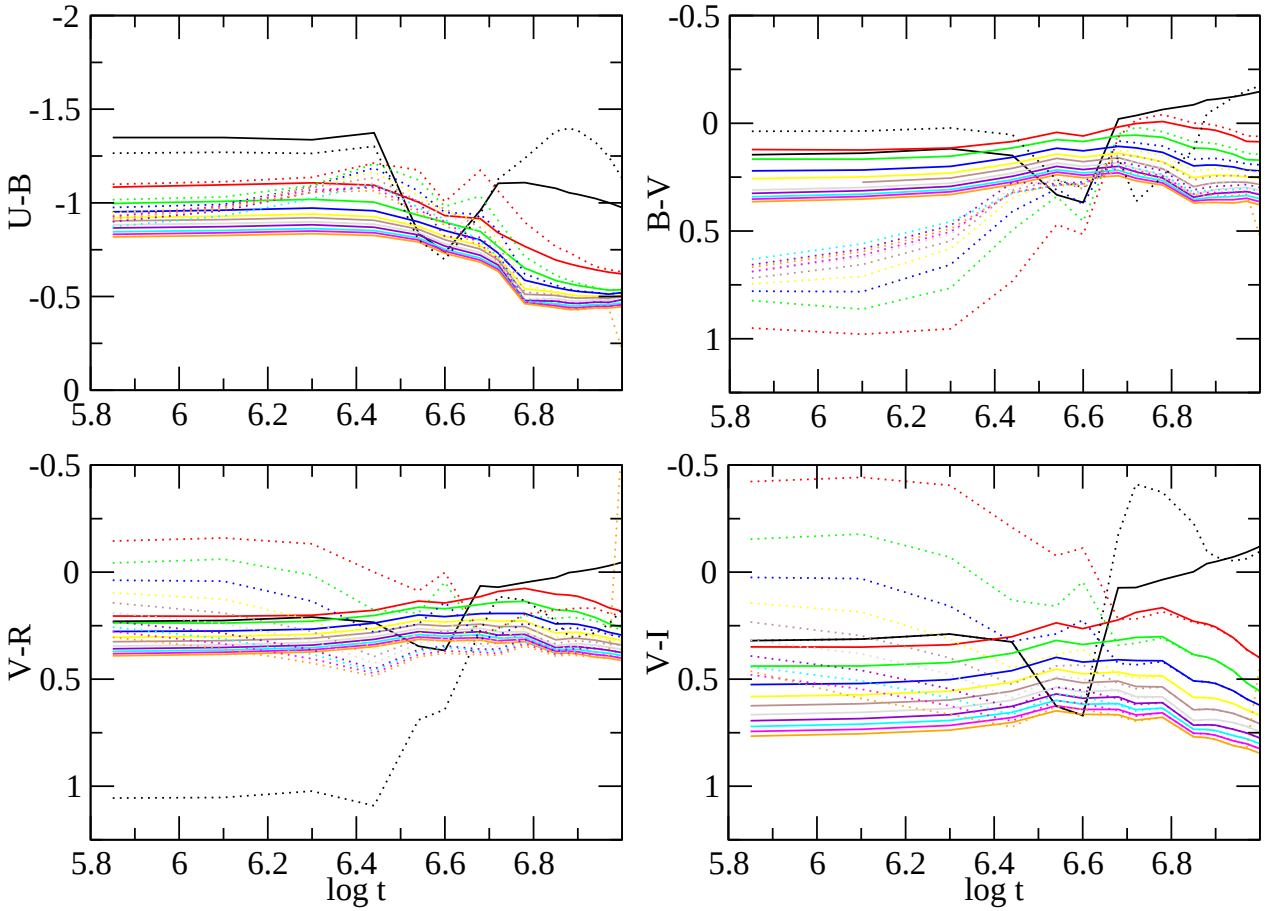

Figure 3.24: Stellar continuum colours (solid lines) and the contaminated colours with the emission lines (dotted lines). SAM 33%

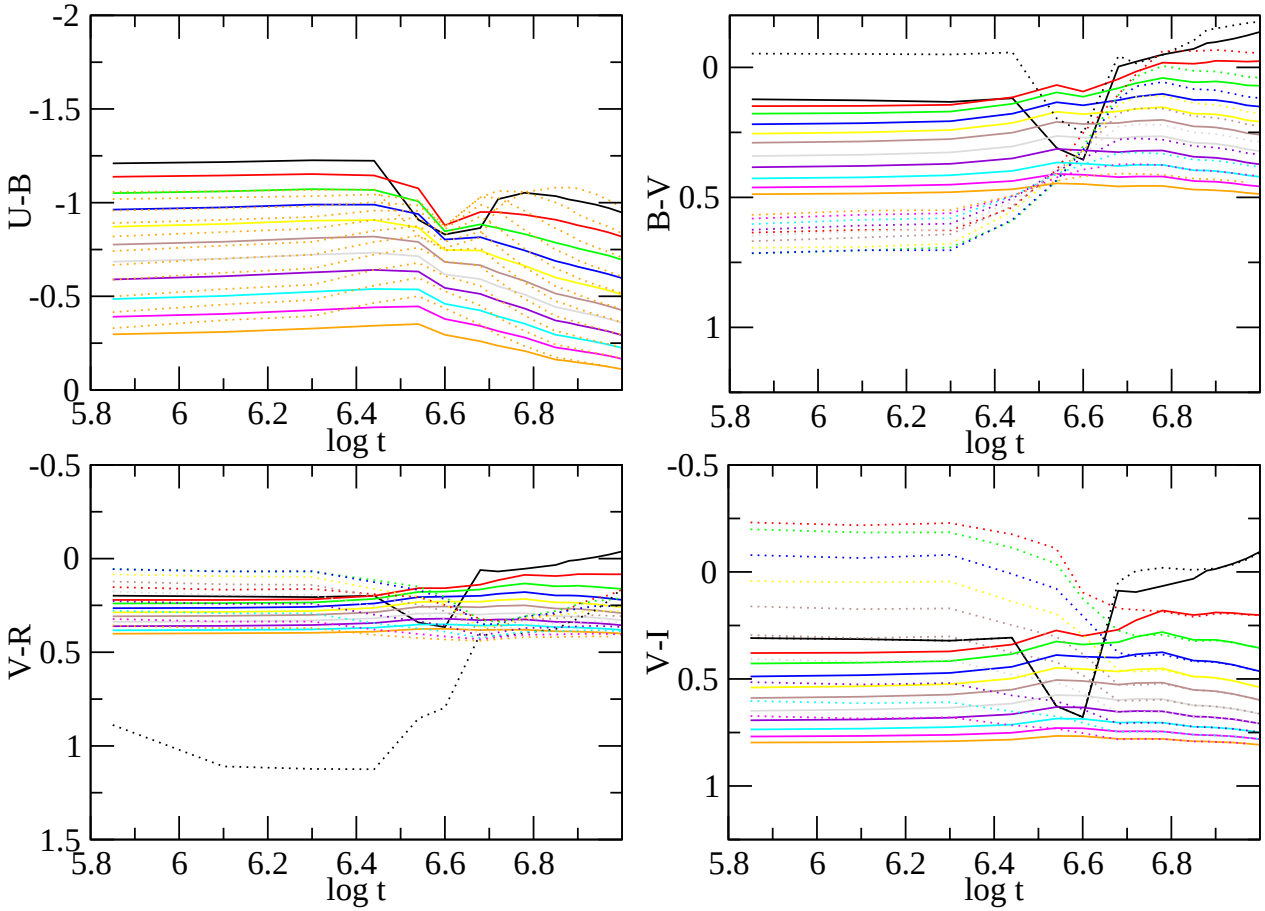

Figure 3.25: Stellar continuum colours (solid lines) and the contaminated colours with the emission lines (dotted lines). HAM, k=0.65, ϵ=10%

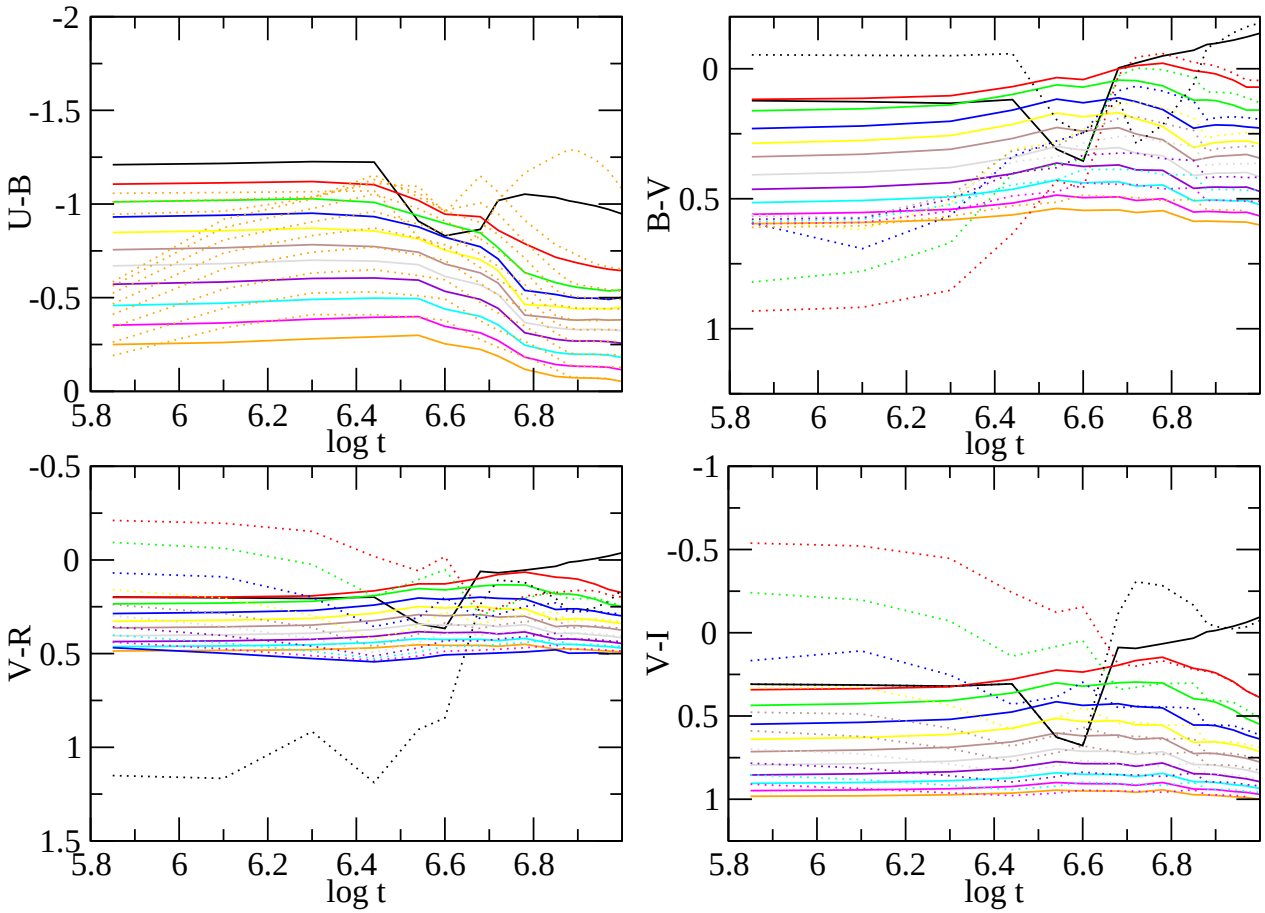

Figure 3.26: continuum colours (solid lines) and the contaminated colours with the emission lines (dotted lines). HAM, k=0.65, ϵ=33%

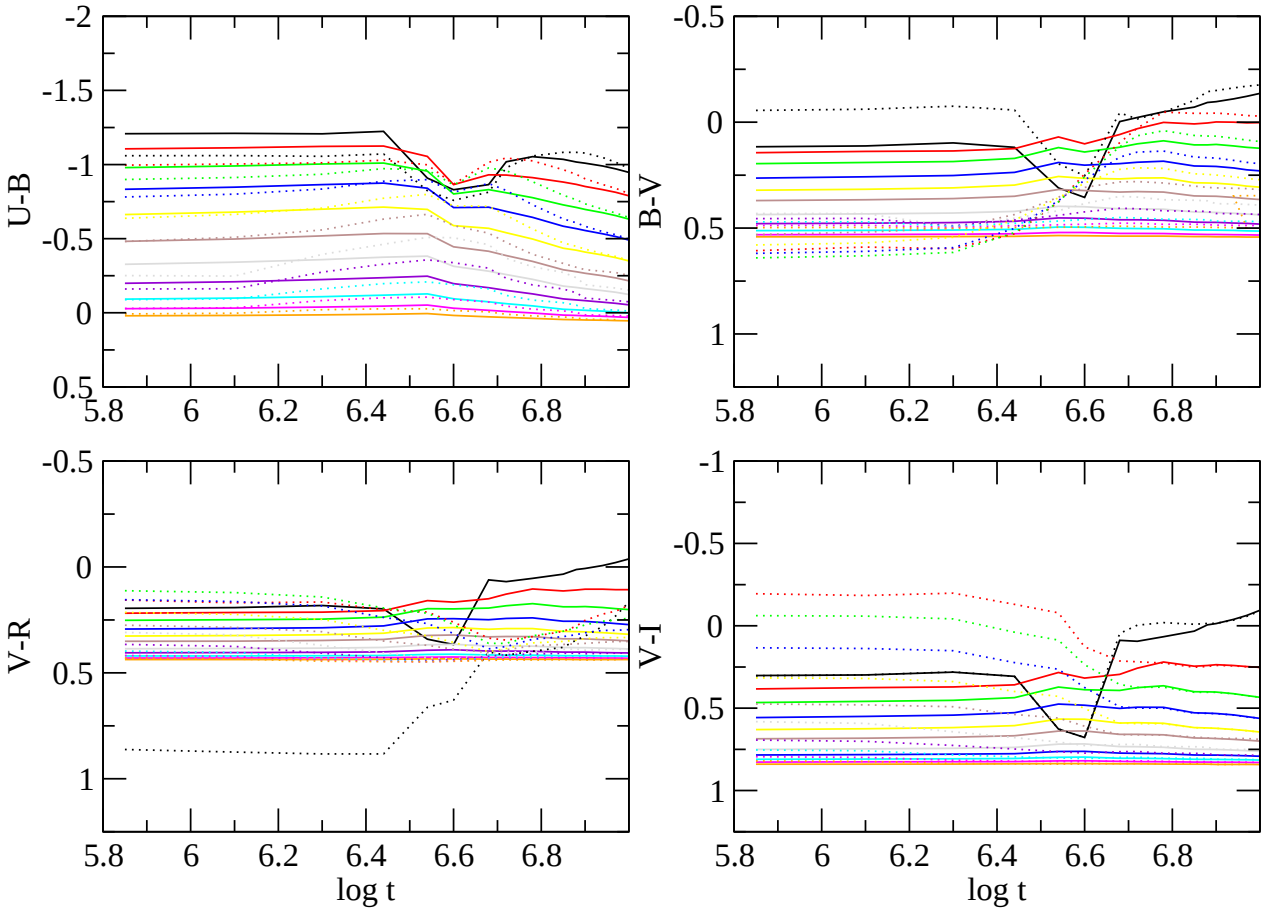

Figure 3.27: Stellar continuum colours (solid lines) and the contaminated colours with the emission lines (dotted lines). HAM, k=0.5, ϵ=10%

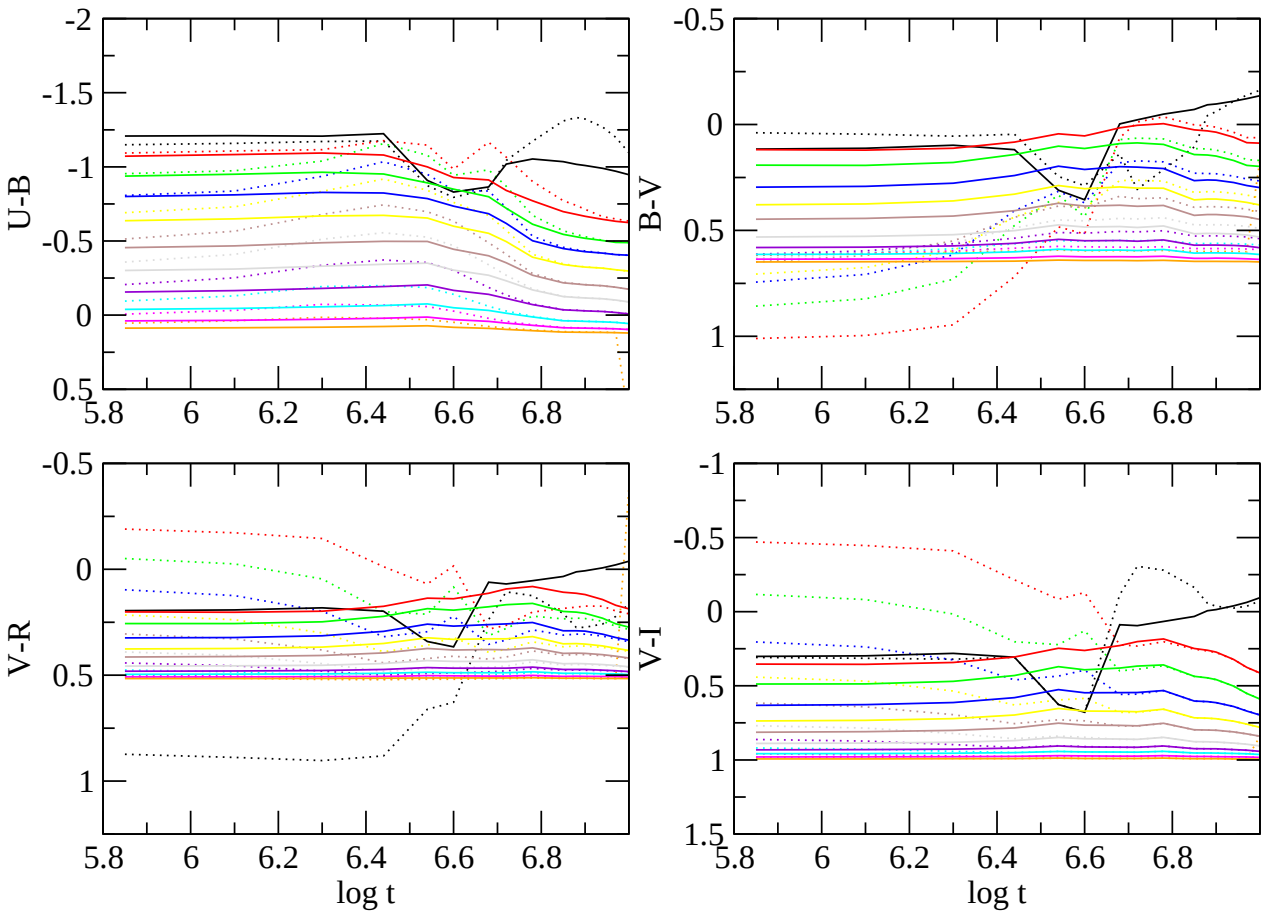

Figure 3.28: Stellar continuum colours (solid lines) and the contaminated colours with the emission lines (dotted lines). HAM, k=0.5, ϵ=33%

The equivalent width of H_β.

The evolution of the EW(H_β) with time compared with the evolution of the EW($_\beta$) of the SSPs of different metallicities, can be seen in Figure 3.29. In both SAM and HAM, the equivalent width of the first burst corresponds to the EW(H_β) of a SSP of very low metallicity (Z=0.0001), showing higher values than the successive bursts, even after 4 Myr from the SF, due to the absence of an underlying population. In SAM the next bursts are very intense too. In these models, the metallicity grows fast to Z=0.004 and Z=0.008. Low efficiency models maintains the EW(H_β) between the two SSPs with low metallicity, Z=0.0001 and Z=0.0004.

The bursts of HAM evolve in the same way because the evolution of the metallicity is similar to SAM. However, the initial EW(H_β) of each burst decreases more along the successive bursts, showing a difference from the first burst to the last one of one order of magnitude in k=0.65 model, and almost two in k=0.5 models due to the higher contribution of the underlying continuum.

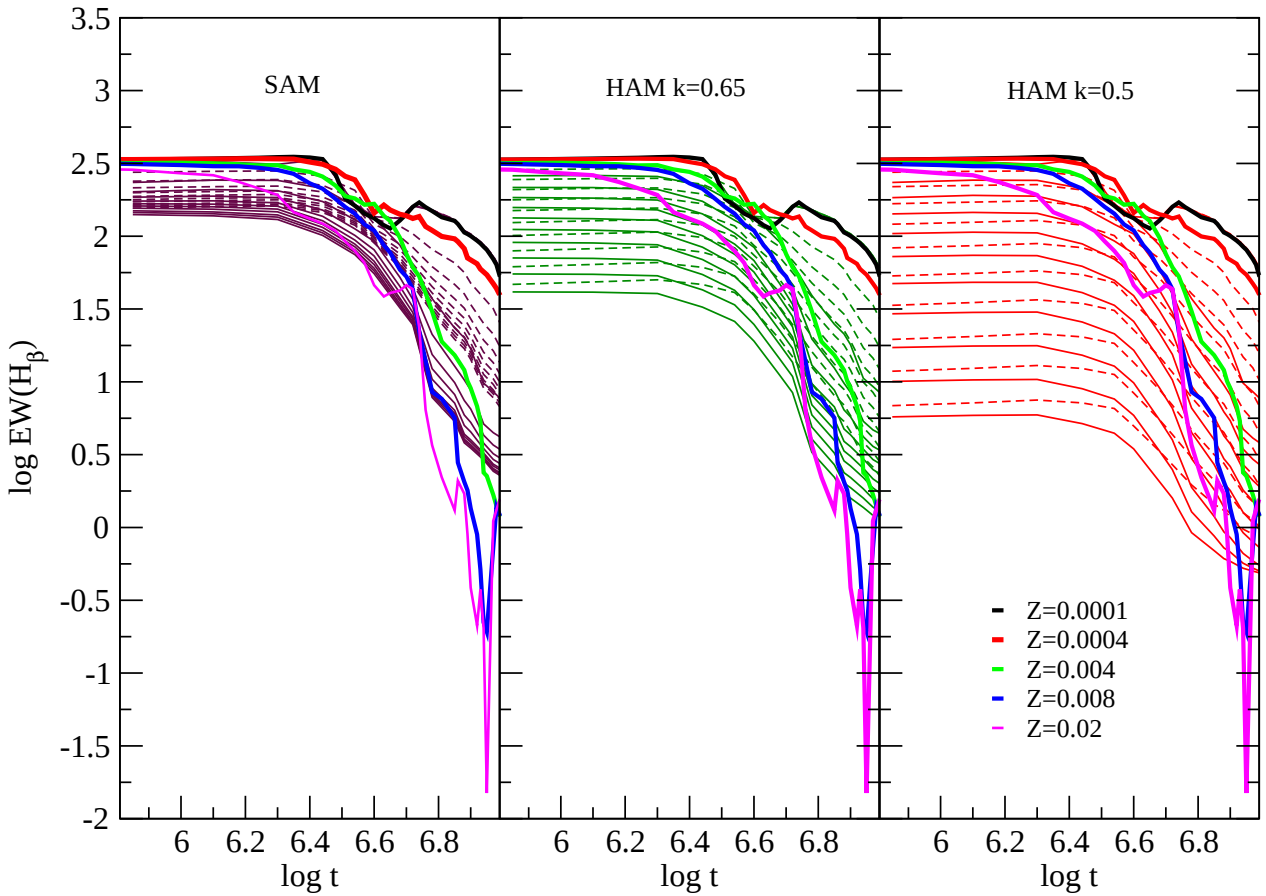

Figure 3.29: Evolution of the equivalent width of H_β with time along each burst of star formation. Left panel corresponds to SAM, central panel corresponds to HAM with k=0.65, and right panel to HAM, k=0.5. High and low efficiency models are represented with solid and dashed lines respectively. Every model is compared to the evolution of the equivalent widths of the SSPs of different metallicities from MGVB09 used for this set of models.

We represent the EW(H_β) vs the colours of the continuum in Figure 3.30. The left panel is the SAMs, with both efficiencies, the central one corresponds to HAM with k=0.65 and in the right, the HAM with k=0.5. We can see that SAMs now show a smooth decrease in the equivalent width from burst to burst that we did not get before with the use of GV95 model. However, it is still not enough to cover the range in colour shown by HII galaxies. HAMs are able to reproduce the whole range in EW(H_β) and in colours making the contribution of the continuum to the total SED of the previous generations of stars higher than the current burst. With HAM k=0.65 we reproduce both the trend and the range of data. HAM with strong attenuation, k=0.5, reach lower values of EW(H_β) and redder colours, verifying that the only way to reproduce this trend is assuming an attenuation and not increasing metallicity or age separately. The initial efficiency of star formation does no affect, as much as attenuation does, to the EW(H_β) and to the colour, except slight features produced by differences in the metallicity.

In Figure 3.31 the equivalent width of H_β as a function of the oxygen abundance is represented, similar to Figure 3.11. We can see the two time scales: one within the burst, from the star formation up to 10 Myr, and other along the whole evolution of the galaxy. The first bursts of every model is similar. The metallicity grows from 0 evolving each model in quite different ways. The results of SAM cover a bigger range than HAM, due to the attenuation, that makes the oxygen abundance to be almost constant in the last star formation episodes. Second and third bursts show how the metallicity grows also within a burst, the SFR is very high and the ejections of massive stars are very noticeable in such a low abundance scenario. After that, the SFR decreases and the abundance of the burst is maintained constant. HAM with k=0.5 does not reach the observational data with the highest values of O/H. Low efficiency models have the same behaviour but covering the low metallicity range.

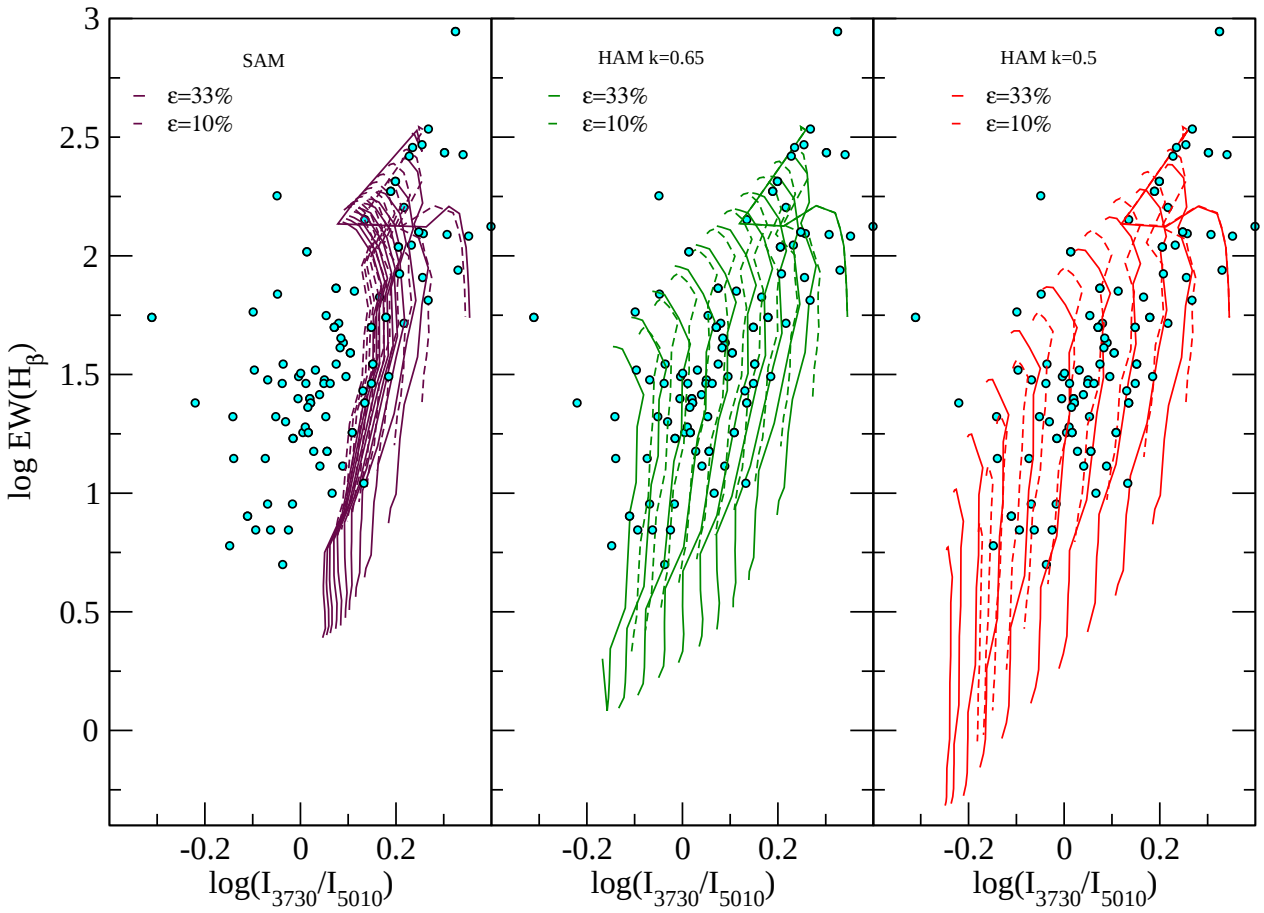

Figure 3.30: Equivalent width of H_β vs. the ratio $I_{(3730)}/I_{5010}$ for the models of the 2nd set, compared with observational data from Hoyos & Díaz (2006); Terlevich et al. (1991); Salzer et al. (1995). Left panel corresponds to SAM, central panel is HAM, k=0.65, and right panel shows HAM with k=0.5. High and low efficiency are solid and dashed lines respectively.

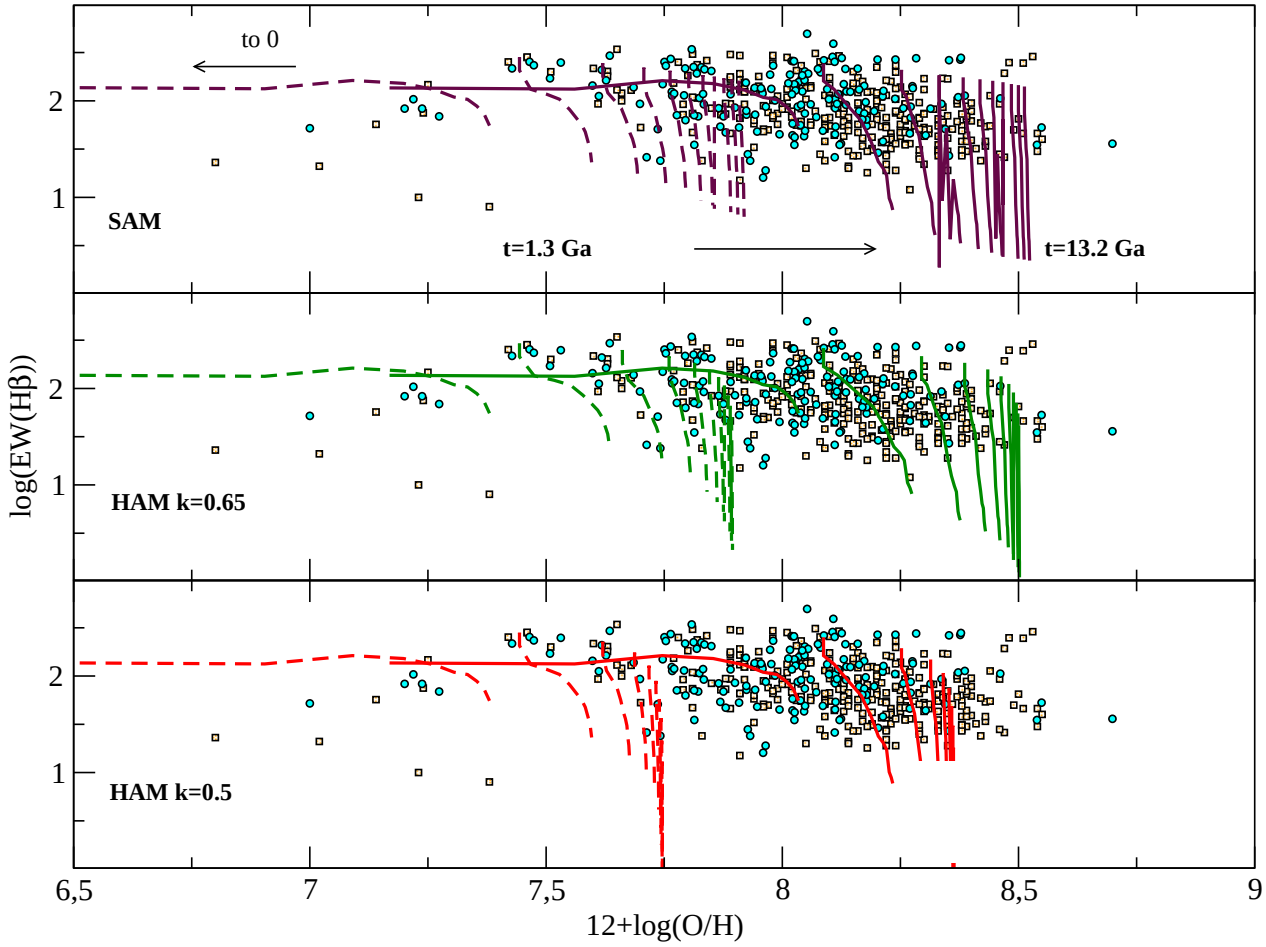

Figure 3.31: Evolution of EW(H_β) with oxygen abundance for every model of the second set. Solid lines represent the high efficiency models and dashed lines the low efficiency ones.

3.2.3 Conclusions.

We have made a new grid of models using the new evolutionary synthesis code PopStars (MGVB09). In the previous set of models, we saw that it was necessary to decrease the initial efficiency of star formation to reach the low metallicities shown by some galaxies in diagnostic diagrams. We also saw that, in order to reproduce the range of the continuum colours, it was necessary to increase the contribution by the underlying population of the previous bursts to the total continuum. Including this effect, we can reproduce the extra reddening shown by HII galaxies, without increasing metallicity or age separately; increasing both at the same time with the contribution of the underlying non ionizing population.

The new models are characterized by different types of attenuation: a Standard Attenuation, similar to the first set of models, and a High Attenuation, including an attenuation factor as a free parameter to be adjust. In addition, we have made models with different initial efficiency to cover the whole range in metallicity shown by HII galaxies. Finally we have 6 models, two efficiencies for each attenuation type. However, the high efficiency models do not reach the high excitation zone in diagnostic diagrams because of the use of the new synthesis code MGVB09, which does not produce such high amount of ionizing photons that we got before, with the use of GV95 models. High Attenuation Models reproduce well the trend and the range of data in EW(H_β) vs Colour diagrams, which confirms that, in order to reproduce the reddening shown in HII galaxies, the contribution by the non ionizing population of the previous burst to the total SED must be higher than the contribution by the current burst of star formation, that is, this burst has to involve less star formation.

Once we have solved the problems araisen from the first set of models, we have to attend to the new question:

How can we reach the zone of the galaxies with more excitation in diagnostic diagrams?

1. Increasing initial efficiency of star formation: If we increase the initial efficiency of the burst we make the metallicity to grow very quickly, producing two effects:

-It can make the oxygen abundance to be higher than the upper limit of HII galaxiy data. The bursts would be too strong and too metallic, as in previous, and discarded models.

- More efficiency does not necessary produce more excitation. In fact, it can make the oxygen emission lines to decrease. Attending to the diagnostic diagrams of the SSPs taken from Martín Manjón et al. (2009) (MGVMD09,

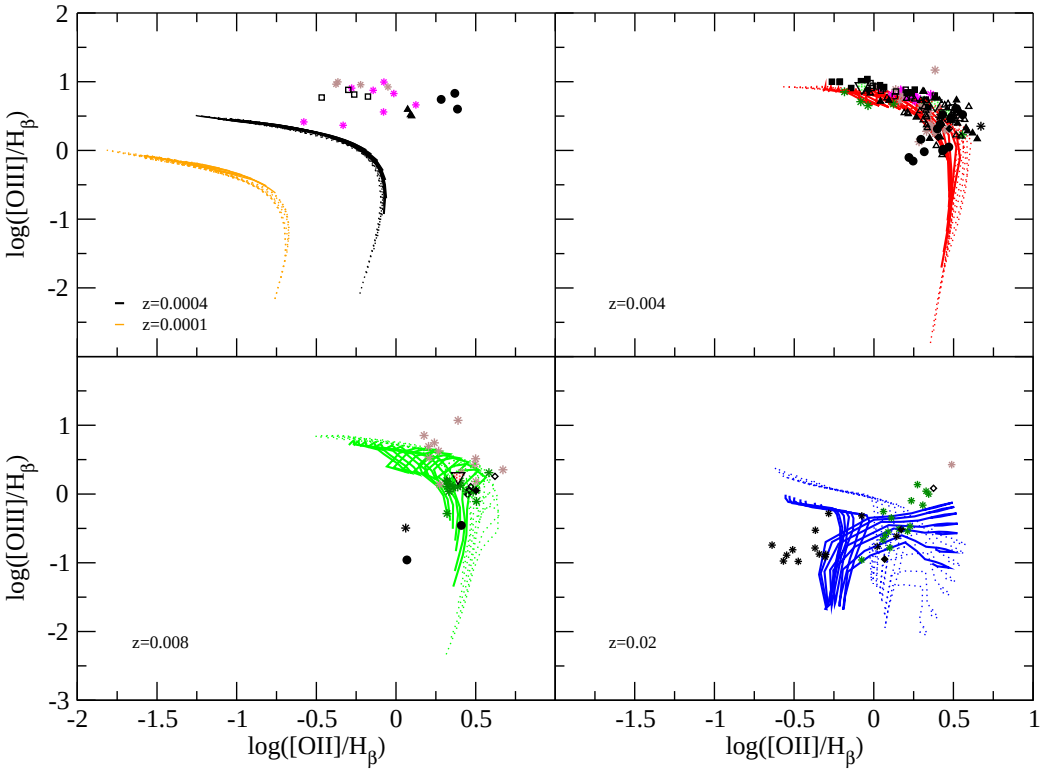

Figure 3.32: Diagnostic diagrams of SSPs from MGVMD09. Each panel shows a different metallicity model and the corresponding observational data range of HII regions from: Zaritski et al. (1994) (circles), Izotov & Thuan (2004) (squares), Castellanos, Díaz, & Terlevich (2002) (diamonds), van Zee & Haynes (2006) (triangles up), García-Vargas et al. (1997) (red triangles down), and taken from Díaz et al. (2007, and references therein) we include CNSFR (black stars), high metallicity HII regions (green stars), low metallicity HII regions (brown stars) and HII galaxies (magenta stars). Filled symbols represent objects with n_H=100 cm^{-3}, and not filled the objects with n_H = 10 cm^{-3}. Solid lines correspond to models with n_H=100 cm^{-3} and dashed lines to models with n_H = 10 cm^{-3}.

in prep.), we can see in Figure 3.32, that the low metallicity SSPs lie at the left part of the panel with low values of [OIII] and [OII] due to the absence of oxygen abundance. When metallicity increases, models show higher values of [OIII], up to a maximum value which correspond to log[OIII]/H$_\beta$=1, reached by Z=0.004 models. Models with lower and higher metallicity can not reproduce [OIII] values higher than this limit. For metallicities higher than Z=0.004 , emission lines decrease again and move to lower values of [OIII] and higher values of [OII]. For Z=0.008, emission line values are very similar to those of Z=0.004, but showing lower values of [OIII]. Z=0.02 models show very low values of both emission lines and do not overcome log([OII]/H$_\beta$)=0.5. This will be better seen in Appendix A.

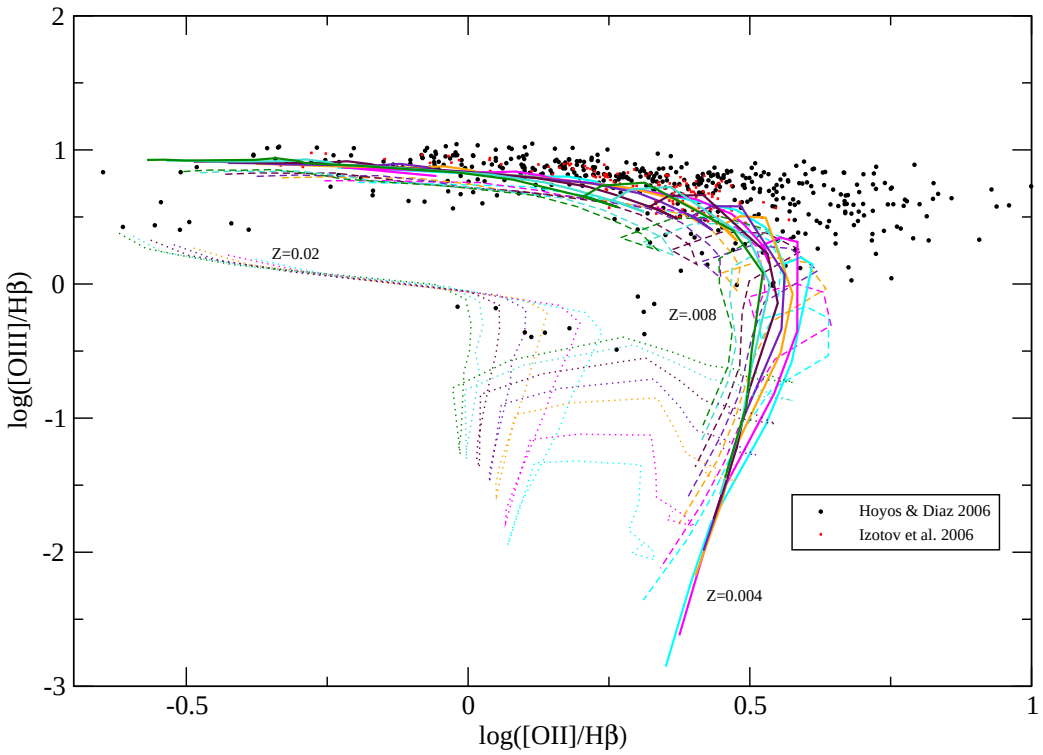

Figure 3.33: Diagnostic diagrams of SSPs MGVMDB09 for three of the most common metallicities shown by HII galaxies, Z=0.004, Z=0.008 and Z=0.02 and $n_H = 10$ cm^{-3}, with the observational data from Hoyos & Díaz (2006); Izotov et al. (2006). Different colours of the lines represent different total masses: 0.12×10^5 $M_\odot$ (cyan), 0.20×10^5 $M_\odot$ (magenta), 0.40×10^5 $M_\odot$ (orange), 0.60×10^5 $M_\odot$ (violet), 1.00×10^5 $M_\odot$ (maroon), 1.50×10^5 $M_\odot$ (turquoise) and 2.00×10^5 $M_\odot$ (green)

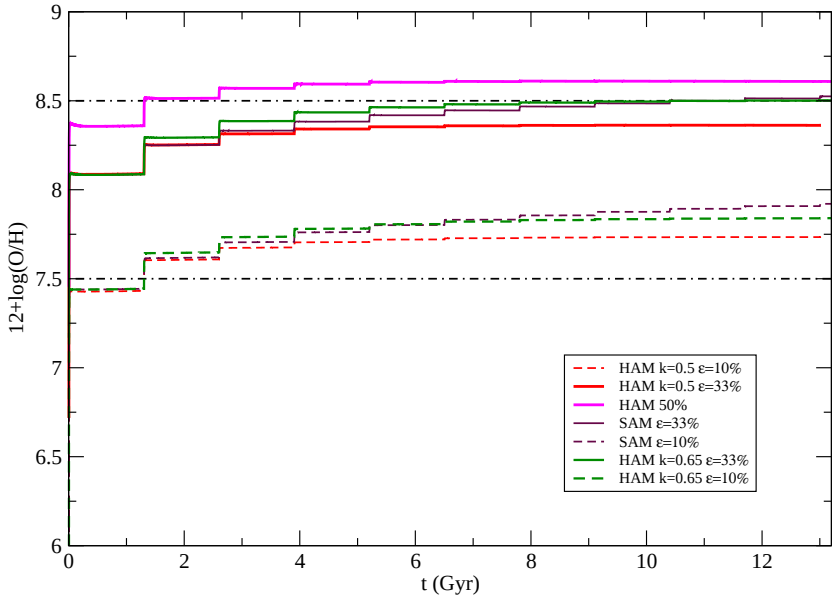

Figure 3.34: Evolution of oxygen abundance of the models including the model with 50% of initial efficiency

Thus, to increase efficiency make the emission lines to decrease, which would be worse. We also check this effect making a new model of very high initial efficiency, 50%, and an attenuation factor k=0.5. Figure 3.34 is the evolution of the oxygen abundance and Figure3.35 is a diagnostic diagram of this model, compared with other HAM. We can see that both described effects in the figures. With such high efficiency, we are out of the observational data range in oxygen abundance. The diagnostic diagram shows a comparison between ϵ=50% model and ϵ=33% model using the same attenuation factor, k=0.5. We have plotted the first burst, at t=0.7 Myr, and the second burst, at t=1.3 Gyr, of each model. The first burst of 50% (black thick line) reproduce the upper part of the diagram, the galaxies with a higher excitation, while the first burst of the 33% model (red thick line) lie below the black one. However, at t=1.3 Gyr, is the highest efficiency model the one which lie below the red line, reproducing the galaxies with less excitation. The emission lines are not maintained in the upper part of the diagram, falling down very fast due to the increase of the metallicity

2. Increasing the initial efficiency and the attenuation of the bursts: Increasing both parameters at the same time, we achieve more mass involved in star formation (more ionizing photons), and the first burst reaches before a metallicity value of Z=0.004, while the successive burst keep this

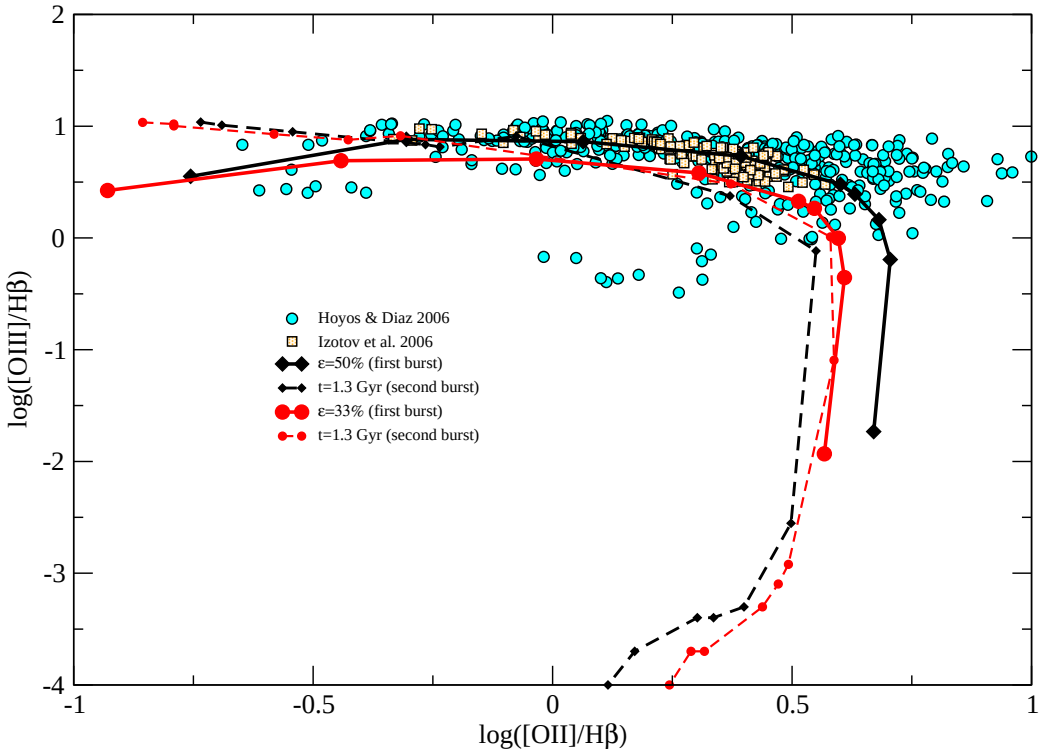

Figure 3.35: Diagnostic diagrams for the two first bursts of the models with k=0.5, black lines and red lines correspond to models with 50% and 33% of initial efficiency respecively.

metallicity along the evolution of the galaxy.

3. Decreasing the inter-burst time: Although with a decrease of the time between burst we would not achieve more ionizing photons from massive stars, we could get more mass involved in the SF and less metallicity in each burst, rising up the excitation.

3.3 Third set of models: fine-tuning of the High Attenuation Models.

This third set are High Attenuation Bursts models but with an attenuation factor lower than in previous section, in order to decrease the star formation rate of the successive burst and keep the metallicity within the observed limits without allowing the maximum metallicity of the model to grow over a value of Z=0.004.

For this new grid **k=0.2**. We have made two models:

-H=10 (1/H= 0.1 yr^{-1}) The first burst of star formation involves 50% of the available gas to form stars (50×10^6 $M_\odot$).

-H=1.83 (1/H=0.564 yr^{-1}) , which corresponds to the 12% of the available gas to form the stars of the first burst.

Every code have been applied to this model as we did for HAM of the previous section. Only the most important results are going to be shown.

Chemical evolution.

The star formation rates are very low (see Figure 3.36) , except for the first burst, which involves a lot of mass in the star formation. The attenuation is very hard and it makes the burst to be very weak from the 5th-6th burst to the end of the evolution. From the eighth burst in high efficiency model, and sixth in the low efficiency model, the oxygen abundance does not grow because of the absence of massive stars ejecting gas to the interstellar medium, keeping the abundance value almost constant until the end of the evolution and inside the observational limits (Figure 3.37)

Evolutionary stellar population synthesis.

The number of ionizing photons decreases rapidly from burst to burst (Figure 3.38). In last bursts, the star formation is very weak and not enough massive stars to ionize the gas are formed, with Q(H) being very low to produce emission lines.

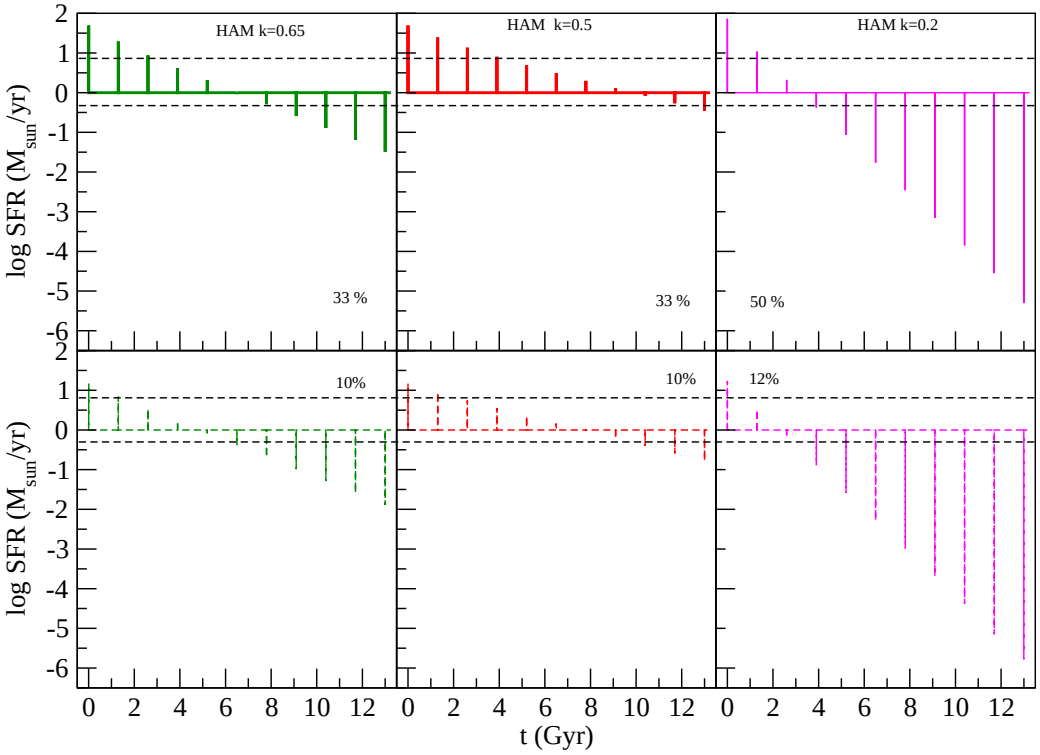

Figure 3.36: Star formation rates of the new models of the third set compared with the HAM of the second set.

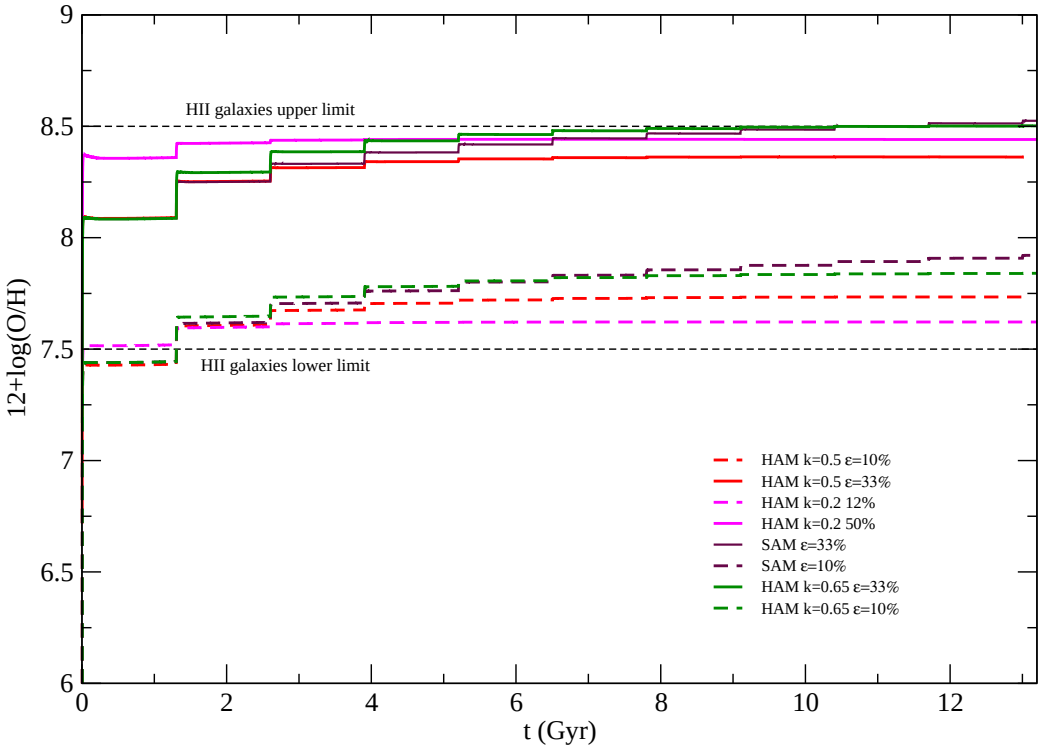

Figure 3.37: Evolution of the oxygen abundance of the new models of the third set compared with the HAM of the second set.

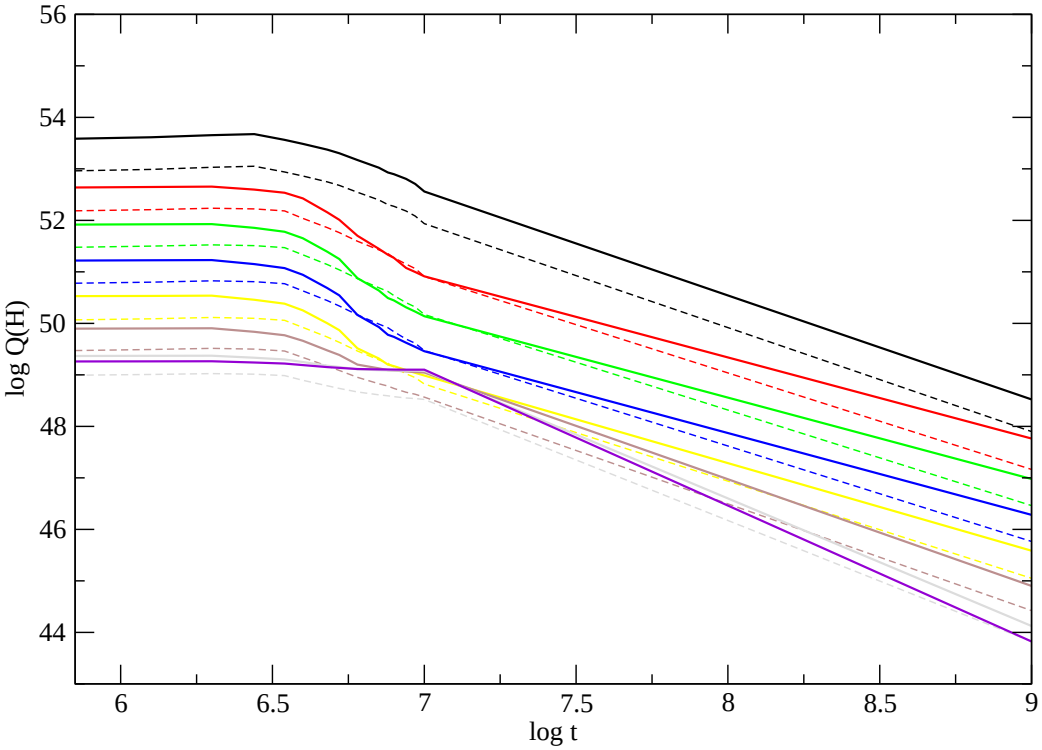

Figure 3.38: Evolution of the number of ionizing photons along 1 Gyr after each star formation burst with k=0.2. Solid lines represent the models with high initial efficiency (50%) and dashed lines low initial efficiency (12%.)

The evolution of the continuum colours can be seen in Figure 3.39. The colours do not change too much along the first 7 Myr. The first burst shows features of very metal deficient population, and the next two burst present changes around 4 Myr due to the WR stars. The colours in the successive bursts are maintained along 10 Myr due to the weak SF.

Photoionization: the ionized gas.

The photoionization models have been made in the same way we did in previous sections.

In Figures 3.40 can be seen that models with high efficiency reach the highest values of [OIII]. The metallicity of the first burst has grown very fast, reaching before the upper limit of Z=0.004 due to the increase of mass involved in the star formation. The rest of the bursts do not exceed this limit and they reproduce the part of the diagram of high excitation.

The model of 12% reproduces the galaxies located in the right, at the lower part of the panel, with low values of [OIII], where low metallicity

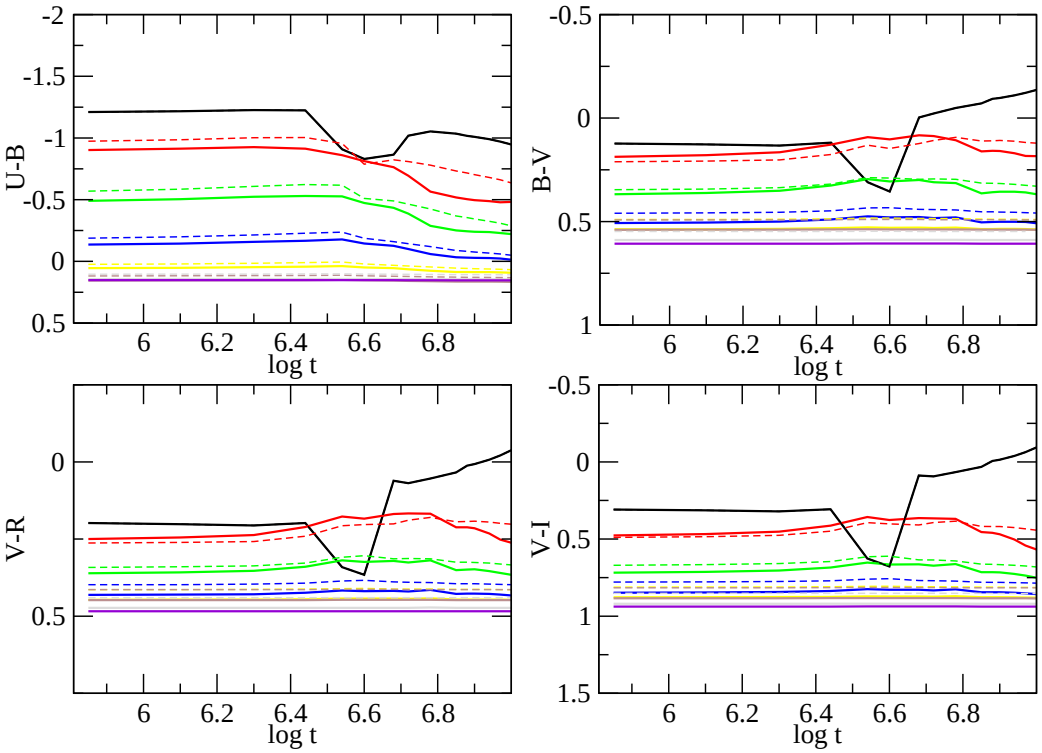

Figure 3.39: Evolution of the colours of the continuum. The first burst of every models is the black thick line. Solid lines are 50% models and dashed lines12% models. Each burst is represented with a different colour.

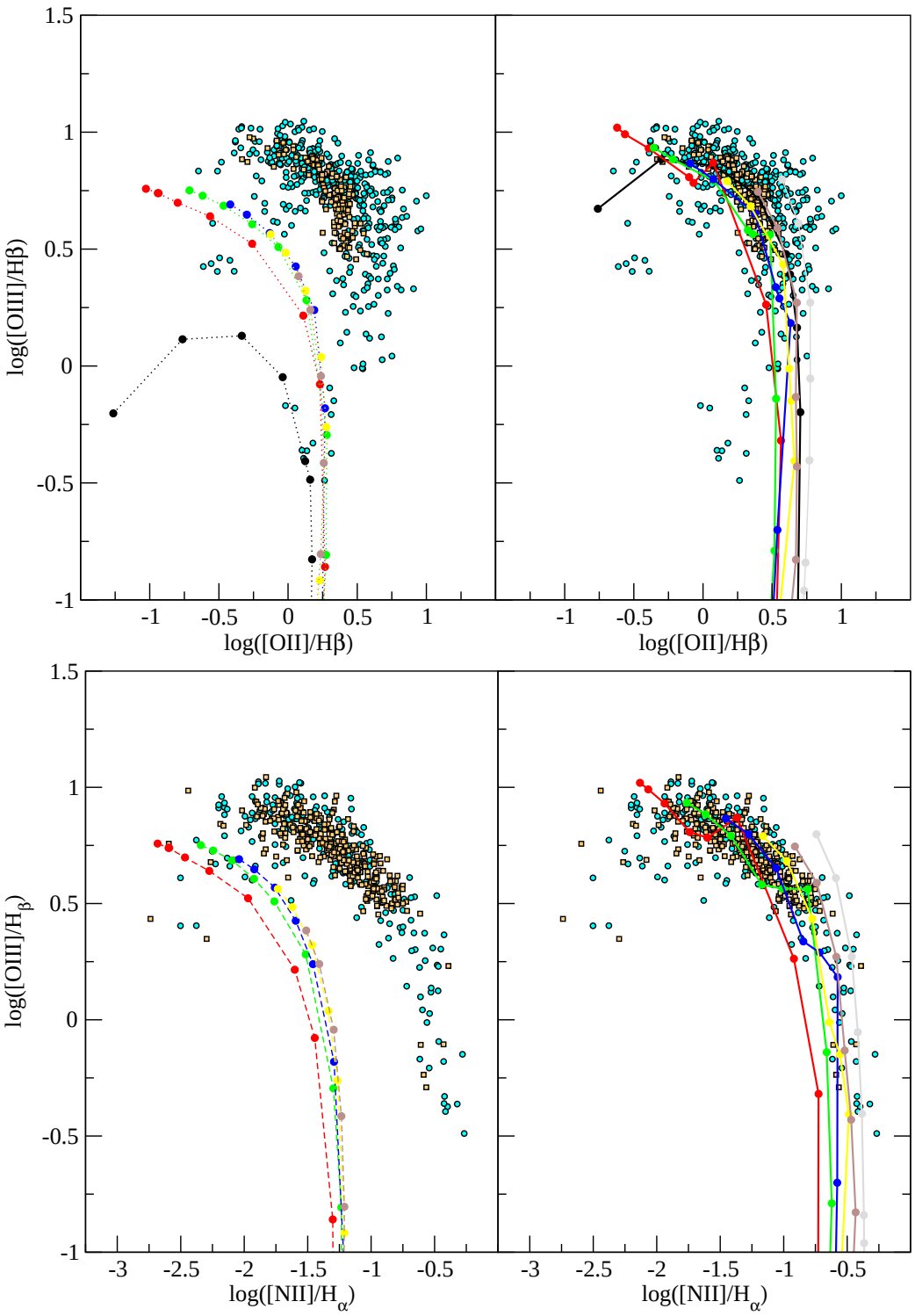

Figure 3.40: The upper panels show the excitation diagnostic diagrams and lower panels the metallicity diagnostic diagrams for the models of the third set. High efficiency model can be seen in the right, and low efficiency model in the left.

galaxies are.

Combined continuum and emission line diagnostics.

In Figures 3.41 and 3.42 we see the evolution of the colours of the continuum and the contribution of the emission lines. The emission lines are strong in the first bursts, and very weak in the lasts, due to the smooth SF.

These models show an evolution of H_β similar to the previous HAMs for the first bursts (Figure 3.43). Due to the strong attenuation of the bursts, the contribution of the underlying population of the previous bursts is very strong compared with the contribution of the continuum of the current burst, making the EW(H_β) to decrease very much. With these models we still cover the observational data range, but the last bursts are too much attenuated, showing equivalent widths much more lower than observations. The HII galaxies of the sample have been chosen according to some characteristics of a recent star formation (strong emission lines), and selection effects may imply that there are not galaxies with such a low star formation similar to our last bursts. However, the trend and the range is still reproduced by our attenuated models. We can always adjust the attenuation factor in order to avoid this problem and get bursts with enough star formation to cover the observational range.

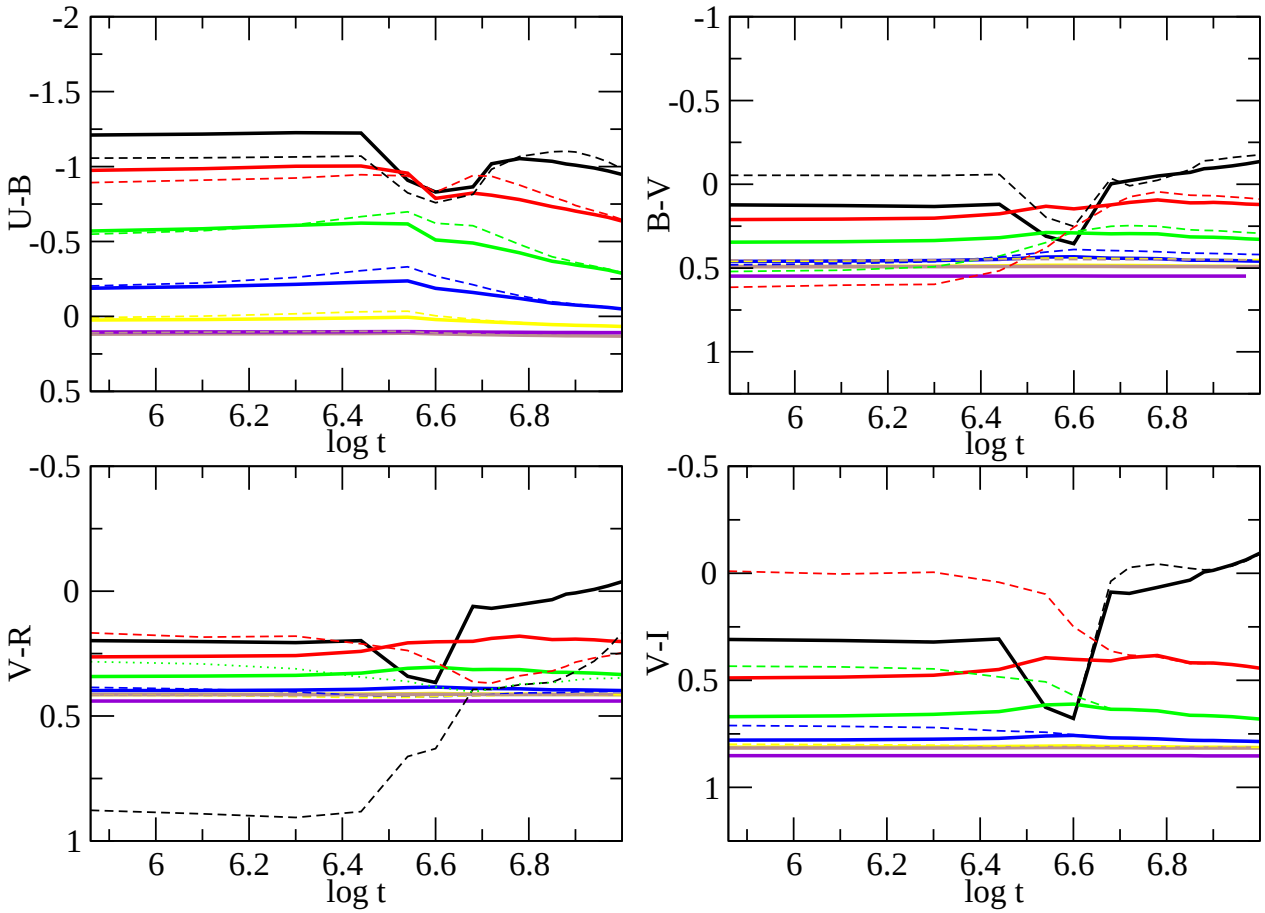

Figure 3.41: Colours of the continuum of the low efficiency model (12%), and the colours of the continuum contaminated with the contribution of the strong emission lines (dashed lines).

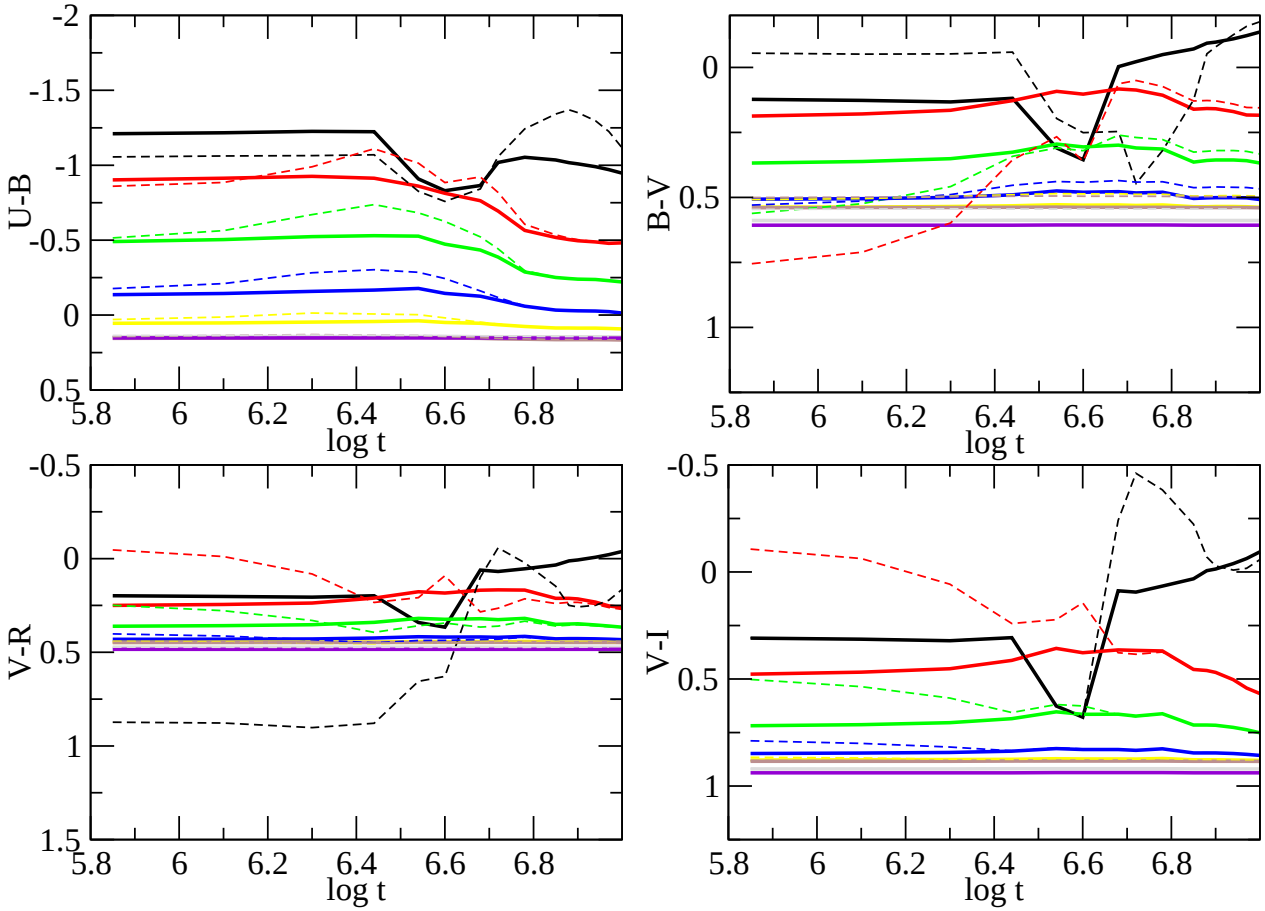

Figure 3.42: Colours of the continuum of the high efficiency model (50%), and the colours of the continuum contaminated with the contribution of the strong emission lines (dashed lines).

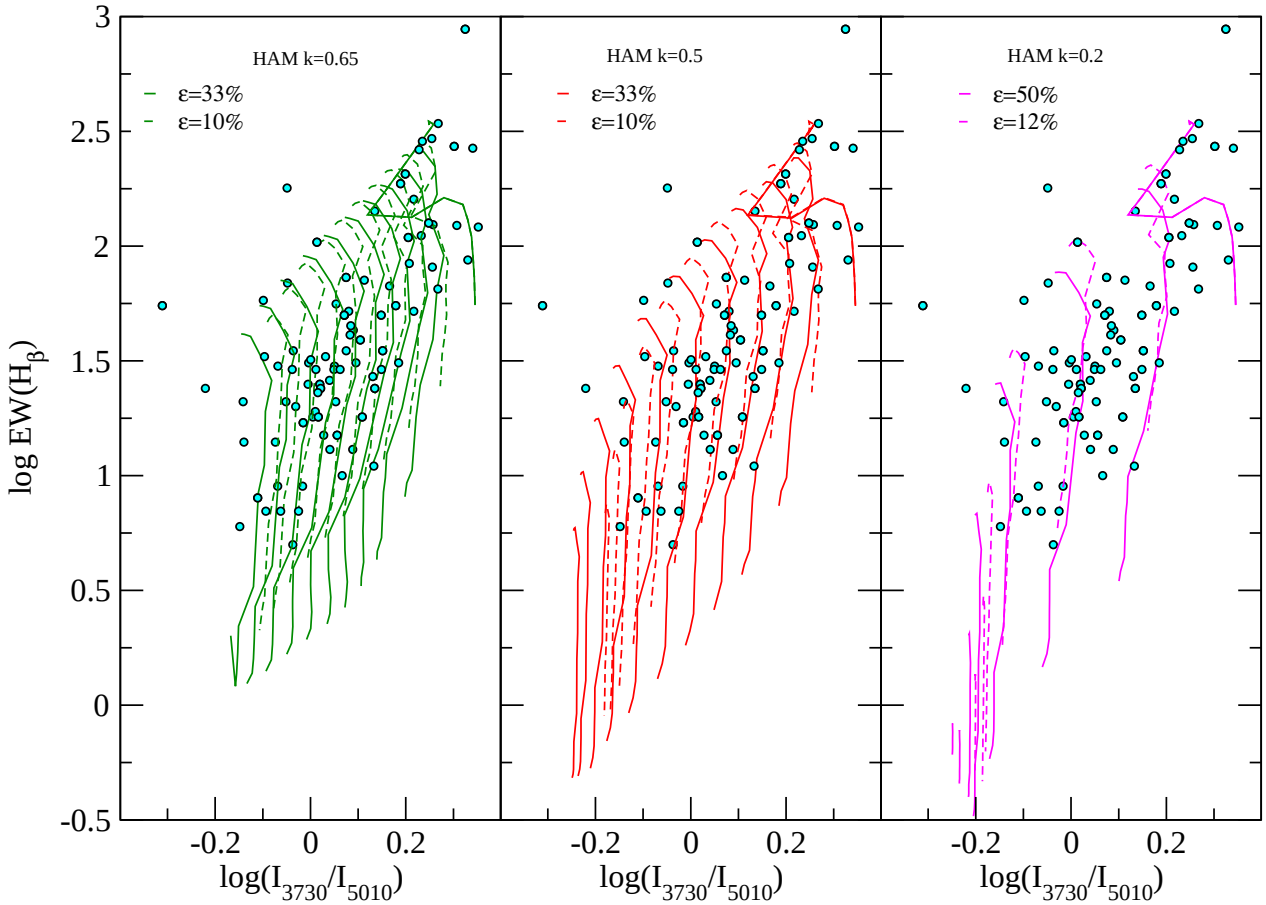

Figure 3.43: Evolution of the EW(H_β) with a pseudo-colour (I_{3730}/I_{5010}) ratio for the HAMs of the second set, k=0.65 (left panel), k=0.5 (central panel) and HAM of the third set, k=0.2 (right panel). Dashed lines correspond to the low efficiency models.

3.4 Models with Δt< 1.3 Gyr.

We are going to check the other possible solution to the "excitation problem" : decrease the inter-burst time.

In order to study the effect on changing the space between bursts, we have done a new grid of models. They consist in HAMs, with k=0.65 and k=0.5, the two initial efficiencies of the second grid: 33% and 10%, and three different times between bursts:

Δt = 0.5 Gyr(500 Myr)
Δt = 0.1 Gyr(100 Myr)
Δt = 0.05 Gyr(50 Myr)

Now the evolution will not last 13.2 Gyr, but (11xΔt) Gyr.

Chemical evolution.

Some small differences in the total metallicity are going to be the clue to achieve the results that we are trying to obtain. The reduction of the inter-burst time has two main consequences:

1. Stars eject mass of gas and elements to the ISM throughout the time, and if the next burst takes place before, the mass of gas available for the new burst will be less than in the second set. It implies that the mass involved to form stars in each new burst is less than before (the model uses a percentage of the available mass of gas for the star formation, not a fixed quantity). This effect is more evident when the inter-burst time is less than 500 Myr. For wider intervals, there are not large differences in the mass of stars created.

2. Less interburst time also involves that the evolution of the metallicity is more slow and smoother. From one burst to the next, assuming intervals of less than 500 Myr, the total metallicity Z does not grow as much as in the 2nd set as we can see in Figure 3.45.

Evolutionary stellar population.

The evolution of the number of ionizing photons with time is quite similar to the second set, therefore, differences in mass of stars created in each burst does not affect to this parameter at all. Only models with interburst time less than 100 Myr show a softer decrease in Q(H) after 5 Myr from the star formation (Figure 3.46). Most of the bursts, except the first one which is similar in every model, have metallicities between Z=0.004 and Z=0.008, which do not show important differences in the first 7 Myr.

The continuum colours show more significant differences because the contribution to the total continuum of the previous generations of stars is

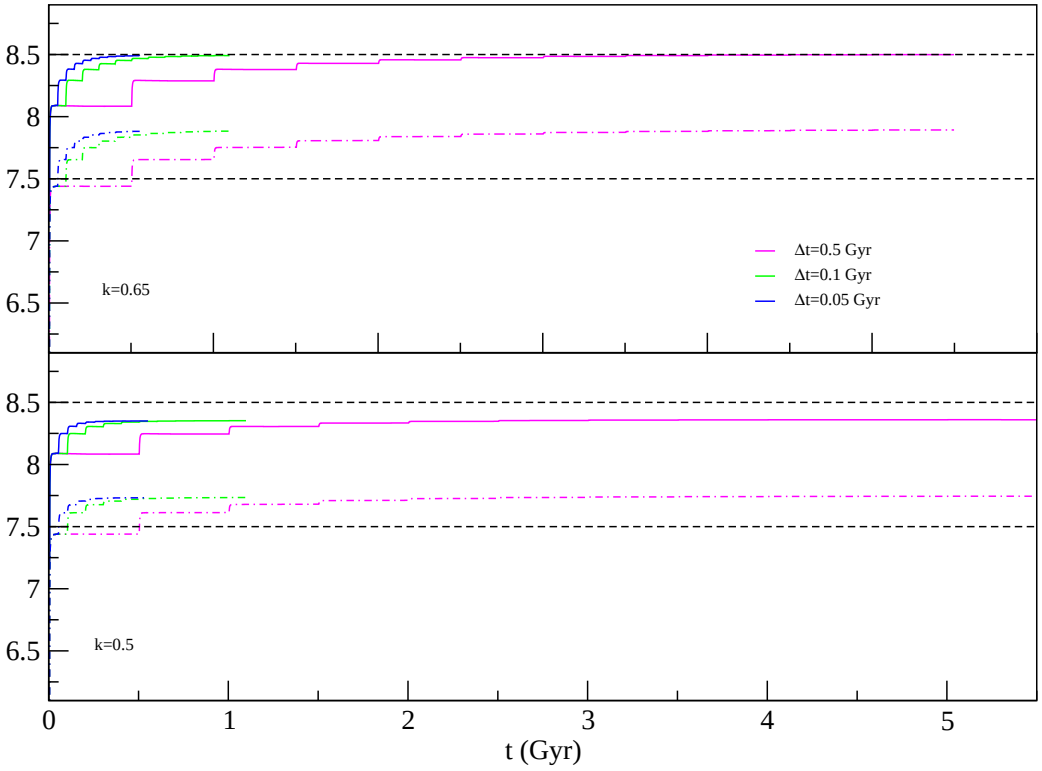

Figure 3.44: Evolution of the oxygen abundance with time for each one of the new models with different inter-bursts times. Each model have a different total time of evolution.

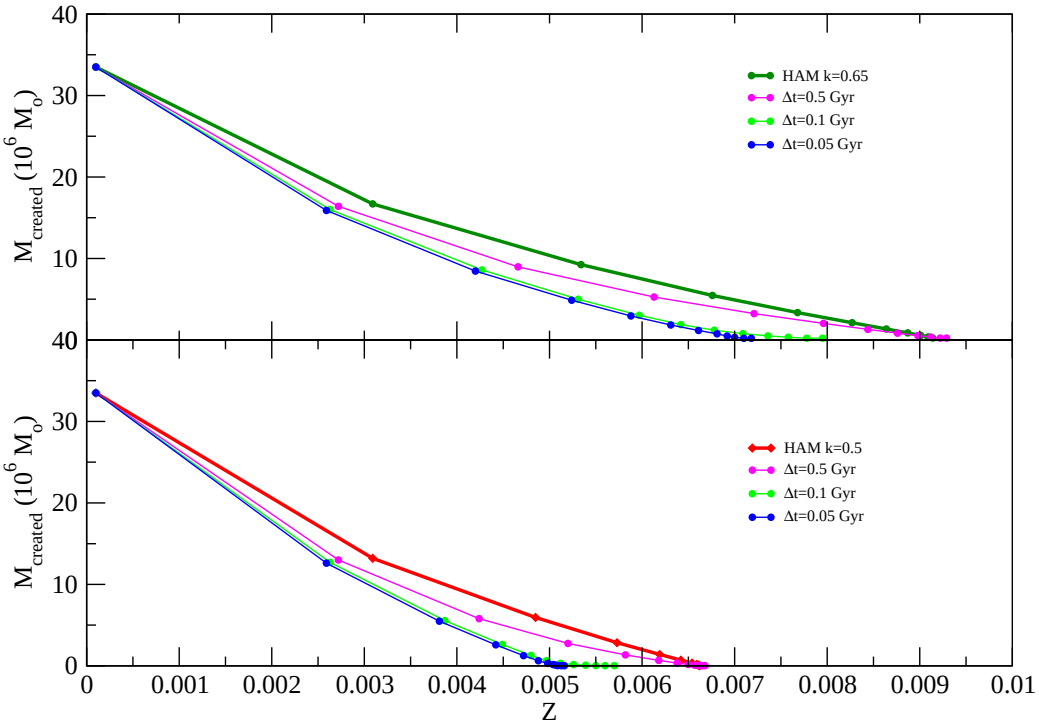

Figure 3.45: Evolution of the mass of stars created in each burst with the metallicity reached. Upper panel corresponds to models with k=0.65 and 33% of initial efficiency. HAM of the second set is represented with the green line and the modes with different interburst times, 0.5 Gyr, 0.1 Gyr and 0.05 Gyr are magenta, green and blue line respectively. Lower panel corresponds to those models with k=0.5. HAM of the 2nd set is the red line, and the models of the third set, with the same colours of the upper panel.

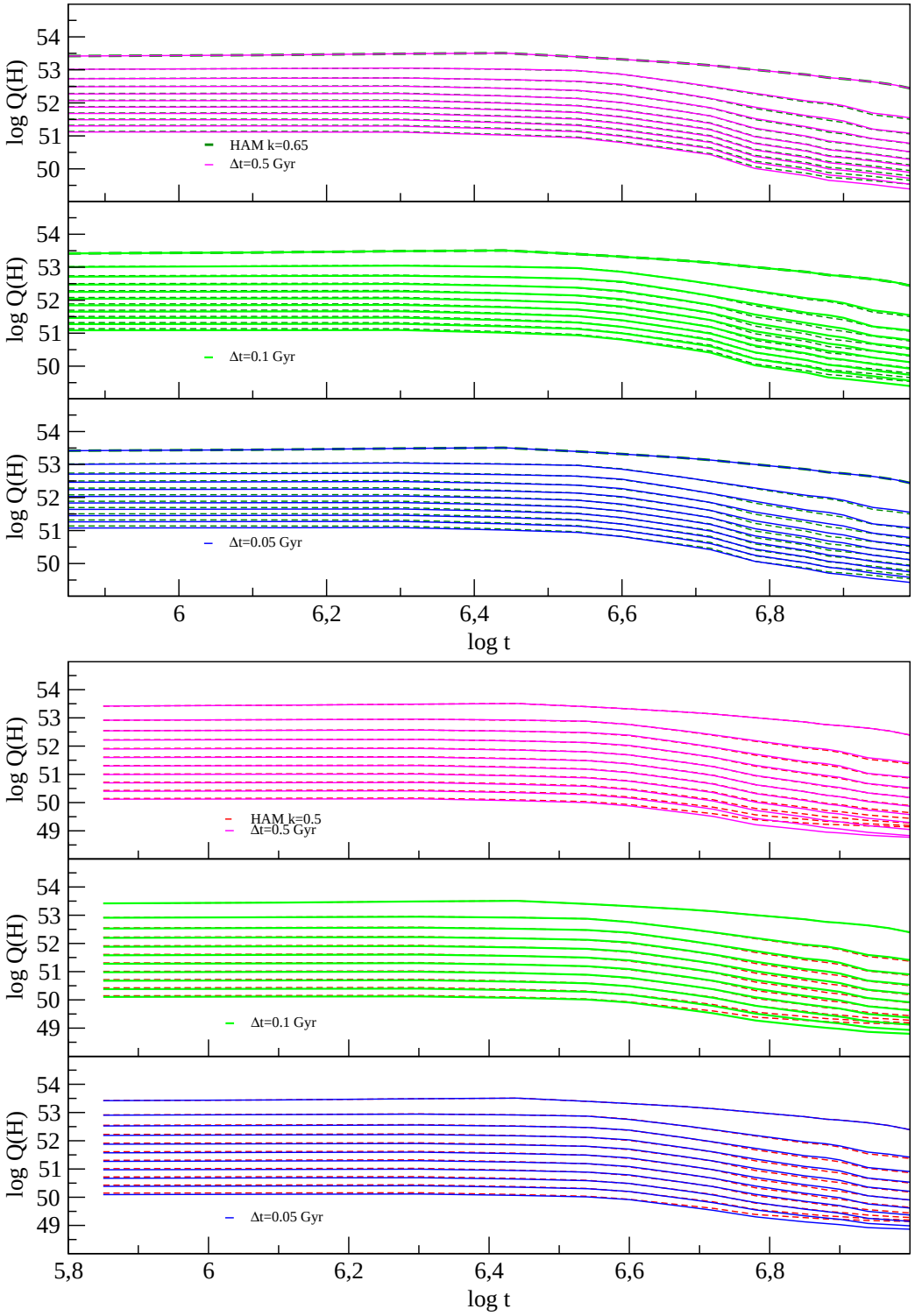

Figure 3.46: Evolution of the number of ionizing photons for each new model compared with the model of the second set with the same attenuation factor.

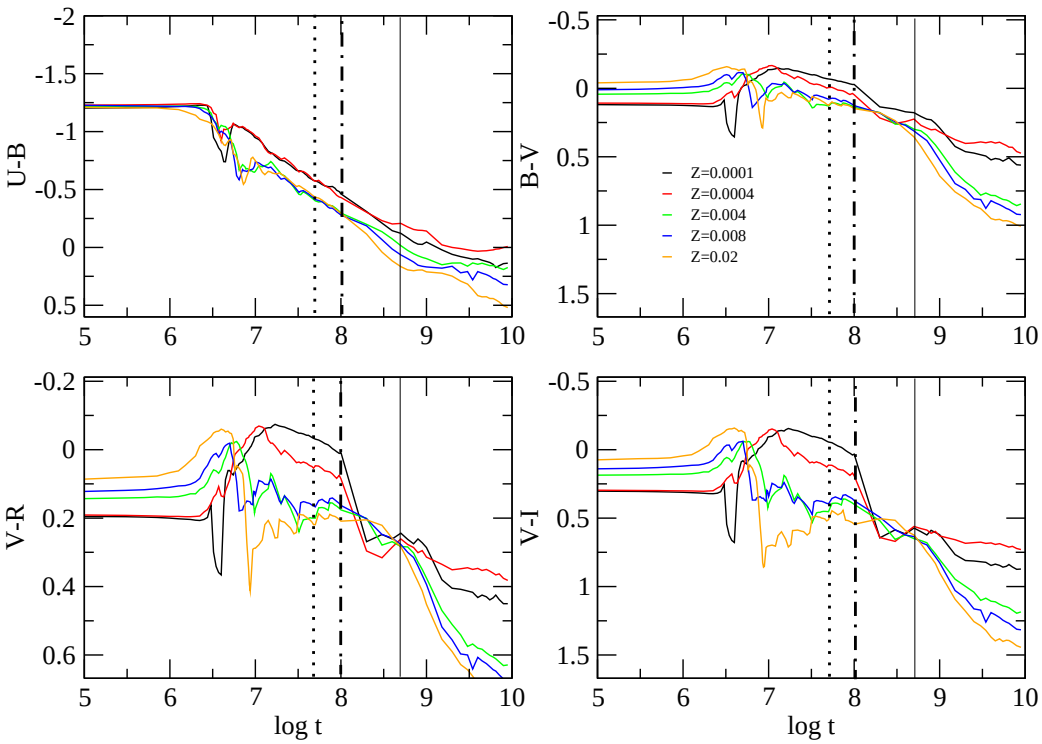

Figure 3.47: Evolution of the continuum colours of the SSPs with different metallicities. Vertical lines shows the time when the bursts take place. Dotted lines correspond to t=0.05 Gyr, dashed line to t=0.1 Gyr and solid line to t=0.5 Gyr.

higher than before, when assuming a longer inter-burst time. We can see the colours of the SSPs along 10 Gyr after the star formation with different metallicities at ages where the next burst take place in Figure 3.47. Thus, 500 Myr after the star formation, the population is evolved and it contributes to the colours of the next burst shifting them to the red. However, when the new burst takes place after 50 Myr, the colours are still too blue, especially in low metallicity models, and their contribution will not shift the next burst to the red. In fact, this contribution will make the colours of he new burst to be bluer than the previous one, as happens in Δt=0.05 Gyr models. In Figure 3.48, 3.49 we can see the evolution of the colours. The first burst is similar in every model, and, the closer the next burst takes places, the bluer is the second burst. Comparing the model results with the same efficiency, we see that models with Δt=0.05 Gyr are more similar to SAM. Then, the reduction of the time between burst compensates the effect of the attenuation producing less reddening, but a higher contribution to the total continuum.

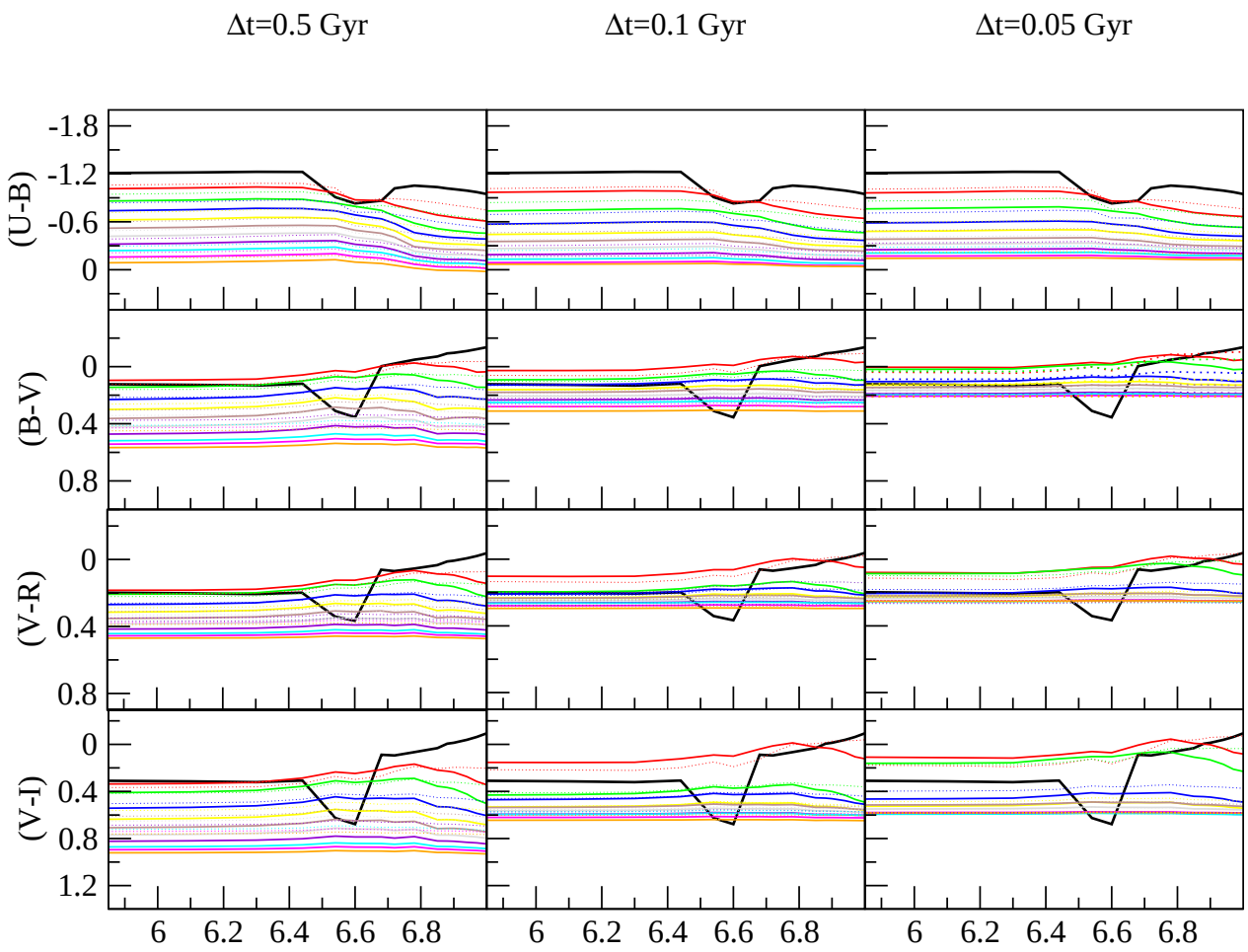

Figure 3.48: Evolution of the continuum colours for the three different models with k=0.65. Solid lines correspond to high efficiency models and dotted lines to low efficiency models.

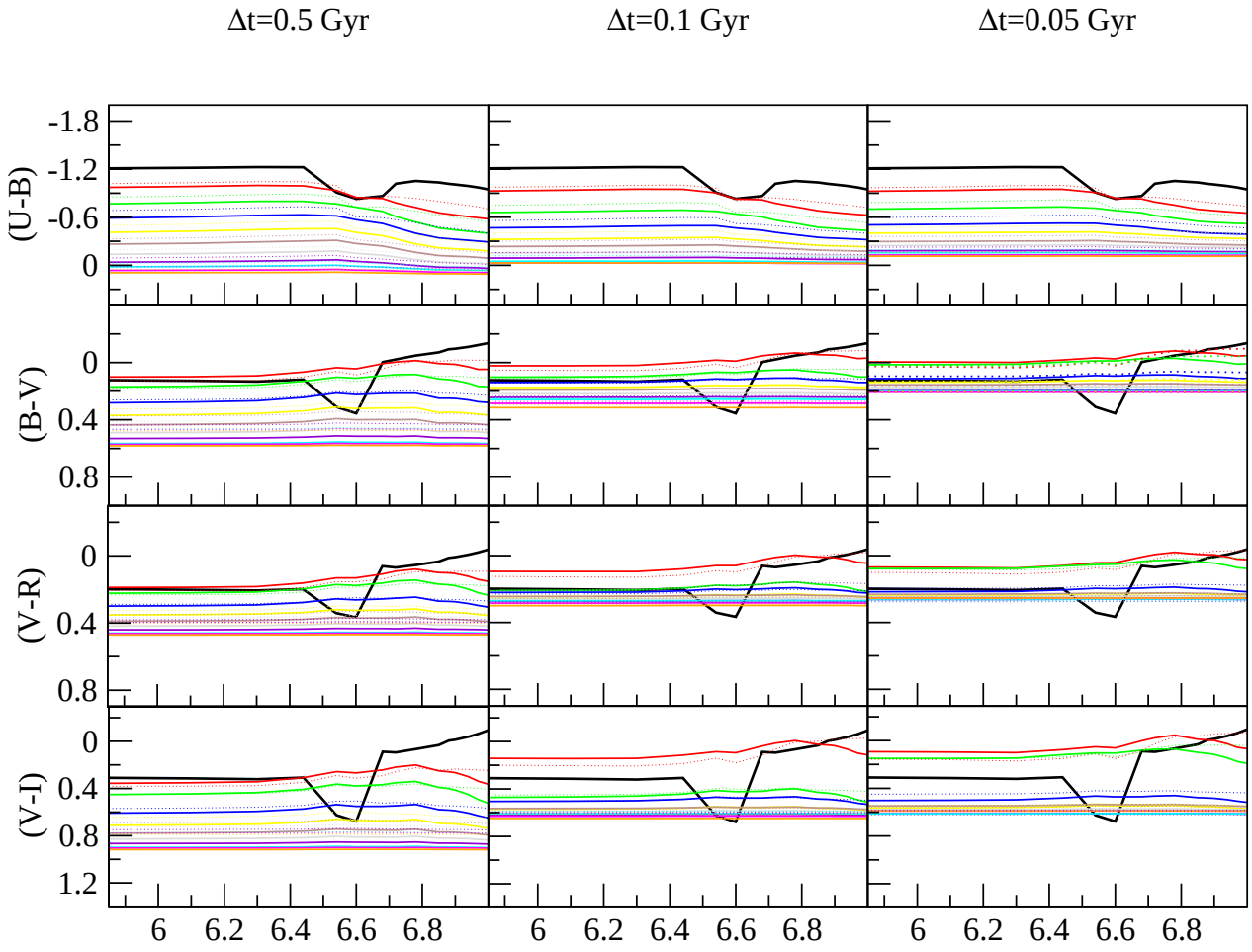

Figure 3.49: Evolution of colours of the continuum for the three different models with k=0.5. Solid lines correspond to high efficiency models and dotted lines to low efficiency models.

Photoionization: the ionized gas.

In this set, due to the fact that some bursts have less metallicity than the previous models and the mass created in each burst is lower in each burst, the radii will be quite different, producing some changes in the ionization parameter. Those changes will be present in intermediate bursts at ages between 3 and 5 Myr after the SF, producing variations in emission lines.

In Figures 3.50 and 3.51 can be seen that models with less inter-burst time show greater intensities of emission lines, covering a wider range in [OII]/H_β. Due to the slow evolution of the metallicity, the model lasts more time to reach the threshold metallicity of Z=0.004, maintaining the emission lines in the high excitation zone for more time. Thus, the bursts show a younger and bluer stellar continuum. This effect is more clear in [NII] lines. The minor the inter-burst time, the negative is the [NII]/H_α ratio, that is, the bursts are less metallic. With smaller inter-burst time, intermediate mass stars have no time to eject the nitrogen and subsequent bursts show lower values of this ratio.

Combined continuum and emission line diagnostics.

As we have seen before, the reduction of the time between bursts counteracts the effect of the attenuation in colours. The underlying population is less evolved and produces less reddening at low metallicities. However, the EW(H_β) decreases from burst to burst in a steeper way than in the second set. In Figure 3.52 we see that the EW(H_β) decreases rapidly while resulting colours are not sufficiently shifted to the red to cover the range shown by HII galaxies.

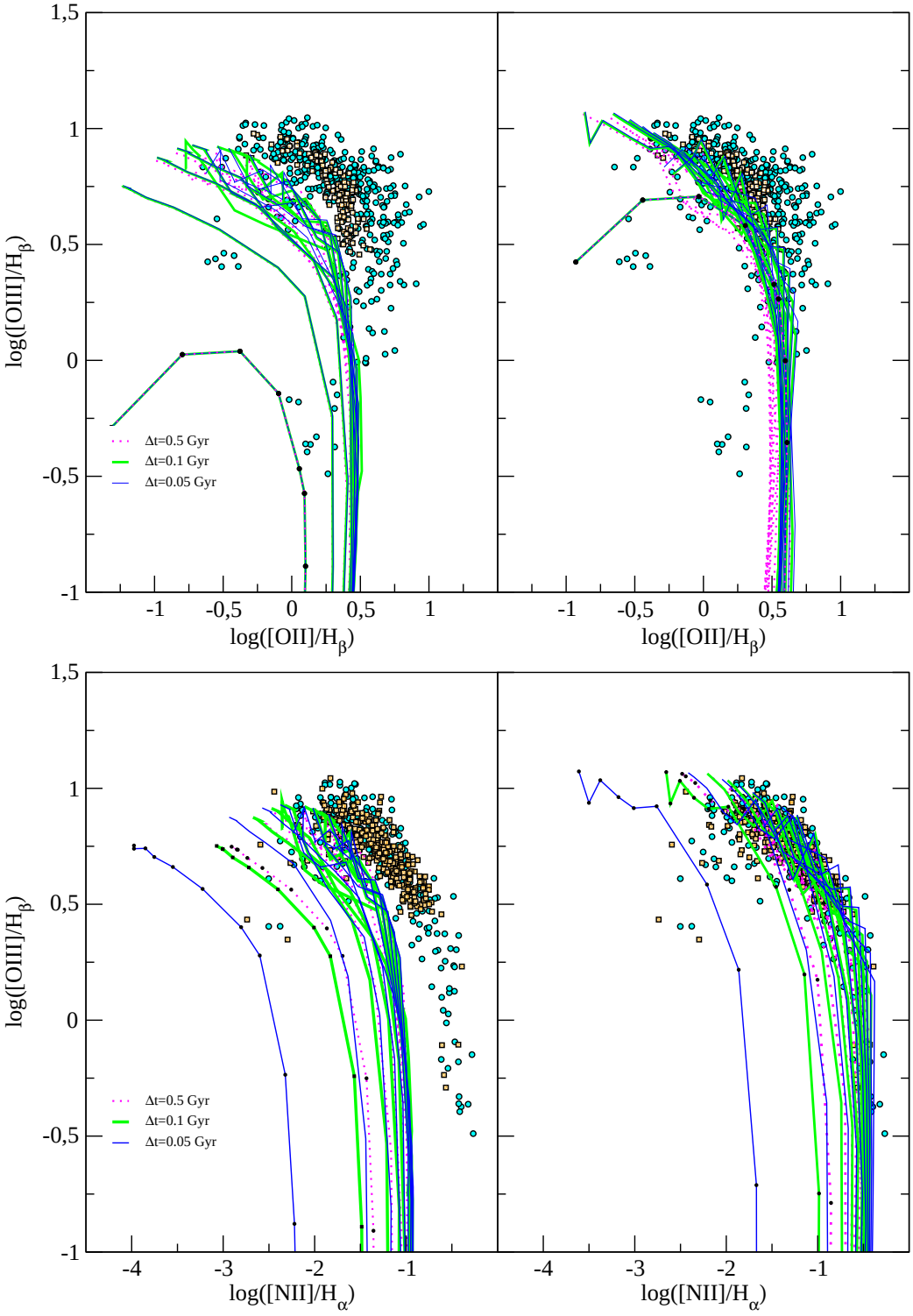

Figure 3.50: Diagnostic diagrams for HAM with k=0.65 and different inter-burst times. The first burst of each model is marked with small black dots along its evolution. In lower panels, due to the absence of enough nitrogen in the first burst of each model, they do not appear, and the burst sequence begins in the second one.

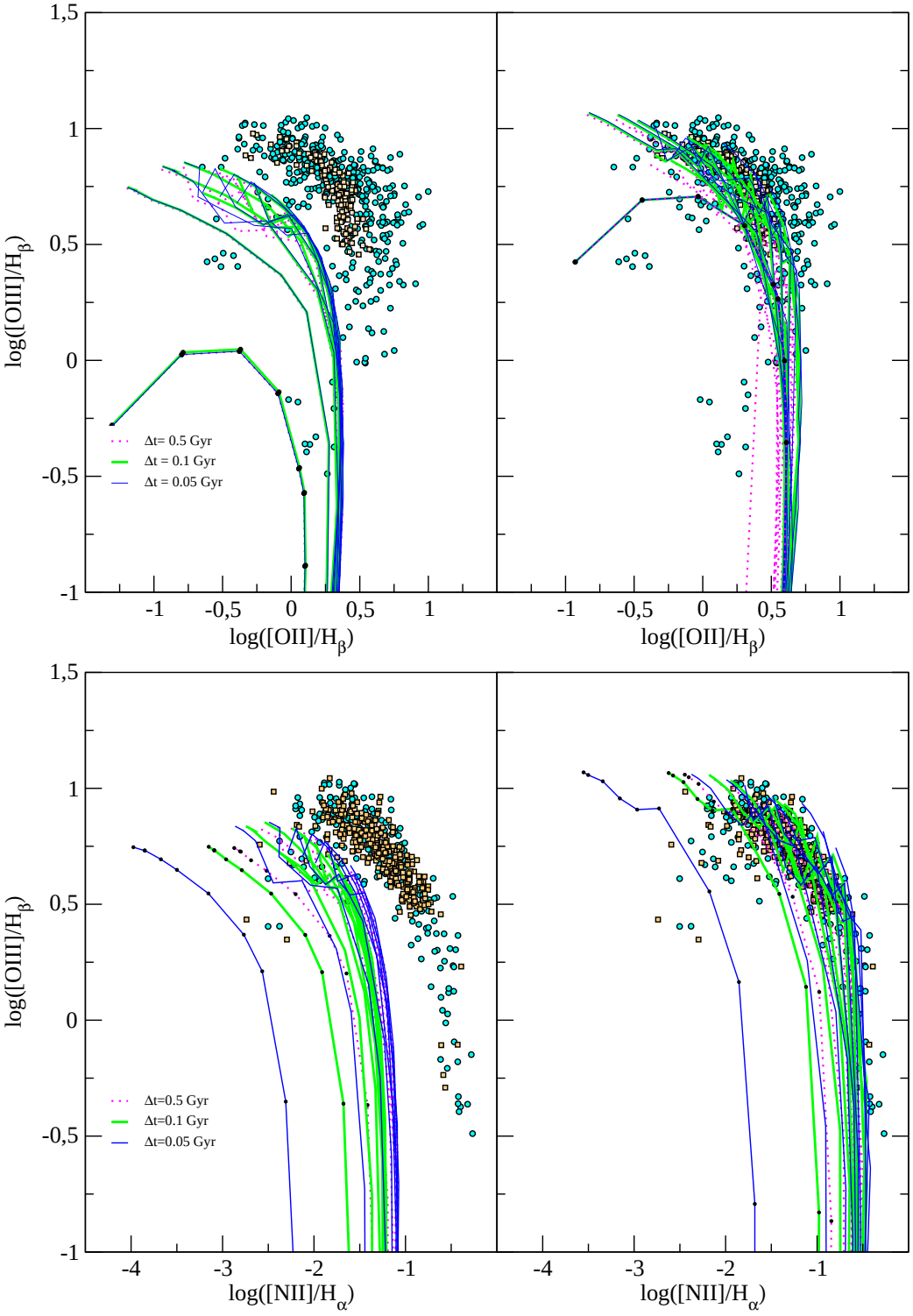

Figure 3.51: Diagnostic diagrams, similar to those of the previous figure, for HAM k=0.5 and different inter-burst times.

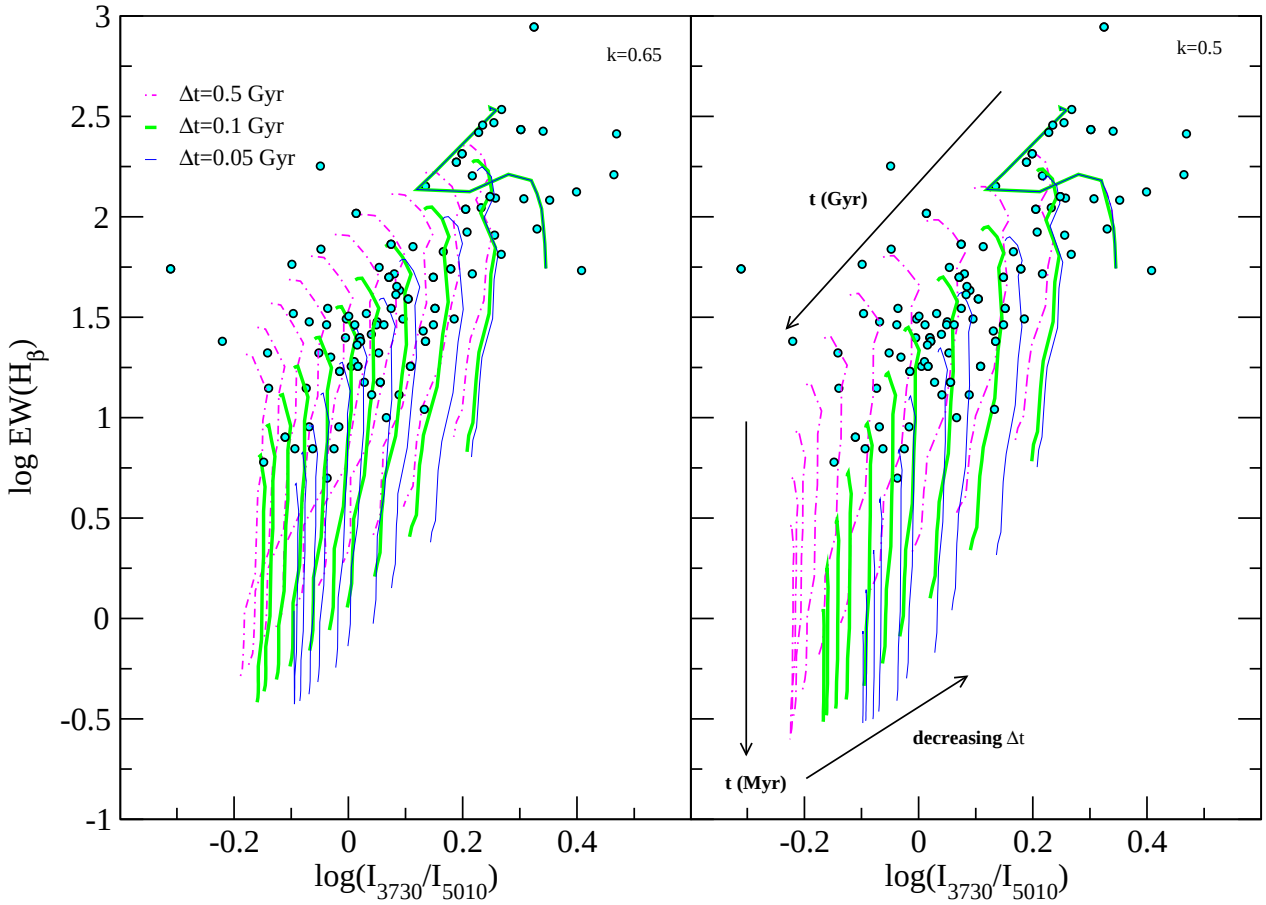

Figure 3.52: EW(H_β) vs. the ratio I_{3730}/I_{5010} for models with different inter-burst times. Left panel shows HAM with k=0.65 and right panel with k=0.5. Models with less inter-burst time do not reach colours as red as models with Δt=1.3 Gyr. However, due to the higher continuum contribution by the previous star generations, the EW(H_β) decreases more from burst to burst.

The models with Δt lower than 100 Myr are more similar to those of SAM. It makes the models to have a new restricted parameter in order to reproduce simultaneously the characteristics of HII galaxies, regarding chemical evolution and spectro-photometric features, together with attenuation and initial efficiency.

Chapter 4

Discussion: what is this for?

4.1 Global analysis of results.

The main results of our work can be summarized as follows:

-Standard Attenuation Models reproduce the chemical present abundances and the ionized gas properties since it is the current burst of star formation which dominates the observed light and produces the emission lines. Both the chemical properties of the gas and the properties of the ionized gas depend directly on the initial efficiency assumed for each model. However, the bursts of this type of models are too strong and the equivalent widths of H_β do not change sufficiently from one burst to the next: the contribution of the underlying population is still not enough to provide an adequate covering of the observational data range.

-High Attenuation Models seem to reproduce better the trend of the observed data. The chemical properties of the gas and the ionizing population characteristics are reproduced by these models which at the same time reproduce the trends shown by colours and EWs in the observed ranges.

Emission lines properties and chemical abundances may be easier to reproduce than the properties of the continuum, and can be matched just with a SSP as input to the photoionization model (emission lines) or with a chemical evolution model (abundances and SFR). As we have seen in previous sections, the most significative feature to reproduce is the equivalent width of H_β, as well as the colours of the continuum, that is, the combined properties of the ionized gas and the stellar continuum, for which the use of the three theoretical tools together is required. One of the goals of this work has been to develop an adequate technique to predict all of these quantities simultaneously and in a consistent way.

In Figure 4.1, upper panel, we have plotted the run of the equivalent

width of H_β with the contribution, by mass, of the new burst with respect to the mass of the underlying population when this new burst takes place. Every model follows the same trend, and there are not big differences among them. In fact, it would be possible to adjust all models with a same line, showing a low dispersion. It can be seen that, in order to decrease by 50% the equivalent width value, the current burst of star formation would have to involve the 10% of the mass of the underlying evolved population, assuming 1.3 Gyr for the interburst time. In the same case, the continuum colours changes by 25%, as seen in the lower panel.

On the other hand, continuum colours are metallicity dependent, specially at late stages or last bursts, where the reddening in high efficiency models is higher than in low efficiency ones. When the mass of the burst involves around 1% of the underlying mass, differences between the colours of models with both efficiencies start to appear, showing a maximum dispersion of 6%.

In Figure 4.2 we also include models with shorter inter-burst times, 0.5, 0.1 and 0.05 Gyr. In the upper panel, we see that the differences between these models are more noticeable than in the models with 1.3 Gyr of inter-burst time. The stellar continuum contributes more to the decrease of EW(H_β), because it maintains a high luminosty, specially in models with shorter inter-burst time and less metallicity. In these models, the mass involved in the current burst does not have to be so low to decrease appreciably the EW(H_β). IN the models with 1.3 Gyr of inter-burst time, the current burst mass has to reach 10% of the underlying population mass while when the inter-burst time is 0.5 gyr, this contribution can be as high as 40% in order to decrease EW(H_β) by the same relative amount. In the lower panel we see that models with Δt=0.5 Gyr, and also with Δt=0.1 Gyr, are more similar to HAM with 1.3 Gyr of inter-burst time, and models Δt=0.05 looks like SAM due to the poor reddening produced by these bursts, indicating that this inter-burst time is not valid at all to reproduce the trends of observed HII galaxies.

If we want to make that a two-burst model (which is the most studied case), produce a decrease of a certain percentage of the equivalent width or a certain reddening in colour, we can obtain how much mass has to be involved in the second burst knowing previously the mass of the first burst and how it evolves with time until the second star formation episode starts. In Figure 4.3 we can see this evolution of the mass in stars (normalized to 1 $M\odot$) along 1.3 Gyr, the maximum inter-burst time taken in our models. The stellar mass decreases because massive stars die and we can use this plot to know how much mass of the stars formed in the previous burst will stay when the next burst takes place.

Therefore, the redenning of the colour is determined by the efficiency,

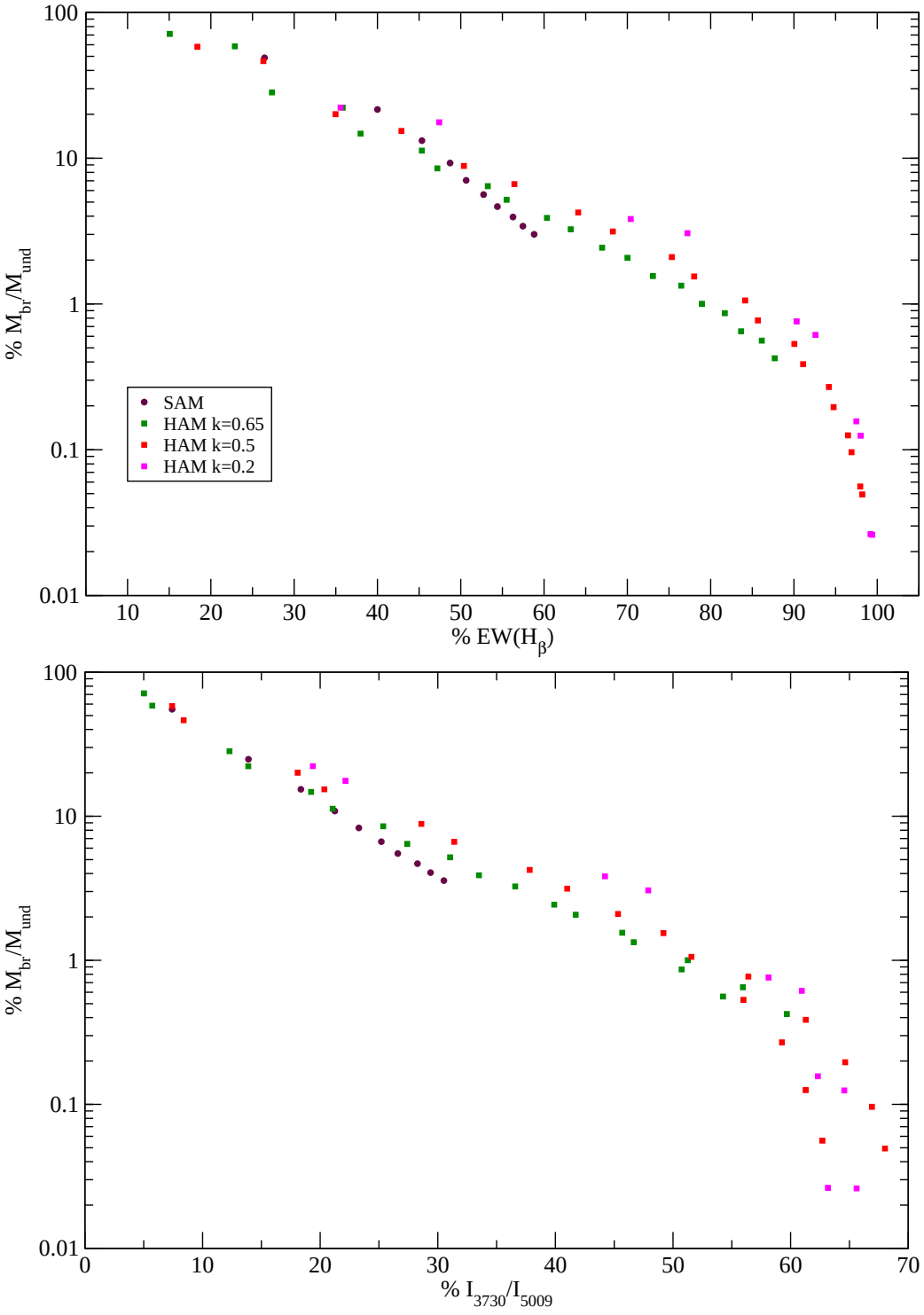

Figure 4.1: Mass of stars involved in the new burst with respect to the mass of the underlying population as a function of the change in the equivalent width of H_β (upper panel) and of the continuum pseudo-colour (lower panel) for both SAM and HAM. Taking into account different masses for the new burst we are able to decrease a certain percentage the EW(H_β) and colours.

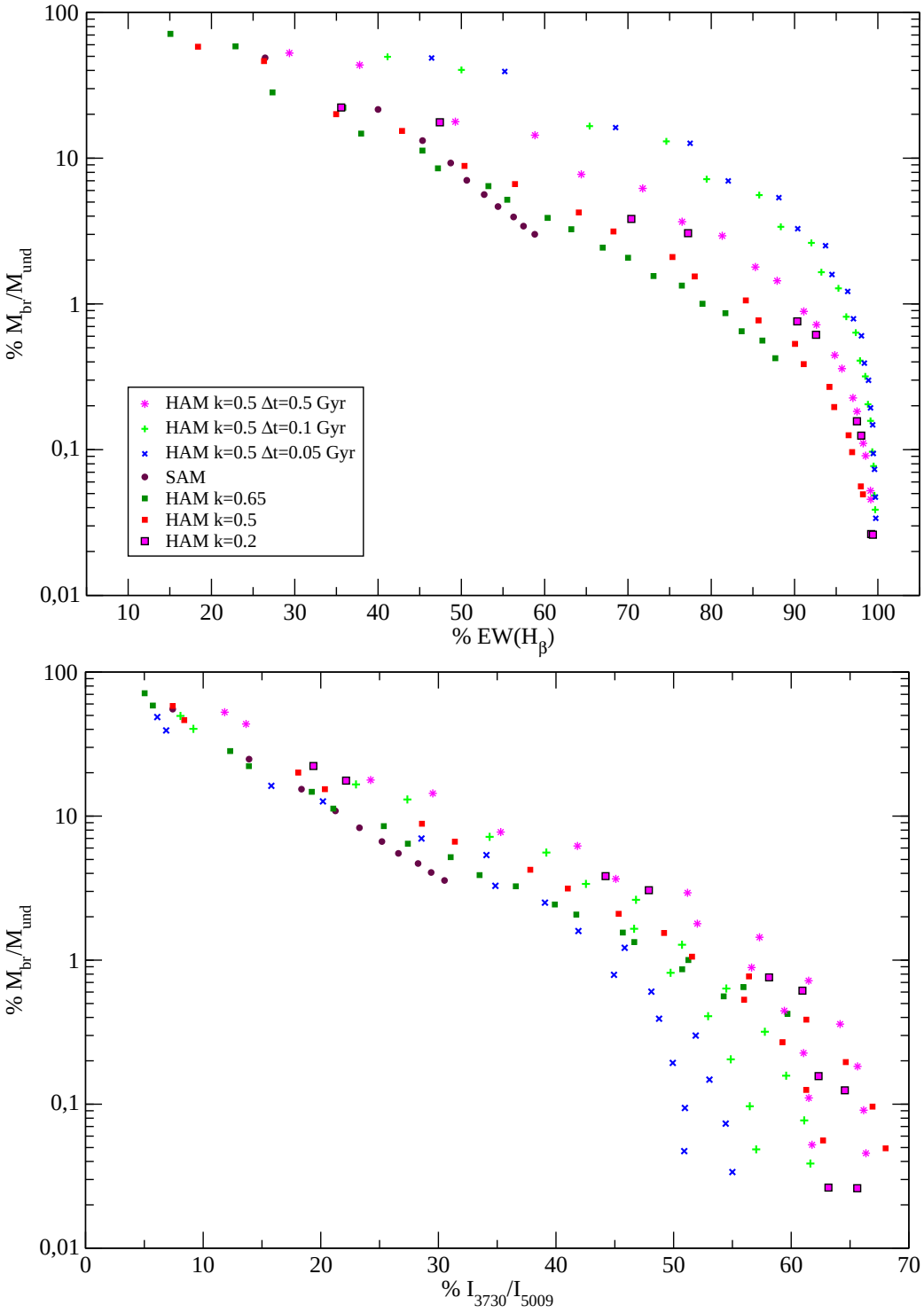

Figure 4.2: Figure similar to 4.1 including models with $\Delta t<1.3$ Gyr.

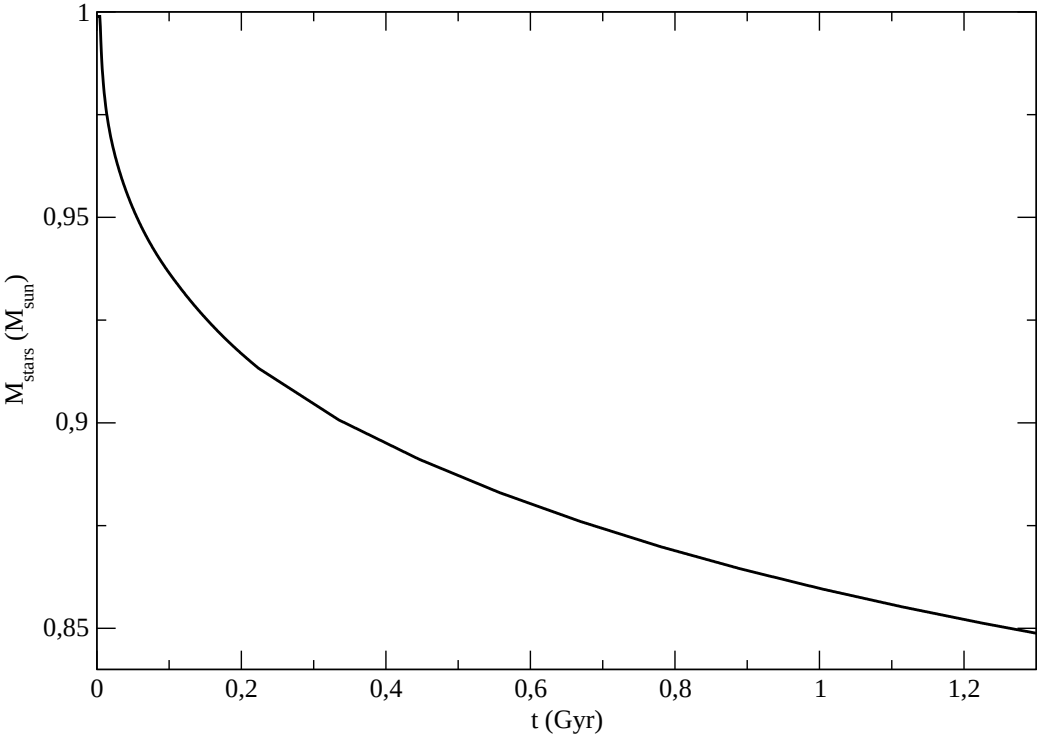

Figure 4.3: Evolution of the stellar mass (in $M_{\odot}$) of the first burst along 1.3 Gyr.

specially at high metallicities, and also by the attenuation and inter-burst time. However, the decrease of the EW(H_β) from a burst to the next one depends mainly on the attenuation and/or on the inter-burst time, while the initial star formation efficiency does not change very much the behaviour of this parameter.

Our models have three free input parameters which we need to adjust to reproduce HII galaxy data:

- **Initial Efficiency:** Defines the amount of gas consumed to form stars in the first burst of the model.
- **Attenuation:** How the initial efficiency of star formation is attenuated in the subsequent bursts
- **inter-burst time:** Every burst takes place instantaneously and it is followed by quiet periods whose duration can change.

The **initial efficiency** determines the star formation history and the initial element abundances (and total metallicity). The initial efficiency also leads the behaviour of the ionized gas: the emission lines are produced by the ionizing photons of the massive stars present in the current burst, and it is determined by the mass involved in this star formation episode.

The **attenuation** determines how the metalllicity or elemental abundances and the star formation rate evolve in the successive bursts of star formation, and it makes these quantities to stay between the limits of the observations. The most important characteristic dominated by the attenuation of the bursts is the contribution by the underlying population of the previous burst to the total continuum. Hereby, both the equivalent width of the H_β line and the colours of the stellar continuum are determined by this parameter. The higher the attenuation of the current bursts, the higher the contribution of the previous bursts to the total SED in each new burst.

Once a initial efficiency value is assumed, the attenuation factor has to be determined trying to keep the model results within the range of the observations, specially what concerns to the oxygen abundance.

According to our models, the initial efficiency can not be higher than 0.6-0.62 (that is, 60% of the available mass of gas), in our case this would be around 60×10^6 M$\odot$. For higher efficiencies, the oxygen abundance obtained would be out of the range shown by HII galaxies. For initial efficiencies in the range $0.6< \epsilon \leq 0.5$, the attenuation factor has to be less than 0.2, but this factor is too low and star formation would disappear after a few bursts. On the contrary, for efficiencies $0.3\leq \epsilon \leq 0.5$, the attenuation has to be high, $0.2\leq k\leq 0.65$, because the initial burst involving so much mass creates a large

number of massive stars. This implies that the metallicity increases abruptly maintaining their values high along the following bursts. For this reason, the successive bursts must involve less mass to avoid the metallicity to grow very fast above the observed limits. For initial efficiencies $0.12 \leq \epsilon \leq 0.3$, the attenuation factor can take values from 0.2 to 0.95. However, for high values of k we do not get enough contribution by the underlying continuum, in spite of being within the observational data range. The minimum initial efficiency that we can assume for these models is around 10%-12% of the mass of gas. For these efficiencies, the minimum attenuation factor is k=0.2 and the maximum is 0.95, as said before. [1]

The **inter-burst time** is a secondary parameter which has a similar effect to changing the two previous parameters, ϵ and k, simultaneously. Being the burst closer to each other (but allways $\Delta t > 10$ Myr), the contribution of the underlying continuum is higher and the EW(H_β) decreases more rapidly from burst to burst. However, the decrease of the inter-burst time compensates the effect of the increase of the attenuation, which makes the colours to be more similar to those of SAM, an extra reddening being then necessary in order to reproduce the trend shown by HII galaxies. The inter-burst time is another restricted parameter for our models, which can not be less than 100 Myr.

4.2 Discussion: connecting star-bursting models with star formation scenarios and/or evolutionary phases.

Star formation scenarios.

The three parameters that we have to adjust in order to reproduce the observational data of HII galaxies can take different values that could be identified with different star formation scenarios. The three hypotheses, (a) short star-formation episodes with large quiescent periods, (b) long moderate star-formation episodes with short quiescent periods and almost continuous star formation with few overimposed sporadic bursts (c) could be reproduced by changing our model parameters.

The star-bursting scenario (a) is what we have been considering for almost the whole work. The effects of an instantaneous burst can be seen during

[1] We have not included models with increasing star formation efficiency or models with initial metallicity more smaller than the lower limit observed in HII galaxies, that is the abundance of IZw18.

10 Myr after the burst takes place. Long quiescent periods or, in our case, null star formation periods, have been considered to last more than 1 Gyr, which would be the minimum age of the underlying population belonging to the previous burst. Bursts ocurred before the immediately previous one have very poor contribution to the current total continuum luminosity, and the use of this long time for the inter-burst period produces a similar result to assuming a two-burst model for some parameters, as EW(H_β). However, differences appear between both scenarios since the ISM is enriched by every single burst ocurring during the galaxy life time, colours are shifted to the red, and stellar populations older than 1 Gyr are going to be found.

The gasping star formation scenario (b) can be simulated by increasing the attenuation of the burst and reducing the inter-burst time. With the change in these two parameters we could make the star formation smoother and more moderate. Being the bursts closer in time, the quiescent periods are shorter. Since some of our models suffer a high attenuation, when we use inter-burst times shorter than 100 Myr, they could be considered as gasping models. As we have seen, this has consequences when reproducing some observational data. Increasing the attenuation, we obtain a major contribution to the continuum by the previous bursts, and if, in addition, we reduce the inter-burst time, mostly for lower metallicities, this contribution will make the underlying population to be younger and the colours to be bluer. This approach would make possible to find intermediate age stellar populations, younger than 1 Gyr, even after several star bursts. With larger inter-burst times only the inmediately previous stellar generation contributes substancially to the present continuum, but stellar generations previous to this one would be noticeable if we reduce the time between bursts. However, to extend the star-burst phase would be more complicated. Longer phases are in principle posible by concatenation of starbursts, but population synthesis modelling of BCD spectra does not favour extended periods of star formation (Mas-Hesse & Kunth, 1999). Then, if the starburst phase is short, there should be many of these episodes during the galaxy lifetime, as we have modelled. According to Sánchez Almeida et al. (2008), there should be one BCD phase each 0.3 Gyr, which agrees with our models.

In the continuous star formation scenario (c), the star formation rate must be very low and extended. If we reduce the inter-burst time to a minimum value and, simultaneously, we reduce the intensity of each burst, we obtain a very low star formation rate not comparable to a starburst, that is, we would simulate a continuous star formation scenario. In fact, most of the observations of HII galaxies may be reproduced by a young stellar population 3-5 Myr old, with most massive stars being essentially coeval, but as Mas-Hesse & Kunth (1999) demonstrated, it is also possible to obtain

similar results with a continuous star formation, lasting at least 20 Myr since the beginning of the star formation.

However, as we have seen in our third set of models, if log (SFR) < -3 approximately, there are not enough ionizing photons to produce emission lines. In this case we are not reproducing the so-called star-forming galaxies, but another type of galaxy or another stage of their evolution.

A low continuous star formation rate cannot be neglected, especially in low metallicity galaxies. According to van Zee et al. (1997) the galaxy UGC 9128 presents a SFR of 1.7×10^{-4} $M_\odot$ yr^{-1}. With this continuous star formation rate, the mass of stars created in 1 Gyr is 0.17×10^{6} $M_\odot$. In our models, the stellar mass created in the firsts bursts is, in most cases, one order of magnitude higher. Taking into account the gas ejection by massive stars, the mass available to form stars in the next burst would be almost the same as if no star formation between bursts would take place. For the last bursts of high efficiency models, but mostly in low efficiency models (which implies low metallicities) this very low star formation between bursts could be important.

Models of dwarf galaxies without current star formation episodes have been calculated by Gavilán (2009). These models have very low star formation rates, even using a high efficiency star formation value. The star formation processes would consume the gas more or less rapidly, depending on the efficieny, and it would be possible to have an extended and continuous star formation during the whole evolution of the galaxy. Since they use a time step of 10^7 yr and massive stars produce effective ionizing photons during their first Myr of their lifes, no emission lines are found. In these models, the gas is forming stars continuously, so, stars of all ages would be found in every moment. It is necessary to reduce the time step of the code to find emission lines and a real young ionizing stellar population. In our models we would have to reduce to extremely low values the time between bursts and reduce the efficiency of the star formation. Very low efficiencies imply very low metallicities, so, it would be necessary to decrease the attenuation in order to reach the oxygen abundance values shown by HII galaxies.

In the previous section we saw that in order to reproduce correctly the continuum colours, getting redder along the successive bursts, the separation between bursts can not be shorter than 100 Myr. Otherwise, the predominant colour would be blue, making the next burst bluer than observations demand. Even for galaxies like I Zw 18 or SBS0335-052, the age of the underlying population does not seem to be younger than 100 Myr (Papaderos et al., 1998; Thuan et al., 1997), in agreement with our results. Therefore, we can say that, with our models, although it is possible to simulate a continuous star formation model, some observable parameters of HII galaxies can not be

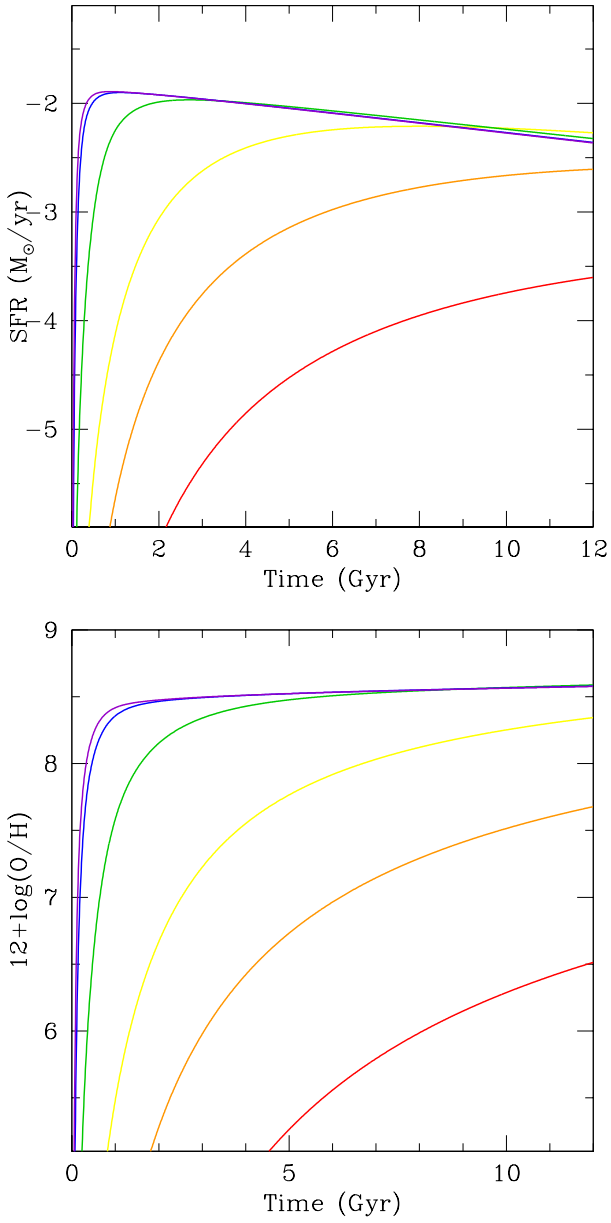

Figure 4.4: Star formation rates and evolution of the oxygen abundance along the time for continuous star formation models (Gavilán 2009), using an initial mass of gas of 10^8 $M_\odot$ and an infall time of 8 Gyr. The highest and the lowest efficiency models are represented as blue and red lines respectively.

reproduced this way, so, this star formation scenario would not be viable at all for this kind of galaxies.

Evolutionary phases of a BCD.

Instead of considering the continuous star formation as a different global scenario, we can study it as a phase between bursts. In this way we could change the perspective of the problem and study the caracteristics of the galaxy from the inter-burst low activity periods, that is, after the first 10 Myr from the last star formation episode.

During the previous sections we have been dealing with star-forming galaxies, more exactly with HII galaxies, or BCDs, without taking into account the properties of any other type of galaxies, or any evolutionary connection with other dwarfs. As we said in Chapter 2, the BCD galaxy can be considered just a star-forming phase or a stage in the evolution of a gas rich dwarf galaxy. In this scenario, we can consider the inter-burst time in our models as a QBCD phase. We assume the BCD phase to be the 10^7 yr after the star burst, during which its effects are still visible (emission lines or changes in metallicity due to massive stars ejections) and the QBCD phase would correspond to the inter-burst periods.

We have seen how the BCDs colours can be contaminated by the emission lines, showing in some cases different trends in the colours of the ionizing continuum (see Chapter 3, *i.e.* Figure 3.25). Once corrected on this contamination, the colours observed are those corresponding to the ionizing continuum of a given galaxy, always during the BCD phase, that is, the blue colours of the young ionizing population which dominates the emitted light. In order to study the colours in the inter-burst periods and know the properties of the underlying population of the host galaxy, we should further eliminate the continuum arising from the starburst.

Figures 4.5 and 4.6 show the B-V vs V-I and V-I vs V-R colour-colour diagram for model HAM, k=0.65 and 33% of initial efficiency. Black circles show the stellar continuum colours while blue solid ones show the colours computed including the contribution by the stronger emission lines. The inclusion of the contribution by the emission lines to the continuum colours shifts the position of the model points almost perpendicularly to the originally computed ones. The location of the blue points is mainly determined, even at zero redshift, by the contribution of strong [OIII]4959,5007 emission lines to the V band. To characterise the colours of the inter-burst pahse in our models, we have used the SSPs colours taken from the PopStar code directly. We have used these colours for ages from log t=7 to log t=10.38, that is, without taking into account the BCD phase.

Although they are not exactly the colours of our inter-burst periods, they cover the ranges of metallicities without showing larger differences with the true bursting models.

In B-V vs V-I diagram we show the data by Cairós et al. (2001a,b) as red dots with error bars. This set of observations corresponds to readily observed colours, including both continuum and line emission, and no reddening correction has been applied. It can be seen that some of the data are impossible to reproduce by the models which do not take into account the contribution by emission lines, even if some amount of reddening is invoked (the arrow in the diagram shows the correction corresponding to 1 mg visual extinction). On the other hand the data by Cairós et al. (2002) of resolved locations in Mrk 370, shown in the figure as green triangles are very well reproduced by our continuum colours. The data of Mrk 370 are based on UBVRI broadband and H_α narrow band observations. In this case, they subtract the contribution of the underlying continuum of the old stellar population, removing the contribution from emission lines and correcting for extinction, measuring in this way true colours of the young star-forming knots. Magenta triangles correspond to Mrk370 colours including the emission lines contribution and the host galaxy. The contribution of the underlying component makes the colours redder than the BCD ones, also well reproduced by or models. Orange dots are the QBCDs (Sánchez Almeida et al., 2008), from SDSS/DR6 database. They have selected QBCDs assuming them to be like BCD host galaxies. The colours of the SSP with ages older than 10 Myr can reproduce these observations, indicating that they correspond to the colours of a more evolved population than the one corresponding to the current burst in BCD. However, some of these orange dots lie in the BCD zone, indicating that this data sample also contains a certain proportion of BCDs, following a continuous evolutionary sequence.

In Figure 4.6 we plot (V-I) vs (V-R), where we have also included the data of BCDs and its hosts from Telles & Terlevich (1997). This sample consists of 15 BCDs for which they obtain the colours of the underlying stellar continuum within the starburst by subtracting the contributions of the emission lines and the colours of the BCD stellar continuum. They also give the colours of the BCD subtracting the contribution of the underlying galaxy by assuming the mean surface brightness of the extensions, or hosts, to be constant and representative of the underlying galaxy within the starburst regions. The data of the stellar continua not corrected from emission lines (blue squares) are well reproduced by our models, represented by the blue dots. Stellar continuum colours corrected from emission lines (red big squares), are close to black dots, corresponding to our continuum BCD phase. The colours of the isolated host galaxy (grey squares) show redder colours

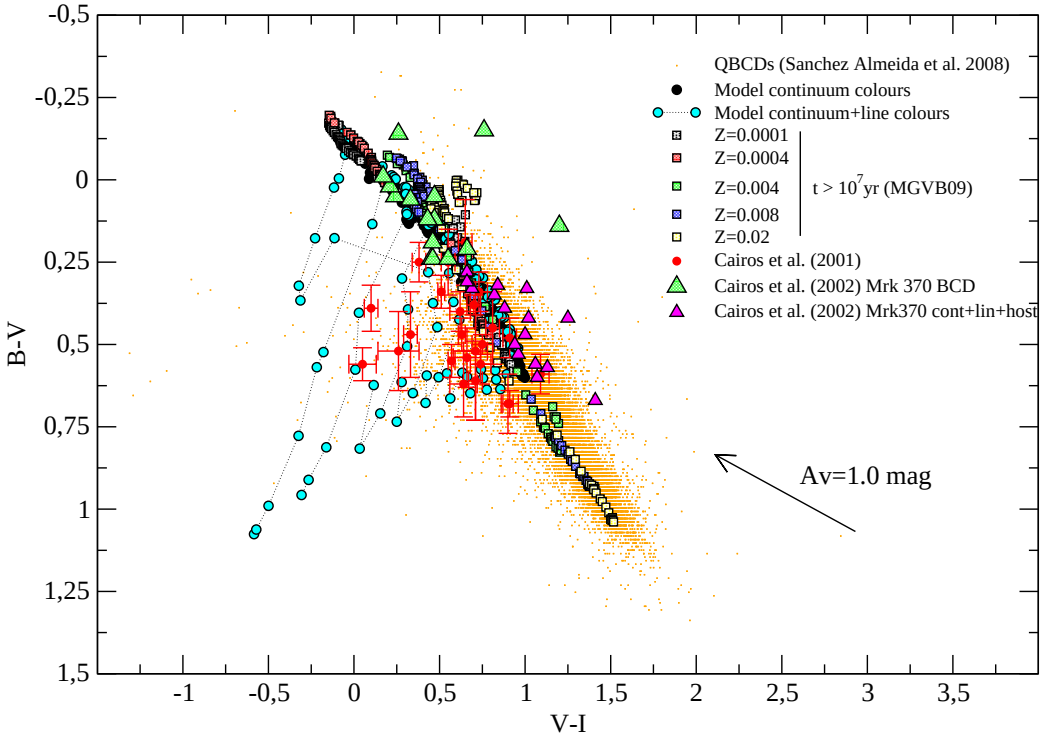

Figure 4.5: (B-V) vs (V-I) colour-colour diagram for HAM with k=0.65, including the stellar continuum colours of the starburst phase (black dots), these continuum colours contaminated by the emission lines (blue dots) and the colours of the inter-burst periods for 5 metallicities (coloured squares). Observational data taken from Cairós et al. (2002); **?** and Sánchez Almeida et al. (2008).

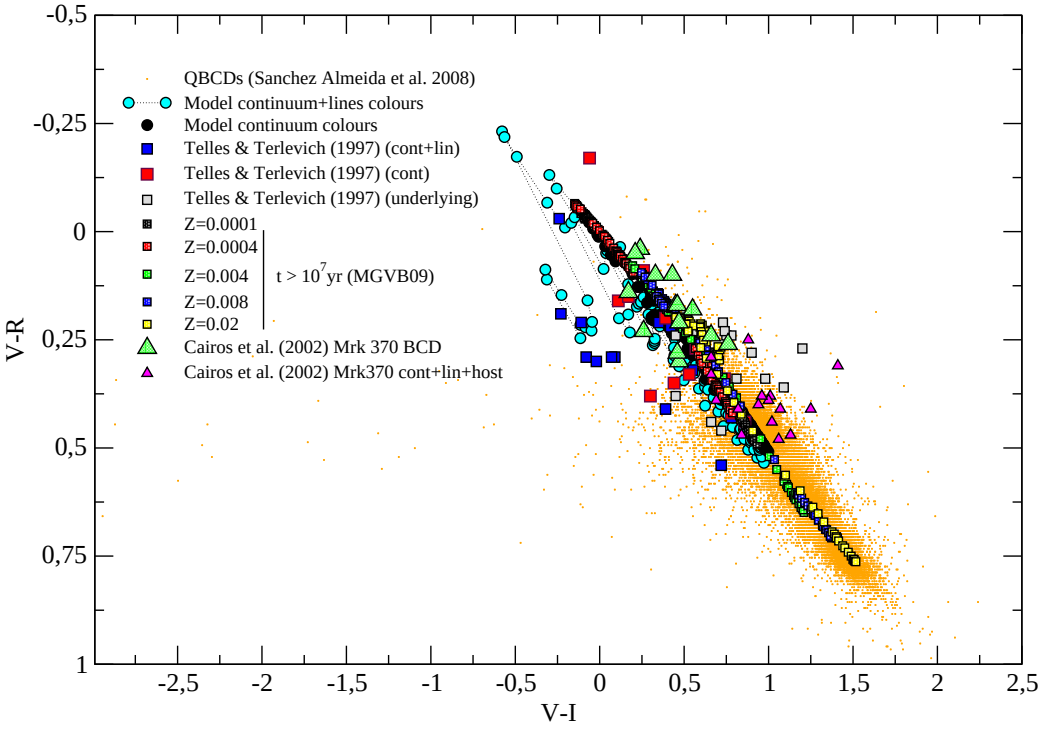

Figure 4.6: (V-I) vs (V-R) colour-colour diagram of HAM k=0.65, including the stellar continuum colours (black dots), these continuum colours contaminated by the emission lines (blue dots) and the colours of the inter-burst periods for 5 metallicities (coloured squares). Observational data taken from Cairós et al. (2002); Telles & Terlevich (1997) and Sánchez Almeida et al. (2008).

than the BCD component, in agreement with QBCDs, Mrk370 host and model colours with ages older than 10 Myr.

In order to compare directly with the SDSS photometry system, we also have plotted (g-r) vs (r-z) colours for QBCDs and our models. SSPs colours in the *ugriz* system have been computed directly. For our bursting models we have used our own transformation between Johnson and *ugriz* filter systems, obtained from the SSPs colours from both systems given in MGVB09. In this plot we see that QBCD data show colours similar to our models contaminated with the emission lines contribution. This region of the diagram, with (g-r) colours between 0.5 and 0.0 overlaps with BCD colours of the same sample, in agreement with the assumption that these objects have emission lines but have some old stellar generations which make the colours to be redder.

Once we have seen that BCDs and QBCDS colours are reproduced by our models, during the first 10 Myr after the begining of star formation and

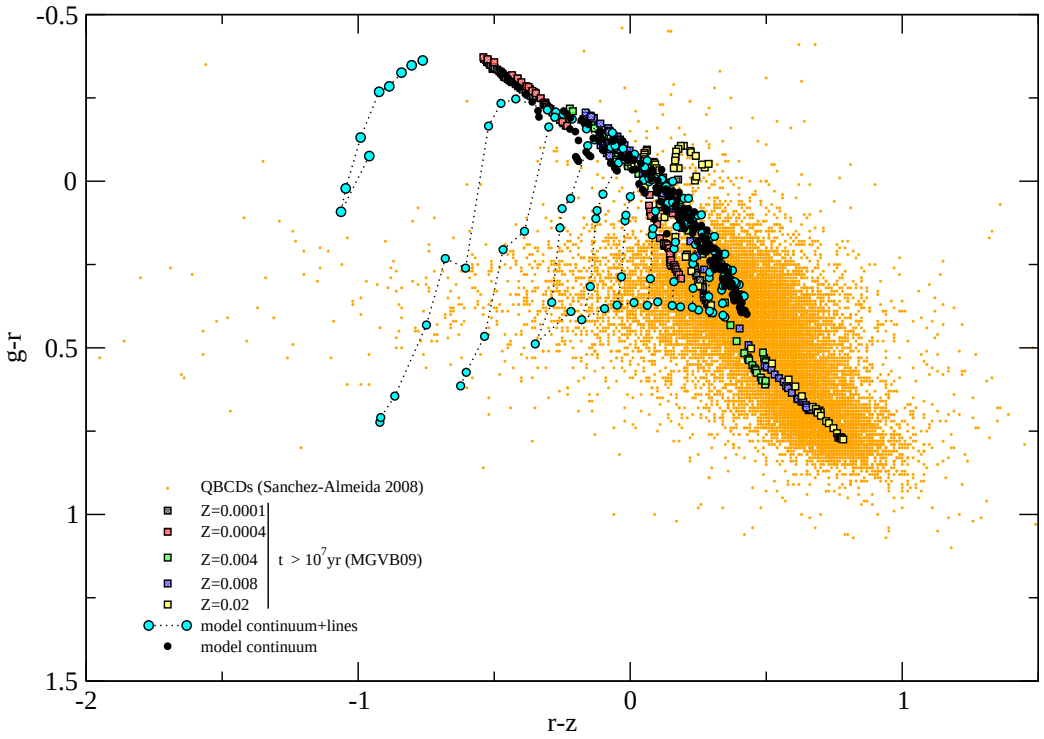

Figure 4.7: Colour-colour diagram for HAM k=0.65 models, including colours contaminated by the emission lines in *ugriz* system. Observational data from Sánchez Almeida et al. (2008).

after 10 Myr up to more than 1 Gyr respectively, we can confirm that both types of galaxy colours overlap and could be considered as different phases in the evolution of the same object.

4.3 Application of χ^2 test to observed galaxies.

As an application of our models we have performed a χ^2 test to a very well observed objects. We have chosen IIZw40 for which we have taken the values of 13 emission line ratios, equivalent width of H_β and continuum pseudo-colour I(3730)/I(5010), all taken from Terlevich et al. (1991).

Parameter	Value	Error (%)
$[OII]$3727Å	0.275	5
$[NeIII]$3869Å	0.347	15
$[OIII]$4363Å	0.077	15
$[HeI]$4471Å	0.033	30
$[OIII]$4959Å	2.621	5
$[OIII]$5007Å	8.095	5
$[HeI]$5876Å	0.134	15
$[OI]$6300Å	0.019	20
$[NII]$6548Å	0.033	15
H_α	4.700	10
$[NII]$6584Å	0.089	10
$[SII]$6716Å	0.089	20
$[SII]$6731Å	0.087	20
EW(H_β)	268	10
I_{3730}/I_{5010}	4.890	20

Table 4.1: Emission line values of II Zw 40 taken from Terlevich et al. (1991)

Each of our models is characterized by the three parameters described above, and will provide an **age** and a **burst number** as results for the observed galaxy, that is, the age of the current ionizing population and the age of the underlying population. For each model we have 11 bursts and the evolution of the emission lines for 12 different ages from logt=5.85 to logt=7.00, within the bursts.

We therefore have a set of results as a 11x12 matrix, shown in table 4.2. For each matrix element (b_i, t_j), where i goes from 1 to 11, and j from 1 to

age/burst	b_1	b_2	b_3	...	b_{11}
t_1	–	–	–	...	–
t_2	–	–	–	...	–
t_3	–	–	–	...	–
.	.	.	.	...	.
.	.	.	.	...	.
.	.	.	.	...	.
t_{12}	–	–	–	...	–

Table 4.2: Table of a model parameter distribution

12, we have a set of results which may be compared directly with the same observed parameters of the galaxy. What we want to know is, which one of these pair of quantities, (b_i, t_j), better fit the observed galaxy.

For each model we have 15 parameters to compare with the observations: [OII]3727Å, [NeIII]3869Å, [OIII]4363Å, [OIII]5007Å, [OIII]4959Å, [NII]6584Å, [NII]6548Å, [OI]6300Å, [HeI]4471Å, [HeI]5876Å, [SII]6716Å, [SII]6731Å, H_α, EW(H_β), I_{3730}/I_{5010} (obtained with equation 3.5.) In order to compare the same kind of parameters, we have taken de EW(H_β) as a luminosity ratio multipliying it by the wavelength of H_β, 4861Å .

The χ^2 calculation has been made as:

$$\chi^2 = \Sigma_{n=1}^{15} \frac{(O_n - T_n)^2}{\sigma_n^2} \tag{4.1}$$

where O_n is the observed parameter, T_n the model parameter and σ_n is the error of the observed quantity. We use the reduced parameter, χ^2_{red}, to study the probability distributions:

$$\chi^2_{red} = \frac{(\chi^2 - \chi^2_{min})}{dim.} \tag{4.2}$$

In this equation χ^2_{min} is the minimum value of all χ^2 of the model, and *dim* is the dimension of the problem, that is, the number of models, or possible pairs (b_i, t_j) resulting from each χ^2 calculation. In our case, **dim= (i-1)×(j-1)=110**, where i and j are the number of columns and rows respectively.

In order to find the probability of that galaxy be in the burst i and have an age j, we use the chi-distribution, with χ^2_{red} and the degrees of freedom calculated as:

d.f= number of free parameters-number of bound parameters.

For our study:

d.f.= parameters to compare with observations-burst and age=15-2=13

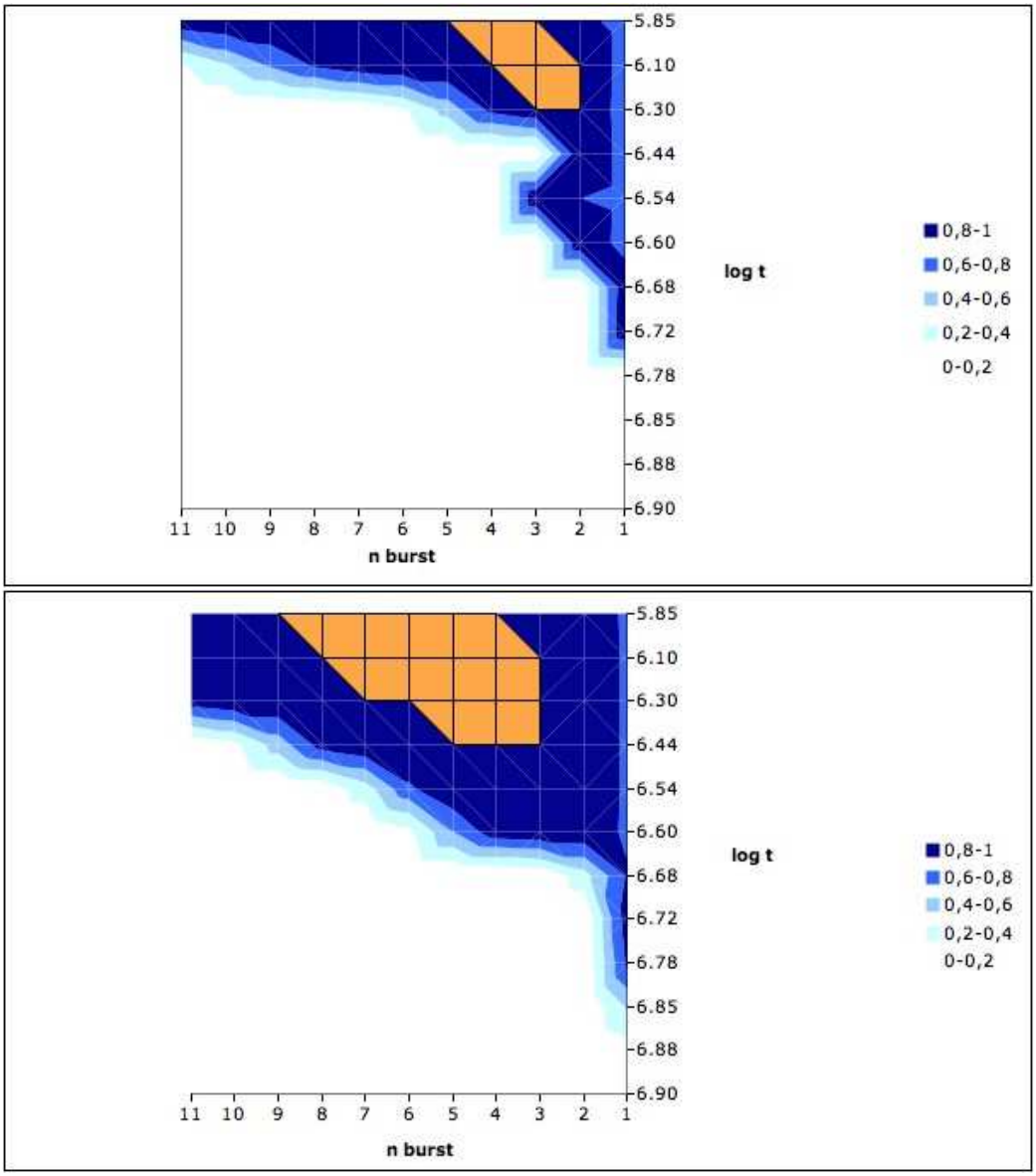

Figure 4.8: Probability distribution for IIZw40 using HAM k=0.65 ϵ=33% (upper panel) and ϵ=10% (lower panel). Orange region indicates the maximum probability zone.

We have used for this study the High Attenuation Models with k=0.65 and both efficiencies, high (33%) and low (10%). These models have been chosen because their bursts show more differences among them than other more attenuated HAM. With these models and the calculations described above, we obtain the results shown in Figures 4.8. According to our model of high efficiency HAM (Figure 4.8, upper panel), IIZw 40 (12+log(O/H)=7.7) could be in the first bursts in its evolution, where emission lines are representative of a not very metallic stellar population. This galaxy shows the highest probability of being in one of the first three bursts of star formation, with an ionizing population less than 2 Myr old (orange zone). There is also a certain probability that this galaxy, in this case the ionizing population being less than 5 Myr old. These probability decreases as the number of the burst, thus, metallicity, increases. In the last bursts, the metallicity is too high, and emission lines produced by such a metallic population can not reproduce the observed values. In the low efficiency model (Figure 4.8, lower panel), the maximum probability is extended along a wider range of bursts. The metallicity does not increase as much as in high efficiency model, and II Zw 40 could then be between its 3rd and 8th burst of star formation. It is also probable to find ionizing populations 6 Myr old in the first bursts and older than 2 Myr for the last one.

In Figure 4.9 we show the position of II Zw 40 in the diagnostic diagrams involving the strongest emission lines of the ionizing gas. The agreement with the χ^2-test position of the maximum probability indicates that the oxygen lines have a higher weight in the calculation than other emission lines. [NII] lines are more representative of metallicity, indicating that II Zw 40 has an oxygen abundance intermediate between those provided by our two efficiency models.

We have seen in the Figure 4.9 (also in other diagnostic diagrams) that single-valued relation between metallicity and emission lines ratios does not exist, being possible to obtain the same metallicity for an object in two different possitions in the emission line diagnostic diagram. This means that there are several possible star formation histories which give the same results, which is the 'quid' of the problem: the study of the ionizing populations is not enough to know the whole star formation history of the galaxy. The underlying population can influence two of the parameters used in this study, EW(H_β) and the continuum ratio. However, most of the parameters which have been compared with the observations are emission lines, produced by the ionizing population. Thus, the wheight of the ionizing population is higher than the weight of the underlying stars and more information, or a similar study for stellar continuum characteristics, is needed in order to obtain the probability distribution for the ages of the non ionizing population.

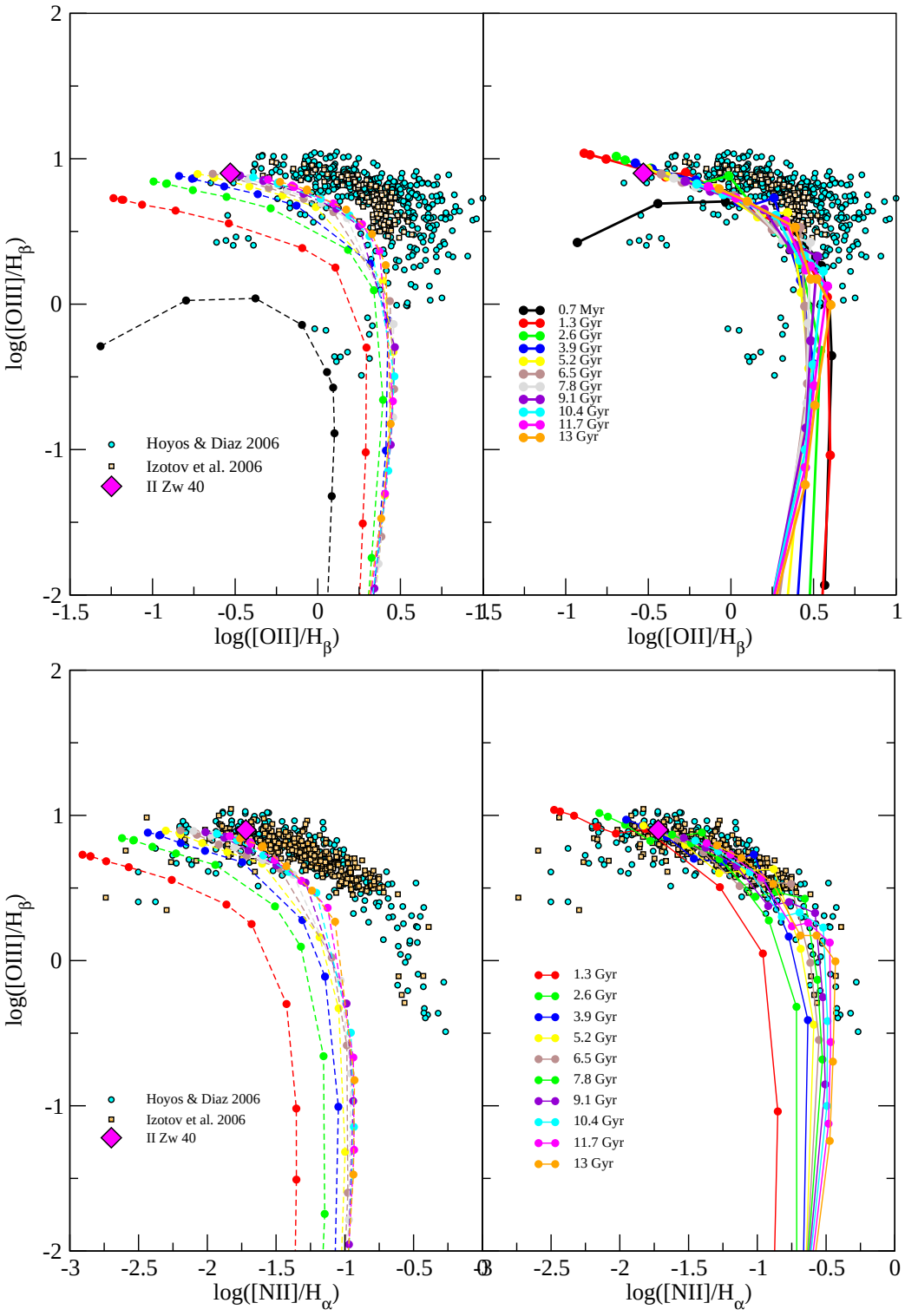

Figure 4.9: Diagnostic diagram involving the more intense and representative lines including IIZw40. HAM k=0.65.

Parameter	Value	Error
N/H	20×10^{-7}	1×10^{-7}
O/H	500×10^{-7}	6×10^{-7}
S/H	140×10^{-7}	50×10^{-7}
(V-I)	0.020	0.01
(R-I)	-0.230	0.01

Table 4.3: Abundance ratios and colours of II Zw 40 (Díaz et al., 2007; Telles & Terlevich, 1997, respectively)

We have done the same χ^2 test for some abundance ratios (O/H, N/H and S/H) and some colours (V-I and R-I taken as luminosity ratios L_V/L_i and L_R/L_i), for the low attenuation HAM in order to restrict the maximum probability zone. In the first place, we have done the test for each set of data (abundances, colours and emission lines) separately , and once this is done, we have put all the parameters together to make one test using the whole information from the observed galaxy.

In Figure 4.10 we can see the results for the three tests made separately. The upper panel is the result of the emission line test, discussed before. The chemical abundance ratios give us information about the star formation and the enrichment history. We have obtained that the galaxy is in its third burst of star formation with a very narrow maximum likelihood zone, as shown in the center panel. Although the metallicity in this model rises more slowly than in the high efficiency ones, the values are well reproduced by these burst and age.

The colours, taken as luminosity ratios, have been taken form Telles & Terlevich (1997), and we have chosen the total colours, which include the stellar continuum, the contribution of the emission lines and the host galaxy. In this case, the maximum likelihood zone is around the third burst too (bottom panel). However, due to the inclussion of the contribution of the emission lines to the broad band colours, this zone is shifted to younger bursts, indicating that the ionizing population can be reproduced by more bursts besides the third one (from the third to the eighth), as we have seen in the emission line test above.

When we make the same study taking all the parameters together, we obtain the result shown in Figure 4.11. We have used 21 comparison parameters (13 emission line ratios, EW(H_β), the adjacent continuum ratio,I_{3730}/I_{5010}, 3 abundance ratios and 3 colours) which have been normalized as χ^2-$\cdot\chi^2_{min}$ divided by the degrees of freedom of each parameter set. The total probability distribution have been made with the sum of these

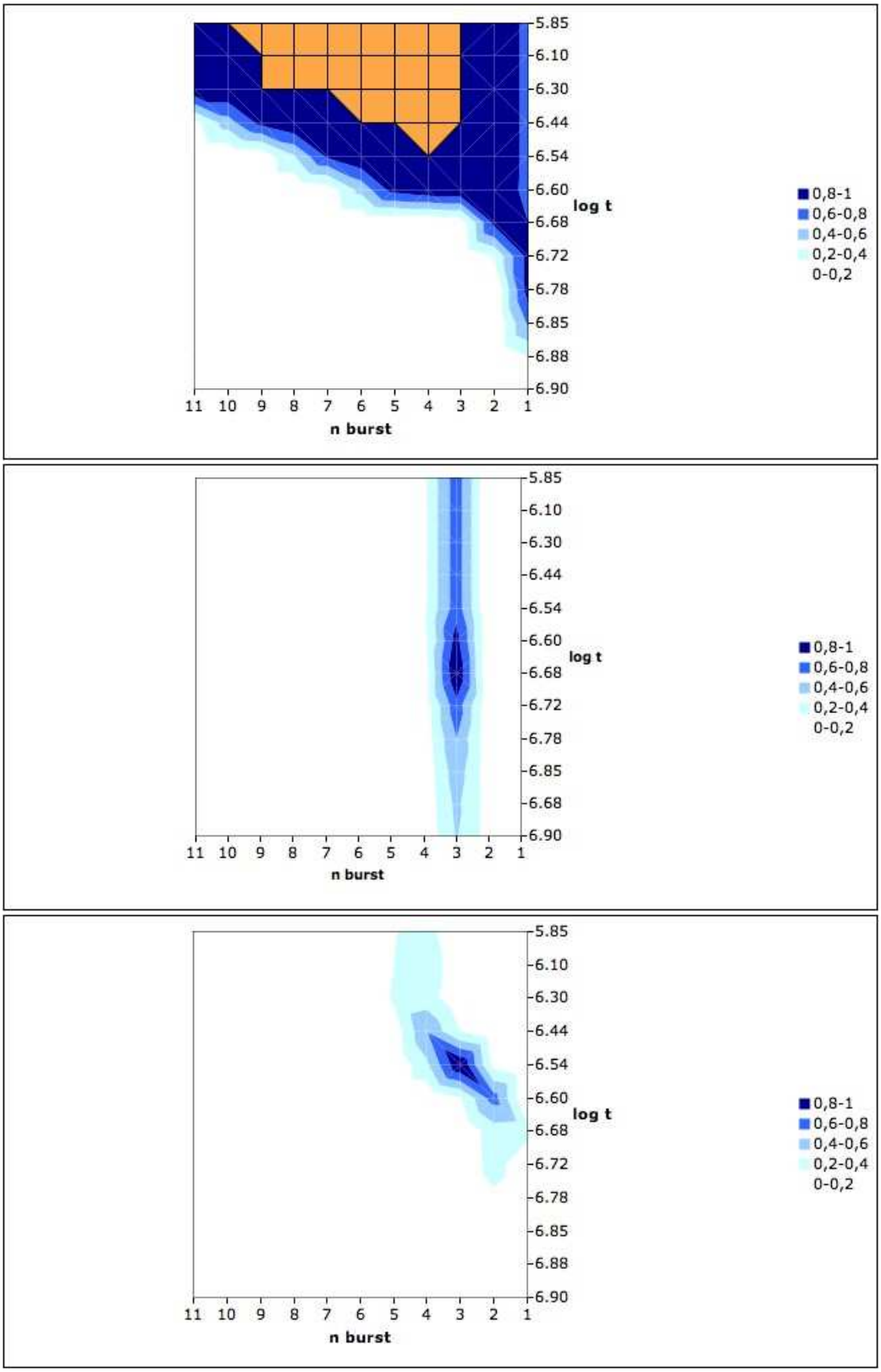

Figure 4.10: Probability distribution for IIZw40 using HAM k=0.65 ϵ=10% for emission lines (upper panel), the chemical abundace ratios (center panel) and total colours (lower panel)

normalized χ^2 and a total number of degrees of freedom taken as the sum of the degrees of freedom of each set (13+1+1). The underlying component has more weight than the current stellar generation which extends the maximum probability region to a large number of bursts. According to this figure, this galaxy is on its third burst of star formation, indicating that the underlying population could have an average age of 2.6 Gyr, its current stellar ionizing population is 3 Myr old, and the total mass in stars is about 17×10^6 $M_\odot$ with the mass of the ionizing population 3.77×10^6 $M_\odot$. These result are in very good agreement with the findings of Vanzi et al. (1996): the age of the ionizing population is 4 Myr, the total mass in stars is 20×10^6 $M_\odot$ and no star formation have taken place in the last 10^9 yr, being the mass of the underlying population about one order of magnitud higher than the mass of the current ionizing stellar population.

Some preliminary results have been obtained for other galaxies whose colour-magnitud diagrams of their resolved stellar populations and their stellar ages are known. We have made a similar work with the NW component of I Zw 18, comparing the emission line intensities and abundances taken from Skillman & Kennicutt (1993) and the integrated colours from Izotov et al. (1999). The test has been made with a model with low initial efficiency of 10%, an attenuation factor of k=0.5, and 50 Myr of inter-burst time. We have used a model with less inter-burst time than before due to the lower metal content of I Zw 18 (12+log(O/H)=7.17 Skillman & Kennicutt, 1993). This model is still very efficient and its bursts are too strong and separated to be compared with a galaxy like I Zw 18. Nevertheless, we see in Figure 4.12 that, according to this model, the maximum likelihood zone is very extended also along the first burst, that can be interpreted as the existence of a mixed population of very young and intermediate age stars. The ionizing population could be 4 Myr old and the underlying population has an age of $\sim$100 Myr. However, in order to make studies of galaxies with such a low oxygen abundance, we need models of lower initial efficiency and more moderate star formation to increase the metallicity more slowly and have enough resolution to date the underlying population. As we have said in this work, low metallicity galaxies are better reproduced by models with a low and continuous star formation. With coeval bursts, all stars of all masses are formed at the same time and metallicity grows up quickly.

Finally, for SBS 1415+437 (12+log(O/H)=7.61), another well studied galaxy we have used the same model in the II Zw 40 study, and the observational data taken from Guseva et al. (2003). We have obtained that the ionizing stellar population is 4-4.7 Myr old, while the underlying population could be between 1.3 to 2.6 Gyr (Figure 4.13). This results agree with those given by Aloisi et al. (2005), who obtain that the age of the evolved

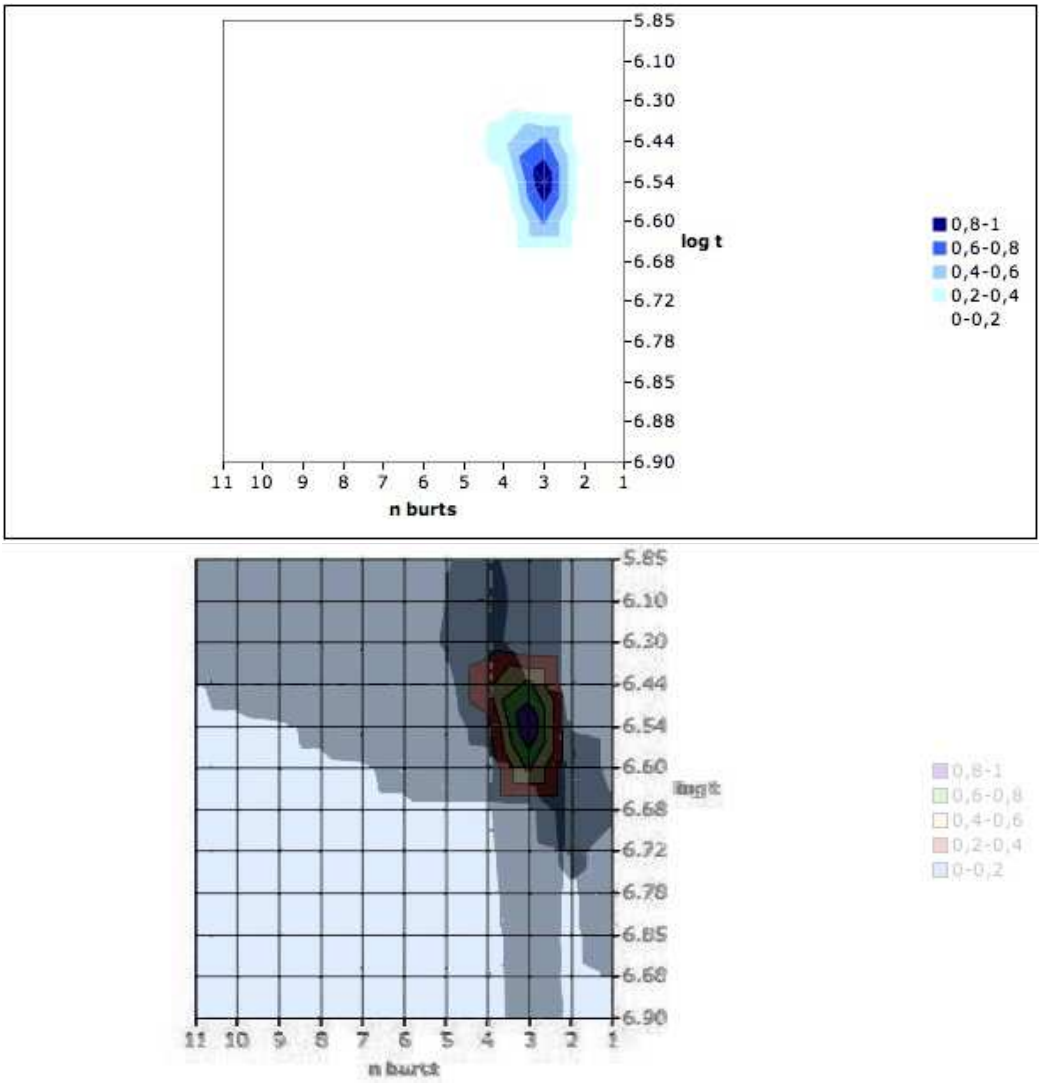

Figure 4.11: Probability distribution for IIZw40 using HAM k=0.65 ϵ=10% for the chemical abundace ratio, total colours and emission lines compared simultaneously. Lower panel is the resulting zone made by the superpossed three χ^2-tests of Figure 4.10, which is the intersection of the three maximum probability zone. It can bee seen that the two figures agree.

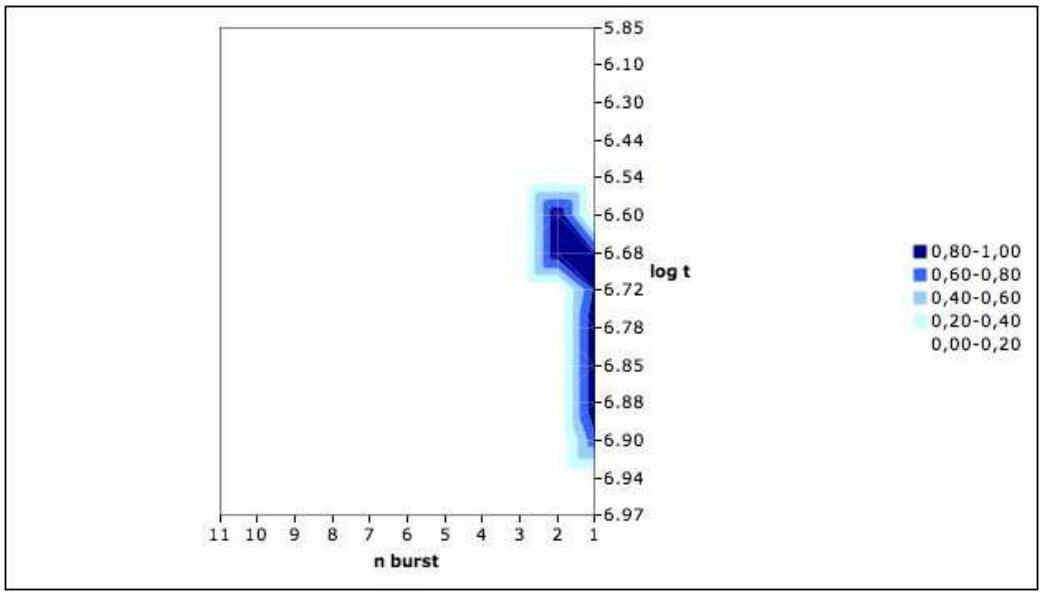

Figure 4.12: Probability distribution for IZw18 using HAM k=0.5 ϵ=10% and Δt=0.05 Gyr. An age from 4 Myr is obtained for the ionizing population and of the order of 100 Myr for the old stellar component.

component is $>$ 1.3 Gyr, and also with the work of Yakobchuk (2008), who obtain an age of no more that 2 Gyr for the old component, and ages younger than 5 Myr for the young stellar population.

Besides the acceptable results obtained, we do not consider this kind study of the underlying population complete at all. More data both in abundances and colours in order to have enough information and the same weight for each galaxy component is needed. Also more accurate models to reproduce very low metallicity galaxies. However, this very preliminary example demonstrates how a complete set of data may provide the whole information about the evolutionary scenario of a given galaxy, and that with this simple method is, in principle, possible to get an intial guess about the age of the galaxy and its stellar content.

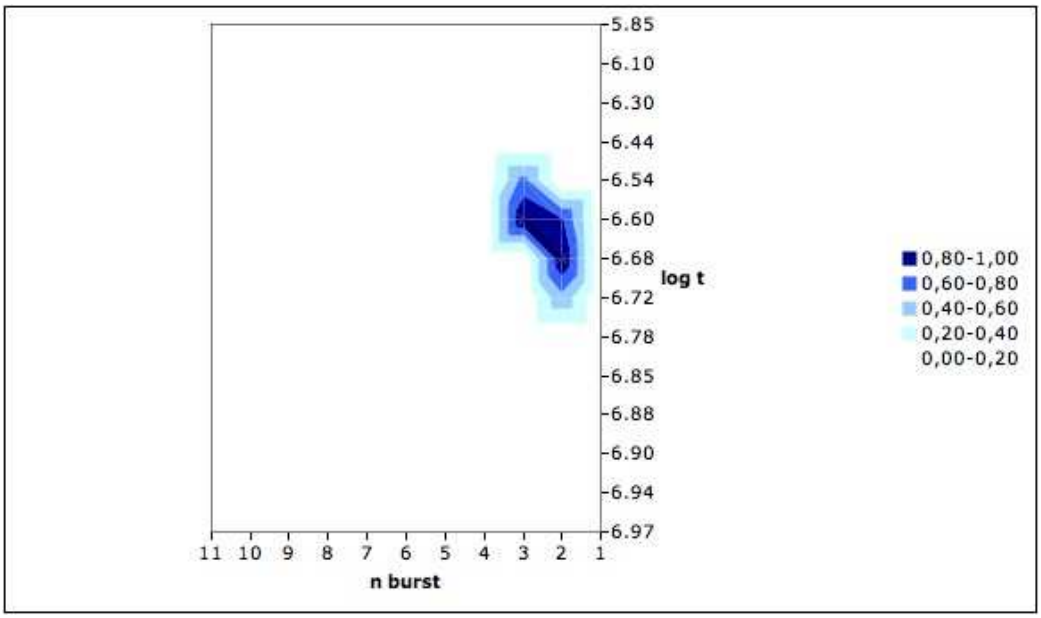

Figure 4.13: Probability distribution for SBS 1415+437 using HAM k=0.65 ϵ=10%. The age obtained of the ionizing population is from 4 to 4.7 Myr, and for the underlying population from 1.3 to 2.6 Gyr.

Chapter 5

Summary and final conclusions.

Summary.

HII galaxies are a subset of BCDs characterized by showing low metallicities and strong emission lines produced by the massive stars created in a recent burst of star formation. These two characteristics do not mean that HII galaxies are real young systems, but they are experiencing a current star formation episode that could not rather be the first one.

Observations show clear evidences about the existence of an old, non-ionizing population, formed previously in most of the galaxies. Some studies find not only evolved populations of stars with ages older than 1 Gyr, they also find evidences for intermediate populations of AGB stars with ages between 10^8 and 10^9 yr, giving rise to different hypotheses about the star-formation processes and scenarios for this type of galaxies.

The distribution of the equivalent widths of H($_\beta$) shows that only a few HII galaxies have values higher than 150 Å . In addition, a correlation between the EW(H_β) and the continuum colour (U-V) is found for this kind of galaxies: the higher values of the equivalent widths are shown by the bluer galaxies, while the lower values of EW(H_β) correspond to those showing redder colours. This trend can not be reproduced by single stellar populations and is only explained if the ionizing population is overimposed on an older stellar population more evolved to produce a redder (U-V) colour. Another correlation between EW(H_β) and the oxygen abundance exists: the lower values of EW(H_β) correspond to objects with higher abundances, which indicates the presence of more evolved populations in addition to the current one which dominates the light of the galaxy.

Historically, the most common assumption for HII galaxies is that their star formation takes place in a **bursting mode**. It consists in successive

instantaneous star formation bursts interposed between long periods of null or very low star formation activity. If these periods are shorter and bursts are more extended and moderate, we are under a **gasping star formation scenario**. On the contrary, if the star formation is low and moderate during the whole life of the galaxy, and only some sporadic bursts take place, a **continuous star formation scenario** is appealed. These scenarios have not been tested with theoretical models which support the correlations described before. Models that can reproduce simultaneously the data relative to the current ionizing population and the data which give us information about the evolutionary history of the star formation have not been made or applied to this kind of galaxies yet.

The aim of this work has been to develop the adequate technique to make models for these galaxies, studying its viability in the prediction of the observed correlations and then prove if the results under a bursting star formation scenario reproduce the emission lines, continuum colours, equivalent widths and chemical abundances simultaneously.

The models are based on the successive bursts star formation hypothesis. Each galaxy is modelled assuming an initial amount of unprocessed gas of 10^8 $M_\odot$.The evolution is computed along a total duration of 13.2 Gyr during which successive starbursts take place. Since any of the possible scenarios of the star formation histories described show clear evidences to be able to explain the observed data, we also try to check the hypotheses suggested by some authors as more or less continuous, stronger or smoother bursts, ...

In order to do that, we have developed a grid of theoretical models performed by the combination of three tools: a chemical evolution code, an evolutionary synthesis code and a photo-ionization code, all of them previously calibrated (in fact, the evolutionary synthesis results used as inputs for a photoionization code for SSP's have been calibrated againts the HII regions data in this work –see Appendix A). This must be done in a self-consistent way, *i. e.* taking the same assumptions about stellar evolution and nucleosynthesis, and the resulting metallicity in every time step. The chemical evolution code provides the star formation history of the galaxies as well as the time evolution of the abundances in their interstellar medium, that can be confronted with observations. The evolutionary synthesis code provides the spectrophotometric evolution of the integrated stellar population. Finally, the photo-ionization code uses the properties of the ionizing stellar population to calculate the emission line spectra of the ionized gas.

These models have three free input parameters which can be changed to obtain different model results:

1. **Initial Efficiency**. It determines the initial star formation rate (SFR) and the initial metallicity of the gas. It also leads the ionizing gas behaviour: emission lines are determined by the amount of massive stars and the metallicity of the amitting gas. With this parameter we can control the amount of old pristine stars that we are going to find in the next star formation burst underlying populations.

2. **Attenuation of the following bursts**. This parameter determines the evolution of the gas keeping metallicity between the observational data limits. The attenuation controls the strength of the bursts. The more attenuated, the less star formation rate, making the previous stellar generations to have more weight in the total current spectrum, hence modifying the equivalent width and the colours of the continuum.

3. **inter-burst time** The contribution of the underlying population can be determined by the time between bursts too. inter-burst periods are the quiescent phases in the BCD . The shorter the inter-burst time, the younger the intermediate population stars which are part of the host BCD galaxy, that is, all those generations of stars which have not ionizing stars, showing ages of more than 10^7 yr.

These three parameters determine the star formation which can be adjusted in order to extrapolate to any other kind of star formation scenario. To manage a gasping or continuous star formation it is necessary to reduce the intensity of the bursts, both with the initial efficiency and with the attenuation, at the same time we reduce the inter-bursts time to reproduce the characteristic quiescent periods of each star formatio scenario. Under a continuous star formation, an extremelly low star formatio rate is needed, as well as a minimum inter-burst time, in order to have enough gas to form stars during the galaxy lifetime. On the other hand, the different characteristics shown by the star formation histories can also be due to that we are observing the same objects in different evolutionary stages, that is, just during the burst, in the post-burst phase or in the inter-burst periods.

Conclusions.

We have computed models with different starbursting properties: high and low initial star formation efficiency, equal strenght and attenuated bursts, as well as several values of the attenuation factors and time between bursts.

In order to reproduce the observable characteristics of HII galaxies we only have to adjust the three input parameters. From the comparison of models and data we conclude:

1. The initial efficiency must be between 0.10 and 0.60 (more probably 0.50, depending on the other input parameters) in order to produce a first burst which provides oxygen abundances inside the observed values.

2. It is necessary to attenuate the following bursts in order to keep the gas chemical properties within the limits of the observational data. Without this attenuation, the star formation rate and the oxygen abundances are too high and do not reproduce the local HII galaxies observed values.

3. Most HII galaxies require the contribution of previous stellar generations to explain the correlations shown by their continuum properties. The chemical and spectro- photometric properties, (equivalent widths and colours) obtained by our models reproduce these correlations if the contribution of the underlying population to the total continuum is higher than the contribution of the current burst of star formation which dominates the observed spectrum. This is fitted by adjusting the attenuation factor, once the initial efficiency is fixed.

4. There are two possibilities to reproduce the properties of galaxies with intense high excitation emission lines while keeping the SFR and oxygen abundances within the range of the observations: a) A high initial efficiency with a strong attenuation (high ϵ and low k) or b) An interburst time shorter than 1.3 Gyr and longer than 100 Myr. With shorter periods than 100 Myr the underlying continuum is too blue and its contribution to the colour do not reproduce the trend shown by HII galaxies. The three model parameters can take the values listed in Table 5.2.

5. With our models we are able to compute the stellar continuum colours as well as the continuum colours contaminated with the emission lines, that is, the broad band colours which are not corrected from the contribution of the more intense emission lines. This contribution makes the colours to be shifted almost perpendicullary to the stellar continuum ones, specially at early ages during the first bursts of star formation, where the emission lines are more intense. The contamination of the continuum by the emission lines can make the observed galaxies appear younger that they really are and can hide the evidence for an underlying old population.

6. If we consider that the different star formation scenarios correspond to different phases in the life of a single galaxy, our models are able to

Initial Efficiency (ϵ)	Attenuation factor (k)	inter-burst time (Δt, Gyr)
0.6-0.5	$<$0.2	$\geq$0.1
.	.	.
0.3	$\leq$0.65	$\geq$0.1
.	.	.
.	.	.
.	.	.
0.12-0.10	$\leq$0.95	$\geq$0.1

Table 5.1: Summary of the possible initial efficiencies, attenuation factor and inter-burst time values. For high initial efficiencies, the attenuation factor has to be low. For low initial efficiencies, k can take higher values. Inter-burst time can take any value longer than 100 Myr.

reproduce the characteristics of each one of these phases by modifiying the model parameters. Considering the BCD phase as the first 10 Myr after a star formation burst, and the quiescent phase as the inter-burst periods, we can reproduce the galaxies both in a high activity and in a post-starburst (or pre-starburst) phase. The main difference between these phases are the existence of emission lines produced by the ionized gas. Their intensity, and their contribution to the total continuum colour, can be modified by the initial efficiency. With the attenuation factor we can produce a more or less reddened stellar continuum due to the contribution of host galaxy, the age of these old stars being determined by the inter-burst time.

Future work.

Much work must still be done to know and understand the star formation histories of BCDs. The first step is to derive the properties of their stellar populations, which is not an easy task in such complex objects. Most of them cannot be resolved into individual stars and the use of evolutionary synthesis models are needed in order to study the integrated properties. The emitted spectrum at any location in the galaxy is the sum of cntributions by: the starbursts, the nebula surrounding the young stars, and the emission of the underlying old stars, as we have seen along this work, all of them possibly affected by dust (an ingredient not taken into account in our models)

It is not easy to enumerate all the things that could be useful for a better understanding and development of this framework, and to improve its application. Basically, there are two possible action fronts for a future work,

obviously, theoretical and observational works. Theoretical work includes improvements in the models and the codes used, and observational work refers to improvements in observational data samples to compare with and to apply our models in order to obtain their star formation history in a more detailed way. Theoretical future work includes:

1. The first, and natural, next step in this work is to assume different star formation scenarios to the ones shown here. Using the same theoretical codes, under the same assumptions, we can make models assuming more or less bursts, different attenuations, different inter-bursts times, allways keeping the values between the observed ranges. A larger number of bursts would imply shorter inter-burst times and more attenuation for metalicity to increase more slowly and consume less amount of gas. More attenuation would imply more efficiency in order to reproduce the upper limits of the HII galaxies, and, different inter-burst time would require to adjust the other two parameters depending on if we want to increase or decrease this phase.

2. The application of our Self-Consistent Evolutionary Model to a particular case according to the lines presented in our preliminary work for II Zw 40 or I Zw 18, is a natural step to follow.

3. More detailed chemical evolution models can be made. For the present work we have used a simplified version of Mollá & Díaz (2005) model. No gas mass outflows or infalls have been included. We have seen in previous sections that bursting chemical evolution models include galactic winds in their computations. In our models it has not been necessary to reproduce the observations, however, in order to apply the code to a particular case, or in order to obtain an specific result, this effect must be taken into account. Galactic winds could make possible to increase the efficiency of the burst without decreasing the attenuation, hence reproducing less metallic galaxies and showing strong emission lines for more time, or even gas poor galaxies, whose gas could have been lost, with a new adjustment of the parameters of our model.

4. Photoionization codes could be improved too with the use of more complicated geometries for the ionized cloud, the use of a non constant density, a filling factor not equal to 1, etc.

   We could make the models using radial zones instead of one integrated zone. This new approach could allow us to make surface photometric analysis and that could then be compared with observations in order to

study the properties of the host galaxies, or extensions of HII galaxies, and the non ionizing underlying populations. This would require new assumptions in the three theoretical codes used.

Observational work must involve some points:

1. The most important need to complete this work is the obtenction of an homogeneous sample that can provide chemical, spectral and photometric data with spatial resolution at the same time, that its, in the same observation.

   Two dimensional spectroscopy (IFS) allows to collect simultaneously the spectra of many different regions of an extended object, combining photometry and spectroscopy in the same data set. Each single exposure contains spatial and spectral information about all SF regions and also the low surface brightness component. Several works have already been done with IFS (Kehrig et al., 2006; García-Lorenzo et al., 2008) but the sample is still short.

2. More observations in the near IR is needed in order to obtain more accurate information about the underlying populations,

3. Observations at moderate or intermediate redshift woul provide the opportunity to compare our model predictions back in time in order to study the evolutionary nexus among different dwarf galaxies, and study the properties of their counterparts at these redshifts as we have done with LCBGs and HII galaxies.

5.1 Resumen y conclusiones.

Resumen.

Las galaxias HII son un subconjunto de Galaxias Compactas Azules (GCA), que se caracterizan por sus bajas metalicidades y líneas de emisión estrechas e intensas producidas por las estrellas masivas creadas en un brote reciente de formación estelar. Estas dos características no significan que las galaxias sean realmente jóvenes, sino que están experimentando un brote de formación actual pero que podría no ser el primero.

Las observaciones muestran claras evidencias de la existencia de una población vieja no ionizante, formada previamente, en la mayoría de las galaxias. Algunos estudios encuentran no solo poblaciones viejas de más de 1 Ga, sino que también evidencias de poblaciones intermedias de estrellas AGB con edades entre 10^8 y 10^9 años. Esto ha dado lugar a diferentes hipótesis sobre procesos y escenarios de formación estelar para este tipo de galaxias.

La distribución de anchuras equivalentes de la línea de H_β muestra que solamente unas pocas galaxias HII tienen valores mayores de 150 ÅÀdemás existe una correlación entre la EW(H_β) y el color del continuo (U-V): los valores más altos de EW(H_β) son mostrados por las galaxias más azules, mientras que los valores más bajos son característicos de galaxias más enrojecidas. Esta tendencia no puede ser reproducida mediante poblaciones estalres símples y solamente es explicada si la población ionizante se encuentra sobre una población estelar más evolucionada que produce los colores más rojos de (U-V). Otra correlación entre EW(H_β) y la abundancia de oxígeno muestra que los valores más bajos de EW(H_β corresponden a objetos con mayores abundancias, lo que indicaría la presencia de poblaciones más evolucionadas además de la actual que domina la luz de la galaxia.

Históricamente, lo más común ha sido considerar que la formación estelar en este tipo de galaxias tiene lugar en forma de brotes. Este proceso consiste en brotes de formación estelar instantáneos sucesivos, intercalados con largos periodos de nula o muy baja actividad. Si esos periodos son más cortos y los brotes son más extensos y moderados, estaríamos bajo un **escenario formación estelar "jadeante" (gasping)**. Por el contrario, si la formación estelar es nula o moderada durante la mayor parte de la vida de la galaxia, y solamente tienen lugar brotes esporádicos, estamos bajo un **escenario de formación estelar continua.** Estos escenarios no han sido probados con modelos que sustenten las correlaciones descritas anteriormente, y modelos que reproduzcan simultáneamente los datos relativos a la población ionizante

y la historia evolutiva de formación estelar no han sido desarollados, o al menos aplicados a este tipo de galaxias.

El propósito de este trabajo ha sido desarrollar la técnica adecada para hacer modelos para esas galaxias, estudiando primero su viabilidad en la predicción de las correlaciones observadas y probando que los resultados, bajo un escenario de brotes de formación estelar, reprduce las lineas de emisión, los colores del continuo, las anchuras equivalentes y las abundancias químicas de manera simultánea.

Los modelos se basan en la hipótesis de formación estelar con brotes instantáneos sucesivos. Cada galaxia es modelizada considerando una cierta cantidad de gas sin procesar de 10^8 $M_\odot$. Se deja evolucionar a lo largo de 13.2 Ga durante los cuales tienen lugar varios de estos brotes. Como ninguno de los tres escenarios descritos muestran claras evidencias de ser los adecuados para reproducir todos los datos observacionales, también hemos hecho modelos con brotes más o menos seguidos, más fuertes y más suaves, etc. Para ello hemos desarrollado un conjunto de modelos teóricos mediante la combinación de tres herramientas: un código de evolución química, un código de síntesis evolutiva y un código de fotoionización, todos ellos previamente calibrados (De hecho, el código de síntesis evolutiva usado como entrada para el modelo de fotoionización ha sido calibrado con datos de regiones HII en el Apéndice de este mismo trabajo). Todo esto debe ser realizado de manera autoconsistente, es decir, con las mismas consideraciones sobre evolución estelar, nucleosíntesis, y con un resultado de la metalicidad para cada paso de tiempo. El código de evolución química nos da la historia de formación estelar de las galaxias, así como la evolución de las abundancias químicas en le medio interestelar, que puede ser comparado con las observaciones. El código de síntesis evolutiva nos proporciona la evolución espectrofotométrica de la población estelar integrada. Finalmente, el código de fotoionización usa las propiedades de la población ionizante para calcular el espectro de líneas de emisión del gas ionizado.

Estos modelos tienen tres parámetros de entrada, los cuales tenemos que modificar para obtener diferentes efectos en los resultados:

1. **Eficiencia Inicial**. Determina la tasa inicial de formación estelar y la metalicidad inicial del gas. También es la responsable del comportamiento del gas ionizado: las líneas de emisión son determinadas por la cantidad de estrellas masivas y la metalicidad del gas usado para formarlas. Con este parámetro controlamos la cantidad de estrellas viejas primigenias que vamos a encontrar cuando estudiemos la población subyacente del siguiente brote de formación estelar.

2. **Atenuación de los brotes siguientes**. Este parámetro determina

la evolución del gas, manteniédolo dentro de los límites de las observaciones. La atenuación es la que da la fuerza del brote. Cuanto más atenuado sea el brote, menor será la tasa de formación estelar, haciendo que las generaciones de estrellas previas tengan más peso en el espctro total actual, modificando las anchuras equivalentes y los colores del continuo.

3. **Tiempo entre brotes**. La contribucuón de la población subyacente puede ser determinada por este parámetro también. Los periodos entre brotes son las fases de quiescencia de las GCA, es decir, todas las generaciones que no tienen estrellas ionizantes, mostrando edades de más de 10 Ma.

Estos tres parámetros determinan la formación estelar que puede ser ajustada para extrapolar a cualquier otro escenario de formación estelar. Para conseguir una formación estelar jadeante (gasping) o una formación estelar continua, es necesario reducir la intensidad de los brotes, tanto con la eficiencia inicial como con la atenuación, al mismo tiempo que reducimos el espacio entre brotes para reproducir los periodos de quiescencia de cada escenario. Para una formación estelar continua se necesita una tasa de formación estelar extremadamente baja y un especio entre brotes mínimo para tener suficiente gas para formar estrellas durante la vida de la galaxia. Por otro lado, las diferentes características de las historias de formación estelar mostradas pueden ser debidas a que estemos observando un objecto en diferentes estados evolutivos, esto es, durante el brote de formación estelar, justo después del brote o en el periodo entre brotes.

Conclusiones.

Teniendo en cuenta los efectos que producen los parámetros de entrada, hemos reaizado modelos con diferentes propiedades de los brotes de formación estelar: alta y baja eficiencia inicial, brotes sucesivos de la misma intensidad y atenuados, así como diferentes factores de atenuación y tiempo entre brotes.

Para reproducir las características observacionales de las galaxias HII, solamente tenemos que ajustar cada uno de los tres parámetros de entrada. De la comparación con los datos de las observaciones podemos concluir:

1. La eficiencia inicial debe estar entre 0.10 y 0.60 (siendo más adecuada una eficiencia máxima de 0.50, dependiendo de los otros parámetros de entrada) para producir una abundancia de oxígeno en el primer brote de formación estelar que entre dentro de los límites de los valores observados.

2. Es necesario atenuar los brotes de formación estelar para mantener las propiedades químicas del gas dentro de los límites de las observaciones. Sin esa atenuación, la tasa de formación estelar y la abundancia de oxígeno muy altas, lo que no reproduce los valores de las galaxias HII locales observadas.

3. La mayor parte de las galaxias HII requieren una contribución de las generaciones de estrellas previas a la actual para explicar las correlaciones descritas en este trabajo. Las propiedades químicas y espectrofotométricas, anchuras equivalentes y los colores obtenidos por nuestros modelos reproducen dichas correlaciones si la contribución de la población subyacente al continuo total es mayor que la contribución del brote actual de formación estelar que domina el espectro observado. En nuestros modelos esto es ajustado mediante el factor de atenuación, una vez fijada la eficiencia inicial de formación estelar.

4. Para repoducir las galaxias con líneas intensas de alta excitación, manteniedo la tasa de formación estelar y las abundancias de oxígeno dentro del rango de valores observados, podemos: a) Aumentar la eficiencia inicial de formación estelar y aumentar la atenuación de los brotes (alta ϵ y baja k), o bien B) Tomar tiempos entre brotes menores de 1.3 Ga pero mayores de 100 Ma. Con periodos más cortos de 100 Ma, el continuo subyacente va a ser más azul, y su contribución al continuo total no va a producir un enrojecimiento suficiente para reproducir la tendencia de las galaxias HII. La Tabla 5.2 resume los posibles valores que pueden tomar los parámetros de entrada para las galaxias HII.

Eficiencia Inicial (ϵ)	Factor de Atenuación (k)	Tiempo entre brotes (Δt, Ga)
0.6-0.5	$<$0.2	$\geq$0.1
.	.	.
0.3	$\leq$0.65	$\geq$0.1
.	.	.
.	.	.
.	.	.
0.12-0.10	$\leq$0.95	$\geq$0.1

Table 5.2: Resumen de los posibles valores para la eficiencia inicial, factor de atenuación y tiempo entre brotes. Para eficiencias iniciales altas, el factor de atenuación tiene que ser bajo, y para eficiencias bajas, k puede tomar valores mayores. El periodo entre brotes puede tomar cualquier valor mayor de 100 Ma.

5. Con nuestros modelos podemos computar tanto los colores de los continuos estelares como los colores de los continuos contaminados por las lineas de emisión, es decir, los colores de banda ancha sin corregir de la contribución delas lineas intensas. Este efecto hace que los colores contaminados estén desplazados casi perpendicularmente de los colores del continuo estelar, sobre todo a edades tempranas de los primeros brotes, donde las líneas son más intensas. La contaminación de los colores con las lineas de emisión puede hacer que las galaxias observadas, cuyos colores no han sido corregidos de este efecto, parezcan más jóvenes de lo que realmente son, escondiendo las evidencias de la población subyacente.

6. Considerando que los diferentes escenarios de formación estelar son en realidad diferentes fases en la vida de una misma galaxia, nuestros modelos son capaces de reproducir las características de cada una de estas fases modificando los tres parámetros de entrada según las cantidades observadas que queremos reproducir, ya que éstos determinan el estado de la galaxia en cada una de estas fases de su vida. Si consideramos la fase BCD de la galaxia como los primeros 10 Ma después del brote de formación estelar, y la fase quiescente como los periodos entre brotes, podemos reproducir las galaxias en su fase de máxima actividad y en la fase post-brote (o pre-brote). La principal diferencia entre estas fases es la existencia de lineas de emisión producidas por el gas ionizado. Su intensidad, y su contribución al color del continuo total puede ser modulada por la eficiencia inicial de formación estelar. Con el factor de atenuación podemos producir un mayor o menos enrojecimiento del continuo producido por la galaxia subyacente o anfitriona, siendo la edad de las estrellas de esa población subyacente determinada por el tiempo entre brotes.

Appendix A

PopStar evolutionary synthesis models: optical emission-line spectra from HII regions.

In this Appendix we present the synthetic emission line spectra of the HII regions photoionized by young stellar clusters. The ionizing spectral energy distributions are those obtained by the PopStar code MGVB09 (Mollá, García-Vargas & Bressan, 2009) for six metallicities, including a very low metallicity set, Z=0.0001. These models assume that the radius of an HII regions is the distance at which the ionized gas is deposited by the action of the mechanical energy from the winds and supernovae from the central ionizing young cluster. As we have said before in previous chapters, this approach has the advantage of eliminating the ionization parameter as a free variable in the models, giving it a real meaning since now its value is obtained from the cluster physical properties (mass, age and metallicity) and from the medium chemical characteristics (density and abundances). This set include, for a Salpeter IMF (M_{low}=0.15, M_{up}=100), six metallicities and seven values of the cluster mass, and studies the detailed evolution of the cluster between 0.1 and 5.2 Myr. Two values of the electron density, 10^{-3} and 100 cm^{-3} have been considered for the surrounded medium. We show our results together with a large and homogeneous data set of HII regions whose metallicities have been consistently computed with the model abundances and according to the most appropriate method for each metallicity range. This allows us a fair comparison among models and observations to test our results.

PopStar includes also very low metallicity models, for Z=0.0001, which have not been included in previous similar works. The peculiarity of these models is that the nebular [OIII] lines intensities (at 4363, 4959, 5007 Å) are very low and similar to those coming from very high metallicity models

(solar or super-solar), what has important implications on the metal content determination from diagnostic diagrams.

A.1 Models for HII regions.

We have studied the evolution of a cluster along the first 5 Myr, in 21 steps of time. Older clusters have not ionization photons enough to produce a visible emission line spectrum, although these older clusters are still detectable in H_α images (see García-Vargas et al., 2009, , in preparation, for details about HII regions photometry) The ionizing clusters have been assumed to form in a single burst with different masses. Seven values of the total cluster mass have been adopted for each metallicity: 0.12, 0.20, 0.40, 0.60, 1.00, 1.50 and 2.00×10^5 $M_\odot$. This mass range provides the observed number of ionizing photons of most of medium to large extragalactic HII regions. We have used in all the cases the SEDs described in the previous section as the ionizing spectra of the HII regions.

In order to obtain the emission line spectrum of the modeled HII regions for different metallicities, the photoionization code CLOUDY (Ferland et al., 1998) has been used. The gas is assumed to be ionized by the massive stars of the young cluster. As the ionizing spectra of the HII regions we have taken the SEDs from the evolutionary synthesis models from Mollá, García-Vargas & Bressan (2009), as we have explained in the above section.

The shape of the ionizing continuum, the number of ionizing photons, Q(H), and the HII region radius, R_s, set by the action of the cluster mechanical energy, come directly from the physical ionizing cluster parameters: mass, age and metallicity.

The chemical composition of the gas and its spatial distribution, assuming a given geometry, together with the medium density are used as inputs for the photoionization code. It is assumed that both, the cluster and the surrounding gas have the same chemical composition. The solar abundances are taken from Grevesse & Sauval (1998). The use of these solar abundances implies that $Z_\odot = 0.017$, thus, Z = 0.02 of our models does not correspond to the solar value but to 1.17 $Z_\odot$. [1] Solar abundances are summarized in Table A.1, Column 2. Some refractary elements, Na, Al, Si, Ca, Fe and Ni, must be depleted, due to the presence of dust grains mixed with the ionized gas which can affect to the UV photons absortion and decrease the electronic

[1] Asplund et al. (2005) have obtained lower abundances that lead to a value $Z_\odot = 0.012$. However, these new determinations are still questioned by some authors (Bahcall et al., 2005; Drake & Testa, 2005; Antia & Basu, 2005) because they do not fit the helioseismological constraints.

Table A.1: Abundances, $logX/H$ used in the models (Grevesse & Sauval, 1998).

El.	solar	solar	0.0001	0.0004	0.004	0.008	0.02	0.05
					depleted			
He	-1.09	-1.09	-1.24	-1.24	-1.20	-1.16	-1.07	-0.90
C	-3.48	-3.48	-5.71	-5.11	-4.11	-3.81	-3.41	-3.01
N	-4.08	-3.96	-6.19	-5.59	-4.59	-4.29	-3.89	-3.49
O	-3.17	-3.18	-5.41	-4.81	-3.81	-3.51	-3.11	-2.71
Ne	-3.92	-3.92	-6.15	-5.55	-4.55	-4.25	-3.85	-3.45
Na	-5.67	-6.67	-8.90	-8.30	-7.30	-7.00	-6.60	-6.20
Mg	-4.42	-5.42	-7.65	-7.05	-6.05	-5.75	-5.35	-4.95
Al	-5.53	-6.53	-8.76	-8.16	-7.16	-6.86	-6.46	-6.06
Si	-4.45	-4.75	-6.98	-6.38	-5.38	-5.08	-4.68	-4.28
S	-4.67	-4.67	-6.90	-6.30	-5.30	-5.00	-4.60	-4.20
Ar	-5.60	-5.60	-7.83	-7.23	-6.23	-5.93	-5.53	-5.13
Ca	-5.64	-6.64	-8.87	-8.27	-7.27	-6.97	-6.57	-6.17
Fe	-4.50	-5.50	-7.73	-7.13	-6.13	-5.83	-5.43	-5.03
Ni	-5.75	-6.75	-8.98	-8.38	-7.38	-7.08	-6.68	-6.28

temperature. The solar depleted abundances according to Garnett et al. (1995) depletion factors are in Column 3. For each metallicity, the element abundances heavier than helium have been scaled by a constant factor, with respect to the hydrogen content, according to the solar depleted abundances, as given in Columns 4 to 8 of the same Table A.1.

The hydrogen density has been considered constant throughout the nebula and equal to the electron density for a complete ionization. We have done models with two different values of n_H, 10 cm^{-3} and 100 cm^{-3} , in order to check the density effect on the emitted spectrum. A density of 10 cm^{-3} is more appropriate for small-medium isolated HII regions while 100 cm^{-3} is more appropriate for modelling HII galaxies, large circumnuclear HII regions, often found around the nuclei of starbursts and AGNs.

Although the constant density hypothesis is not realistic when detailed nebular studies are done, it can be considered representative when the nebula integrated spectrum is analyzed. The ionized gas is assumed to be located in a thin spherical shell at that distance R_s (defined in 2.17) from the ionizing source, considering the approximation of a plane-parallel geometry.

Using the number of ionizing photons, Q(H), the nebula size, R_s, and the hydrogen density, n_H we can obtain the ionization parameter, u, given by:

$$u = \frac{Q(H)}{4\pi c n_H R_s^2} \tag{A.1}$$

where c is the light's speed. With these assumptions, u recovers its physical meaning since it is directly derived from the physical cluster's properties. Then, for a given n_H, each model is computed as a function of the cluster's mass, age and metallicity.

The values of u getting from the parameters of our model set are within the range of the observed values for HII regions.

The models assume that the nebula is ionization bounded. No dust, associated to the molecular H_2 clouds (Panuzzo et al., 2003), has been included in our models. Since the current set of models have been computed for medium to large extragalactic HII regions, whose measured reddening is usually very low and often consistent with the galactic reddening, we have not included dust effects. Only when these models will be used for obscured compact HII regions or for large star forming regions like starbursts galaxies, dust effect should be taken into account.

A.2 Results.

A.2.1 Emission lines.

Once the photoionization code is applied, we obtain for every set of models the emission line spectra of the associated HII region produced by the ionizing cluster. We have represented the evolution of those intense emission lines along the first 5.2 Myr after the cluster formation. After this age no emission line spectrum is obtained due to the lack of enough ionizing photons. We have considered for this study the most important emission lines in the visible spectrum.

Table A.2: Emitted line spectrum from a HII region of mass 4×10^4 and Z=0.008 as a function of cluster parameters for $n_H = 10$ cm^{-3}.

Zmet	*logage* yr	*Mass* $M_\odot$	[*OII*] 3727 Å	[*OIII*] 5007 Å	[*OIII*] 4959 Å	[*OIII*] 4363 Å	[*OI*] 6300 Å	[*NII*] 6584 Å	[*NII*] 6548 Å	[*SII*] 6716 Å
0.008	5.00	4E+4	0.7333	3.4653	1.1513	0.0135	0.0176	0.2067	0.0700	0.1439
0.008	5.48	4E+4	0.7598	3.7440	1.2439	0.0157	0.0191	0.2086	0.0707	0.1518
0.008	5.70	4E+4	0.7777	3.8734	1.2868	0.0168	0.0199	0.2118	0.0718	0.1566
0.008	5.85	4E+4	0.8002	4.0092	1.3320	0.0179	0.0207	0.2154	0.0730	0.1613
0.008	6.00	4E+4	0.8173	3.7708	1.2528	0.0162	0.0206	0.2224	0.0754	0.1630
0.008	6.10	4E+4	0.8216	3.5551	1.1811	0.0148	0.0202	0.2247	0.0761	0.1614
0.008	6.18	4E+4	0.8721	3.4737	1.1541	0.0141	0.0206	0.2353	0.0797	0.1674
0.008	6.24	4E+4	1.0183	3.3336	1.1075	0.0132	0.0196	0.2452	0.0831	0.1718
0.008	6.30	4E+4	1.2726	2.8937	0.9614	0.0107	0.0186	0.2695	0.0913	0.1798
0.008	6.35	4E+4	1.3907	2.4403	0.8107	0.0083	0.0183	0.3040	0.1030	0.1948
0.008	6.40	4E+4	1.6005	1.8277	0.6072	0.0055	0.0168	0.3545	0.1201	0.2165
0.008	6.44	4E+4	1.6845	1.6089	0.5345	0.0046	0.0168	0.3977	0.1348	0.2387
0.008	6.48	4E+4	1.7731	1.2363	0.4107	0.0031	0.0148	0.4701	0.1593	0.2726
0.008	6.51	4E+4	1.4888	1.5149	0.5033	0.0041	0.0203	0.4528	0.1535	0.2898
0.008	6.54	4E+4	1.8269	2.2802	0.7576	0.0082	0.0430	0.5276	0.1788	0.4025
0.008	6.57	4E+4	2.2636	2.5096	0.8337	0.0099	0.0668	0.6802	0.2305	0.5446
0.008	6.60	4E+4	2.8331	2.1881	0.7269	0.0083	0.1096	0.9467	0.3208	0.8051
0.008	6.63	4E+4	2.2526	1.3095	0.4350	0.0037	0.0792	0.8990	0.3046	0.7338
0.008	6.65	4E+4	2.2870	0.8892	0.2954	0.0022	0.0742	0.9855	0.3340	0.8031
0.008	6.68	4E+4	2.5193	0.4779	0.1588	0.0011	0.0759	1.1634	0.3942	0.9595
0.008	6.70	4E+4	2.5274	0.2800	0.0930	0.0000	0.0718	1.2389	0.4198	1.0320
0.008	6.72	4E+4	2.3745	0.1107	0.0368	0.0000	0.0661	1.2597	0.4269	1.1007

Table A.3: (Cont.) Emitted line spectrum from a HII region of mass 4×10^4 and Z=0.008 as a function of cluster parameters for $n_H = 10$ cm^{-3}.

$[SII]$ 6731 Å	$[SIII]$ 6312 Å	$[SIII]$ 9069 Å	$[SIII]$ 9532 Å	$[NeII]$ 3869 Å	HeI 4471 Å	HeI 5836 Å	$HeII$ 4686 Å	H_α 6563 Å	$\log u$	$\log R$ cm
0.1013	0.0138	0.2971	0.7367	0.2536	0.0337	0.0956	0.0000	2.9379	-0.42	19.45
0.1069	0.0147	0.3020	0.7489	0.2786	0.0336	0.0954	0.0000	2.9351	-0.97	19.72
0.1103	0.0153	0.3070	0.7614	0.2905	0.0336	0.0952	0.0000	2.9337	-1.21	19.85
0.1136	0.0159	0.3132	0.7768	0.3029	0.0336	0.0951	0.0000	2.9328	-1.37	19.93
0.1148	0.0155	0.3184	0.7896	0.2855	0.0336	0.0953	0.0000	2.9358	-1.56	20.02
0.1136	0.0149	0.3180	0.7885	0.2692	0.0336	0.0955	0.0000	2.9390	-1.64	20.07
0.1178	0.0151	0.3286	0.8150	0.2639	0.0336	0.0954	0.0000	2.9384	-1.77	20.14
0.1208	0.0159	0.3505	0.8692	0.2509	0.0336	0.0953	0.0000	2.9368	-1.86	20.18
0.1264	0.0160	0.3652	0.9057	0.2080	0.0336	0.0953	0.0000	2.9372	-1.98	20.24
0.1368	0.0148	0.3548	0.8800	0.1684	0.0336	0.0955	0.0000	2.9414	-2.08	20.28
0.1519	0.0135	0.3391	0.8410	0.0968	0.0336	0.0955	0.0000	2.9453	-2.18	20.30
0.1674	0.0129	0.3319	0.8231	0.0825	0.0335	0.0954	0.0000	2.9454	-2.25	20.32
0.1909	0.0116	0.3150	0.7812	0.0580	0.0334	0.0949	0.0000	2.9460	-2.32	20.33
0.2030	0.0107	0.2960	0.7341	0.1019	0.0336	0.0957	0.0000	2.9520	-2.37	20.36
0.2825	0.0144	0.3320	0.8234	0.2274	0.0337	0.0955	0.0028	2.9391	-2.55	20.43
0.3824	0.0163	0.3458	0.8575	0.2943	0.0336	0.0948	0.0113	2.9321	-2.72	20.49
0.5649	0.0156	0.3239	0.8034	0.3339	0.0331	0.0931	0.0347	2.9283	-2.96	20.54
0.5136	0.0099	0.2534	0.6285	0.1979	0.0334	0.0947	0.0139	2.9397	-2.97	20.49
0.5615	0.0081	0.2202	0.5462	0.1423	0.0334	0.0946	0.0049	2.9385	-3.07	20.51
0.6702	0.0066	0.1840	0.4564	0.0843	0.0327	0.0926	0.0024	2.9323	-3.25	20.53
0.7204	0.0055	0.1568	0.3889	0.0554	0.0315	0.0893	0.0028	2.9310	-3.35	20.55
0.7675	0.0000	0.1149	0.2850	0.0244	0.0284	0.0805	0.0000	2.9330	-3.50	20.57

Emission-line evolution.

Figures A.1a) to e) show the evolution with time of H_α Luminosity and several emission line ratios: [OIII]$\lambda\lambda$5007,4959/H_β, [OII]λ3727/H_β, [OII]/[OIII], [OI]λ6300/H_α and [NII]λ6584/H_α for models of a given metallicity, as said in each caption. We have chosen the strongest emission lines to represent the most relevant ionization stages and elements. In each figure we show the evolution up to 5.2 Myr after the star burst. Each colour corresponds to a different cluster mass, from 0.12×10^5 $M_\odot$ to 2×10^5 $M_\odot$, and both density cases, n_H=10 cm^{-3} and n_H=100 cm^{-3}, are represented in the same panel as solid and dashed lines, respectively.

For the lowest abundance models (Z< 0.0001) emission line ratios with oxygen lines are very weak (see the different scale in each metallicity panel) and its evolution is smooth. For higher metallicity cases, the emission lines are intense, increasing with the cluster mass. In the first Myr of the evolution, [OIII] line is intense and then it decreases to rise again at 3-4 Myr, due to the presence of WR stars, that makes the equivalent effective temperature of the cluster to become higher and causes an increasing of the excitation during a short time. The emergence and the duration of the WR features depends on the mass and metallicity of the cluster as discussed in MGVB09. The line [OII]3727Å shows moderate variations with metallicity. As the number of ionizing photons decreases with time, [OII]/H_β ratio grows after 3 Myr of the star formation, being almost constant before that age for low metallicity models. The [OII]/[OIII] ratio is very low for all metallicities at ages lower than 4 Myr. During the first stages of the burst evolution, the ionization is high and the [OIII]λ5007Å line is very intense when compared to [OII]λ3727 Å being the [OII]/[OIII] ratio very low for young regions. Model with Z=0.004 shows more intense oxygen emission lines. The rest of the models, whether higher or lower metallicity, show line ratios below them, being well up, as will be better seen in next sections, when study diagnostic diagrams.

The low ionization line [OI]λ6300Å is an indicator of the presence of strong winds and supernovae (Stasińska & Leitherer, 1996), and therefore, is a burst age indicator. On the basis on the photo-ionization models only, this line increases with cluster age and [O/H] abundance, therefore has larger values for old, evolved and high metallicity HII regions. If we would add shock contributions (not included in our models), the intensity of [OI]λ6300 Å would be even higher.

In Figures A.3 and A.4 we have plotted the resulting emission line sulfur ratios as a function of the burst age, separately from the rest of emission line ratio evolution figures, in order to use them as age constraints. Figure

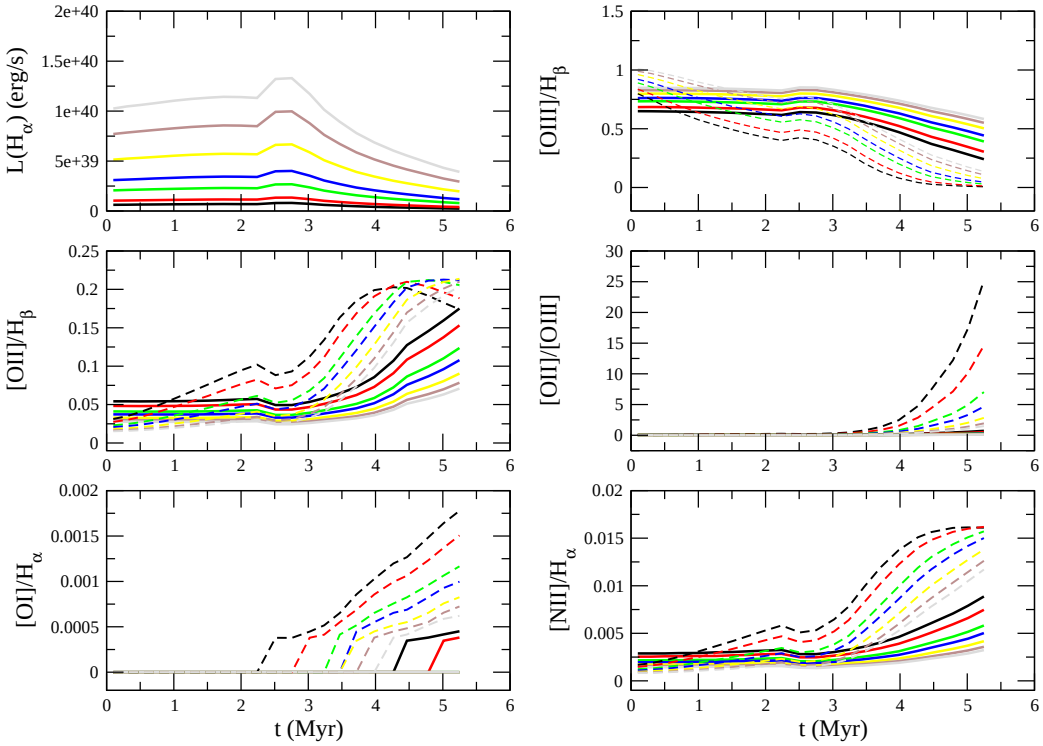

Figure A.1: a). Evolution of the luminosity and five emission line ratios for Z = 0.0001. The ratios are [OIII]/H$_\beta$, [OII]/H$_\beta$, [OII]/[OIII], [OI]/H$_\alpha$ and [NII]/H$_\alpha$. The more appropriate hydrogen recombination line has been chosen to minimize reddening effects. Solid lines correspond to models with $n_H = 10$ cm^{-3} while dotted lines correspond to models with $n_H = 100$ cm^{-3}. Black, red, green, blue, yellow, brown and grey lines correspond to different cluster masses: 0.12, 0.20, 0.40, 0.60, 1.00, 1.50 and 2.00 $\times$ 10^5 M, respectively.

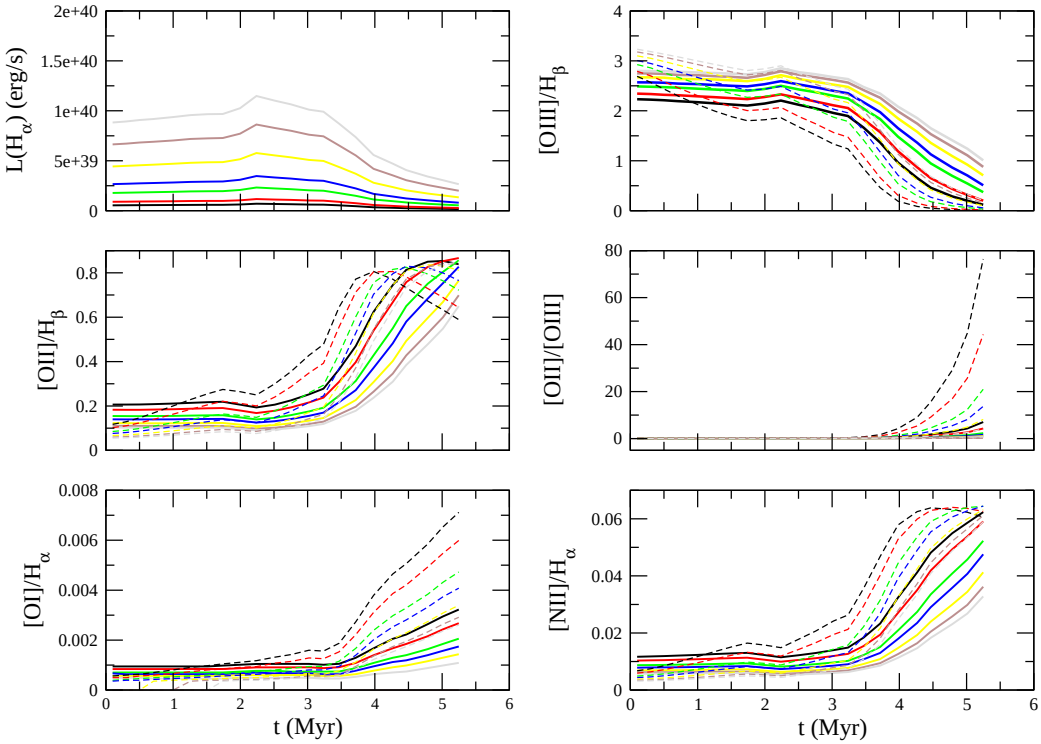

Figure A.2: b).Evolution of emission lines for Z = 0.0004. Different colours and line code have the same meaning than in Fig. A.1a.

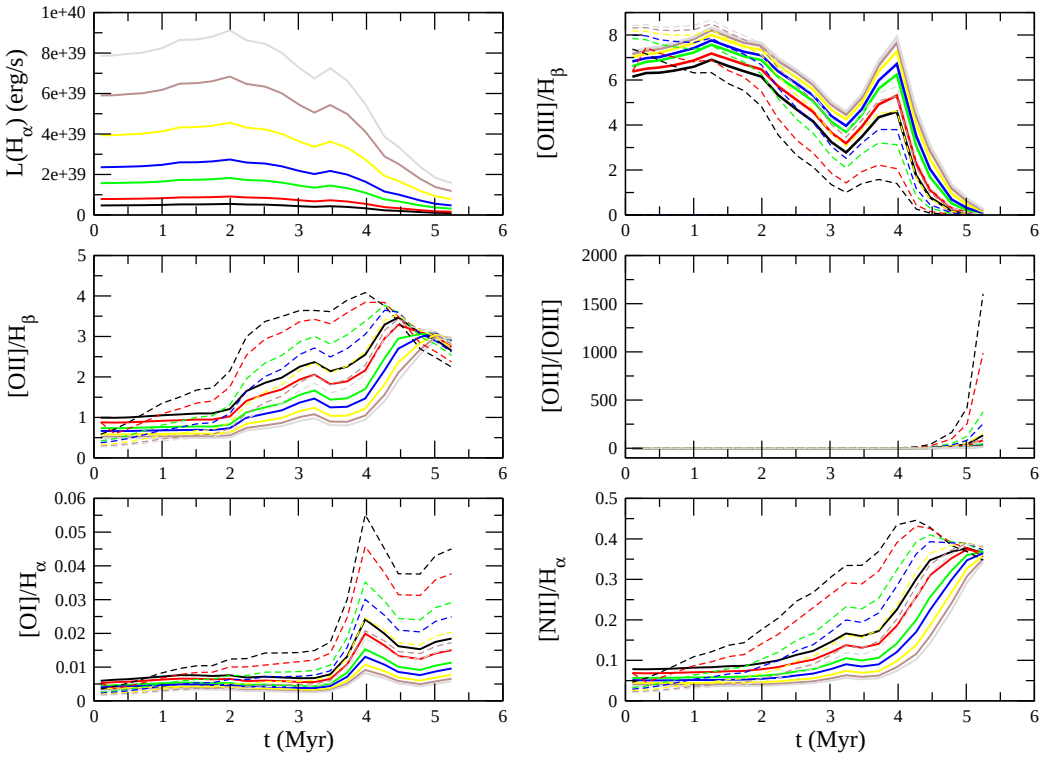

Figure A.2: c). Evolution of emission lines for Z = 0.004. Different colours and line code have the same meaning than in Fig. A.1a.

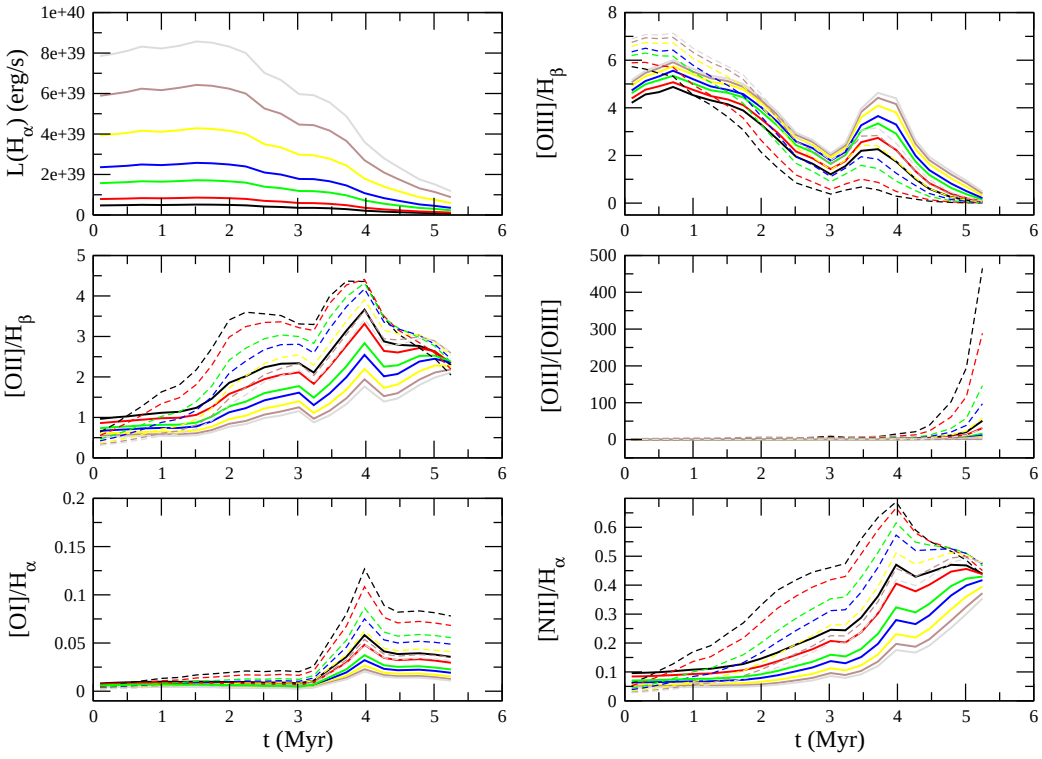

Figure A.2: d). Evolution of emission lines for Z = 0.008. Different colours and line code have the same meaning than in Fig. A.1a.

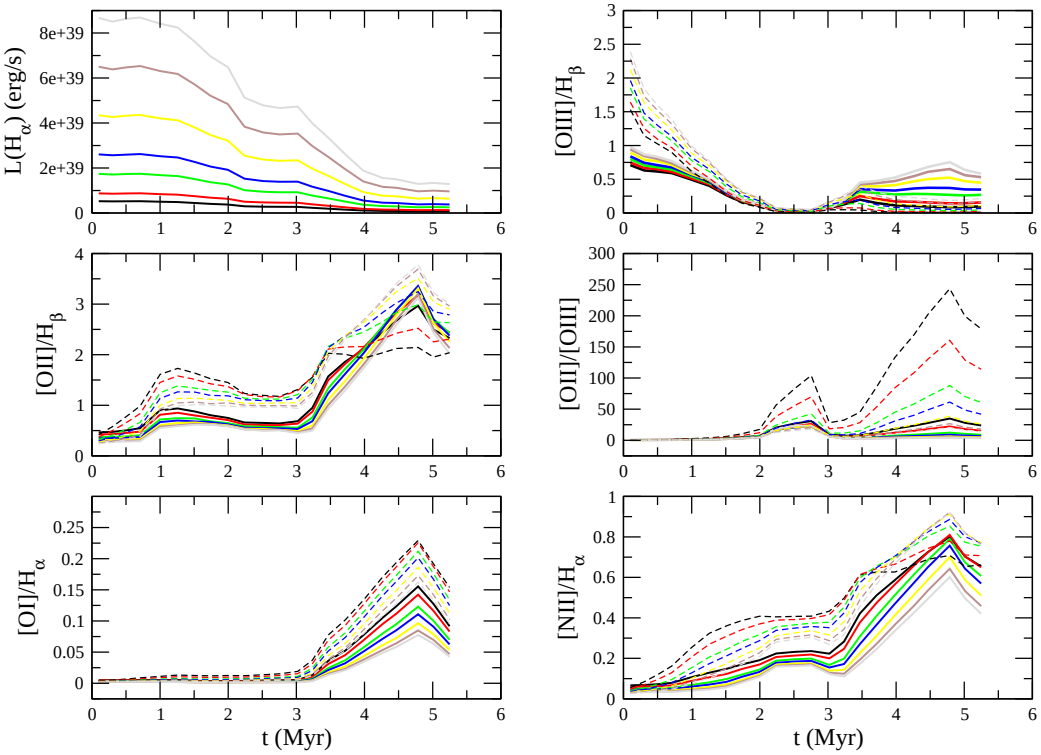

Figure A.2: e). Evolution of emission lines for Z = 0.02. Different colours and line code have the same meaning than in Fig. A.1a.

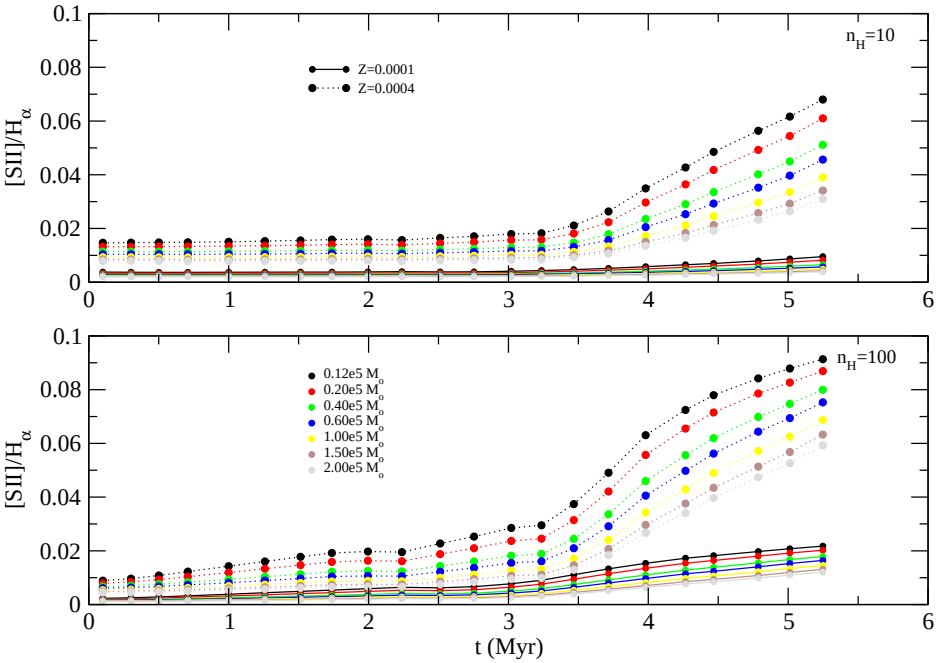

Figure A.3: Ratio [SII]$\lambda\lambda$6717,31/ *vs* time (in Myr) for low metallicities (Z=0.0001 and Z=0.0004) and all masses. Solid lines join models for Z=0.0001 while dotted lines join models for Z=0.0004. Different colours correspond to different values of the cluster mass. Models with values of $n_H = 10$ cm^{-3} have been plotted in the upper panel while models with $n_H = 100$ cm^{-3} have been plotted in the lower one.

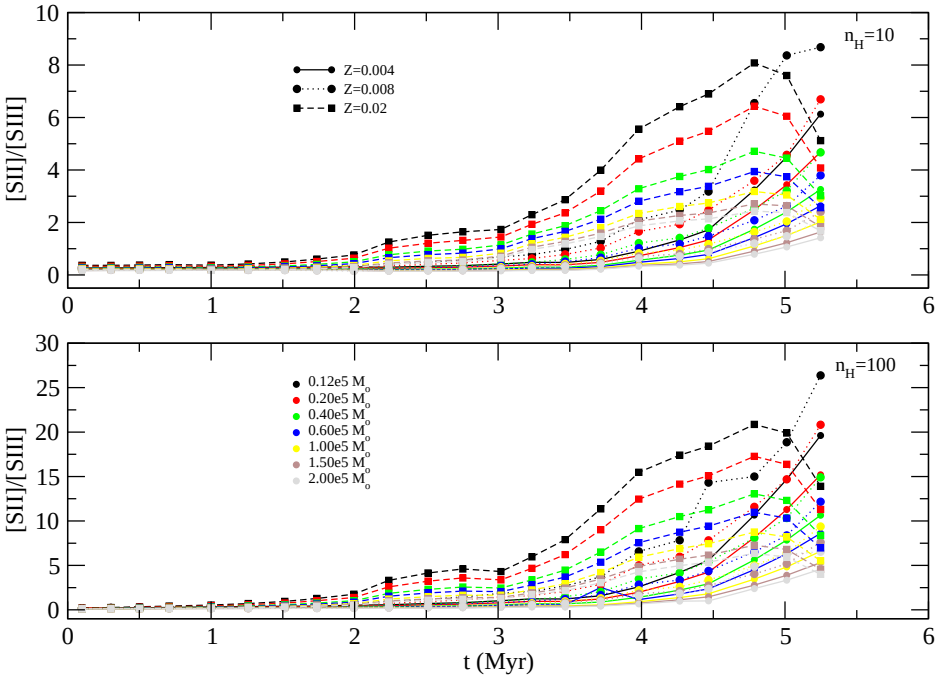

Figure A.4: Ratio [SII]6717+6731/[SIII](9069+9532) *vs* time (in Myr) for high metallicities (Z=0.004, 0.008, 0.02) and all masses. Solid lines join models for Z=0.004, dotted lines are those for Z=0.008 and dashed lines join models for Z=0.02. Different colours correspond to different values of the cluster mass. Models with values of $n_H = 10$ cm^{-3} have been plotted in the upper panel while models with $n_H = 100$ cm^{-3} have been plotted in the lower one.

A.3 shows the [SII]$\lambda\lambda$6731,6717/H_α ratio for low metallicities (Z=0.001 and Z=0.004) and all masses. Models with different values of n_H have been plotted in different panels. For a given metallicity, the plot shows how this value is quite constant during the first 3 Myr. From 3 to 5 Myr, the parameter increases a little as density increases being also quite unsensitive to mass cluster, in the lowest metallicity case (Z = 0.0001). As the metallicity increases the ratio also increases as the cluster evolves from 3 to 5 Myr.

Figure A.4 plots the [SII]$\lambda\lambda$6731,6717/[SIII]$\lambda\lambda$9069,9532 line ratio, versus time (in Myr). This ratio has been shown to be a good ionization parameter indicator for moderate to high metallicities (Díaz et al., 1991), with little dependence on metallicity, as we pointed out in previous section. We can see how this ratio starts increasing around 2 Myr, being the values higher for higher density.

Finally, we have [NII]/Hα, which is in principle, a good metallicity indicator, growing with increasing metallicity, even for regions with metallicities higher than Z=0.004. The first 3-4 Myr after the burst the ratio keeps almost constant, until the ejection by the massive stars of metals which makes the ratio to increase.

Emission lines and the ionization parameter.

Figures A.5 a) to e) show the intensity, with respect to of the following emission lines: [OII]λ3727Å [OIII]λ5007Å , [OI]λ6300Å [NII]λ6584Å [SII]λ6731Å [SIII]λ9069Å *vs* $logu$, for metallicities Z=0.0001, Z=0.0004, Z=0.004, Z=0.008 and Z=0.02, respectively. We have chosen only the strongest emission lines to represent the most relevant ionization stages and elements. In each figure we show four panels for ages 2 Myr (top left), 3 Myr (top right), 4 Myr (bottom left) and 5 Myr (bottom right). Solid lines correspond to $n_H = 10$ cm^{-3} models while dotted lines correspond to $n_H = 100$ cm^{-3}. In total we have 7 points per density, corresponding to the 7 values of the cluster mass: 0.12, 0.20, 0.40, 0.60, 1.00, 1.50 and 2.00 $\times 10^5$. We can see in the figures that models with $n_H = 10$ cm^{-3} and 100 cm^{-3} show the same trend, and cover different ranges of the ionization parameter, being it higher for the lower density case.

For a given metallicity, the changes in the emission line spectrum and in the ionization parameter are due to the changes in the cluster mass, which determines the number of ionizing photons, and changes in the cluster age, which influences not only the total number of ionizing photons but the overall ionization spectrum hardness and the ionized region size. For example, [OIII]λ5007Å line is intense during the first few Myr of the cluster evolution, for all metallicities, and then it decreases to rise again at 4 Myr

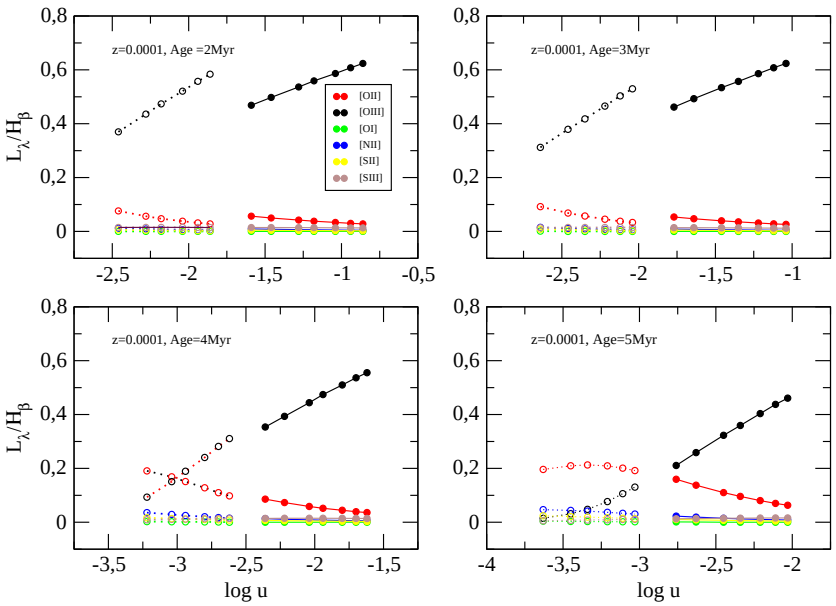

Figure A.5: a). Evolution of emission lines for Z = 0.0001 as a function of the logarithm of the ionization parameter. Solid lines correspond to models with $n_H = 10$ cm^{-3} and dotted lines correspond to models with $n_H = 100$ cm^{-3}.

due to the presence of WR stars that produces a harder ionizing continuum.

From our models we predict an intrinsic sizing effect in the HII regions sequence, which implies a natural decreasing of the ionizing parameter, due to the following explanation: for a very young region, whose ionization is dominated by the O-B stars, the size is still small but the number of ionizing photons is high, resulting in a high ionization parameter. As the cluster evolves, the region's size increases due to the winds, but the number of ionizing photons remains similar (or even decreases) with respect to early phases, resulting in a decreasing of the ionization parameter, that makes the lines to be less intense.

It has to be noticed that for the highest metallicities, this effect is more remarkable. High metallicity regions have less ionizing photons and more winds what implies less ionization parameter. In addition, the effective cooling of the gas passes from the optical emission line spectrum to the near and mid infrared lines as metallicity increases. These two facts explain that in these high metallicity regions, the emission lines are extremely weak, being just at the level of 1 % of the H_β line intensity, been more difficult to be detected for the same telescope and instrument configuration, what has biased the observational samples during years.

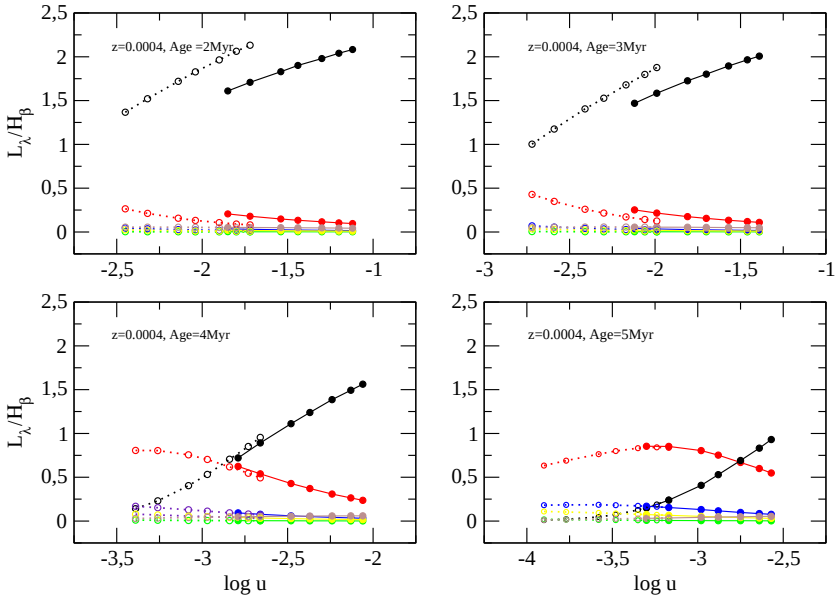

Figure A.5: b). Evolution of emission lines for Z=0.0004 as a function of the logarithm of the ionization parameter.

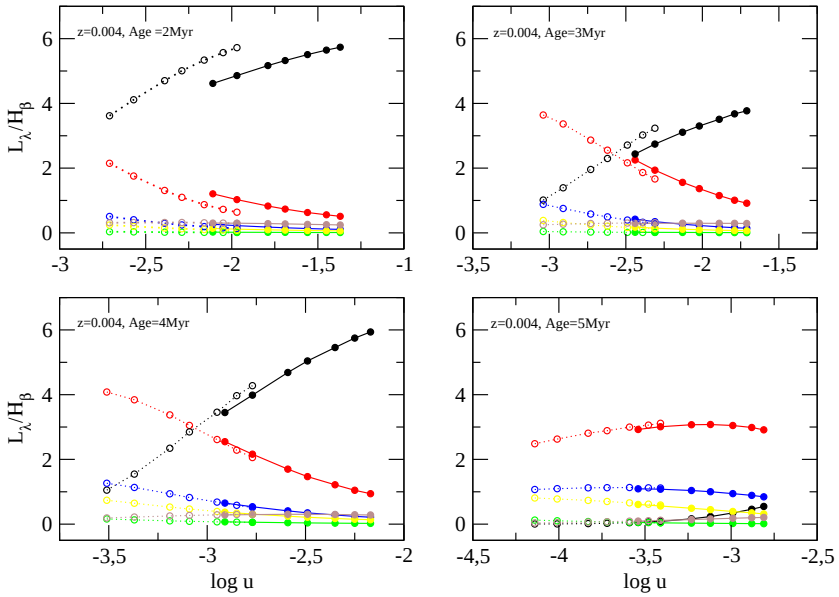

Figure A.5: c). Evolution of emission lines for Z=0.004 as a function of the logarithm of the ionization parameter.

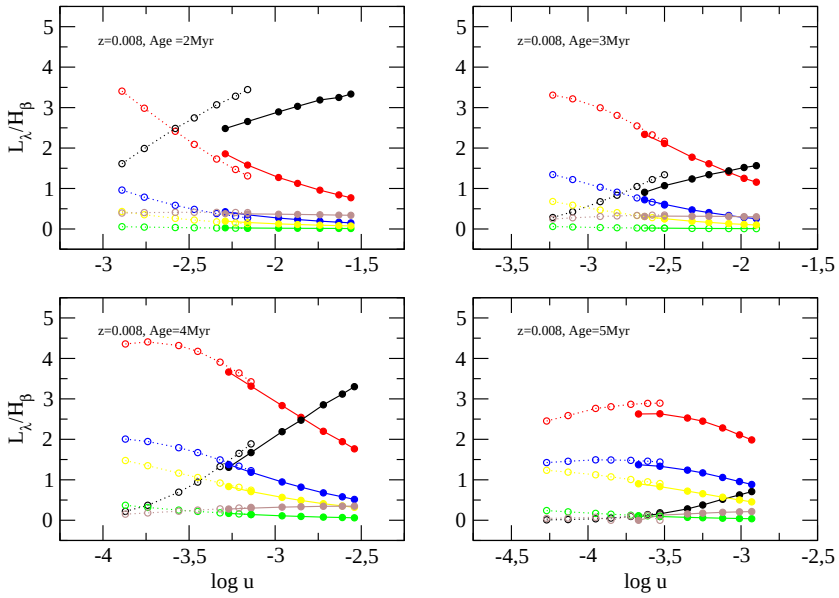

Figure A.5: d). Evolution of emission lines for Z=0.008 as a function of the logarithm of the ionization parameter.

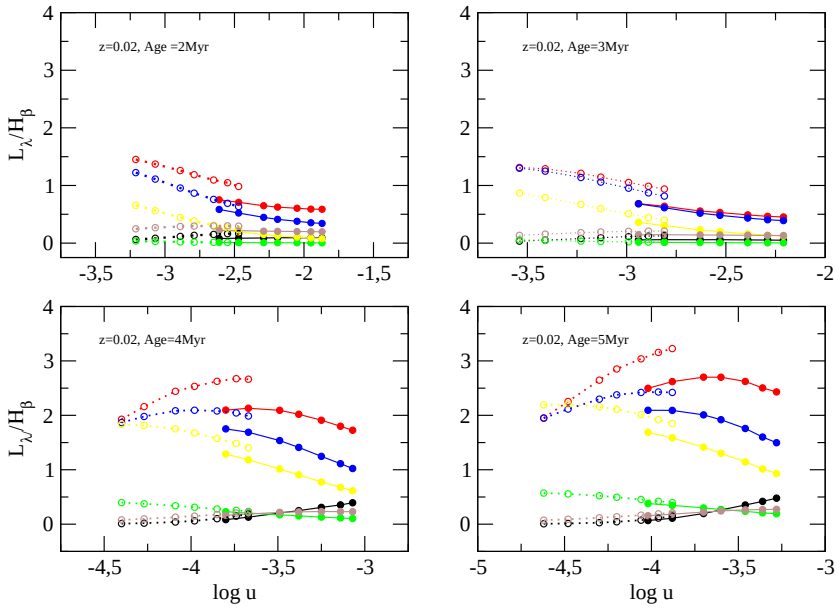

Figure A.5: e). Evolution of emission lines for Z=0.02 as a function of the logarithm of the ionization parameter.

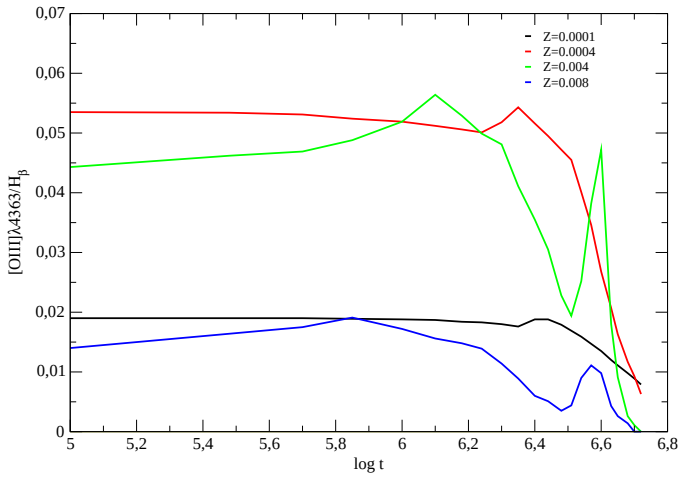

Figure A.6: Evolution of the [OIII]4363ÅH$_\beta$ line for all metallicities and 10^5 M$_\odot$.

Abundance determination in HII regions and consistency with the models.

Emission lines allow us to determine abundances by a direct method based on the electronic temperature of the [OIII] lines, T$_e$. For our models we have obtained oxygen abundances from emission lines in order to check the more effective method to recover the oxygen abundance used as input for the model. An accurate analysis requires the detection of the auroral line [OIII]4363Å with an intensity larger than 5 % with respect to H$_\beta$. In this case, we can obtain electronic temperatures and then oxygen abundances from the [OIII] lines. In Figure A.6 we can see the evolution of [OIII]4363ÅH$_\beta$ for every metallicity and 10^5 M$_\odot$ and n$_H$=10. This emission line intensity is high for Z=0.0004 and Z=0.004, close to 5% of H$_\beta$, however, for both Z=0.0001 and Z=0.008 the intensity is low and very similar. It can make us think that the no detection of this line is not always due to the high metallicity of the observed object, but to the simple absence of oxygen abundance. For Z=0.02 there is no [OIII] line for this density case.

We find, as shown in Figure A.7, that from our photoionization models we obtain the auroral line [OIII]λ4363 Å along the whole cluster evolution for metallicities lower than Z = 0.008 and the [OIII] lines electronic temperature method gives good results for all of them, finding differences between input and derived abundance lower than 0.05dex.

At Z = 0.008, corresponding to an oxygen abundance of 12+log(O/H) =8.5, the [OIII]λ4363Å line intensity ranges from 1.62 % H$_\beta$ 1 Myr after the star formation, to 0.82 % H$_\beta$ 4 Myr after the burst. However, even being

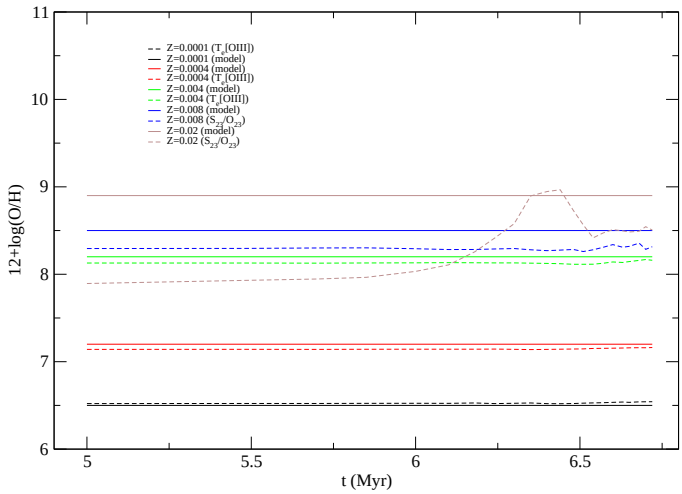

Figure A.7: Comparison between abundances used as inputs for the models (solid lines) of different metallicities and the abundances obtained using different empirical calibrators (dashed lines).

this line detectable at this metallicity, the electronic temperature method is not able to reproduce the input metallicity of the model.

There are indications that simple photoionization models are not able to reproduce the observed T_e in some situations. Stasińska (1978, 2002, 2005) show that abundances derived by T_e-based methods are likely to be biased towards low metallicities when applied to high metallicity HII regions. This differences may be significant in the case of large temperature gradients or fluctuations. In this cases, the temperature obtained from the emission line, e.g. T_l[OIII] from [OIII]λ5007Å line is different from the line ratio temperature T_r and from the mean ionic temperature $T(O^{++})$, being not representative the line or line ratios temperatures obtained from the models of the high ionization zone O^{++}. We have done the same plot of Stasińska (2005) for our models, Fig. A.8, in order to compare a sequence of oxygen abundances derived from the model as a function of the input value. We can see that the value of the oxygen abundance derived from the direct method for low metallicities is close to the input, but for metallicities around 8.6 there are some important deviations. For higer metallicities deviations are much more significative.

The analysis of the abundances of higher metallicity HII regions is even more complicated since oxygen optical lines act as main coolant for the nebula, and a higher oxygen abundance leads to a more effective cooling. As the gas cools down, the electron temperature gets lower and the optical

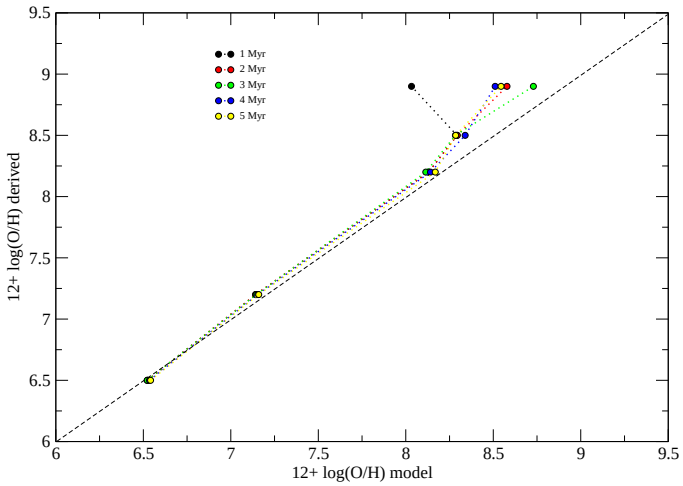

Figure A.8: Comparison between abundances used as inputs for the models, and the abundances obtained using T_e-based methods. Each colour corresponds to a different age sequence. The values of 12+log(O/H) derived empirically are very close to the input value up to 8.6.

[OIII] forbidden lines get weaker. In general, this low excitation makes any temperature-sensitive lines in the optical range too weak to be measured. For this reason we have to use other empirical calibration methods for abundance estimations (Pérez-Montero & Díaz, 2005). In our models, for metallicities Z = 0.008 and Z = 0.02, abundances have been determined from the ratio S_{23}/O_{23}, obtaining quiet good results for Z=0.008 (with a difference of 0.2 dex approximately), but not for Z=0.02, which shows important differences at the beginning of the evolution. For Z = 0.05 we cannot get the oxygen abundance used as input by any empirical method because there is not an effective calibration for such high metallicity (which is approximately $3Z_{\odot}$) in the reference system of Grevesse & Sauval (1998). In Figure A.7 we can see the comparison between model oxygen abundances and the ones obtained with empirical methods.

A.3 General comparison between models and HII regions observations.

A.3.1 Observational data.

(Díaz et al., 2007, and references therein) have data of HII galaxies, high and low metallicity HII regions, and circumnuclear regions. We could not

separate explicitly by density with the [SII] ratio for this data set, but we have asumed n_H= 100 cm^{-3} for HII galaxies and circumnuclear regions and n_H= 10 cm^{-3} for HII regions. Metallicity subdivision have been made according to the abundances given by this work, which have been obtained by different empirical calibration methods. In order to determine the more accurate and effective method, we have tried to use the same method which makes a better fit with the metallicities of our models, that is the S_{23}/O_{23} calibrator. Data from Castellanos, Díaz, & Terlevich (2002) correspond to HII regions in spiral galaxies NGC628, NGC925, NGC1232 and NGC1637. The HII regions have been divided by density, which were determined from the [SII]6717,6731Å. For seven regions, ion weighted temperatures from optical forbidden auroral to nebular line ratios had been obtained, and for six of them oxygen abundances were derived by using empirical calibration methods. The other metallicities have been determined by applying S_{23} method and photoionization models. We have used these metallicities to make the division by ranges as explained in the diagnostic diagram section.

García-Vargas et al. (1997) give data of 4 HII giant circumnuclear regions of NGC 7714. Densities have been determined from [SII] lines. Oxygen abundances were obtained by the electron temperature method thanks to the direct detection of the [OIII]]λ4363 Å line. Zaritski et al. (1994) made an analysis of 159 HII regions in 14 spiral galaxies, from which we have chosen those that have well determined [SII] and [SIII] emission lines to obtain the density and oxygen abundance by the method we consider more effective. The subsample are 36 regions which we have divided by density from the [SII] ratio relation.

van Zee & Haynes (2006) make spectroscopy of 67 HII regions in 21 dIrr. They give data of [OII]λ3727Å [OIII]$\lambda\lambda$5007,4959Å [SII]λ6731,17Å in addition to [SII] ratio, which we have used to make the division by density, and [OIII] ratio to get the electronic temperature of [OIII] line and oxygen abundance.

The data from Izotov & Thuan (2004) are HII regions of 76 BCD with abundances determined from the electronic temperature of [OIII] due to the direct detection of the [OIII]λ4363 Å auroral line. It means that all the regions of this sample have metallicities lower than 8.5 (taking 12 + log[O/H]). The data have been divided by density by the [SII] ratio. Yin et al. (2007) have 531 galaxies and HII regions from SDSS-DR4 sample, from which [OIII]λ4363Å line has been detected and then, the oxygen abundances using this method. From these data we could not get the [SII] ratio, and we could not make the division by density. The observational data sources and the method used to estimate oxygen abundances are summarized in tableA.4.

Table A.4: Observational data used for this work

Reference	Objects	[O/H] method
Díaz et al.2007	HII regions and galaxies,CNSFR	S_{23}/OS_{23}
Castellanos et al.(2002)	HII regions	Direct method T_e and S_{23}
García-Vagas et al.(1997)	HII circumnuclear regions	Direct method T_e
Zaritsky et al.(2004)	HII regions in S	S_{23}/OS_{23}
Van Zee & Haynes(2006)	HII regions in dIrr	Direct method T_e
Izotov & Thuan(2004)	HII regions in BCD	Direct method T_e
Yin et al.(2007)	HII regions	Direct method T_e

Table A.5: Abundance range for data and model comparison

Label	Observed Metallicity Range	Z in plotted models
1	12+log(O/H) < 7.7	0.0004
2	7.7 < 12+log(O/H) < 8.4	0.0040
3	8.4 < 12+log(O/H) < 8.7	0.0080
4	8.7 < 12+log(O/H)	0.0200

A.3.2 Diagnostic diagrams: optical emission line ratios.

Figures A.9 to A.13 show the models results and the observed data in diagnostic diagrams. These diagrams us to study the relationship among different emission line ratios, and to extract information about physical parameters of the ionizing clusters.

Each figure is divided in 4 panels, one per metallicity: Z = 0.0001 and 0.0004 (in the left upper panel), 0.004, 0.008 and 0.02. The highest value of metallicity of the grid, Z = 0.05, has been excluded due to the absence of enough spectroscopical data with those observed abundances. The lower metallicity value is plotted in the same panel of Z=0.0004 to compare the position in the diagram of the emission lines of such low metallicity.

Observational data correspond to different works of the literature, and have been divided by density and subdivided by metallicity. Density division has been made according to the electronic density, n_e derived from the [SII]λ6717/[SII]λ6731 ratio (Osterbrock, 1989). Metallicities have been divided by ranges as described in table A.5.

We show in each panel the observational data whose metallicity corresponds to the one of the models we want to compare with. The

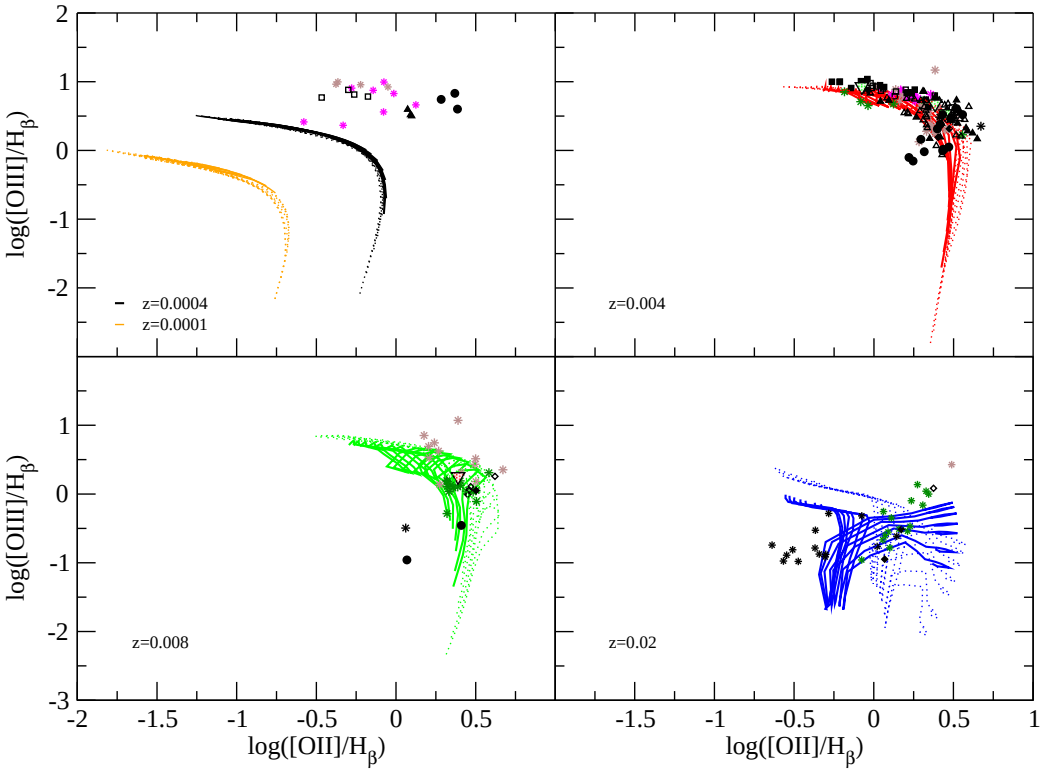

Figure A.9: Diagnostic diagram showing log([OIII]$\lambda\lambda$5007,4959/H$_\beta$) vs log([OII]λ3727/H$_\beta$). Each shell shows a different metallicity model and the corresponding observational data range. Observational data from: Zaritski et al. (1994) (circles), Izotov & Thuan (2004) (squares), Castellanos, Díaz, & Terlevich (2002) (diamonds), van Zee & Haynes (2006) (triangles up), García-Vargas et al. (1997) (red triangles down), and **?** (black stars: cnsfr; green stars: high metallicity HII regiosn; brown stars: low metallicity HII regions; magenta stars: HII galaxies). In those objects whose density can be obtained from SII ratio, filled symbols represents object with n$_H$=100 cm^{-3}, and not filled the objects with n$_H$=10 cm^{-3}.

metallicity of the models is the central value of the different ranges, except ranges 1 and 4 that include data with metallicities up to Z = 0.0004 and over Z = 0.02 respectively.

Oxygen emission line ratios.

HII regions describe a well defined sequence in diagnostic diagrams which include oxygen line ratios, like log([OIII]/H$_\beta$) vs log([OII]/H$_\beta$), as well as log([OII]/[OIII]). In general, observed HII regions do not have ages higher than 3-4Myr and we do not have observational data to fit with the tail of the models. Ionizing parameters are high at this age, lines are intense enough to

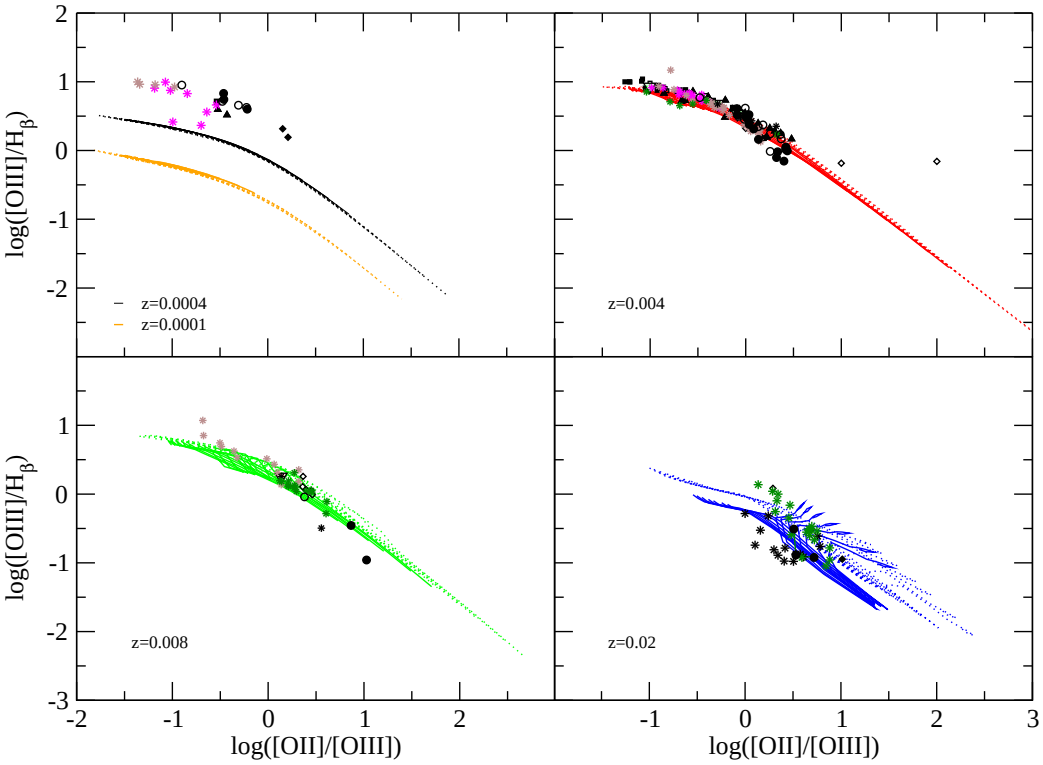

Figure A.10: Diagnostic diagram showing log([OIII]λ5007,4959/H$_\beta$) vs log([OII]λ3727/[OIII]]λ,λ5007,4959). Each shell shows a different metallicity model and the corresponding observational data range. Observational data symbols are the same than in Figure A.9

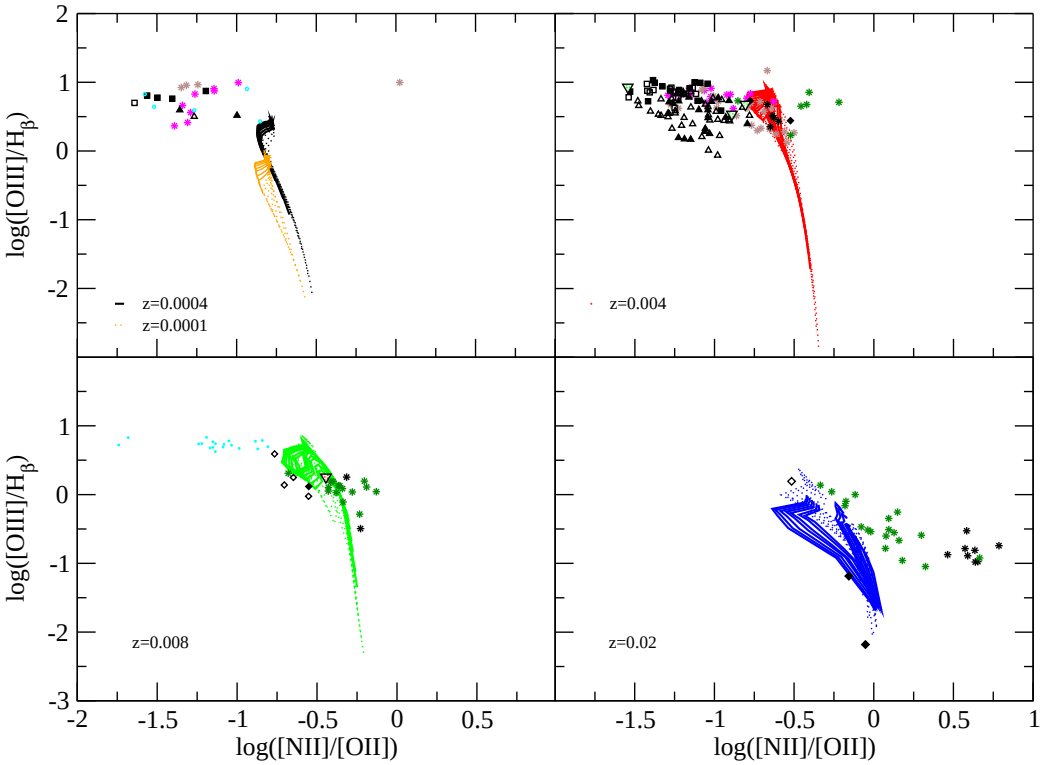

Figure A.11: Diagnostic diagram showing log([OIII]$\lambda\lambda$5007,4959/H$_\beta$) vs log([NII]λ6584/[OII]λ3727). Each shell shows a different metallicity model and the corresponding observational data range. Observational data symbols are the same than in Figure A.9, in addition to blue dots which are HII regions from Yin et al. (2007)

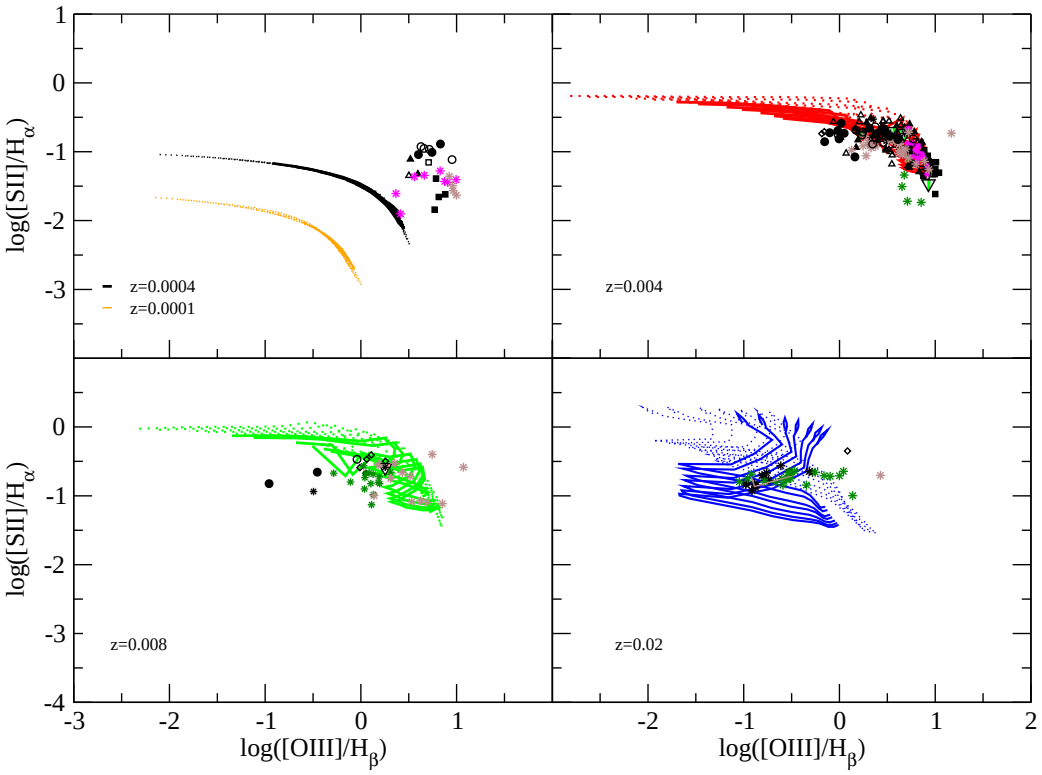

Figure A.12: Diagnostic diagram showing log([SII]λ6731,17/H$_\alpha$) vs log([OIII]$\lambda\lambda$5007,4959/H$_\beta$). Each shell shows a different metallicity model and the corresponding observational data range. Observational data symbols are the same than in Figure A.9

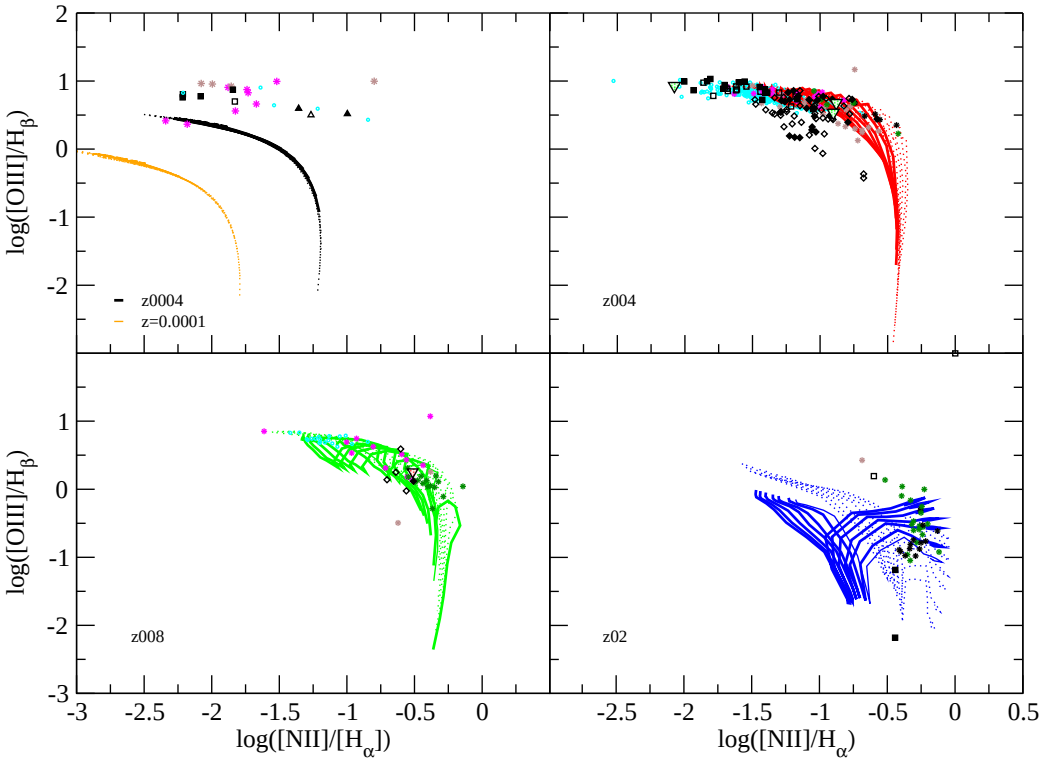

Figure A.13: Diagnostic diagram showing log([OIII]/H$_\beta$) vs log([NII]/H$_\alpha$). Each shell shows a different metallicity model and the corresponding observational data range. Observational data symbols are the same than in Figure A.9 in addition to blue dots which are HII regions from Yin et al. (2007)

be observed. These diagrams show the excitation degree of the ionized gas. The shells corresponding to Z=0.004 and Z=0.008 show a clear sequence and are the more populated shells. Models of higher and lower metallicities have less observational data to compare with. It can be due to: First, a general selection effect: observed HII regions show very intense emission lines, which corresponds to regions with high [OIII]$\lambda\lambda$5007,4959Å line values, and then, regions of low metallicity. And second, the selection effect related directly to the detection of [OIII]λ4363Å line: the detection of this line allow us to determine the oxygen abundance more accurately than other empirical calibrators, and the galaxies laying in this shell are galaxies in this range of metallicity and not older than 5 Myr.

Models of Z=0.0004 and Z=0.02 do not have the aim of reproduce exactly the sequence of the observations, and it is used to define a lower (in the case of Z=0.0004) and upper (in the case of Z=0.02) limit on metallicity for the observed regions: Observational data placed in this shell are regions with metallicities between Z=0.0004 and Z=0.004. The same happens in the other shells: the dispersion could be due to the chosen range of metallicity instead of the exact value of the model.

Our models cover the observational data range corresponding to different cluster masses. Different mass implies different number of ionizing photons and different values of the ionizing parameter. The most massive stellar cluster models have the highest ionization parameters, due to their number of ionizing photons, and the less massive ones fall down, showing a similar evolution, but starting at a lower excitation stage.

As explained before, regions with intense [OIII] lines correspond to the highest ionization stage. For a given cluster mass, as far as the cluster evolve, the high excitation emission lines tend to decrease while [OII]/H_β grows up. This is due to the change of the ionizing parameter with cluster evolution. For a very young region, whose ionization is dominated by the O-B stars, the size is still small and the number of ionizing photons is high, resulting in a high ionization parameter. As the cluster evolves, the region's size increases due to the winds, but the number of ionizing photons remains similar (or even decreases) with respect to early phases, resulting in a decreasing of the ionization parameter, that makes the lines, and in particular the oxygen lines, to be less intense.

This age effect influence also the sample since early ages results in more compact regions (therefore high surface brightness) and with high ionization parameters, what increases the [OIII]line intensity and the possibility of detectability in a given sample taken with the same instrumental configuration. If we would assign an age to the each observation, we would find that most of them are younger than 5 Myr (when ionizing photons are

enough to produce luminosity to be detectable) and from those, most of them are biased to younger ages (less than 3.5 Myr).

Also, we have the influence of the electron density in the ionization parameter and therefore in the diagnostic diagrams. Models with n_H=100 cm^{-3} have lower values of the ionizing parameter. However, the radiation has more particles per cm^{-3} to ionize, and the excitation degree is higher, producing that the sequence lay up to the models of lower density. More significant differences between the models of both densities are found in the highest metallicity diagrams, Z=0.02. For low density models, is easy to discriminate the cluster's mass while for high density, the age sequence is well defined, but there is not dispersion and it is not possible to distinguish among the cluster masses.

Sulfur and nitrogen emission line ratios.

In large star forming regions, like starburst, the relationship between the exitation parameter [OIII]/H_β and the metallicity indicator [NII]/H_α gives us information about the youngest populations plus the star formation rate (Kennicutt et al., 1994). At the beginning of the evolution, H_α emission line is intense due to the amount of mass involved in the star formation. In this way, knowing the strength of the H_α line, is possible to derive the cluster's mass and the star formation rate. As the galaxy evolves, H_α emission line decreases, while [NII] increases because of the gas ejection of stars. However, for HII regions when a SSP is assumed the use of this diagnostic diagram is quite different.

The [NII]λ6584/[OII]λ3727 ratio was introduced as a good metallicity indicator by Dopita et al. (2000) due to its sensitivity to abundance. Nitrogen is a secondary element, or at least it has a strong secondary component, which makes the ratio [NII]/[OII] to increase with abundance. The mean temperatures of HII regions decrease with metallicity and high abundances. When the electron temperature become too low to excite transitions, [OII] decreases while [NII] is maintained excited, then [NII]/[OII] increases with increasing abundance. A good correlation has been found to exist between this ratio and the N^+/O^+ ionic abundance ratio, which can bee assumed to trace the N/O ratio (Pérez-Montero & Díaz, 2005). Díaz et al. (2007) have shown a very tight correlation between [NII]/[OII] ration and N/O ratio for high metallicity HII regions and circumnuclear star forming regions, which follow a sequence of increasing N/O ratio with increasing emission line ratio.

In our diagnostic diagrams we can see how this ratio changes with metallicity. For low metallicity models, both the [OIII]/H_β ratio and [NII]/[OII] ratio are low. As metallicity increases both line ratios also

increase. When metallicity reaches the limit of Z=0.004, [OIII] starts to decrease but [NII]/[OII] ratio is still growing. At Z=0.02 the models show low values of [OIII] and high values of [NII]. The only observational data in this part of the plot are high metallicity HII regions and CNSFR (CircumNuclear StarForming Regions), showing higher values of [NII]/[OII] than the high metallicity HII regions, which indicates higher N/O abundance rations as can be sen in the sequence of Díaz et al. (2007).

Figure A.12 shows the ratio [SII]/H_α *vs* [OIII]/H_β also quite reddening-independent. We can see that high values of [SII] line imply a low ionization parameter, and therefore a low [OIII] emission line intensity. However, [OIII] line is very metallicity dependent, and a low value of this emission line intensity could be due to a high metallicity and not to a low ionization parameter produced by an evolved population. Although both ratios are ionization parameter indicators, the values of u derived from oxygen emission line ratios can be lower than u the values derived from sulfur emission line ratios, which are not so metallicity dependent.

Appendix B

List of acronyms

AGB Asymptotic Giant Branch

BCD Blue Compact Dwarf

CBM Closed Box Model

CMD Colour-Magnitude Diagram

CNSFR Circumnuclear Star Forming Region

dE Dwarf Elliptical

dIrr Dwarf Irregular

dSph Dwarf Spheroidal

EW Equivalent Width

GEHR Giant Extragalactic HII Region

GV95 García-Vargas et al. (1995)

HAM High Attenuation Model

HST Hubble Space Telescope

IFS Integral Field Spectroscopy

IMF Initial Mass Function

IR Infrared

ISM Interstellar Medium

KISS KPNO International Spectroscopic Survey

LCBG Luminous Compact Blue Galaxy

LINER Low-Ionization Nuclear Emission-line Region

LMC Large Magellanic Cloud

LSB Low Surface Brightness

LSBG Low Surface Brightness Galaxy

MGVB09 Mollá, García-Vargas & Bressan (2009)

MWG Milky Way Galaxy

NLTE Non Local Termodinamic Equilibrium

NOT Nordic Optical Telescope

QBCD Quiescent Blue Compact Dwarf

SAM Standard Attenuation Model

SDSS Sloan Digital Sky Survey

SED Spectral Energy Distribution

SF Star Formation /Star Forming

SFH Star Formation History

SFR Star Formation Rate

SNe Supernovae

SSP Single Stellar Population

STB99 Starburst 99 (Leitherer et al. 1999)

UV Ultraviolet

WR Wolf Rayet

11HUGS 11Mpc Hα and Ultraviolet Galaxy Survey

Bibliography

Abaz AJian K. et. al., 2005, AJ, 129, 1755

Aller L. H., 1984, Physics of thermal gaseous nebulae Dordrecht, D. Reidel Publishing Co. (Astrophysics and Space Science Library. Volume 112)

Aloisi A., van der Marel R. P., Mack J., Leitherer C., Sirianni M., Tosi M., 2005, ApJ, 631, L45

Amorín, R. O. and Muñoz-Tuñón, C. and Aguerri, J. A. L. and Cairós, L. M. and Caon, N., 2007 A&A, 467, 541A

Antia, H. M. and Basu, S. 2005 ApJL, 620, L129

Aparicio, A. and Gallart, C., 1995 AJ., 110.2105A

Asplund, M., Grevesse, N., and Sauval, A. J. 2005, in ASP Conf. Ser. 336: Cosmic Abundances as Records of Stellar Evolution and Nucleosynthesis, 25

Bahcall, J. N., Serenelli, A. M., and Basu, S. 2005 ApJL, 621, L85

Bergvall, N. and Östlin, G. 2002 AA, 390, 891B

Bertelli G.,Bressan A., Chiosi C., Fagotto F., and Nasi E., 1994 A&AS, 106,275

Binggeli, B. 1994, in Panchromatic View of Galaxies, ed. G Hensler, C,. Theis and J. Gallagher, 173

Bradamante F.,Matteucci F. and D'Ercole A., 1998 A&A, 337, 338

Bressan A., Fagotto F.,Bertelli G., and Chiosi C., 1993 A&AS, 100, 647

Bressan A., Chiosi C., Fagotto F., 1994, ApJS, 94, 63

Bressan, A., Granato, G.L., and Silva, L. 1998 A&A, 332, 135

Brighenti, F. and D'Ercole, A., 1999 IAUS, 193, 732B

Bruzual, G. and Charlot, S., 2003 MNRAS, 344, 1000B

Cairós L. M., Vílchez J. M., González Pérez J. N.,Iglesias-Páramo J. and Caon N., 2001 ApJS, 133, 321

Cairós L. M., Caon N., Vílchez J. M.,González-Pérez J. N. and Muñoz-Tuñón C., 2001 ApJS, 136, 393

Cairós L. M., Caon N., García-Lorenzo B.,Vílchez J. M. and Muñoz-Tuñón C., 2002 ApJ, 577, 164

Cairós L. M.,García-Lorenzo B., Caon N., Vílchez J. M.,Papaderos P., and Noeske K., 2003 Ap&SS, 284, 611

Cairós L. M., Caon N., García-Lorenzo B., Monreal-Ibero A., Amorín R., Weilbacher P., Papaderos P., 2007, ApJ, 669, 251

Caon, N. , Cairós, L. M., Aguerri . A. L., Muñoz-Tuñón, C.,Papaderos, P. and Noeske, K., 2005 RMxAC, 24, 223C

Carigi L., Hernandez X., and Gilmore G., 2002 MNRAS, 334, 117

Castellanos, M., Díaz, A.I. and Terlevich, E., 2002 MNRAS, 329, 315C

Castor, J., McCray, R. and Weaver, R., 1975 ApJ, 200, L107

Chabrier, G. 2003, ApJL, 586, L133

Chiosi, C. and Matteucci, F., 1982 A&A, 110, 54C

Clegg R. E. S. andMiddlemass D., 1987 MNRAS, 228, 759

Díaz, A.I. , Terlevich, E. , Vílchez, J.M. , Pagel, B.E.J. and Edmunds, M.G., 1991 , MNRAS,253, 245D

Díaz, A.I. , Terlevich, E. ,Castellanos, M. and Hägele, G.F. 2007 MNRAS, 382, 251

Dekel, A. and Silk, J., 1986 ApJ, 303, 39D

Dopita, M. A., Kewley, L. J., Heisler, C. A. and Sutherland, R. S., 2000 ApJ, 54, .224D

Dopita, M.A., Fischera, J. Sutherland R.S. , Kewley, L.J., Leitherer, C., Tuffs, R.J. , Popescu, C.C. , van Breugel, W. and Groves, B.A., 2006 ApJ SUpp Series 167, 177

Dottori H. A., 1981 Ap.& Space Sience, 80, 267

Doublier, V., 1999 sf99.proc, 48D

Drake, J. J. and Testa, P., 2005 Nature, 436, 525

Dye, S. 2008 MNRAS, 389, 1293D

Ellis, R. S., 1997 upa. conf, 159E

Evans, R., Davies, J. I. and Phillipps, S., 1990 MNRAS.245, 164E

Fagotto, F., Bressan, A., Bertelli, G. and Chiosi, C., 1994 A&AS, 104,365F

Fagotto, F., Bressan, A., Bertelli, G. and Chiosi, C.,1994 A&AS, 105,29F

Fagotto, F., Bressan, A., Bertelli, G. and Chiosi, C.,1994 A&AS, 105,39F

Ferguson, H. C. and Binggeli, B., 1994 A&ARv, 6, 67F

Ferland G. J., 1980 PASP, 92, 596

Ferland G. J., Korista K. T., Verner D. A., Ferguson J. W., Kingdon J. B. and Verner E. M., 1998 PASP, 110, 761

Ferrini F., Matteucci F.,Pardi C. and Penco U., 1992, ApJ, 387, 138

Ferrini F., Mollá M., Pardi M. C. and Díaz A. I., 1994 ApJ, 427, 745

Ferrini F., Penco U. and Palla F., 1990 A&A, 231, 391

Franco, J., Diaz-Miller, R. L., Freyer, T. and Garcia-Segura, C., 1998 ASPC, 141, 154F

Franco, J., 2003 RMxAC, 15, 149F

Fritze-v. Alvensleben, U.,1999 ASPC, 192, 273F

Fukugita, M., Ichikawa, T., Gunn, J. E., Doi, M., Shimasaku, K. and Schneider, D. P., 1996 AJ, 111, 1748F

Gallagher, III, J. S., Hunter, D. A. and Tutukov, A. V., 1984 ApJ, 284, 544G

Gallagher, J. S., Mould, J. R., de Feijter, E., Holtzman, J., Stappers, B., Watson, A., Trauger, J., Ballester, G. E., Burrows, C. J., Casertano, S., Clarke, J. T., Crisp, D., Griffiths, R. E., Hester, J. J., Hoessel, J., Krist, J., Matthews, L. D., Scowen, P. A., Stapelfeld, K. R. and Westphal, J. A., 1996 ApJ, 466, 732G

Galli D., Palla F.,Ferrini F., and Penco U., 1995 ApJ, 443, 536

García-Lorenzo,B., Cairós,L.M., Caón,N., Monreal-Ibero,A. and Kehrig, C. arXiv:0801.2467v1

García-Vargas, M.L., González-Delgado, R.M., Pérez, E., Alloin, D., Díaz, A. and Terlevich, E., 1997 ApJ, 478, 112G

García-Vargas,M.L., Mollá, M., & Bressan, A. 1998, A&AS, 130, 513

García-Vargas,M.L., Bressan, A., & Díaz, A.I. 1995 A&AS, 112, 13

García-Vargas,M.L., Mollá, M. & Martín-Manjón, M.L. 2009, MNRAS, in preparation

Garnett D. R., 1990, ApJ, 363, 142

Garnett D. R., Shields G. A., Peimbert M., Torres-Peimbert S., Skill-manE. D., Dufour R. J., Terlevich E. and Terlevich R. J., 1999 ApJ, 513, 168

Garnett D. R., Dufour R. J., Peimbert M., Torres-Peimbert S., Shields G. A., Skillman E. D., Terlevich E., Terlevich R. J., 1995, ApJ, 449, L77

Gavilán M., Buell J. F. and Mollá M., 2005 A&A, 432, 861

Gavilán M., Mollá M., and Buell J. F., 2006 A&A, 450, 509
gav09 Gavilán M. PhD Thesis, UAM, 2009.

Gerola, H., Seiden, P. E. and Schulman, L. S. 1980 ApJ, 242, 517G

Gil de Paz, A. and Madore, B. F., 2005 ApJS, 156, 345G

Grebel, E. K.,1997 RvMA, 10, 29G

Grebel, E. K., 1998 astro.ph, 6191G

Grevesse, N. and Sauval, A. J., 1998 SSRv, 85, 161G

de Grijs, R. and O'Connell, R. W. 2004 A&G, 45f,27D

Guseva N. G., Papaderos P., Izotov Y. I., Green R. F., Fricke K. J., Thuan T. X., Noeske K. G., 2003, A&A, 407, 105

Guzman, R.,1997 RMxAC, 6, 99G

Guzmàn, R.,1999 ASPC, 187, 271G

Hammer F., Gruel N., Thuan T. X., Flores H., and Infante L., 2001 ApJ, 550, 570

Heckman, T. M. 200 5ASSL, 329., 3H

Henry R. B. C., Edmunds M. G. and Köppen J., 2000 ApJ, 541, 660

Hillier,D.J. and Miller D.L. 1998 ApJ, 496, 407

Hoyos C., Díaz A. I., 2006, MNRAS, 365, 454

Hoyos C., Guzmán R., Bershady M. A., Koo D. C. and Díaz A. I., 2004 AJ, 128, 1541

Hoyos, C., Koo, D. C., Phillips, A. C., Willmer, C. N. A. and Guhathakurta, P., 2005 ApJ, 635L, 21H

Hoyos, C., Guzmán, R., Díaz, A. I., Koo, D. C. and Bershady, M. A., 2007 AJ., 134.2455H

Hunter, D. A. and Gallagher, III, J. S., 1986 PASP, 98, 5H

Iwamoto K., Brachwitz F., Nomoto K., Kishimoto N., Umeda H., Hix W. R., Thielemann F., 1999, ApJS, 125, 439

Izotov Y. I. and Thuan T. X., 1998 ApJ, 500, 188

Izotov Y. I., Papaderos P., Thuan T. X., Fricke K. J., Foltz C. B., Guseva N. G., 1999, astro, arXiv:astro-ph/9907082

Izotov Y. I. and Thuan T. X., 1999 ApJ, 511, 639

Izotov Y. I. and Thuan T. X., 2004 ApJ, 616,781I

Izotov Y. I., Thuan T. X. and Guseva N. G., 2005 ApJ, 632, 210I

Izotov Y. I., Stasińska G., Meynet G., Guseva N. G. and Thuan T. X., 2006 A&A, 448, 955

Jangren, A. and Bershady, M. A., 2000 ASPC, 215, 102J

Kallman, T. R. 2001 ASPC, 247, 175K

Kamaya, H., 2005 A&A, 434, 163K

. Kehrig, C., Vílchez1,J.M., Sánchez , S.F., Telles,E., Martin-Gordón, D., and López-Martín, L. arXiv:astro-ph/0611123v1

Kennicutt, Jr., R. C., 1989 ApJ, 344, 685K

Kennicutt, Jr., R. C., 1998 ARA&A, 36, 189K

Kennicutt, Jr., R. C., Tamblyn, P. and Congdon, C. E., 1994 ApJ, 435, 22K

Kennicutt, Jr., R. C. and Lee, J. C. and Funes, J. G. and Sakai, S. and Akiyama, S.,2005 ASSL, 329, 187K

Kormendy, J., 1985 ApJ, 295, 73K

Koo D. C., Guzman, R., Faber, S. M., Illingworth, G. D., Bershady, M. A., Kron, R. G. and Takamiya, M., 1995 ApJ, 440L, 49K

Krüger, H. and Fritze-v. Alvensleben, U. and Loose, H.-H. and Fricke, K. J.,1991 A&A, 242, 343K

Kroupa P., 2001, MNRAS, 322, 231

Kroupa, P., 2002, Science, 295, 82

Kunth, D. and Sargent, W. L. W., 1986 ApJ, 300, 496K

Larsen T. I., Sommer-Larsen J. and Pagel B. E. J., 2001 MNRAS, 323, 555

Lee, J. C., Salzer, J. J. and Melbourne, J., 2004 ApJ, 616, 752L

Lee, J. C, Kennicutt R. C, Funes S.J., J, Sakai S., and Akiyama,S. arXiv:0810.5132v1

Legrand F., Kunth D., 1998, astro, arXiv:astro-ph/9805042

Legrand F., 2000 A&A, 354, 504

Legrand F., Kunth, D., Roy, J.-R., Mas-Hesse, J. M. and Walsh, J. R., 2000 A&A, 355, 891L

Legrand, F., Tenorio-Tagle, G., Silich, S., Kunth, D. and Cerviño, M., 2001 ApJ, 560, 630L

Leitherer C., Schaerer D., Goldader J. D., Delgado R. M. G., Robert C.,Kune D. F., de Mello D. F., Devost D. and Heckman T. M., 1999 ApJS, 123, 3

Lejeune T., Cuisinier F. and Buser R., 1997 A&A Supl.S., 125, 229

Lequeux J., 1979, A&A, 71, 1

Liang Y. C., Yin S. Y., Hammer F., Deng L. C., Flores H. and Zhang B., 2006 ApJ, 652, 257

Lilly, S., Schade, D., Ellis, R., Le Fevre, O., Brinchmann, J., Tresse, L., Abraham, R., Hammer, F., Crampton, D., Colless, M., Glazebrook, K., Mallen-Ornelas, G. and Broadhurst, T., 1998 ApJ, 500, 75L

Mac Low, M.-M. and Ferrara, A., 1998 LNP, 506, 559M

Macri L. M., Stanek K. Z., Bersier D., Greenhill L. J. and Reid M. J., 2006 ApJ, 652, 1133

Maeder A., 1992, A&A, 264, 105

Maeder A., Meynet G., 2008, RMxAC, 33, 38

Marconi, G., Matteucci, F. and Tosi, M., 1994 MNRAS.270, 35M

Marconi, G. and Tosi, M. and Greggio, L. and Focardi, P.,1995 AJ., 109, 173M

Marzke, R. O. and da Costa, L. N., 1997 AJ, 113, 185M

Mas-Hesse J. M. and Kunth D., 1999 A&A, 349, 765

Masegosa J., Moles M. and Campos-Aguilar A., 1994 ApJ, 420, 576

Matteucci F., Chiosi C., 1983, A&A, 123, 121

Matteucci F., Tosi M., 1985, MNRAS, 217, 391

Meyer M. R., Adams F. C., Hillenbrand L. A., Carpenter J. M., and Larson R. B., 2000, Protostars and Planets IV, 121

Mollá and M., Díaz A. I., 2005 MNRAS, 358,521M

Mollá M. and García-Vargas M. L., 2000 A&A, 359, 18

Mollá, M., Vílchez J. M., Gavilán M. and Díaz A. I., 2006 MNRAS, 372, 1069

Mollá, M. and García-Vargas,M.L. 2000 A&A, 359,18

Mollá, M. ,García-Vargas,M.L. & Bressan, S. 2009, MNRAS submitted.

Mouhcine M. and Contini T., 2002 A&A, 389, 106

Moy E., Rocca-Volmerange B. and Fioc M., 2001 A&A, 365, 347

Nava A., Casebeer D., Henry R. B. C., and Jevremovic D., 2006 ApJ, 645, 1076

Noeske, K. G., Iglesias-Páramo, J., Vílchez, J. M. and Fricke, K. J., 2001 Ap&SS.276, 577N

Noeske, K. G., Koo, D. C., Phillips, A. C., Willmer, C. N. A., Melbourne, J., Gil de Paz, A. and Papaderos, P., 2006 ApJ, 640L.143N

Nomoto K., Thielemann F.-K. and Yokoi K., 1984 ApJ, 286, 644

Osterbrock, D. E., "Astrophysics of gaseous nebulae and active galactic nuclei", University Science Books, 1989, 422 p., 1989 agna.book, O.

Perez-Montero, E. and Diaz, A.I. 2005 MNRAS, 361, 1063-1076.

Panuzzo P., Bressan A., Granato G. L., Silva L. & Danese L. 2003, A&A, 409, 99

Panuzzo, P., Silva, L., Granato, G. L. , Bressan, A. and Vega, O. 2005, The Spectral Energy Distributions of Gas-Rich Galaxies: Confronting Models with Data, American Institute of Physics Conference Series 761.Ed.Popescu, C. C. & Tuffs, R. J.

Papaderos, P., Loose, H.-H., Fricke, K. J. and Thuan, T. X., 1996 A&A, 314, 59P

Papaderos, P., Loose, H.-H., Thuan, T. X. and Fricke, K. J.,1996 A&AS, 120, 207P

Papaderos, P., Izotov, Y. I., Fricke, K. J., Thuan, T. X. and Guseva, N. G., 1998 A&A, 338, 43P

Pasetto, S., Chiosi, C. and Carraro, G., 2003 A&A, 405, 931P

Pauldrach, A., Hoffmann, T.L., and Lennon, M. 2001 A&A. 375, 161

Pilyugin L. S., 1993, A&A, 277, 42

Pisano, D. J., Garland, C., Guzman, R., Perez-Gallego, J., Castander, F. and Gruel, N., 2007 AAS, 21114115P

Portinari L., Chiosi C. and Bressan A., 1998 A&A, 334, 505

Raimann, D., Storchi-Bergmann, T., Bica, E., Melnick, J. and Schmitt, H., 2000 MNRAS, 316, 559R

Rauch T., 2003 A&A 403, 709

Recchi, S. and Hensler, G., 2004 ANS, 325, 63R

Recchi, S., Matteucci, F., D'Ercole, A. and Tosi, M., 2004 A&A, 426, 37R

Recchi, S., Matteucci, F. and D'Ercole, A., 2001 MNRAS.322, 800R

Recchi, S., Matteucci, F., D'Ercole, A. and Tosi, M., 2002 A&A, 384, 799R

Recchi, S., Matteucci, F., D'Ercole, A. and Tosi, M., 2003 Ap&SS, 284, 623R

Roy J.-R., Kunth D., 1995, A&A, 294, 432

Ruiz-Lapuente P., Blinnikov S., Canal R., Mendez J., Sorokina E., Visco A. and Walton N., 2000, Memorie della Societa Astronomica Italiana, 71, 435

Sánchez Almeida, J., Muñoz-Tuñón, C., Amorín, R., Aguerri, J. A., Sánchez-Janssen, R. and Tenorio-Tagle, G., 2008 ApJ, 685, 194S

Salpeter, E.E. 1955 ApJ, 121, 161

Salzer, J. J.,1989 ApJ, 347, 152S

Salzer, J. J. and Norton, S. A., 1999 ASPC, 170, 253S

Salzer J. J., Moody J. W., Rosenberg J. L., Gregory S. A.and Newberry M. V., 1995 AJ, 109, 2376

Sargent W. L. W. and Searle L., 1970 ApJ, 162, L155

Scalo J. M., 1986, Fundamentals of Cosmic Physics, 11, 1

Scalo J., 1998, in ASP Conf. Ser. 142: The Stellar Initial Mass Function (38th Herstmonceux Conference), 201

Schombert, J. M., McGaugh, S. S. and Eder, J. A., 2001 AJ, 121, 2420S,

Schulte-Ladbeck, R. E. and Hopp, U., 1998 AJ, 116.2886S

Searle, L., Sargent, W. L. W. and Bagnuolo, W. G., 1973 ApJ, 179, 427S

Shi F., Kong X. and Cheng F.-Z., 2006, Chinese Journal of Astronomy and Astrophysics, 6, 641

Silk, J., Wyse, R. F. G. and Shields, G. A., 1987 ApJ, 322L, 59S

Simpson, C. E., Gottesman, S. T., 2000 AJ., 120.2975S

Skillman, E. D. and Bender, R.,1995 RMxAC, 3, 25S

Skillman E. D., Kennicutt R. C., Jr., 1993, ApJ, 411, 655

Smith, J. A. Tucker, D. L. Kent, S. Richmond, M. W., Fukugita, M., Ichikawa, T., Ichikawa, S.-i., Jorgensen, A. M., Uomoto, A., Gunn, J. E., Hamabe, M., Watanabe, M., Tolea, A., Henden, A., Annis, J., Pier, J. R., McKay, T. A., Brinkmann, J., Chen, B., Holtzman, J., Shimasaku, K.and York, D. G. 2002 AJ., 123.2121S

Smith, L., Norris, R., & Crowther, P. 2002 MNRAS, 337, 1309

Stasińska, G. 1978 A&A 66,257

Stasińska, G., 2002 RMxAC, 12, 62S.

Stasińska, G., 2005, A&A 434,507.

Stasińska G. and Izotov Y., 2003 A&A, 397, 71

Stasińska, G. and Leitherer, C. ,1996 ApJSS, 107, 661-691.

Stasińska, G., Schaerer, D. and Leitherer, C., 2001 A&A, 370, 1S

Sung, E.-C., Chun, M.-S., Freeman, K. C. and Chaboyer, B., 2002 ASPC, 273, 341S

Tajiri, Y. Y. and Kamaya, H., 2002 A&A, 389, 367T

Talbot R. J., Jr., and Arnett W. D., 1973, ApJ, 186, 51

Taylor C. L., Brinks E., Pogge R. W., Skillman E. D., 1994, AJ, 107, 971

Telles, E. and Terlevich, R., 1995 MNRAS.275., 1T

Telles E. and Terlevich R., 1997 MNRAS, 286..183T

Telles E., Melnick J. and Terlevich R., 1997 MNRAS, 288, 78T

Terlevich R., Melnick J., Masegosa J., Moles M. and Copetti M. V. F., 1991 A&ASS, 91, 285

Terlevich R., Silich S., Rosa-González D. and Terlevich E., 2004 MNRAS, 348, 1191

Thuan, T. X., 1985 ApJ, 299, 881T

Thuan T. X. and Izotov Y. I., 2005 ApJ, 627, 739

Thuan, T. X. and Izotov, Y. I. and Lipovetsky, V. A.,1995 ApJ, 445, 108T

Thuan, T. X., Izotov, Y. I. and Lipovetsky, V. A., 1997 ApJ, 477, 661T

Tinsley, B. M., 1968 ApJ, 151, 547T,

Tolstoy E., 2003, Ap&SS, 284, 579

Tosi, M., Greggio, L., Marconi, G. and Focardi, P.,1991 AJ., 102, 951T

van den Hoek, L. B., de Blok, W. J. G., van der Hulst, J. M. and de Jong, T., 2000 A&A, 357, 397V

van Zee, L., Haynes, M. P. and Salzer, J. J. 1997AJ, 114, 2479V

van Zee, L.,2001 AJ., 121.2003V

van Zee L., Barton E. J., Skillman E. D., 2004, AJ, 128, 2797

van Zee, L. & Haynes, M.P., 2006, ApJ, 636, 214V

Vanzi L., Rieke G. H., Martin C. L., Shields J. C., 1996, ApJ, 466, 150

Vazdekis, A., Peletier, R. F., Beckman, J. E. and Casuso, E., 1997 ApJS, 111, 203V

Vázquez G. A., Carigi L., and González J. J., 2003 A&A, 400, 31

Vázquez G. A., Leitherer C., Schaerer D., Meynet G., Maeder A., 2007, ApJ, 663, 995

Werk, J. K., Jangren, A. and Salzer, J. J., 2004 ApJ, 617.1004W

Woosley S. E. and Weaver T. A., 1995 ApJS, 101, 181

Wyse R. F. G., 1997 ApJL, 490, L69

Wyse, R. F. G. and Silk, J., 1985 ApJ, 296L, 1W

Yakobchuk, T. N. *Kinematics and Physics of Celestia Bodies*, 2008, Vol.24, No. 1, pp 10-18. Edit. Allerton Press, Inc. 2008.

Yin S.Y., Liang Y.C., Hammer F., Brinchmann J., Zhang B., Deng L.C. and Flores H., 2007 A&A, 462, 535Y

York D. G., et al., 2000 AJ, 120, 1579

Zaritski, D., Kennicutt, R.C., and Huchra, J.P, 1994 ApJ, 420, 87-109